# ORDER EVOLUTION IN Ni-Cr-Mo ALLOYS

*By*

**AMIT VERMA**

(Enrolment No. PHYS 01200904006)

**BHABHA ATOMIC RESEARCH CENTRE**

***A thesis submitted to the***
***Board of Studies in Physical Sciences***

***In partial fulfillment of requirements***
***for the Degree of***

**DOCTOR OF PHILOSOPHY**

***of***

**HOMI BHABHA NATIONAL INSTITUTE**

**August, 2015**

# Homi Bhabha National Institute

## Recommendations of the Viva Voce Committee

As members of the Viva Voce Committee, we certify that we have read the dissertation prepared by Amit Verma entitled "Order Evolution in Ni-Cr-Mo Alloys" and recommend that it may be accepted as fulfilling the thesis requirement for the award of Degree of Doctor of Philosophy.

| | |
|---|---|
| Chairman – Dr. S. L. Chaplot | **Date:** |
| Guide / Convener – Dr. J. B. Singh | **Date:** |
| Examiner - Dr. N. K. Mukhopadhyay | **Date:** |
| Member 1 – Dr. M. Vijayalakshmi | **Date:** |
| Member 2 – Dr. N. Prabhu | **Date:** |
| Member 3 – Dr. Madangopal K. | **Date:** |

Final approval and acceptance of this thesis is contingent upon the candidate's submission of the final copies of the thesis to HBNI.

I/We hereby certify that I/we have read this thesis prepared under my/our direction and recommend that it may be accepted as fulfilling the thesis requirement.

**Date:**

**Place:**

**Dr. J. B. Singh**
**(Guide)**

# STATEMENT BY AUTHOR

This dissertation has been submitted in partial fulfillment of requirements for an advanced degree at Homi Bhabha National Institute (HBNI) and is deposited in the Library to be made available to borrowers under rules of the HBNI.

Brief quotations from this dissertation are allowable without special permission, provided that accurate acknowledgement of source is made. Requests for permission for extended quotation from or reproduction of this manuscript in whole or in part may be granted by the Competent Authority of HBNI when in his or her judgment the proposed use of the material is in the interests of scholarship. In all other instances, however, permission must be obtained from the author.

AMIT VERMA

# DECLARATION

I, hereby declare that the investigation presented in the thesis has been carried out by me. The work is original and has not been submitted earlier as a whole or in part for a degree / diploma at this or any other Institution / University.

AMIT VERMA

# List of Publications arising from the thesis

## International Journals

1. "Delineating the Roles of Cr and Mo during Ordering Transformations in Stoichiometric $Ni_2(Cr_{1-x},Mo_x)$ Alloys", **A. Verma**, J.B. Singh, N. Wanderka, J.K. Chakravartty, *Acta Materialia*, **2015**, 96, 366-377.
2. "Abnormal kinetics of ordering transformation in $Ni_2(Cr_{0.5}, Mo_{0.5})$ alloy", **A. Verma**, J.B. Singh, J.K. Chakravartty, *Journal of Alloys and Compounds*, **2015**, 639, 341-345.
3. "On the evolution of long-range order from short-range order in a $Ni_2(Cr_{0.5}Mo_{0.5})$ alloy", **A. Verma**, N. Wanderka, J. B. Singh, M. Sundararaman, J. Banhart, *Journal of Alloys and Compounds*, **2014**, 586, 561-566.
4. "Statistical analysis of composition fluctuations and short-range order in stoichiometric Ni–Cr–Mo alloys", **A. Verma**, N. Wanderka, J.B. Singh, B. Kumar, J. Banhart, , *Ultramicroscopy*, **2013**, 132, 227-232.
5. "Resistivity and Transmission Electron Microscopy Investigations of Ordering Transformation in Stoichiometric $Ni_2(Cr_{0.5}Mo_{0.5})$ Alloy", **A. Verma**, J. B. Singh, M. Sundararaman, N. Wanderka, *Metallurgical and Materials Transactions A*, **2012**, 43, 3078-3085.

## Under Preparation

6. Stability of $Ni_2(Cr_{1-x}Mo_x)$ superstructure in stoichiometric $Ni_2(Cr,Mo)$ alloys using x-ray diffraction and 3-dimenisonal atom probe evidences.

## Conferences

1. "Disorder-order transformation in stoichiometric $Ni_2(Cr,Mo)$ alloys" **A. Verma**, J. B. Singh, N. Wanderka, J. Kishor, J. K. Chakravartty, *Poster presented at National conference on Advanced technologies for material processing and diagnostics held at cochin, Kerala,* **18th to 20th September 2014.**

2. “Ordering mechanisms in stoichiometric $Ni_2$(Cr,Mo) alloys”, **A. Verma**, N. Wanderka, J. B. Singh, J. K. Chakravartty, J. Banhart; *International conference on Atom Probe Tomography and Microscopy (APT&M); Stuttgart, Germany,* **2014.**
3. “Order transformation in $Ni_2$(Cr,Mo) alloy”, **A. Verma**, N. Wanderka, N. Lazarev, J.B. Singh, M. Sundararaman, J. Banhart, *International Field emission symposium (IFES), May 21-25, Tuscaloosa, Albama, USA,* **2012**.
4. “Short Range Order and its Correlation with Anti Phase Boundaries in $Ni_2$(Cr,Mo) Alloy”, **A. Verma**, N. Wanderka, N. Lazarev, J.B. Singh, M. Sundararaman, *Verhandlungen der Deutschen Physikalischen Gesellschaft, March 25-30, Berlin*, **2012**.
5. “Order-Disorder Transformation in a Ni-Cr-Mo Alloy”, **A. Verma**, J. B. Singh, M Sundararaman, N. Wanderka, *TMS, March 11-15, Orlando, FL,* **2012**.
6. “Ordering Processes in $Ni_2$(Cr,Mo) Alloy Investigated by TEM and 3D-AP,N. Wanderka”, **A. Verma**, Nikolai Lazarev, M Sundararaman, J.B. Singh, *TMS, March 11-15, Orlando, FL,* **2012.**
7. “Ordering transformation and its microstructural characterization in $Ni_2(Cr_{0.5}Mo_{0.5})$ alloy”, **A. Verma,** N. Wanderka, N. Lazarev, M. Sundararaman, J. Banhart, *Euromat, Montpellier, France 12-15 September,* **2011**.

AMIT VERMA

## DEDICATIONS

*Dedicated to my mother, father, sister, brother*

*my wife and my little angel*

# ACKNOWLEDGEMENTS

I would like to express my sincere gratitude towards Dr. J. B. Singh for his guidance, continuous support, and encouragement throughout my dissertation work. I would like to express my gratitude to Dr. M. Sundararaman for innumerable discussions and guidance during my formative years.

A part of the experimental work presented here was carried out at Helmholtz-Zentrum Berlin (HZB), Berlin under the collaborative research program between BARC, India and HZB, Berlin. I would like to express my sincere gratitude to Dr. Nelia Wanderka for introducing me to the powerful analytical tool 3-dimenional atom probe and for her continuous support during this work. Valuable discussions on the TEM work are also gratefully acknowledged. Her great joy of getting new results and encouragements always motivated me. I would also like to thank Dr. Florian Vogel, Dr. Anna Manzoni, Ms. Claudia Leistner and Ms. Christiane Förster from HZB for their continuous support and advice during the work carried out at HZB. I am also grateful to Drs. John Banhart and Fransisco Moreno for making my stay comfortable at HZB. I express my sincere gratitude to Dr. Christian Abromeit for initiating the collaborative research program, which gave me the opportunity to visit HZB and gain a world class research experience.

I am thankful to Dr. J. K. Chakravartty, Director, Materials Group & Head, Mechanical Metallurgy Division, for constant encouragement and keen interest in the work.

I thank Dr. Madangopal Krishnan, Head, Glass and Ceramics Division, for many fruitful discussions that have helped me during the course of the work. I would also like to thank Dr. B. C. Maji for his always readiness to help during the work.

I thank Dr. U. D. Kulkarni, Head, Metal Science Section, Materials Science Division, for many fruitful discussions that have helped me during the course of the work.

I wish to acknowledge my colleagues Kum. Shabana Khan, Kum. Malvika K., Shri Manoj Thota and Shri Sandeep Kumar for their constant support during this work.

I also thank Dr. Jyoti Prakash, Dr. Bhaskar Paul, Shri Brij Kumar and Dr. Sandeep Sharma for their support and constant encouragement.

Finally, I gratefully acknowledge my family members for their immense support. I would like to specially acknowledge my wife and daughter who supported me throughout the work that helped me to sail through the difficult times. Their understanding and smiles encouraged me to complete the work.

# CONTENTS

**Page No:**

# SYNOPSIS

## 1. Motivation

Ni-Cr-Mo-base alloys such as HASTELLOYS C-4, C-22, and C-276, HASTELLOY S, HAYNES 242, Alloy 625, and Alloy 686 are important alloys for chemical and nuclear industries due to their excellent corrosion, oxidation and pitting resistance properties with good mechanical strength at elevated temperature [1]. Most of them are normally used in solid solution condition and are generally considered non-hardenable by conventional ageing treatments. However, prolonged ageing of these alloys in the temperature range of 400 °C to 700 °C results in the precipitation of a long-range order (LRO) $Ni_2(Cr,Mo)$ phase (which has a $Pt_2Mo$ prototype oI6 structure) from the disordered face-centered-cubic (fcc) matrix [2, 3]. Formation of the $Ni_2(Cr,Mo)$ phase results in reduction of the solute contents, mainly Cr and Mo, in the matrix, which leads to degradation in the corrosion and oxidation resistance properties and increase in mechanical strengths of the alloys. Further, formation of the ordered $Ni_2(Cr,Mo)$ phase occurs via an intermediate short-range order (SRO) state. Such SRO is believed to form due to localized compositional changes or chemical heterogeneities in the disordered crystalline state, which are introduced either due to statistically favoured tendency of unlike atoms to be the nearest neighbours or due to clustering of atoms [4]. There appears to be no experimental study correlating SRO with chemical heterogeneities, though theoretical studies by Kulkarni et al. [5] suggests the existence of heterogeneities of $N_2M_2$ type in binary Ni-Mo alloys exhibiting SRO.

Further, evolution kinetics of the $Ni_2(Cr,Mo)$ phase varies from one alloy to another, probably, due to different concentrations of Cr and Mo solutes in them. For example, this phase forms after prolonged ageing in Alloy 625 (containing Cr = 25.5 and Mo = 5.64 (at.%)) [6], while, it forms within a short time in Haynes 242 (containing Cr = 9.7 and Mo = 16.5

(at.%)) [7]. A recent theoretical study by Hu et al. [8] have suggested that $Ni_2(Cr_{1-x}Mo_x)$ superlattices are energetically more stable relative to $Ni_2Cr$ up to x = 0.25, while least stable for x = 0.5. They have attributed this difference to a change in the nature of atomic bonding from covalent type character in alloys up to $Ni_2(Cr_{0.75}Mo_{0.25})$ compositions to metallic type in $Ni_2(Cr_{0.5}Mo_{0.5})$ alloy. These studies suggest a role of the relative concentrations of Cr and Mo atoms on the stability and evolution kinetics of the ordered $Ni_2(Cr,Mo)$ and micro-mechanisms associated with it.

## 2. Objectives

The objectives of the dissertation are:

(i) Characterization of SRO and its correlation with chemical heterogeneities present in stoichiometric Ni-Cr-Mo alloys with different Cr and Mo solutes;

(ii) Effect of Cr and Mo solutes on ordering transformation in stoichiometric Ni-Cr-Mo alloys;

(iii) Effect of SRO on ordering kinetics in Ni-Cr-Mo alloys;

(iv) Stability of the $Ni_2(Cr_{1-x},Mo_x)$ superstructure with respect to Cr and Mo solutes in stoichiometric $Ni_2(Cr,Mo)$ alloys.

## 3. Experimental

To meet above objectives, ternary Ni-Cr-Mo alloys of $Ni_2(Cr_{1-x}Mo_x)$ (where, x = 0, 0.25, 0.37, 0.5) stoichiometry prepared by non-consumable vacuum arc melting were investigated with following initial microstructures: (i) as solution treated condition; (ii) as splat-quenched conditions; (iii) aged condition. Ordering kinetic studies were carried out by ageing these alloys at temperatures from 525°C to 750°C for different time periods ranging from 2 min to 500 h. Order evolution studies were carried out using resistivity, differential scanning calorimeter (DSC), X-ray diffraction and transmission electron microscopy (TEM). Chemical heterogeneities and compositions of long-range ordered nano-sized domains were identified employing a voltage-pulsed 3-dimenional atom probe (3D-AP) technique. Different statistical approaches were used to analyze the nature of chemical heterogeneities. Microhardness of alloys was measured using a Vicker's hardness tester with a load of 1 Kg.

## 4. Salient Results and Discussion

**(i)** Arc-melted $Ni_2Cr_{0.63}Mo_{0.37}$ and $Ni_2Cr_{0.5}Mo_{0.5}$ alloys in solution treated condition exhibited SRO characterized by the presence of diffuse intensity maxima at {1 ½ 0} and 1/3{2 2 0} positions in the electron diffraction patterns (Fig. 1). While binary Ni-Mo and ternary Ni-Cr-Mo alloys with off-stoichiometric composition are known to exhibit a SRO characterized by diffuse diffraction intensity maxima at {1 ½ 0} positions (termed as {1 ½ 0} SRO) [5, 7, 9], the existence of additional diffuse intensity maxima at 1/3{2 2 0} positions suggested the presence of a different SRO in the investigated alloys. Superlattice reflections at 1/3{2 2 0}

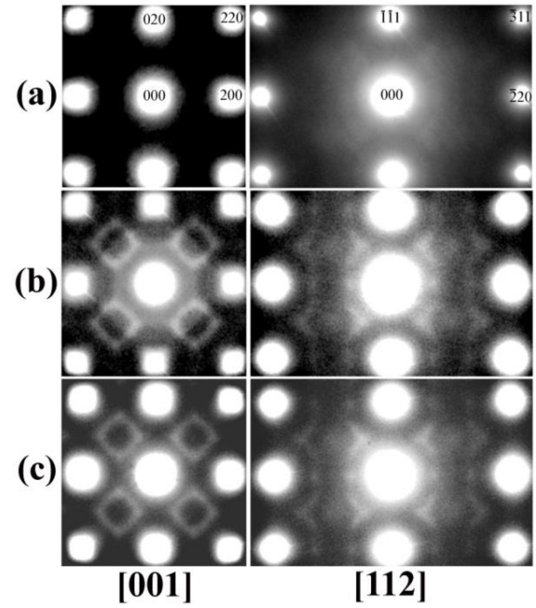

**Figure 1:** SAED patterns with [001] and [112] zone axes obtained from (a) $Ni_2Cr$ (b) $Ni_2(Cr_{0.63}Mo_{0.37})$ and (c) $Ni_2(Cr_{0.5}Mo_{0.5})$ alloys in solution treated and water quenched state. The presence of diffuse intensity maxima revealed the existence of short-range order.

positions in the reciprocal space are characteristic of a $Ni_2(Cr,Mo)$ ordered phase [6]. On the contrary, electron diffractions of solution treated binary $Ni_2Cr$ alloy did not reveal any diffuse intensity maxima (Fig. 1) though the existence of {1 ½ 0} SRO has been reported in $Ni_2Cr$ on the basis of diffuse neutron scattering studies [10] and the same was confirmed using resistivity during the present study also. Inability of the TEM to reveal SRO in $Ni_2Cr$ is due to nearly similar atomic scattering factors of Ni and Cr atoms. Since $Ni_2(Cr_{0.75}Mo_{0.25})$ alloys exhibited similar ordering characteristics (shown later), similar SRO was presumed to exist in the two alloys. Statistical analysis of 3D-AP data of solution treated $Ni_2Cr$ and $Ni_2Cr_{0.5}Mo_{0.5}$ alloys revealed the predominant presence of chemical heterogeneities of Ni-25at%Cr type in $Ni_2Cr$ alloy and of Ni-50at%(Cr+Mo) type in $Ni_2Cr_{0.5}Mo_{0.5}$ alloy [11]. The sizes of two heterogeneities were about 7.4 nm and 8 nm, respectively. This indicated that there existed certain correlation between the observed SRO and chemical heterogeneities in the two alloys. It is important to mention here that sizes of chemical heterogeneities measured from the 3D-AP data represented the spatial extent of regions within which a few sub-nanometer sized domains having statistically favored atomic arrangements existed. It was presumed here that these sub-nanometer size domains caused the appearance of diffuse intensity maxima.

**(ii)** A systematic study on the order evolution in $Ni_2(Cr_{1-x}Mo_x)$ alloys established that the kinetics of the order evolution is governed by the Cr and Mo solutes in these alloys. This was established by combined analysis of high temperature resistivity, TEM and DSC studies on solution treated alloys during heating (@ 5°C/min). In $Ni_2Cr$ and $Ni_2(Cr_{0.75}Mo_{0.25})$ alloys, resistivity exhibited three distinct temperature regimes as shown in Figs. 2a and 2b. Resistivity profiles of $Ni_2(Cr_{0.63}Mo_{0.37})$ and $Ni_2(Cr_{0.5}Mo_{0.5})$ alloys exhibited five distinct temperature regimes (shown only for $Ni_2(Cr_{0.5}Mo_{0.5})$ in Fig. 2c). Regime I (from RT to, say, T1 temperature) exhibited a normal linear increase in resistance due to increase of electron-phonon scattering with increase in temperature. Regime II (between T1 and T2) was marked

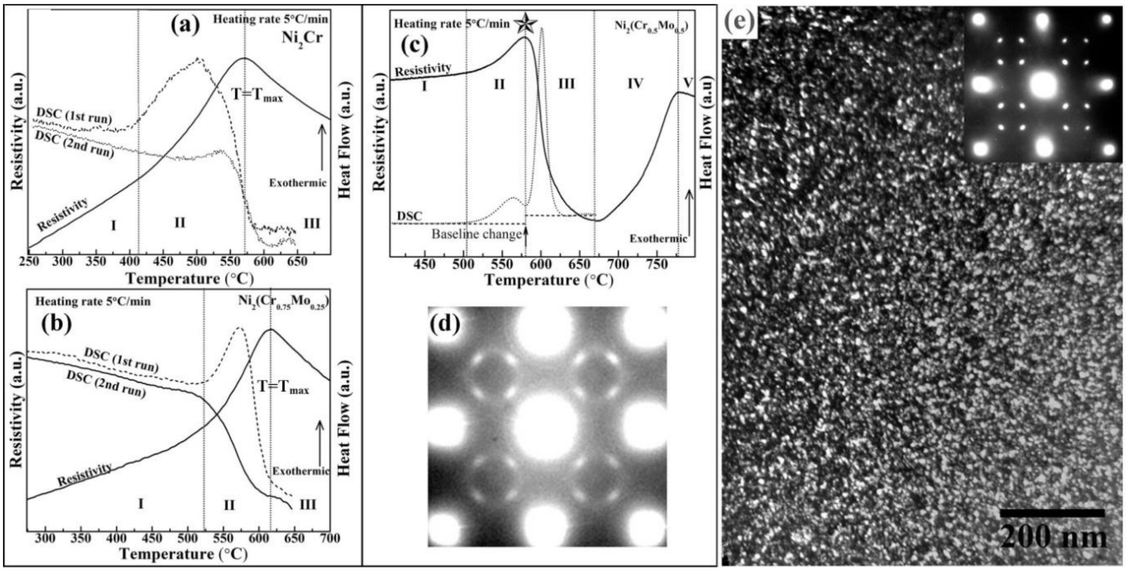

**Figure 2:** (a) to (c) Superimposed resistivity and DSC plots obtained during heating of: (a) $Ni_2Cr$; (b) $Ni_2(Cr_{0.75}Mo_{0.25})$ and (c) $Ni_2(Cr_{0.5}Mo_{0.5})$ alloys. In all cases baseline shift appeared at a temperature corresponding to the resistivity maxima separating regime II from III (shown by a dotted line). (d) <001> zone axes SAED pattern of the $Ni_2(Cr_{0.5}Mo_{0.5})$ alloy, arrested at a temperature marked by a star in (c) during heating, showing distinct LRO reflections and near extinction of SRO intensity. (e) dark field-TEM micrograph of long range ordered phase showing the presence of well developed ordered domains in $Ni_2(Cr_{0.5}Mo_{0.5})$ alloy formed during heating at the end of 2nd exothermic peak in DSC.

by a sharp increase in resistance due to the evolution of SRO. Regime III corresponded to a sharp drop in resistance from T2 to T3 due to the evolution of LRO. Regime IV was again marked by a sharp increase in resistance from T3 due to the dissolution of LRO up to a temperature T4. An interesting feature of the regime V (above T4 to 900 °C) was a slow decrease in resistance with temperature in contrast to that observed in regime I. The anomalous decrease in resistance in region V was attributed to the reappearance of SRO after the dissolution of LRO [12]. Correlation of resistivity behaviour with SRO / LRO in each regime was established on the basis of TEM studies carried out on samples taken by interrupting isochronal heating at different stages of order evolution [12]. On the basis of resistivity studies and TEM investigation it was established that, during order evolution in

$Ni_2Cr_{0.5}Mo_{0.5}$ alloy, 1/3{220} SRO evolved first which then transformed into LRO. On further heating, dissolution of the LRO to fully disordered state took place via an intermediate SRO state again. A similar order evolution mechanism was observed in $Ni_2Cr_{0.63}Mo_{0.37}$ alloy albeit with slower kinetics. However, isochronal resistivity studies on $Ni_2Cr_{0.75}Mo_{0.25}$ and $Ni_2Cr$ alloys exhibited only the evolution of SRO [13].

Isochronal DSC studies were carried out on solution treated Ni-Cr-Mo alloys in the temperature range from room temperature (RT) to 680 °C in two consecutive heating cycles. During the 1st heating cycle, both $Ni_2Cr$ and $Ni_2(Cr_{0.75}Mo_{0.25})$ alloys exhibited the presence of weak exothermic peaks superimposed with a baseline shift which appeared at the end of the peak at a temperature corresponded to the maximum ordering temperature ($T_{max}$) (see Figs. 2a and 2b). These exothermic peaks were absent during the 2nd heating cycle though the characteristic feature of baseline shift, which appeared during 1st heating cycle, remained during the 2nd heating cycle as well (Figs. 2a and 2b). Since exothermic / endothermic peaks and a baseline shift in a DSC thermogram are characteristics of 1st order and 2nd order transformations respectively [14], both 1st order as well as 2nd order mechanisms appeared to be involved in the ordering of $Ni_2Cr$ and $Ni_2(Cr_{0.75}Mo_{0.25})$ alloys. The observation of only baseline shift during the 2nd heating cycle suggested that a 2nd order transformation mode would have continued to operate in the absence of excess quenched-in defects which were eliminated during the 1st heating cycle. In $Ni_2Cr$ and $Ni_2(Cr_{0.75}Mo_{0.25})$ alloys, formation of the ordered phase could not complete during isochronal heating as its formation was associated with larger incubation time [15]. However, during isochronal heating, these alloys still exhibited a tendency of ordering transformation via the evolution of 1/3{2 2 0} SRO for temperature, $T < T_{max}$. Evolution of the 1/3{2 2 0} SRO appeared to be associated with an exothermic peak during isochronal heating. For temperatures, $T \geq T_{max}$, these alloys exhibited a tendency to form {1 ½ 0} SRO via a 2nd order transformation mode as suggested by the baseline shift at T = $T_{max}$ (Fig. 2a and 2b). This was also supported by symmetry considerations of the SRO structure, since $N_2M_2$ structure responsible for the appearance of {1 ½ 0} SRO [5, 11, 16] satisfies all the three Landau-Lifshitz-symmetry rules of 2nd order transformation [5, 17]. Due to sluggish ordering kinetics, the SRO (either 1/3{2 2 0} or {1 ½ 0}) had barely reached its maximum attainable value during heating cycles which caused the appearance of baseline shift at $T_{max}$ in consecutive heating cycles. Further increase of Mo-content in alloys to $Ni_2(Cr_{0.63}Mo_{0.37})$ and $Ni_2(Cr_{0.5}Mo_{0.5})$ resulted in the appearance of two distinct exothermic peaks in each alloy during the 1st heating cycle (shown only for $Ni_2(Cr_{0.5}Mo_{0.5})$ in Fig. 2c). However, during the 2nd heating cycle, both the exothermic peaks disappeared in both the alloys. This implied the absence of any ordering transformation in the thermogram obtained during 2nd heating cycle. The 2nd heating cycle, thus, could be used as a true baseline response of the calorimeter as it was obtained in identical experimental conditions of 1st heating cycle. Interestingly, a baseline correction after subtracting thermogram obtained during 2nd heating cycle from 1st heating cycle revealed a baseline shift at the end of 1st exothermic peak (marked by arrow in Fig. 2c) in these alloys also. Microscopic evidences of samples arrested at the end of both exothermic peaks in $Ni_2(Cr_{0.5}Mo_{0.5})$ alloy was used to understand the microstructural changes occurring at the end of each exothermic peaks. It was found that diffuse 1/3{2 2 0} SRO reflections transformed into sharp reflections at the end of 1st exothermic peak (Fig. 2d), while well developed LRO domains appeared after the finish of 2nd exothermic peak (Fig.2e). It was, therefore, concluded that the 1st exothermic peak contributed to the formation of ordered phase via a continuous ordering mechanism, while the 2nd exothermic peak appeared to be due to the growth of these ordered domains. Resistivity and calorimetry studies together suggested that

the evolution of the ordered $Ni_2(Cr,Mo)$ phase would occur via a continuous ordering mechanism involving both 1st order and 2nd order transformation mode, while the growth/dissolution of ordered phase would occur via 1st order mode. The 2nd order transformation mode would also operate during the transition of the alloy from long-range order to short-range order state.

Activation energies determined by kinetic analysis of different exothermic peaks in these alloys are given in Table 1. It could be seen from Table 1 that the activation energies for the 1st exothermic peak in $Ni_2(Cr_{0.75}Mo_{0.25})$ and $Ni_2(Cr_{0.63}Mo_{0.37})$ alloys were about 298 ± 15.8 kJ/mol and 295 ± 10.5 kJ/mol, respectively, which were almost similar. These values were close to lattice diffusion of Cr in Ni-Cr alloy [18] which implied that the formation of ordered phase in two alloys is governed by lattice diffusion of Cr. The increase of Mo-content to $Ni_2(Cr_{0.5}Mo_{0.5})$ composition, however, decreased its activation energy to about 247 ± 9.8 kJ/mol and increased the ordering kinetics as mentioned earlier. This decreased activation energy in $Ni_2(Cr_{0.5}Mo_{0.5})$ alloy could be correlated with weaker atomic bonding in this alloy which allowed the diffusion of Mo to contribute the formation of ordered phase [8, 13]. On the basis of the present study, it was concluded that the $Ni_2(Cr,Mo)$ phase evolves with a sluggish ordering kinetics when its formation was governed only by the lattice diffusion of Cr, but its kinetics increased in alloys beyond certain Cr and Mo solute concentration when

**Table 1:** Activation energy values obtained by Kissinger and Augis-Bennett methods in $Ni_2(Cr_{1-x}Mo_x)$ alloys.

| **Methods** | **Activation energy in kJ/mol$^{-1}$** | | | | |
|---|---|---|---|---|---|
| | **$Ni_2(Cr_{0.75}Mo_{0.25})$** | **$Ni_2(Cr_{0.63}Mo_{0.37})$** | | **$Ni_2(Cr_{0.5}Mo_{0.5})$** | |
| | | **1st Peak** | **2nd Peak** | **1st Peak** | **2nd Peak** |
| **Kissinger** | 296.3 ± 15.8 | 293.5 ± 10.5 | 204.5 ± 2.8 | 247.5 ± 9.7 | 253.0 ± 4.6 |
| **Augis-Bennett** | 299.6 ± 15.8 | 295.7 ± 10.5 | 207.9 ± 2.9 | 245.5 ± 9.8 | 256.9 ± 4.6 |
| **Average** | 298 ± 15.8 | 294.6 ± 10.5 | 206.2 ± 2.9 | 246.5 ± 9.8 | 255.0 ± 4.6 |

lattice diffusion of Mo also started contributing to its formation. This change was found to occur at $Ni_2(Cr_{0.5}Mo_{0.5})$ composition. On the contrary, the activation energy value associated with the 2nd exothermic peak increased from 206 ± 2.9 kJ/mol (in $Ni_2(Cr_{0.63}Mo_{0.37})$) to 255 ± 4.6 kJ/mol alloy in $Ni_2(Cr_{0.5}Mo_{0.5})$ alloy. Nearly similar activation energies (~ 250 kJ/mol) for formation and growth peak in $Ni_2(Cr_{0.5}Mo_{0.5})$ alloy signified identical diffusing species for the formation and growth processes, while a much smaller value (~ 206 kJ/mol) for the growth in $Ni_2(Cr_{0.63}Mo_{0.37})$ alloy could be attributed to the diffusion of Mo in Cr [13].

**(iii)** Existence of the SRO appeared to play an important role on the evolution of $Ni_2(Cr,Mo)$ ordered phase in Ni-Cr-Mo alloys. In order to study the effect of SRO on the evolution of order, above mentioned investigations were also carried out on splat-quenched alloys. TEM investigations of splat-quenched $Ni_2Cr_{0.63}Mo_{0.37}$ and $Ni_2Cr_{0.5}Mo_{0.5}$ alloys did not reveal the presence of any SRO in either alloy, though the alloys retained crystallinity in the splat-quenched state which was confirmed by TEM and x-ray diffraction evidences. Instead, the SRO could be induced during ageing in the temperature range 525°C to 750°C. Ageing of the splat-quenched $Ni_2Cr_{0.5}Mo_{0.5}$ alloy revealed the simultaneous appearance of diffuse intensity maxima at {1 ½ 0} and 1/3{220} positions after 120 min and 10 min at 525°C and 625°C temperatures, respectively, and within 2 min at 700°C as well as 750°C. On further ageing, the SRO started transforming to LRO after about 300 min, 30 min, 5 min and 10 min at the four temperatures, respectively. Though sharp reflections of ordered phase could be developed after 5 min of ageing at 700°C, but was superimposed with traces of diffuse intensity of the {1 ½ 0} SRO. This suggested that the formation of ordered domains would have occurred via nucleation and growth mode at ageing temperatures ≥ 700°C. The same alloy in the solution treated state revealed the transition of SRO to LRO within 60 min and 3 min, at 525°C and 625°C temperatures respectively, and well developed ordered domains formed within 2 min at 700°C. Microstructural observations of SRO and LRO on splat-quenched and solution treated $Ni_2Cr_{0.5}Mo_{0.5}$ alloys are given in Table 2. This investigation revealed a sluggish ordering kinetics in the splat-quenched state which was due to lower driving force for ordering due to the suppression of chemical heterogeneities in splat-quenched state (confirmed by 3D-AP) [19]. The suppression of chemical heterogeneities drastically modified the pair interactions which are primarily important for order evolution in the smaller amplitude limit of concentration waves [19, 20] and thus resulted in a sluggish ordering kinetics.

**(iv)** Stability of the $Ni_2(Cr_{1-x}Mo_x)$ superstructure was analyzed in the light of change in the microhardness, lattice parameter and composition of ordered domains in the ordered alloy. Room temperature microhardness study of these alloys in solution treated conditions revealed a linear increase of hardness up to x = 0.37 (i.e., from $Ni_2Cr$ to $Ni_2(Cr_{0.63}Mo_{0.37})$ alloys) followed by its decrease in $Ni_2(Cr_{0.5}Mo_{0.5})$ alloy (Fig. 3a). This was surprising because replacement of Cr by Mo in $Ni_2Cr$ alloys was expected to impart solid solution strengthening due to relatively bigger atomic size of the latter as observed in alloys with compositions up to $Ni_2(Cr_{0.63}Mo_{0.37})$. In a recent study, Hu et al. [8] have theoretically shown that in $Ni_2(Cr_{1-}$

**Table 2:** Microstructural observations of SRO and LRO on splat-quenched and solution treated $Ni_2Cr_{0.5}Mo_{0.5}$ alloys.

| Ageing Temperature | Microstructural state of $Ni_2(Cr_{0.5}Mo_{0.5})$ alloy | | | |
|---|---|---|---|---|
| | As-splat state | | Solution treated state | |
| | Incubation time for | | Incubation time for | |
| | SRO | LRO | SRO | LRO |
| 525 °C | 120 min | > 300 min | Already present | 120 min |
| 625 °C | 10 min | 60 min | Already present | 3 min |
| 700 °C | 2 min | 5 min | Already present | < 2 min |
| 750 °C | 2 min | 10 min | Already present | Not investigated |

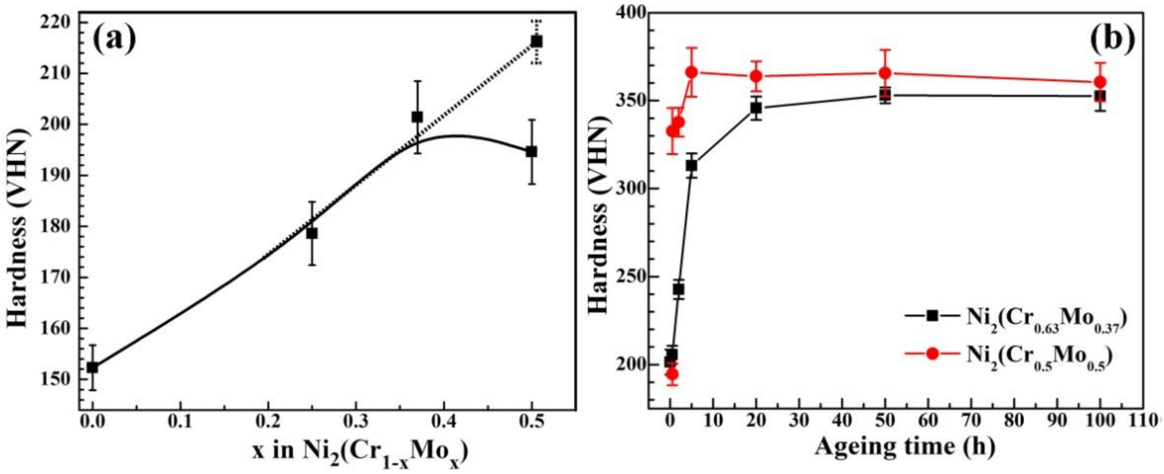

**Figure 3:** Plot of microhardness change; (a) with Mo-increase in stoichiometric $Ni_2(Cr_{1-x}Mo_x)$ alloys in solution treated and water quenched states and (b) of $Ni_2(Cr_{0.63}Mo_{0.37})$ and $Ni_2(Cr_{0.5}Mo_{0.5})$ alloys with ageing time at 680°C.

$_x$Mo$_x$) superstructures atomic bonding retains its covalent character up to $Ni_2(Cr_{0.63}Mo_{0.37})$ composition and changes to metallic type at $Ni_2(Cr_{0.5}Mo_{0.5})$ composition. This established a direct correlation between hardness and atomic bonding suggesting of weaker atomic bonding in $Ni_2(Cr_{0.5}Mo_{0.5})$ alloy. On the other hand, both $Ni_2(Cr_{0.63}Mo_{0.37})$ and $Ni_2(Cr_{0.5}Mo_{0.5})$ alloys in the ordered states exhibited similar hardness values (~ 350 VHN) (Fig. 3b). In the $Ni_2(Cr_{0.5}Mo_{0.5})$ alloy hardness could reach its maximum value within few minutes of ageing at 680°C, while few hours of ageing was required to attain the maximum hardness in the $Ni_2(Cr_{0.63}Mo_{0.37})$ alloy. $Ni_2Cr$ and $Ni_2(Cr_{0.75}Mo_{0.25})$ alloys required prolonged ageing times to reach a hardness plateau. Almost similar hardness of $Ni_2(Cr_{0.63}Mo_{0.37})$ and $Ni_2(Cr_{0.5}Mo_{0.5})$ alloys in the LRO state cannot be explained on the basis of weaker atomic bonding in the $Ni_2(Cr_{0.5}Mo_{0.5})$ superstructure as suggested by Hu et al. [8]. However, in view of the least stability of the $Ni_2(Cr_{0.5}Mo_{0.5})$ superstructure [8], possibility of other superstructures associated with higher stability could not be ruled out.

In order to explore the possibility of more than one superstructures, x-ray diffraction studies were carried out to monitor the change in lattice parameter during ageing of

$Ni_2(Cr_{0.63}Mo_{0.37})$ and $Ni_2(Cr_{0.5}Mo_{0.5})$ alloys at 680°C where ordering kinetics was maximum. This analysis was carried out by monitoring the position and broadening of the fundamental {111} peak as structure factor considerations limited the detection of superlattice peaks in the present case. Usually, a fundamental peak broadens due to strain effect and / or crystallite size, which would not have any significant influence during ageing in the present case. {111} peaks in both the alloys revealed a continuous increase of broadening with ageing time until they started splitting in two different peaks as shown in Fig. 4. Splitting of the peaks started after 50 h of ageing in both the alloys and the $Ni_2(Cr_{0.5}Mo_{0.5})$ alloy exhibited well separated peaks after 100 h. Microstructural evidences of both these alloys after 100 h of ageing confirmed nearly complete transformation of the disordered matrix into the order structure. The presence of well separated diffraction peak in the $Ni_2(Cr_{0.5}Mo_{0.5})$ alloy could, thus, be interpreted as an ordered structure with different lattice parameters, which could be correlated with two compositions.

In order to confirm the existence of ordered domains of two different compositions, 3D-AP investigations were carried on the two alloys aged for 100 h at 680°C. Compositional

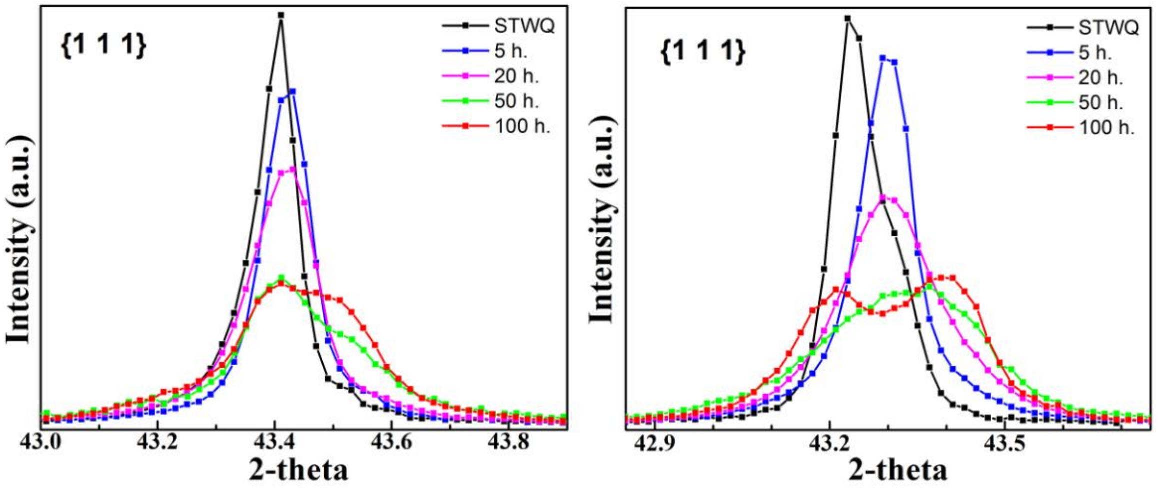

**Figure 4:** Peak broadening of X-ray diffraction peak with ageing time at 680°C from {111} planes in; (a) $Ni_2(Cr_{0.63}Mo_{0.37})$ alloy and (b) $Ni_2(Cr_{0.5}Mo_{0.5})$ alloys. The peak splitting was evident at ageing times of 50 h and 100 h in both the alloys.

analysis of ordered domains in $Ni_2Cr_{0.63}Mo_{0.37}$ alloy revealed them to be of two different compositions, viz., Ni-13.1at%Cr-20.2at%Mo and Ni-21.1at%Cr-12.5at%Mo, while there existed three different composition of ordered domains in $Ni_2(Cr_{0.5}Mo_{0.5})$ alloy, viz., Ni-12.6at%Cr-20.6at%Mo, Ni-21.5at%Cr-12.2at%Mo and Ni-18.7at%Cr-15.6at%Mo. This study, thus, revealed two common compositions of ordered domains, i.e. Mo-rich (~$Ni_2(Cr_{0.37}Mo_{0.63})$) and Cr-rich (~$Ni_2(Cr_{0.63}Mo_{0.37})$), in both the alloys. The existence of ordered domains with a third type of composition (close to $Ni_2(Cr_{0.5}Mo_{0.5})$ composition) in the $Ni_2(Cr_{0.5}Mo_{0.5})$ alloy could be due to un-partitioned composition left over in the alloy during the formation of Cr-rich and Mo-rich ordered domains. The absence of $Ni_2(Cr_{0.5}Mo_{0.5})$ superstructure in $Ni_2(Cr_{0.63},Mo_{0.37})$ alloy, further, established its least stability among other compositions. This analysis established a greater stability of the ordered structure at

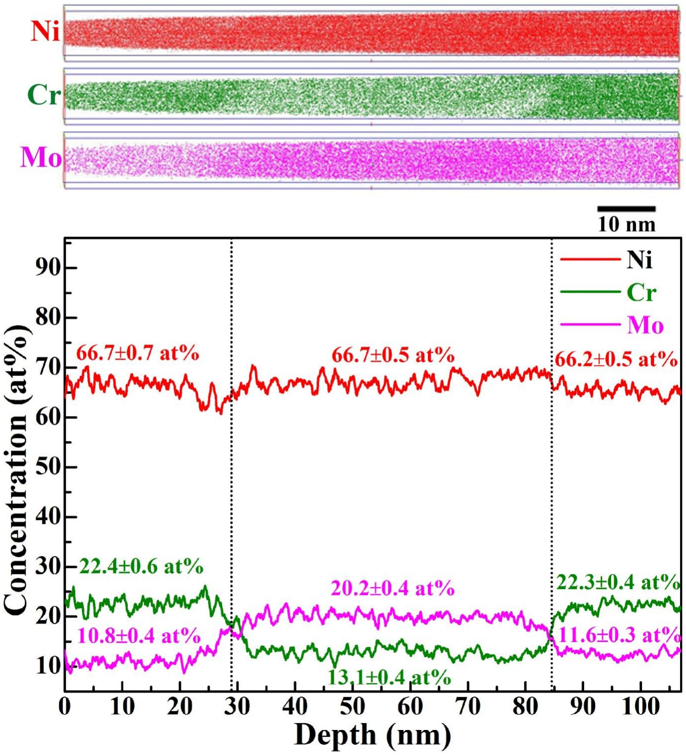

**Figure 5:** 3D-AP reconstruction map of Ni, Cr and Mo species in $Ni_2(Cr_{0.63}Mo_{0.37})$ alloy aged for 100 h at 680°C. The corresponding concentration profile along the length of the reconstruction revealed the presence of Cr-rich and Mo-rich ordered domains.

$Ni_2(Cr_{0.63}Mo_{0.37})$ and $Ni_2(Cr_{0.37}Mo_{0.63})$ compositions, suggesting that the ordered structure has the lowest formation energies at these compositions. This appeared to be at variance with the work of Hu et al. [8] who have identified minimum formation energy at $Ni_2(Cr_{0.75},Mo_{0.25})$ composition. This could be because they have not studied alloys between $Ni_2(Cr_{0.75},Mo_{0.25})$ to $Ni_2(Cr_{0.5},Mo_{0.5})$ compositions. The difference in the extent of x-ray peak splitting in $Ni_2(Cr_{0.63}Mo_{0.37})$ and $Ni_2(Cr_{0.5}Mo_{0.5})$ alloys could be due to the difference in amounts of Cr-rich and Mo-rich ordered domains in two alloys. Relative concentrations of Cr and Mo solutes would limit the volume fraction of Mo-rich ordered domains in $Ni_2(Cr_{0.63}Mo_{0.37})$ alloy.

## 5. Conclusion

- The present investigation established that SRO in $Ni_2(Cr_{0.63}Mo_{0.37})$ and $Ni_2(Cr_{0.5}Mo_{0.5})$ alloys was different from that in $Ni_2Cr$ and $Ni_2(Cr_{0.75}Mo_{0.25})$ alloys by the presence of additional diffuse diffraction intensity spots at 1/3{220} positions in the former. The different SRO in these alloys was correlated with different types of chemical heterogeneities.
- The increase of Mo drastically changed the ordering kinetics beyond $Ni_2(Cr_{0.63}Mo_{0.37})$ compositions. It was concluded that ordered phase evolved with a sluggish ordering kinetics when only lattice diffusion of Cr governed its formation, while ordering kinetics accelerated when lattice diffusion of Mo also contribute to its formation. The order phase evolved either via a continuous mode or nucleation and growth mode depending upon ordering temperature chosen below the order-disorder phase boundary.
- These alloys exhibited sluggish ordering kinetics in the absence of SRO.
- The ordered $Ni_2(Cr,Mo)$ structure has been found to most stable at $Ni_2Cr_{0.63}Mo_{0.37}$ and $Ni_2Cr_{0.37}Mo_{0.63}$ compositions irrespective of the relative concentration of Cr and Mo solutes in these alloys.

**Future work**

A detailed theoretical or computational investigations of stability of $Ni_2(Cr_{1-x},Mo_x)$ superstructure beyond $Ni_2(Cr_{0.75},Mo_{0.25})$ compositions extended up to $Ni_2(Cr_{0.37},Mo_{0.63})$ compositions has been proposed as one of the future scope of work. Since present work laid a foundation of complete microstructural understanding of order evolution in these alloys detailed mechanical properties testing of these alloys also has been proposed as another future work.

Signature of Student: Date:

Doctoral Committee:

| S.No. | Name | | Signature | Date |
|---|---|---|---|---|
| 1. | Dr. S.L. Chalplot | Chairman | | |
| 2. | Dr. J. B. Singh | Guide/ Convener | | |
| 3. | Dr. M. Vijayalakshmi | Member | | |
| 4. | Dr. N. Prabhu | Member | | |
| 5. | Dr. Madangopal K. | Technical Advisor | | |

## References:

[1] M.J. Cieslak, T.J. Headley, A.D. Romig. The Welding Metallurgy of Hastelloy alloys C-4, C-22 and C-276, Metallurgical Transactions A 17A (1986) 2035-2047.

[2] H.M. Tawancy, M.O. Aboelfotoh. High strength and high ductility in a nanoscale superlattice of $Ni_2$(Cr,Mo) deformable by twinning, Scripta Materialia 59 (2008) 846-849.

[3] H.M. Tawancy. Order Strengthening in a Nickel base Superalloy (Hastelloy Alloy S), Metallurgical Transactions A 11A (1980) 1764-1765.

[4] B.D. Cullity. Elements of X-RAY Diffraction. In: Cohen M, (Ed.). United States of America: Addison-Wesley Publishing Company, Inc., 1956.

[5] U.D. Kulkarni, S. Banerjee. Phase separation during the early stages of ordering in $Ni_3Mo$, Acta Metallurgica 36 (1988) 413–424.

[6] M. Sundararaman, L. Kumar, G.E. Prasad, P. Mukhopadhyay, S. Banerjee. Precipitation of an Intermetallic Phase with $Pt_2Mo$-Type Structure in Alloy 625, Metallurgical and Materials Transactions A 30A (1999) 41-52.

[7] M. Kumar, V.K. Vasudevan. Ordering reactions in an Ni-25Mo-8Cr alloy, Acta Materialia 44 (1996) 1591-1600.

[8] R. Hu, G.M. Cheng, J.Q. Zhang, J.S. Li, T.B. Zhang, H.Z. Fu. First principles investigation on the stability and elastic properties of $Ni_2Cr_{1-x}M_x$ (M=Nb, Mo, Ta, and W) superlattices, Intermetallics 33 (2013) 60-66.

[9] S. Banerjee, U.D. Kulkarni, K. Urban. Initial stages of ordering in $Ni_3Mo$-thermal and irradiation ordering experiments, Acta Metallurgica 37 (1989) 35–48.

[10] R. Caudron, M. Sarfati, M. Barrachin, A. Finel, F. Solal. In situ diffuse scatterings of neutrons on binary alloys, Physica B 180 & 181 (1992) 822-824.

[11] A. Verma, N. Wanderka, J.B. Singh, B. Kumar, J. Banhart. Statistical analysis of composition fluctuations and short-range order in stoichiometric Ni–Cr–Mo alloys, Ultramicroscopy 132 (2013) 227-232.

[12] A. Verma, J.B. Singh, M. Sundararaman, N. Wanderka. Resistivity and Transmission Electron Microscopy Investigations of Ordering Transformation in Stoichiometric $Ni_2(Cr_{0.5}Mo_{0.5})$ Alloy, Metallurgical and Materials Transactions A 43 (2012) 3078-3085.

[13] A. Verma, J.B. Singh, N. Wanderka, J.K. Chakravartty. Delineating the Roles of Cr and Mo during Ordering Transformations in Stoichiometric $Ni_2(Cr_{1-x},Mo_x)$ Alloys, Acta Materialia Under Review.

[14] G.W.H. Höhne, W.F. Hemminger, H.J. Flammersheim. Differential Scanning Calorimetry. Second Edition ed., Springer, Germany, 2003.

[15] L. Karmazin, J. Krejci, J. Zeman. Gamma Phase and $Ni_2Cr$-type long-range order in Ni-rich Ni-Cr-Mo alloys, Materials Science and Engineering A 183 (1994) 103-109.

[16] A. Verma, N. Wanderka, J.B. Singh, M. Sundararaman, J. Banhart. On the evolution of long-range order from short-range order in a $Ni_2(Cr_{0.5}Mo_{0.5})$ alloy, Journal of Alloys and Compounds 586 (2014) 561-566.

[17] D. De Fontaine. K-space symmetry rules for order–disorder reactions, Acta Metallurgica 23 (1975) 553–571.

[18] K. Monna, H. Suto, H. Oikawa. J. Jpn. Inst. Metals 28 (1964) 188-192.

[19] A. Verma, J.B. Singh, J.K. Chakravartty. Abnormal kinetics of ordering transformation in $Ni_2(Cr_{0.5}, Mo_{0.5})$ alloy, Journal of Alloys and Compounds 639 (2015) 341-345.

[20] H.E. Cook, D. Fontaine de, J.E. Hilliard. A model for diffusion on cubic lattices and its application to the early stages of ordering, Acta Metallurgica 17 (1969) 765-773.

# LIST OF FIGURES

## CHAPTER 1

## CHAPTER 2

---

## CHAPTER 3

---

---

## CHAPTER 4

---

## CHAPTER 5

## CHAPTER 6

## CHAPTER 7

# LIST OF TABLES

## CHAPTER 1

## CHAPTER 2

## CHAPTER 3

## CHAPTER 4

## CHAPTER 5

## CHAPTER 7

# CHAPTER 1

# INTRODUCTION

## 1.1. Background:

Ni-Cr-Mo-base alloys belong to important category of nickel-base alloys due to their excellent corrosion and oxidation resistance properties with good mechanical strength at elevated temperatures. The commercial alloys such as HASTELLOYS C-4, C-22, and C-276, HASTELLOY S, HAYNES 242, Alloy 625, and Alloy 686 are few examples of Ni-Cr-Mo-base alloys (Table 1.1). These alloys contain significant amount of chromium and molybdenum solutes which impart solid solution strengthening to nickel matrix [1]. These solutes also plays decisive role in improving corrosion, oxidation resistance properties and surface stability of these alloys [1, 2]. These alloys offer resistance to uniform corrosion and localized forms of corrosion such as pitting, crevice corrosion, and stress corrosion cracking (SCC). Chromium addition is primarily responsible for the resistance to corrosion in oxidizing environments, while the molybdenum additions improve the resistance to corrosion in reducing environments. Higher nickel content is responsible for the good resistance to SCC in chloride environments. Due to above mentioned benefits of chromium, molybdenum and nickel atoms their concentration have been limited in a range from 14-23 wt%, 8-17 wt% and greater than 50 wt%, respectively, in commercial Ni-Cr-Mo-base alloys. Such alloys combine properties which make them ideally suited for many components of gas turbine engines such as transition ducts, combustor cans, spray bars and flame holders as well as in afterburners, tail pipes and cabin heaters. The exceptional resistance to a wide variety of chemical environments, including strong oxidizers such as ferric and cupric chlorides, chlorine, hot contaminated solutions (organic and inorganic), formic and acetic acids, acetic anhydride, and seawater and brine solutions make them a candidate material for petrochemical industries.

**Table 1.1**: Compositions of few commercial Ni-Cr-Mo-based alloy relevant for present study in wt% *(at%)*

| **Alloy** | **Ni** | **Cr** | **Mo** | **W** | **Nb** | **Fe** | **Co** | **Ti** | **Al** | **Mn** | **Si** | **Mo/Cr (at%)** |
|---|---|---|---|---|---|---|---|---|---|---|---|---|
| 718 (1) | 52.3 *(51.2)* | 19.0 *(21.0)* | 3.0 *(1.8)* | - | 5.0 *(3.1)* | 18.5 *(19.3)* | - | 0.9 *(1.1)* | 0.9 *(1.9)* | 0.2 *(0.2)* | 0.2 *(0.4)* | **0.085** |
| 625 (1) | 62.1 *(63.6)* | 22.0 *(25.5)* | 9.0 *(5.6)* | - | 3.6 *(1.2)* | 2.5 *(2.7)* | - | 0.2 *(0.3)* | 0.2 *(0.5)* | 0.2 *(0.2)* | 0.2 *(0.4)* | **0.22** |
| C- 22 (2) | 55.9 *(58.4)* | 22.0 *(25.9)* | 13.0 *(8.3)* | 3.0 *(1.0)* | - | 3.0 *(3.3)* | 2.5 *(2.6)* | - | - | 0.5 *(0.6)* | - | **0.32** |
| 686 | 62.1 *(62.2)* | 20.4 *(24.5)* | 16.3 *(10.6)* | 3.9 *(1.3)* | - | 0.4 *(0.5)* | 0.04 *(0.04)* | - | 0.2 *(0.5)* | 0.2 *(0.2)* | 0.01 *(0.02)* | **0.42** |
| S (2) | 67.8 *(67.7)* | 15.5 *(18.0)* | 14.5 *(9.1)* | - | - | 1.0 *(1.1)* | - | - | 0.3 *(0.7)* | 0.5 *(0.6)* | 0.4 *(0.9)* | **0.51** |
| C- 4 (2) | 61.2 *(63.5)* | 16.0 *(18.7)* | 16.0 *(10.2)* | - | - | 3.0 *(3.3)* | 2.0 *(2.1)* | 0.7 *(0.9)* | - | 1.0 *(1.1)* | 0.1 *(0.2)* | **0.54** |
| C- 276 (2) | 55.4 *(59.2)* | 16.0 *(19.3)* | 16.0 *(10.5)* | 4.0 *(1.4)* | - | 5.0 *(5.7)* | 2.5 *(2.7)* | - | - | 1.0 *(1.1)* | 0.1 *(0.2)* | **0.54** |
| 242 (3) | 61.9 *(66.6)* | 8.0 *(9.7)* | 25.0 *(16.5)* | - | - | 2.0 *(2.3)* | 1.0 *(1.1)* | - | 0.5 *(1.2)* | 0.8 *(0.9)* | 0.8 *(1.8)* | **1.69** |

(1) - trade mark Inconel

(2) - trade mark Hastelloy

(3) - trade mark Haynes

These alloys are used in service conditions that involve intermediate stresses and corrosion environment at elevated temperatures.

These alloys are generally considered non-hardened by conventional ageing treatments. However, prolonged aging of these alloys in the temperature range of 400°C to 700°C results in the precipitation of a long-range ordered (LRO) $Ni_2$(Cr, Mo) phase (which has $Pt_2Mo$ prototype oI6 structure) from the disordered face-centered-cubic (fcc) matrix which significantly affects the mechanical and corrosion resistance properties of Ni-Cr-Mo alloys. The formation of $Ni_2$(Cr,Mo) phase during service produces substantial lattice contraction and causes significant stresses or dimensional changes (*i.e.*, negative creep) which affects mechanical properties of the alloys [3, 4]. Further, precipitation of the ordered phase changes the slip character from homogenous to heterogeneous by promoting planar slip along {111} [5, 6] which reduces stress corrosion cracking (SCC) resistance properties of the alloys [5-8].

Binary phase diagram of Ni-Cr alloys (Fig. 1.1) suggests the formation of the oP6 phase at temperatures close to 500°C. Phase field of the oP6 phase extends from chromium concentration of about 22.0 at% to 40.0 at% with maximum ordering temperature at about

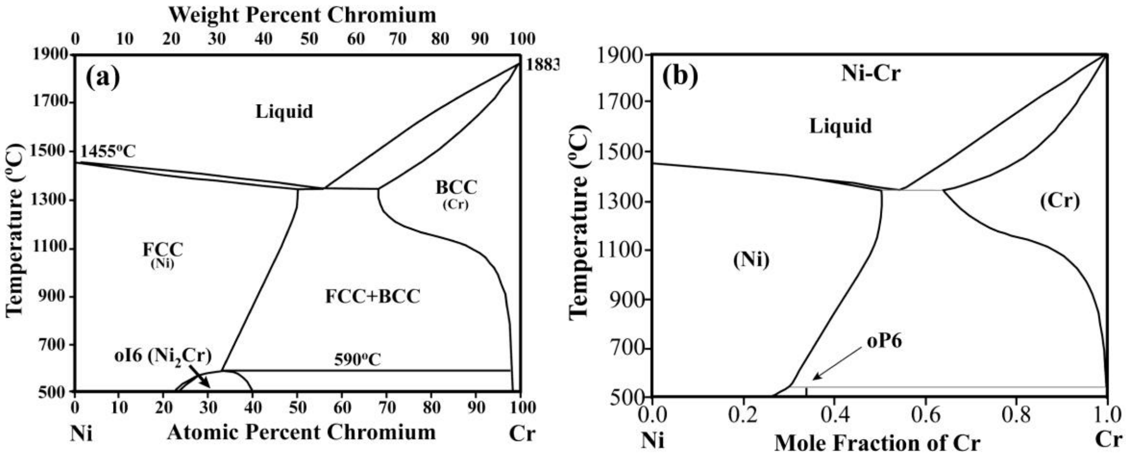

**Figure 1.1:** Phase diagram of Ni-Cr alloy system; (a) experimentally determined by Nash et al. [9]; (b) theoretically calculated by Turchi et al. [10].

590°C at chromium concentration of 33.3 at% [9, 10]. In Ni-Cr alloys formation of the oP6 phase requires several hundred hours of ageing at temperatures close to 500°C [8, 11, 12]. This implies that ordering reaction remains very sluggish at temperatures close to the critical ordering temperature. Though, oP6 phase is also expected to form in Ni-Mo and Ni-W alloys due to similar e/a ratio of these solutes [13], Turchi et al. [10] found that $Ni_2Cr$ phase is most stable and $Ni_2Mo$ is barely stable while $Ni_2W$ phase is the least stable among all. Despite of the fact that the oP6 phase in pure binary Ni-Mo is barely stable, the gradual substitution of Cr by Mo in $Ni_2Cr$ alloys does not lead to a gradual instability of the phase as one would first guess. In-fact Karmazin et al. [14] has experimentally shown an increased stability of the oP6 phase with the substitution of about 25% Cr atoms with Mo atoms in $Ni_2Cr$ alloys. An increase of the stability of oP6 phase with the substitution of Cr by Mo atoms in stoichiometric $Ni_2(Cr_{1-x}Mo_x)$ alloys has also been shown by Pai et al. [15] by increase of solvus temperature of the ordered phase from 627.6°C in $Ni_2Cr$ alloy to 772.6°C in $Ni_2(Cr_{0.5}Mo_{0.5})$ alloy. Contrary to it, the gradual substitution of Cr by W leads to a destabilization of the oP6 phase. The destabilization of the oP6 phase with addition of W has been experimentally demonstrated in a recent study by Chen et al. [16], where they have noticed the suppression of the oP6 phase and the preference for the formation of $DO_{22}$ phase in Ni-26.3Cr-18.8Mo-0.8W (at%) alloy which has the composition close to $Ni_2(Cr,W)$ stoichiometry.

## 1.2. Literature Survey:

### 1.2.1. Ni-Cr-Mo phase diagram:

Ternary phase diagram of Ni-Cr-Mo alloys has been determined by different researchers [2, 17-23]. Jena et al. [24] have extensively reviewed Ni-Cr-Mo phase diagrams determined by various researchers to give the phase diagram shown in fig. 1.2. It is clear from fig. 1.2 that at 1200 °C, the austenite (γ) phase is stable up to 45 at% nickel for chromium rich side, while for molybdenum rich alloys the γ phase extends for nickel concentration higher than ~75 at%. The γ phase region shrinks with decrease of temperature and the composite plot drawn for different temperatures by Gdowski et al. [25] is shown in fig. 1.3. Phase fields of different TCP phases, e.g., σ, P and δ can be seen adjacent to γ phase field depending upon concentrations of chromium and molybdenum (Figs. 1.2). Commercial Ni- Cr-Mo alloys are not strictly ternary systems as they contain other minor solute additions and hence cannot be located on the phase diagram. Cieslak et al. [2] have overcome this problem by determining the chromium, molybdenum and nickel equivalent. The equivalent compositions determined by them [2] for commercial alloys are marked in figs. 1.2 and 1.3. At 1200 °C (Fig. 1.2) the commercial alloys can be seen to fall in the single austenite phase field region. At temperatures lower than 800° C, commercial Ni-Cr-Mo base alloys are susceptible to the formation of TCP phases (Fig. 1.3). However, kinetic considerations are usually not favorable for their nucleation at lower temperatures, though thermodynamically they are stable. At still lower temperature, $Pt_2Mo$-type ordered $Ni_2(Cr,Mo)$ phase forms in Ni-Cr-Mo

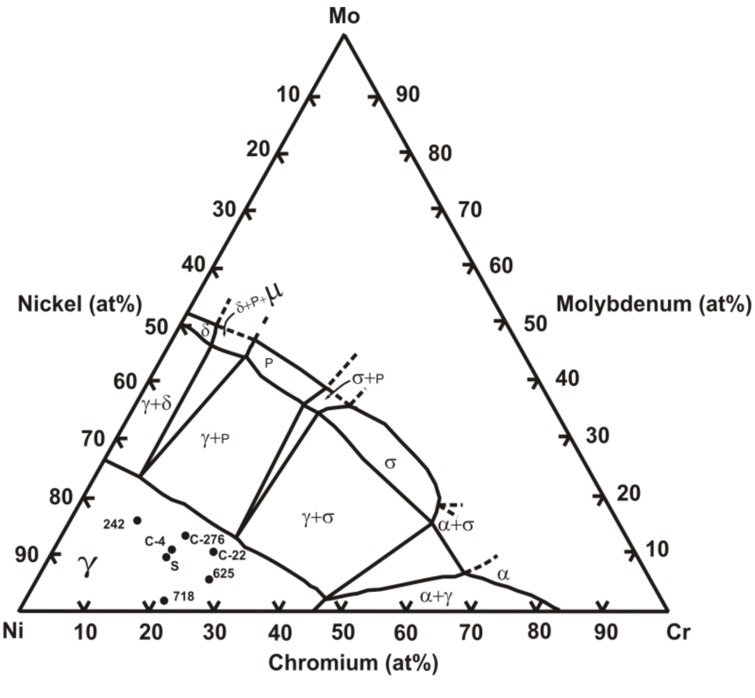

**Figure 1.2:** Isothermal section at 1200 °C of Ni-Cr-Mo phase diagram Rideout et al. [23]

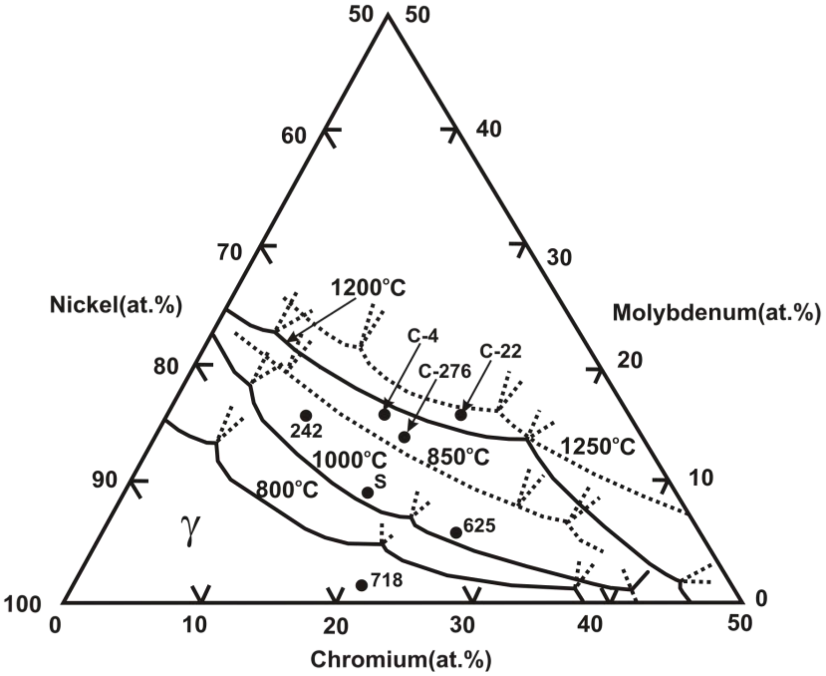

**Figure 1.3:** γ phase boundaries at 1200°C, 1000°C and 800°C in Ni-Cr-Mo system. Solid lines by Class et al. [18], dashed lines by Raghavan et al. [22].

alloys. Turchi et al. [10] have carried out extensive study on the stability of different phases that form in Ni-Cr-Mo ternary alloys using an approach similar to that followed by Chan et al. [26]. Their results show that the $Ni_2(Cr,Mo)$ phase competes with TCP phases in Ni-Cr-Mo alloys at lower ageing temperatures, though kinetically it is the most favored. The isothermal sections of phase diagrams computed for 300°C, 500°C, 620°C and 700°C are shown in fig. 1.4 [10]. It can be seen from fig. 1.4 that phase field of oP6 phase shrinks from 300°C to 500°C and disappears for temperatures ≥ 620°C. This is contrary to experimental evidences of the formation of the $Ni_2(Cr,Mo)$ phase in many Ni-Cr-Mo alloys at $T < 700$ ° C [2, 4, 27-30]. Possible reason for the absence of phase field in the calculated sections of Ni-Cr-Mo phase diagram could be the sluggish nature of the order reaction. By restricting their analysis to fcc matrix and oI6 phase, Turchi et al. [10] have found that oP6 phase reaches its maximum stability at about 0.2 mole fraction of chromium and 0.13 mole fraction of molybdenum in the $Ni_2(Cr,Mo)$ phase , beyond which its stability decreases.

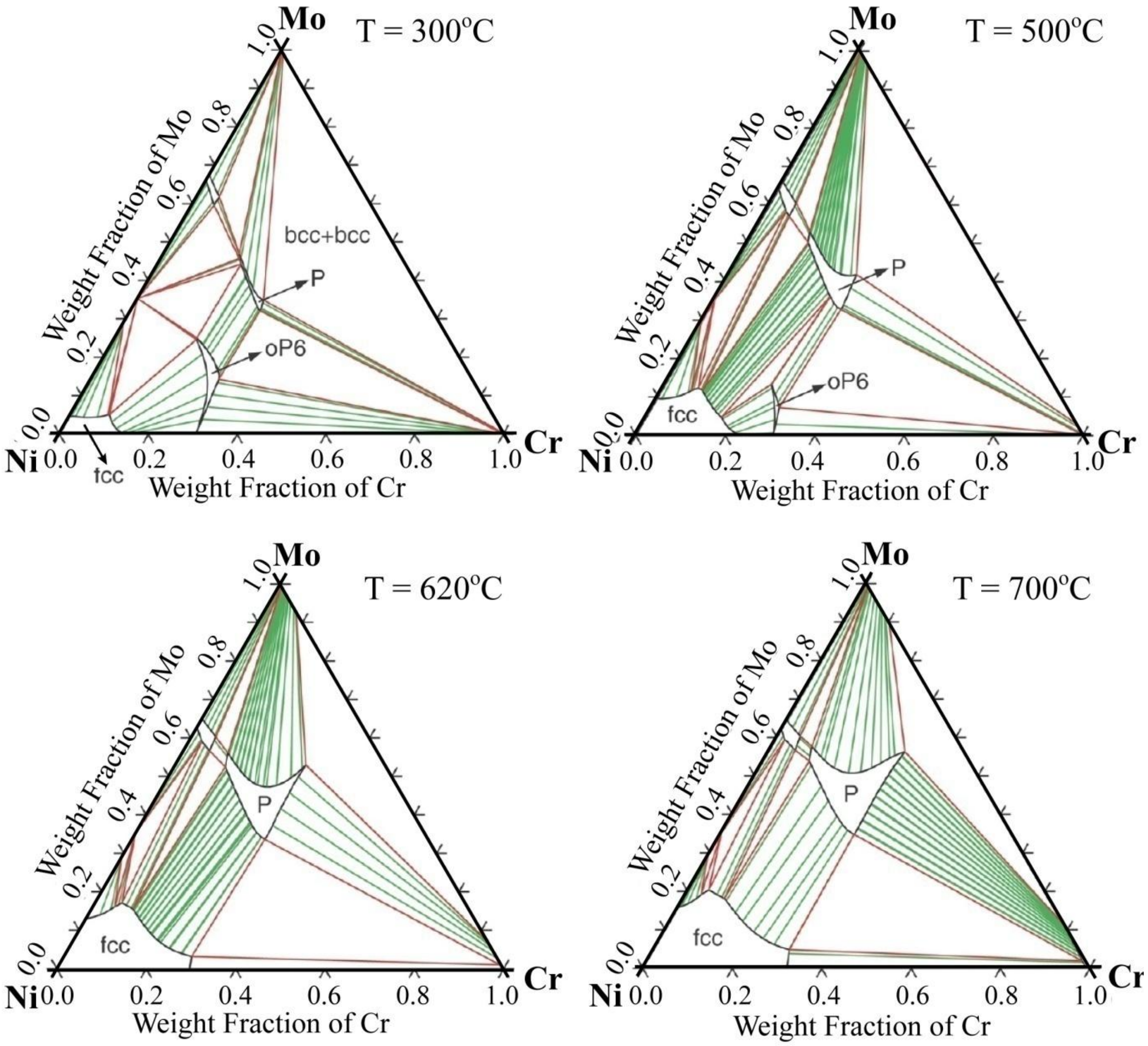

**Figure 1.4:** Phase diagrams of Ni-Cr-Mo alloy system computed by Turchi et al. [10] at different temperatures as marked in the figures.

### 1.2.2. Short-range order and ordering transformations in Ni-Cr-Mo Alloys:

Ni-Mo alloys (in the composition range 8-33 at% Mo) exhibit short-range order (SRO) by the appearance of diffuse intensity maxima at {1 ½ 0} positions in selected area electron diffraction (SAED) which are different from the emerging LRO phases in the alloys [13, 31-36]. Addition of ternary elements to a binary Ni-Mo alloys significantly affects SRO state by exhibiting additional diffuse reflections in the electron diffraction patterns [37, 38]. For example, addition of Al to $Ni_3Mo$ alloys (i.e., Ni–25.0at%Mo–5.0at%Al alloy) induces the appearance of diffuse reflections of $DO_{22}$ structure [37], while addition of Ta or W to $Ni_3Mo$-based alloys results in the appearance of diffuse reflections of oP6 phase, which has been argued to be due to the formation of nuclei of oP6 phase [38]. In general, addition of ternary elements in binary alloys of Ni, Cr and Mo elements causes the appearance of additional diffuse reflections with concurrent {1 ½ 0} reflections in the SRO state of the binary alloy.

Ordering transformation in Ni-Cr-Mo alloys has been studied by many researchers [12, 14, 15, 19, 21, 22, 27, 39]. Most of researchers have used transmission electron microscopy (TEM), X-ray diffraction, and differential scanning calorimetry [12, 14, 15, 22, 27, 39] for studying formation and dissolution of ordered $Ni_2(Cr, Mo)$ precipitates in Ni-Cr-Mo alloys. Resistivity measurements have also been employed in past for investigating SRO and LRO in alloy systems other than Ni-Cr-Mo [40-46]. Resistivity method has been found to be more sensitive in studying processes that involves SRO. Baer [47] was the first to study the ordering in Ni-Cr alloys at compositions close to that of stoichiometric $Ni_2Cr$ phase using resistivity technique. He has noticed a drop in resistivity at 500° C during ageing of binary Ni-Cr alloys containing 25 to 36 at% Cr. Klein et al. [11] have established the evidence of long-range ordered $Ni_2Cr$ structure in Ni-30at.%Cr alloy using electron diffraction. Soltys et al. [45] have used isochronal resistivity experiments to study the SRO in the Ni-10 at% Mo alloy. Lang [41] have shown that the formation of SRO causes an increase of resistivity in Ni-Cr alloys, while Binder et al. [48] Richter et al. [43] have shown that resistivity decrease with the formation of LRO in alloys [43, 48]. It has been shown that formation of the ordered $Ni_2(Cr,Mo)$ phase in Ni-Cr-Mo alloys is preceded by the appearance of a short-range order, though it may take different ordering paths depending upon the ageing temperature [39, 49]. For instance, in Ni-17at%Mo-9.5at%Cr alloys the formation of this phase has been found via continuous ordering mechanisms at $T \leq 700°C$, and, by a nucleation and growth mechanism at higher ageing temperatures [39].

X-ray diffraction has been extensively used to accurately determine phase boundaries of γ and oP6 phase in binary Ni-Cr and ternary Ni-Cr-Mo alloys [12, 14]. Lattice parameter change of the γ phase has been used to follow the ordering transformation in these alloys. A typical plot of lattice parameter change of γ matrix in Ni-33.7at%Cr and Ni-24at%Cr-at%Mo alloys during ageing at different temperatures is shown in fig. 1.5 [12, 14]. This figure shows that lattice parameter of the γ matrix decreases continuously with ageing time and this change is sharp at 500°C and 560°C in Ni-33.7at%Cr and Ni-24at%Cr-8at%Mo alloys,

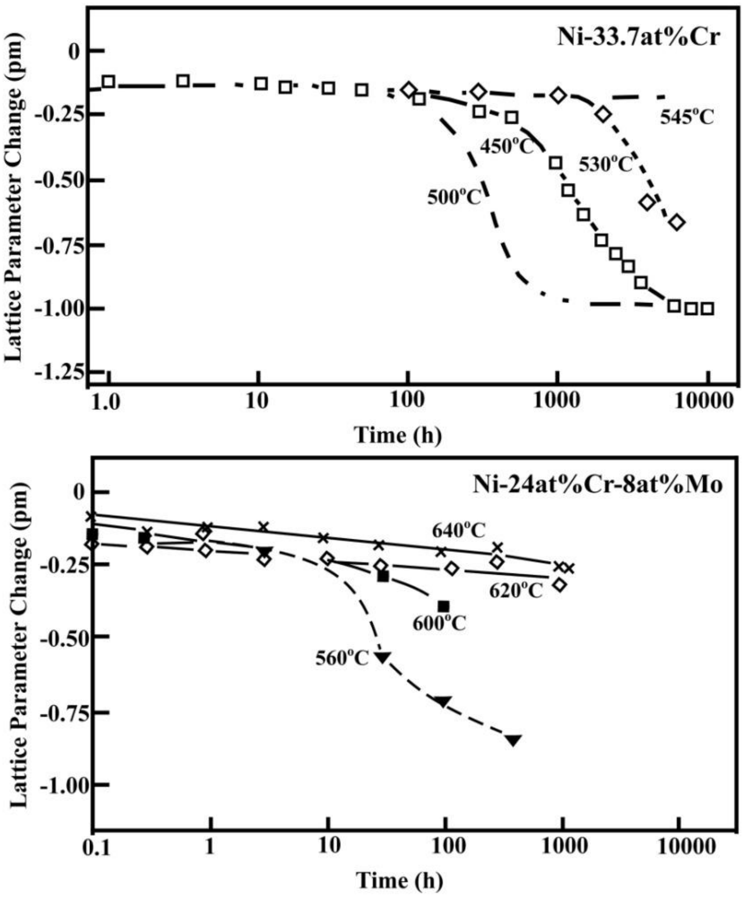

**Figure 1.5:** Lattice parameter change measured during ageing at different temperatures with respect to solution treated state of Ni-33.7at%Cr and Ni-24at%Cr-8at%Mo alloys [12]. Note that the change was steepest at 500°C in Ni-33.7at%Cr and at 560°C in Ni-24at%Cr-8at%Mo alloy.

respectively. On the basis of lattice parameter changes monitored at different ageing temperatures Karmazin et al. [12, 14] have concluded that the transformation kinetics is fastest at 500°C and 560°C, respectively, in Ni-33.7at%Cr and Ni-24at%Cr-8at%Mo alloys. Further, their study reveal a relatively faster ordering kinetics in Ni-24at%Cr-8at%Mo alloy compared to that in Ni-33.7at%Cr alloy. Whereas ageing of several hundred hours is required for any significant change of the lattice parameter in Ni-33.7at%Cr alloy, few tenths of ageing hours is sufficient to bring such changes in Ni-24at%Cr-8at%Mo alloy [12]. It is, therefore, confirmed that 8at% molybdenum addition could have reduced the incubation time for the formation of ordered phase and resulted in an accelerated ordering kinetics. Thus, it appears that ordering kinetics is affected by Mo solutes in Ni-Cr alloys.

### 1.2.3. Mechanisms of ordering:

Transformation reactions, in general, can be classified into different categories depending upon the spatial extent and amplitude of compositional fluctuations that initiate transformations [50]. These modes can be classified as: (i) classical nucleation, initiated by large amplitude compositional fluctuations which have limited spatial extent; (ii) spinodal decomposition, initiated by fluctuations that are small in degree and large in spatial extent [50]. Later, Christian has generalized this classification scheme by suggesting transformation modes either as homogeneous or heterogeneous type [51]. Heterogeneous transformations include both classical homogeneous and heterogeneous nucleation processes, which generally involve spatial partitioning of the system into transformed and untransformed regions, separated by interphase interfaces. In the homogeneous transformations entire ensemble transforms uniformly and the composition and/or the order parameter are progressively increased from initially small values to large values characteristic of a more stable state. The latter is called continuous transformation since the entire system transforms via the "continuous" amplification of initially small fluctuations within the supersaturated or undercooled phase. Spinodal decomposition and spinodal ordering are two limiting cases of continuous transformations which are differentiated by the wavelength of quasi-periodic concentration waves. The transformation is called spinodal decomposition in the longer wavelength limits of concentration waves where spatial periodicity is generally evident, while that occurring at small wavelength end of the spectrum is called "continuous ordering" or "spinodal ordering". During spinodal ordering ordered atomic arrays are produced by concentration waves having wavelength of the order of interatomic separation. Usually continuous transformations are driven by diffusional instabilities which arise when certain large amplitude fluctuations or concentration waves build up and become unbounded at the instability limit. Long wavelength waves occur in the vicinity of (0 0 0), at the center of the first Brillouin zone, while ordering instabilities are usually expected at "special points" of fcc lattices where symmetry elements intersect and extrema of the F″(k) occur, i.e., points where V(k) is a minimum. Ordering instability occurs at temperature $T_i$ (Instability temperature) for which the modulus F″(k) vanishes and is defined as

$$K_B T_i = -2\overline{c}\,(1-\bar{c})V\left(\overrightarrow{K_o}\right)$$

where, $K_o$ is a "special point" wave vector, e.g., <1 ½ 0> the ordering wave, the ordering wave $K_o$ is amplified spontaneously initiating continuous decomposition of the parent phase. These "special point" instabilities represent the uppermost instability limits or "ordering spinodal" [52]. This limit is also called “*coherent instability boundary*” [53]. Below this boundary the order phase would evolve by a continuous ordering mechanism.

Theoretical development of the concept of spinodal decomposition in the works of Hillert [54] and Cahn [55-57] provided a fundamental basis for the evolution of quasi-periodic concentration waves during the decomposition of supersaturated solid solutions.

The concept of concentration waves proved to be useful for describing continuous ordering reactions also in the short wavelength regime of concentration waves [58-60].

The picture that emerges can be summarized as follows: in the vicinity of an instability temperature large-amplitude fluctuations associated with specific concentration waves tend to appear. In the vicinity of a second-order (higher order) phase transition these dynamic fluctuations directly signal the approach to the transformation temperature since the transformation temperature and instability limit coincide; for first-order transitions the instability limit appears at temperatures below the phase boundary. At the instability limit selected concentration waves are rapidly amplified; long wavelengths giving rise to clustering (spinodal decomposition) and short wavelengths giving rise to continuous ordering. As the amplitude of the concentration waves increases the anharmonic terms in the free energy expansion become important and the harmonic waves are distorted or modulated by the emergence and preferred growth of higher-order waves generally producing peaks at other superlattice locations.

## 1.3. Motivation:

On the basis of aforementioned literature, it is clear that Ni-Cr-Mo alloys form an ordered $Ni_2(Cr,Mo)$ phase in the intermediate temperature regime. These alloys, having stoichiometric $Ni_2(Cr,Mo)$ as well as off-stoichiometric compositions, in solution treated state exhibit {1 ½ 0} SRO [39, 49, 61, 62]. Evolution of the order takes place in a continuous manner via gradual decay of intensity at {1 ½ 0} positions with simultaneous emergence of superlattice reflections of the LRO phase [39, 49, 61, 62]. As the {1 ½ 0} SRO has always appeared as a precursor to the formation of ordered $Ni_2(Cr,Mo)$ phase, it is necessary to understand its effect on the evolution of the ordered phase in Ni-Cr-Mo alloys.

Karmazin et al. [12, 14] have shown that increase in Cr solute concentration in binary Ni-Cr alloys shifts phase boundary of the oP6 phase to higher temperature until it reaches maxima at stoichiometric Ni-33.7at%Cr composition beyond which it decreases with further increase of Cr concentration. The addition of Mo in Ni-Cr alloys move the oP6 phase boundary to higher temperature side in Ni-($Cr_{0.75}Mo_{0.25}$) alloys with varying solute concentration (Fig. 1.6). In addition, highest ordering temperature in Ni-Cr-Mo alloys appears at hyper-stoichiometric Ni-36.7at%(Cr+Mo) composition suggesting that Mo substitutes both for Cr and Ni lattice sites in $Ni_2Cr$ ordered phase alloy [14]. The shift of the oP6 phase boundary to higher temperatures with the addition of Mo in Ni-Cr alloys signifies higher thermodynamic stability of the ordered $Ni_2$(Cr,Mo) phase in Ni-Cr-Mo alloys. In addition, different concentrations of Cr and Mo atoms in Ni-Cr-Mo alloys have been shown to affect ordering

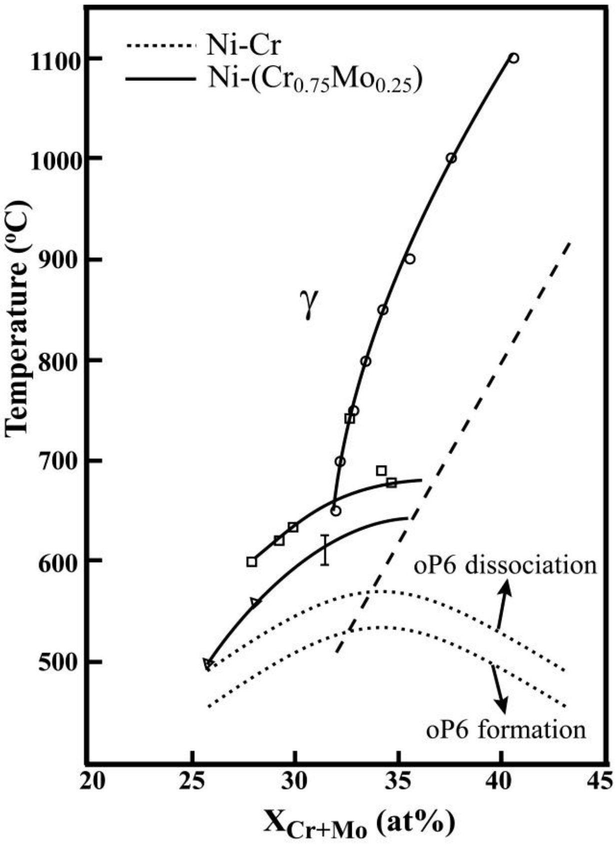

**Figure 1.6:** Temperature-composition plot showing phase boundaries of γ and oP6 phase in (i) Ni-Cr alloys shown by broken lines; (ii) Ni-($Cr_{0.75}Mo_{0.25}$) alloy shown by solid lines. The two parabolic sections shown for both alloys by solid and broken lines represent boundaries for the formation and dissociation of ordered phase [12].

kinetics. The ordered $Ni_2(Cr,Mo)$ phase forms after prolonged ageing at temperatures lower than 600 °C in Alloy 625 [27] (Mo/Cr=0.22, see table 1.1), while it forms within shorter times in Haynes 242 (Mo/Cr=1.22, see table 1.1) [28]. Due to significant effect of Mo addition on the ordering process, it is important to understand the roles of Cr and Mo on the ordering kinetics of the alloys.

In commercial Ni-Cr-Mo alloys, chromium and molybdenum solutes have been considered as important species for the stabilization of oP6 phase [13]. Limited work has been reported on the stability of oP6 phase in the Ni-Cr-Mo alloys. Binary Ni-Cr phase diagram shows the existence of oP6 phase field [9] while it is absent in binary Ni-Mo phase diagram [10, 63]. Yet $Ni_2Mo$ has been observed as metastable phase in hypo-stoichiometric $Ni_2Mo$ alloys [64]. Cr and Mo solutes are considered necessary for the stabilization of the

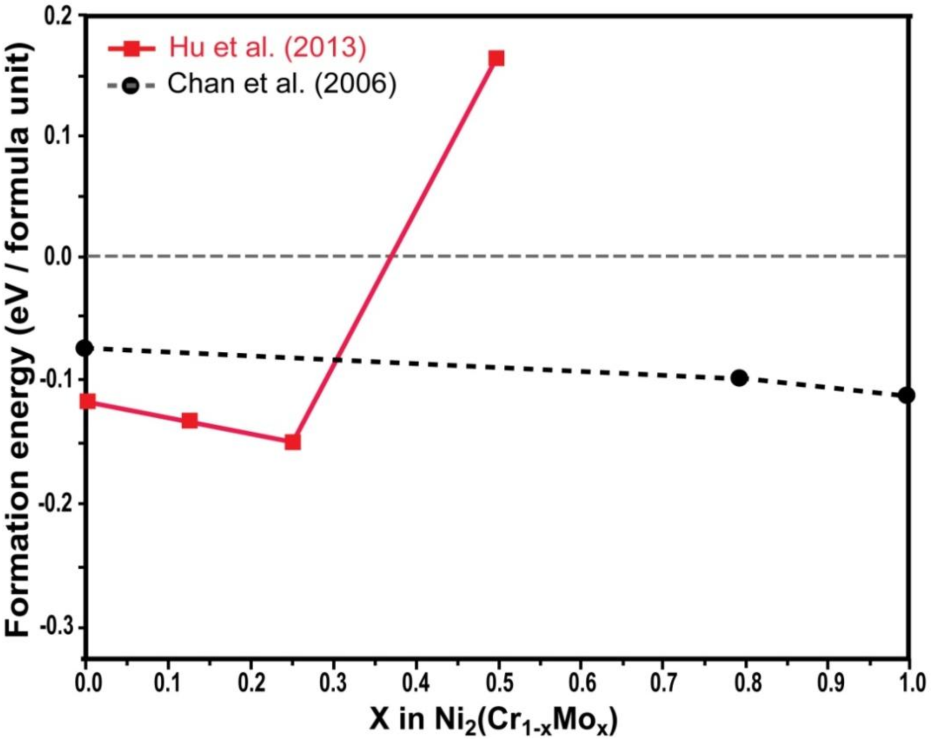

**Figure 1.7:** Plot showing the effect of solute addition on the formation energy of $Ni_2(Cr,Mo)$ phase in different $Ni_2(Cr_{1-x}Mo_x)$ alloys. Broken line shows the effect of Cr substitution in $Ni_2Mo$ alloy [26] and solid line shows the effect of Mo substitution with Cr in $Ni_2Cr$ alloys on the formation energy of $Ni_2(Cr,Mo)$ phase [65].

oP6 phase. Chan et al. [26] and Turchi et al. [10] have shown that formation energy of the $Ni_2(Cr,Mo)$ phase lowers with the substitution of chromium by molybdenum atoms in $Ni_2Cr$ alloy. In fact, the ordering energy decreases from -7.51 kJ/mole in $Ni_2Cr$ to -9.59 kJ/mole in $Ni_2Mo_{0.8}Cr_{0.2}$ alloy which further reduces to -10.43 kJ/mole in $Ni_2Mo$ [26, 66]. Recently, Hu et al. [65] have calculated formation energy of the Cr-rich $Ni_2(Cr_{1-x}Mo_x)$ phase (where, x = 0to 0.5) (Fig.1.7). Their calculation also supports a decrease of the formation energy of ordered phase with the addition of Mo, though stability of the oP6 phase is maximum at $Ni_2(Cr_{0.75}Mo_{0.25})$ composition and least at $Ni_2(Cr_{0.5}Mo_{0.5})$ composition. They have arrived at this conclusion on the basis of the formation energy of oP6 phase which is most negative at $Ni_2(Cr_{0.75}Mo_{0.25})$ composition while positive at $Ni_2(Cr_{0.5}Mo_{0.5})$ composition. However, no experimental evidence support stability of the ordered $Ni_2(Cr,Mo)$ phase at different compositions. Recently, Li et al. [29] have used energy dispersive x-ray (EDX) analysis in TEM to measure chemical composition of few nanometer sized ordered $Ni_2(Cr,Mo)$ domains in Ni-24.5at%Cr-10.8at%Mo alloy and identify it to be about Ni-22.6at%Cr-12.9at%Mo. However, this composition is different than the highest stable $Ni_2(Cr_{0.75}Mo_{0.25})$ phase composition shown by Hu et al. [65]. Since finite interaction volume effects in EDX analysis of compositions of nanometer sized ordered domains can bring large errors in the measured compositions, more accurate methods of determining chemical compositions of nanometer sized ordered domains must be used which can unambiguously and accurately measure their compositions. It is therefore necessary to carry out a detailed analysis of the chemical composition at which the ordered $Ni_2(Cr,Mo)$ phase stabilizes in Ni-Cr-Mo alloys.

### 1.3. Objectives of present study:

Objectives of the present study are:

(v) To characterize SRO in $Ni_2(Cr_{1-x}Mo_x)$ alloys containing varying amounts of Cr and Mo solutes and to identify chemical heterogeneities responsible for its formation;

(vi) To understand the role of Cr and Mo solutes on ordering transformation in stoichiometric $Ni_2(Cr_{1-x}Mo_x)$ alloys and to identify solute species responsible for the order evolution;

(vii) To understand the effect of SRO on order evolution and its kinetics in $Ni_2(Cr_{1-x}Mo_x)$ alloys;

(viii) To identify composition of the stabilized ordered $Ni_2(Cr,Mo)$ phase in Ni-Cr-Mo alloys.

## 1.4. Layout of Thesis:

This dissertation has been divided into eight chapters, including the present chapter (Chapter 1), which provides an **introduction** to this dissertation. A major portion of the literature survey, pertinent to the work has been presented here.

Chapter 2 contains deals with **diffraction aspects of long-range order and short-range order** reported in the dissertation.

Chapter 3 presents the **experimental procedures** followed for carrying out studies presented in this dissertation.

Chapters 4-7 presents **results**, which are divide on the basis of objectives of the study laid out in Chapter 1. Detailed discussion of experimental results pertaining to the set objectives has also been included in these chapters.

Chapter 8 summarizes the overall dissertation work and conclusions that could be arrived at on the basis of studies carried out here.

In addition, there are two appendices to this dissertation. **Appendix I** discusses mathematical treatment required for the diffraction analysis. **Appendix II** discusses methodology required for describing amplification of concentration waves. **Appendix III** provides details of methodology used to determine the instrumental broadening of x-ray diffractometer being used for experimental studies.

**References** used in the dissertation are listed in the end.

# CHAPTER 2

# DIFFRACTION ASPECTS OF LONG-RANGE ORDER AND SHORT-RANGE ORDER

In this chapter diffraction aspects of LRO phases relevant for present study and the crystallographic basis of interpretation of SRO is presented. A more detailed description of crystallographic aspect of $Pt_2Mo$-type of ordered structure, which is the only important phase in present study, and its diffraction aspects w.r.t. electron diffraction, x-ray and neutron diffraction are discussed. Brief overviews of crystals structures of $DO_{22}$ and $D1_a$ phases which are required in describing atomic architecture in the SRO state are discussed. In the last, section crystallographic basis of SRO interpretation is discussed in the light of different models suggested in literature.

## 2.1. General crystallography features of the ordered $Ni_2$(Cr,Mo) phase:

### 2.1.1. Crystal Structure:

The ordered $Ni_2$(Cr,Mo) phase has a body-centered orthorhombic structure of $Pt_2Mo$ - type

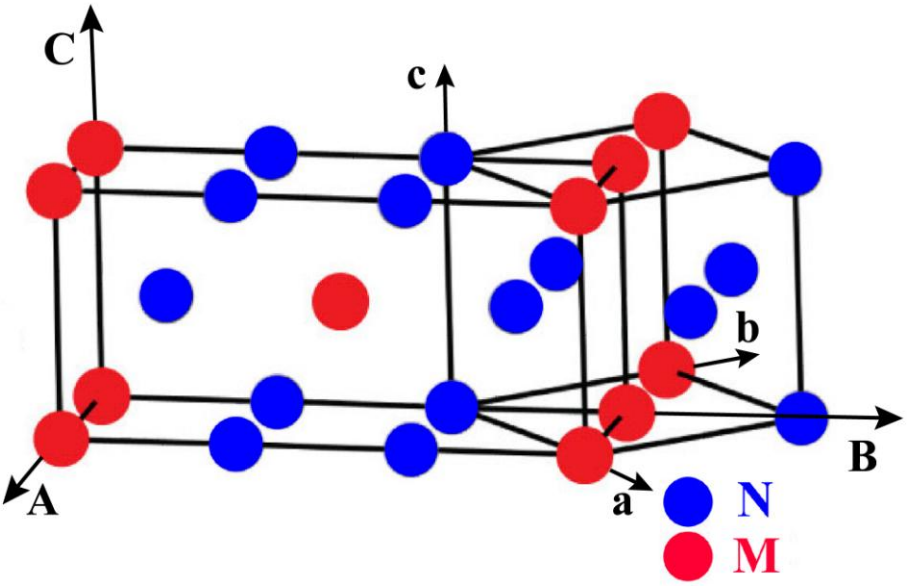

**Figure 2.1:** The unit cell of ordered $Ni_2$(Cr,Mo) structure ($N_2M$ structure) and the corresponding fcc lattice.

($N_2M$ structure) and the corresponding space group is $DO_{2h}^{25}$ - *Immm*. The unit cell of $N_2M$ structure with respect to disordered fcc unit cell (A1 structure) is shown in fig. 2.1. The M atoms occupy the corners and the body center positions of this cell while the other atomic positions are occupied by N atoms and the cell contains 6 atoms.

The $N_2M$ structure can be regarded as a superstructure derived from the disordered A1 structure, and the unit cell vectors in the former can be expressed in terms of vectors in the latter in the following manner for the unit cell shown in fig. 2.1:

$$A = \frac{1}{2}a\,[1\bar{1}0],\ B = \frac{3}{2}a\,[110],\ \text{and } C = a\,[001]$$

, where, ‘a’ is the lattice parameter of fcc unit cell.

The c-axis of the body-centered orthorhombic unit cell can align itself along any one of the three a-axes of the A1 unit cell. Consequently, A and B axes will align themselves along appropriate <110> directions. This results in the formation of six orientational variants of the $N_2M$ structure [27]. Orientations of the axes of the six variants, with respect to the A1 structure, are given in table 2.1. All six variants have equal probability of nucleation in the disordered A1 matrix and have been observed in many alloy systems [39, 67, 68]. The orientation relationship between these variants represented on a standard cubic stereographic

**Table 2.1**: Lattice correspondence and variant nomenclature of the $N_2M$ phase in relation to the fcc lattice [27].

| **Variant** | $[100]_{N_2M}$ | $[010]_{N_2M}$ | $[001]_{N_2M}$ |
|---|---|---|---|
| 1 | $[1\ \bar{1}\ 0]$ | [1 1 0] | [0 0 1] |
| 2 | [1 1 0] | $[\bar{1}\ 1\ 0]$ | [0 0 1] |
| 3 | [1 0 1] | $[1\ 0\ \bar{1}]$ | [0 1 0] |
| 4 | $[1\ 0\ \bar{1}]$ | $[\bar{1}\ 0\ \bar{1}]$ | [0 1 0] |
| 5 | $[0\ \bar{1}\ \bar{1}]$ | $[0\ 1\ \bar{1}]$ | [1 0 0] |
| 6 | $[0\ 1\ \bar{1}]$ | [0 1 1] | [1 0 0] |

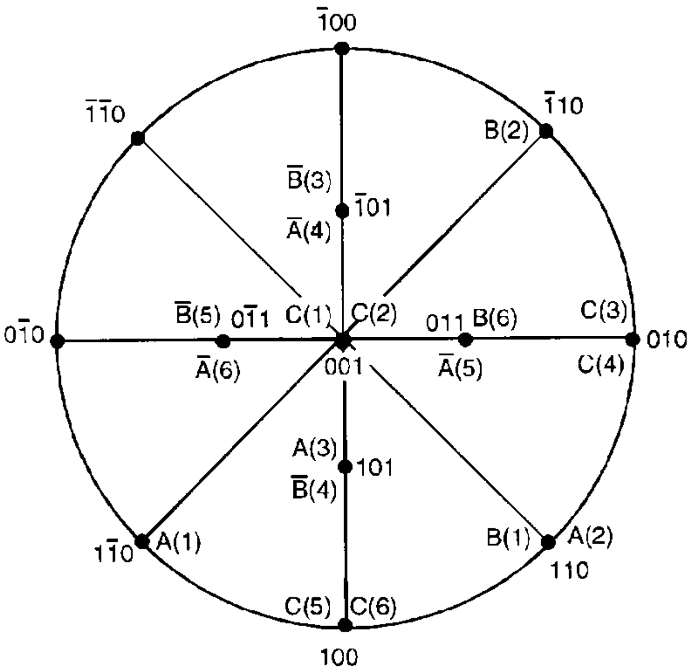

**Figure 2.2:** Standard (001) stereographic projection showing the relationship between six variants of the ordered $Ni_2(Cr,Mo)$ phase [67].

projection is shown in fig. 2.2. It is to be noted that the cell of the $N_2M$ structure shown in fig. 2.1 corresponds to the variant 1.

### 2.1.2. Lattice correspondence with fcc structure:

It is mentioned earlier that $N_2M$ - type superlattice is a derivative of the fcc structure. Since both lattices are defined w.r.t. different coordinate systems, a correspondence between them is established by defining equivalent planes and directions of $N_2M$ structure in correspondence with fcc systems.

If the directions of any vector and the Miller indices of any plane with respect to the original cubic axes are written as column and row matrices $[u]_C$ and $(h)_C$ respectively, the corresponding indices referred to axes defined by the unit cell of the superlattice are given by

$$[u]_S = {}_S\phi^C \, [u]_C \qquad \text{…… (2.1)}$$

$$(h)_S = (h)_C \left[{}_S\phi^C\right]^{-1} \qquad \text{…… (2.2)}$$

Where, ${}_S\phi^C$ and $\left[{}_S\phi^C\right]^{-1}$ are 3 × 3 matrices expressing the correspondence relationship between the two basis, so that the columns of $\left[{}_S\phi^C\right]^{-1}$ are the cube components of the base vectors of the superlattice cell S. Using these matrices it is possible to find the correspondence relationship of any direction or plane between the parent fcc structure and the superlattice structure. The lattice correspondence matrices relating the parent fcc structure to the different variants of the ordered structure of the $N_2M$ phase are listed in table 2.2. Following these equations, some relevant plane and direction correspondences between the fcc phase and different variants of the $N_2M$ phase are given in tables 2.3 and 2.4.

**Table 2.2:** Lattice correspondence matrices relating the fcc phase to different variants of the $N_2M$ phase. Notation ${}_O\phi^C$ represents correspondence from orthogonal basis, O, to cubic basis, C [69].

| **Variant** | ${}_O\phi^C$ | $\left[{}_O\phi^C\right]^{-1} = {}_C\phi^O$ |
|---|---|---|
| 1 | $\frac{1}{2}\begin{bmatrix} 1 & 3 & 0 \\ -1 & 3 & 0 \\ 0 & 0 & 2 \end{bmatrix}$ | $\frac{1}{3}\begin{bmatrix} 3 & -3 & 0 \\ 1 & 1 & 0 \\ 0 & 0 & 3 \end{bmatrix}$ |
| 2 | $\frac{1}{2}\begin{bmatrix} 1 & -3 & 0 \\ 1 & 3 & 0 \\ 0 & 0 & 2 \end{bmatrix}$ | $\frac{1}{3}\begin{bmatrix} 3 & 3 & 0 \\ -1 & 1 & 0 \\ 0 & 0 & 3 \end{bmatrix}$ |
| 3 | $\frac{1}{2}\begin{bmatrix} 1 & 3 & 0 \\ 0 & 0 & 2 \\ 1 & -3 & 0 \end{bmatrix}$ | $\frac{1}{3}\begin{bmatrix} 3 & 0 & 3 \\ 1 & 0 & -1 \\ 0 & 3 & 0 \end{bmatrix}$ |
| 4 | $\frac{1}{2}\begin{bmatrix} 1 & -3 & 0 \\ 0 & 0 & 2 \\ -1 & -3 & 0 \end{bmatrix}$ | $\frac{1}{3}\begin{bmatrix} 3 & 0 & -3 \\ -1 & 0 & -1 \\ 0 & 3 & 0 \end{bmatrix}$ |
| 5 | $\frac{1}{2}\begin{bmatrix} 0 & 0 & 2 \\ -1 & 3 & 0 \\ -1 & -3 & 0 \end{bmatrix}$ | $\frac{1}{3}\begin{bmatrix} 0 & -3 & -3 \\ 0 & 1 & -1 \\ 3 & 0 & 0 \end{bmatrix}$ |
| 6 | $\frac{1}{2}\begin{bmatrix} 0 & 0 & 2 \\ 1 & 3 & 0 \\ -1 & 3 & 0 \end{bmatrix}$ | $\frac{1}{3}\begin{bmatrix} 0 & 3 & -3 \\ 0 & 1 & 1 \\ 3 & 0 & 0 \end{bmatrix}$ |

**Table 2.3:** Plane correspondence of different variants of the $N_2M$ superstructure with respect to fcc lattice.

| CUBIC | PLANE CORRESPONDENCE | | | | | |
|---|---|---|---|---|---|---|
| | **Variant 1** | **Variant 2** | **Variant 3** | **Variant 4** | **Variant 5** | **Variant 6** |
| 111 | 031 | 101 | 101 | $0\bar{3}1$ | $\bar{1}01$ | 031 |
| $\bar{1}11$ | $\bar{1}01$ | 031 | $0\bar{3}1$ | $\bar{1}01$ | $\bar{1}0\bar{1}$ | $03\bar{1}$ |
| $1\bar{1}1$ | 101 | $0\bar{3}1$ | $10\bar{1}$ | $0\bar{3}\bar{1}$ | $0\bar{3}1$ | $\bar{1}01$ |
| $11\bar{1}$ | $03\bar{1}$ | $10\bar{1}$ | 031 | 101 | 031 | 101 |
| 200 | 130 | $1\bar{3}0$ | 130 | $1\bar{3}0$ | 002 | 002 |
| 020 | $\bar{1}30$ | 130 | 002 | 002 | $\bar{1}30$ | 130 |
| 002 | 002 | 002 | $1\bar{3}0$ | $\bar{1}\bar{3}0$ | $\bar{1}\bar{3}0$ | $\bar{1}30$ |
| 220 | 060 | 200 | 132 | $1\bar{3}2$ | $\bar{1}32$ | 132 |
| $\bar{2}20$ | $\bar{2}00$ | 060 | $\bar{1}\bar{3}2$ | $\bar{1}32$ | $\bar{1}3\bar{2}$ | $13\bar{2}$ |
| 202 | 132 | $1\bar{3}2$ | 200 | $0\bar{6}0$ | $\bar{1}\bar{3}2$ | $\bar{1}32$ |
| $20\bar{2}$ | $13\bar{2}$ | $1\bar{3}\bar{2}$ | 060 | 200 | 132 | $1\bar{3}2$ |
| 022 | $\bar{1}32$ | 132 | $1\bar{3}2$ | $\bar{1}\bar{3}2$ | $\bar{2}00$ | 060 |
| $02\bar{2}$ | $\bar{1}3\bar{2}$ | $13\bar{2}$ | $\bar{1}32$ | 132 | 060 | 200 |
| 311 | 161 | $2\bar{3}1$ | 231 | $1\bar{6}1$ | $\bar{1}03$ | 033 |
| $\bar{3}11$ | $\bar{2}\bar{3}1$ | $\bar{1}61$ | $\bar{1}\bar{6}1$ | $\bar{2}31$ | $\bar{1}0\bar{3}$ | $03\bar{3}$ |
| $3\bar{1}1$ | 231 | $\bar{1}\bar{6}1$ | $23\bar{1}$ | $1\bar{6}\bar{1}$ | $0\bar{3}3$ | $\bar{1}03$ |
| $31\bar{1}$ | $16\bar{1}$ | $\bar{2}\bar{3}1$ | 161 | $2\bar{3}1$ | 033 | 103 |
| 131 | $\bar{1}61$ | 231 | 103 | $0\bar{3}3$ | $\bar{2}31$ | 161 |
| $\bar{1}31$ | $\bar{2}31$ | 161 | $0\bar{3}3$ | $\bar{1}03$ | $\bar{2}3\bar{1}$ | $16\bar{1}$ |
| $1\bar{3}1$ | $2\bar{3}1$ | $\bar{1}\bar{6}1$ | $10\bar{3}$ | $0\bar{3}\bar{3}$ | $1\bar{6}1$ | $\bar{2}\bar{3}1$ |
| $13\bar{1}$ | $\bar{1}6\bar{1}$ | $23\bar{1}$ | 033 | 103 | $\bar{1}61$ | 231 |
| 113 | 033 | 103 | $2\bar{3}1$ | $\bar{1}\bar{6}1$ | $\bar{2}\bar{3}1$ | $\bar{1}61$ |
| $\bar{1}13$ | $\bar{1}03$ | 033 | $2\bar{6}1$ | $\bar{2}\bar{3}1$ | $\bar{2}\bar{3}\bar{1}$ | $\bar{1}6\bar{1}$ |
| $1\bar{1}3$ | 103 | $0\bar{3}3$ | $2\bar{3}\bar{1}$ | $\bar{1}\bar{6}\bar{1}$ | $\bar{1}\bar{6}1$ | $\bar{2}31$ |
| $11\bar{3}$ | $03\bar{3}$ | $10\bar{3}$ | $\bar{1}61$ | 231 | 161 | $2\bar{3}1$ |

**Table 2.4**: Direction correspondence of different variants of the $N_2M$ superstructure with respect to fcc lattice.

| **CUBIC** | **DIRECTION CORRESPONDENCE ($Ni_2V$)** | | | | | |
|---|---|---|---|---|---|---|
| | **Variant 1** | **Variant 2** | **Variant 3** | **Variant 4** | **Variant 5** | **Variant 6** |
| 100 | 310 | $3\bar{1}0$ | 310 | $3\bar{1}0$ | 001 | 001 |
| 010 | $\bar{3}10$ | 310 | 001 | 001 | $\bar{3}10$ | 310 |
| 001 | 001 | 001 | $3\bar{1}0$ | $\bar{3}\bar{1}0$ | $\bar{3}\bar{1}0$ | $\bar{3}10$ |
| 110 | 010 | 100 | 313 | $3\bar{1}3$ | $\bar{3}13$ | 313 |
| $1\bar{1}0$ | 100 | 010 | $31\bar{3}$ | $3\bar{1}\bar{3}$ | $3\bar{1}3$ | $\bar{3}\bar{1}3$ |
| 101 | 313 | $3\bar{1}3$ | 100 | $0\bar{1}0$ | $\bar{3}\bar{1}3$ | $\bar{3}13$ |
| $10\bar{1}$ | $31\bar{1}$ | $3\bar{1}\bar{3}$ | 010 | 100 | 313 | $3\bar{1}3$ |
| 011 | $\bar{3}13$ | 313 | $3\bar{1}3$ | $\bar{3}\bar{1}3$ | $\bar{1}00$ | 010 |
| $01\bar{1}$ | $\bar{3}1\bar{3}$ | $31\bar{3}$ | $\bar{3}13$ | 313 | 010 | 100 |
| 112 | 013 | 101 | $9\bar{1}3$ | $\bar{1}\bar{1}1$ | $\bar{9}\bar{1}3$ | $\bar{1}11$ |
| $\bar{1}12$ | $\bar{1}01$ | 013 | $1\bar{1}1$ | $\bar{9}\bar{1}3$ | $\bar{9}\bar{1}\bar{3}$ | $\bar{1}1\bar{1}$ |
| $1\bar{1}2$ | 101 | $0\bar{1}3$ | $9\bar{1}\bar{3}$ | $\bar{1}\bar{1}\bar{1}$ | $\bar{1}\bar{1}1$ | $\bar{9}13$ |
| $11\bar{2}$ | $01\bar{3}$ | $10\bar{1}$ | $\bar{1}11$ | 913 | 111 | $9\bar{1}3$ |
| 121 | $\bar{1}11$ | 913 | 101 | $0\bar{1}3$ | $\bar{9}13$ | 111 |
| $\bar{1}21$ | $\bar{9}13$ | 111 | $0\bar{1}3$ | $\bar{1}01$ | $\bar{9}1\bar{3}$ | $11\bar{1}$ |
| $1\bar{2}1$ | $9\bar{1}3$ | $\bar{1}\bar{1}1$ | $10\bar{1}$ | $0\bar{1}\bar{3}$ | $1\bar{1}1$ | $\bar{9}\bar{1}3$ |
| $12\bar{1}$ | $\bar{1}1\bar{1}$ | $91\bar{3}$ | 013 | 101 | $\bar{1}11$ | 913 |
| 211 | 111 | $9\bar{1}3$ | 913 | $1\bar{1}1$ | $\bar{1}01$ | 013 |
| $\bar{2}11$ | $\bar{9}\bar{1}3$ | $\bar{1}11$ | $\bar{1}\bar{1}1$ | $\bar{9}13$ | $\bar{1}0\bar{1}$ | $01\bar{3}$ |
| $2\bar{1}1$ | 913 | $1\bar{1}1$ | $91\bar{3}$ | $1\bar{1}\bar{1}$ | $0\bar{1}3$ | $\bar{1}01$ |
| $21\bar{1}$ | $11\bar{1}$ | $9\bar{1}\bar{3}$ | 111 | $9\bar{1}3$ | 013 | 101 |

### 2.1.3. Structure Factor:

The positions of six atoms in the unit cell of ordered $N_2M$ structure are given below.

$$\mathrm{N}: 0, \frac{1}{3}, 0; 0, \frac{2}{3}, 0; \frac{1}{2}, \frac{1}{6}, \frac{1}{2}; \frac{1}{2}, \frac{5}{6}, \frac{1}{2}$$

$$\mathrm{M}: 0,0,0; \frac{1}{2}, \frac{1}{2}, \frac{1}{2}$$

The structure factor would therefore be

$$\mathrm{F}_{HKL} = \mathrm{f_N} + \mathrm{f_N}\exp 2\pi\mathrm{i}\left(\frac{H}{2}+\frac{K}{2}+\frac{L}{2}\right) + \mathrm{f_M}\exp 2\pi\mathrm{i}\left(\frac{K}{3}\right) + \mathrm{f_M}\exp 2\pi\mathrm{i}\left(\frac{H}{2}+\frac{K}{6}+\frac{L}{2}\right)$$
$$+ \mathrm{f_M}\exp 2\pi\mathrm{i}\left(\frac{H}{2}+\frac{5K}{6}+\frac{L}{2}\right)$$

This would simplify to the form

$$\mathrm{F}_{HKL} = [1+\exp\pi\mathrm{i}(H+K+L)]\left[\mathrm{f_N} + 2\mathrm{f_M}\mathrm{Cos}\left(\frac{\pi K}{3}\right)\exp\pi\mathrm{i}K\right] \quad .... (2.1)$$

, where, (*HKL*) and (*hkl*) are miller indices of planes referred to ordered $N_2M$ structure and A1 structure, and, $f_N$ and $f_M$ are the atomic scattering factors of N and M atoms, respectively. Since $N_2M$ structure has a body-centered unit cell, all reflections for which *H*+*K*+*L* are odd, structure factor is zero and hence they are forbidden.

For *H*+*K*+*L* = even, expression for structure factor corresponding to the fundamental and superlattice can be summarized as

$F_f = 2\ (\ 2\ f_N + f_M)$ for *K*=3,6....... .... (2.2)

$F_s = 2\ S\ (\ f_N - f_M)$ for *K*≠3,6....... …. (2.3)

where, $F_f$ = structure factor of fundamental reflections and $F_s$ = structure factor of superlattice reflections. The values of F calculated for different *H*, *K* and *L* for order parameter S = 1 are listed in table 2.5. In most of the alloy systems, each sub-lattice position can be occupied by more than one type of atoms. In such situations the atomic scattering factor for each lattice site is taken to be the sum of weighted averages of atomic scattering factor of atoms that occupy each sub-lattice position.

**Table 2.5:** Structure factor calculated for ordered $N_2M$ structure

| ***h* + *k* + *l*** | ***H*** | ***K*** | ***L*** | ***F*** | ***F*²** | **Typical Reflections** | |
|---|---|---|---|---|---|---|---|
| | | | | | | **Orthorhombic Notations** | **A1 Notations** |
| Odd | Odd | Even | Even | 0 | 0 | 100, 102, 300 | 110, 112, 330 |
| | Even | Odd | Even | | | 010, 012, 212 | $\overline{\frac{1}{3}}\frac{1}{3}0$, $\overline{\frac{1}{3}}\frac{1}{3}2$, $\frac{5}{3}\frac{7}{3}2$ |
| | Even | Even | Odd | | | 001, 201, 003 | 001, 221, 003 |
| | Odd | Odd | Odd | | | 111, 311, 331 | $\frac{2}{3}\frac{4}{3}1$, $2\frac{4}{3}1$, 241 |
| Even | Even | *K*/3 Even | Even | $2(2f_N + f_M)$ | $4(2f_N + f_M)^2$ | 002, 200, 202, 060 | 002, 220, 222, 220 |
| | Odd | *K*/3 Odd | Even | | | 130, 132, 330, 332 | 020, 022, 240, 242 |
| | Odd | *K*/3 Even | Odd | | | 101, 103, 161, 361 | 111, 113, $\bar{1}31$, 151 |
| | Even | *K*/3 Odd | Odd | | | 031, 231, 033, 233 | $\bar{1}11$, 131, $\bar{1}13$, $\bar{1}33$ |
| | Even | *K*/3 Non-integral | Even | $2(f_N - f_M)$ | $4(f_N - f_M)^2$ | 020, 022, 220, 042 | $\overline{\frac{2}{3}}\frac{2}{3}0$, $\overline{\frac{2}{3}}\frac{2}{3}2$, $\frac{4}{3}\frac{8}{3}0$, $\overline{\frac{4}{3}}\frac{4}{3}2$ |
| | Odd | | Even | | | 110, 112, 150 | $\frac{2}{3}\frac{4}{3}0$, $\frac{2}{3}\frac{4}{3}2$, $\overline{\frac{2}{3}}\frac{8}{3}0$ |
| | Odd | | Odd | | | 121, 123, 321, 141 | $\frac{1}{3}\frac{5}{3}1$, $\frac{1}{3}\frac{5}{3}3$, $\frac{7}{3}\frac{11}{3}1$, $\overline{\frac{1}{3}}\frac{7}{3}1$ |
| | Even | | Odd | | | 011, 013, 211, 051 | $\overline{\frac{1}{3}}\frac{1}{3}1$, $\overline{\frac{1}{3}}\frac{1}{3}3$, $\frac{5}{3}\frac{7}{3}1$, $\overline{\frac{5}{6}}\frac{5}{6}1$ |

## 2.2. Identification of ordered $Ni_2(Cr,Mo)$ phase:

### 2.2.1. X- ray Diffraction:

Due to tetragonality associated with the ordering transformation, diffraction patterns exhibit a shift and splitting of fundamental peaks. On the basis of reported lattice parameters of both disordered fcc and ordered $N_2M$ phases in Ni-33.3at%Cr alloy [70], expected 2θ peak positions for two phases for Cu-$K_\alpha$ x-rays can be calculated as listed in table 2.6. It is clear from the table 2.6 that upon ordering each fundamental reflection of the disordered lattice split into groups of reflections of the ordered lattice. Whether the reflections within each group will be seen as separate peaks or just as one single broad peak is decided by the resolution of the x-ray diffractometer system and the separation between the lines. The intensity ratios of different reflections of ordered lattice is also given in table 2.6.

One of the ways of identifying ordering is from the presence of superlattice reflections in the XRD pattern. Whether the superlattice reflections could be observed or not is determined by relative intensity between the fundamental and the superlattice peaks. In order to get some quantitative information regarding the possibility of observing the superlattice reflections, the intensity of fundamental and superlattice reflections have been theoretically estimated for the alloy compositions studied here and is given in table 2.7. Details of the calculation are given in Appendix I. It is pertinent to point out at this point that the atomic scattering factors corrected for photoelectric absorption and anomalous scattering have been used to determine the structure factor corresponding to fundamental and superlattice reflections. It is clear from the table 2.7 that the ratio of intensities of superlattice to fundamental reflections is very small and is strongly dependent on alloy composition. This ratio increases with increase of Mo concentration as shown in fig. 2.3.

The consequence of such a low ratio of $I_S/I_F$ is that in a laboratory x-ray diffractometer, superlattice reflections would hardly appear, where, $I_S$ = Intensity of superlattice peak and $I_F$

**Table 2.6:** 2θ values for Fundamental peaks of disordered stoichiometric $Ni_2Cr$ alloy and the corresponding peaks of ordered $Ni_2Cr$ alloy for CuK$_\alpha$ X-ray Source.

| **DISORDERED (fcc)** | | **ORDERED ( $\mathbf{DO_{2h}^{25}}$ – *Immm* )** | | |
|---|---|---|---|---|
| ***h k l*** | **2θ (degrees)** | ***H K L*** | **2θ (degrees)** | **Intensity Ratio** |
| 1 1 1 | 43.943 | 0 3 1 | 43.990 | 1 |
| | | 1 0 1 | 43.990 | 1 |
| 2 0 0 | 51.192 | 1 3 0 | 51.246 | 2 |
| | | 0 0 2 | 51.254 | 1 |
| 2 2 0 | 75.320 | 2 0 0 | 75.406 | 1 |
| | | 0 6 0 | 75.406 | 1 |
| | | 1 3 2 | 75.413 | 4 |
| 3 1 1 | 91.521 | 1 6 1 | 91.637 | 2 |
| | | 2 3 1 | 91.637 | 2 |
| | | 0 3 3 | 91.650 | 1 |
| | | 1 0 3 | 91.650 | 1 |
| 2 2 2 | 96.885 | 2 0 2 | 97.017 | 1 |
| | | 0 6 2 | 97.017 | 1 |
| 4 0 0 | 119.549 | 2 6 0 | 119.740 | 2 |
| | | 0 0 4 | 119.740 | 1 |
| 3 3 1 | 140.636 | 0 9 1 | 140.950 | 1 |
| | | 3 0 1 | 140.951 | 1 |
| | | 1 6 3 | 140.971 | 2 |
| | | 2 3 3 | 140.972 | 2 |
| 4 2 0 | 150.049 | 1 9 0 | 150.467 | 1 |
| | | 3 3 0 | 150.469 | 1 |
| | | 2 6 2 | 150.481 | 2 |
| | | 1 3 4 | 150.521 | 2 |

= Intensity of fundamental peak. Hence, x-ray diffraction cannot be utilized for ordering studies, though the reduction in lattice parameter and broadening of fundamental reflections can give some idea about the transformation, which can be used in conjunction with other techniques.

**Table 2.7:** Theoretically estimated intensities of fundamental and superlattice reflections of alloys under investigation for x-ray diffraction.

| Alloy Description | $I_S$ | $I_F$ | $I_S/I_F$ | $I_S$ | $I_F$ | $I_S/I_F$ | $I_S$ | $I_F$ | $I_S/I_F$ |
|---|---|---|---|---|---|---|---|---|---|
| | ⅓ $(220)_{fcc}$ | $(220)_{fcc}$ | | ⅓ $(311)_{fcc}$ | $(311)_{fcc}$ | | ⅓ $(420)_{fcc}$ | $(420)_{fcc}$ | |
| Alloy 1 | 1899 | 253075 | **0.008** | 2661 | 289751 | **0.009** | 1327 | 399568 | **0.003** |
| Alloy 2 | 4408 | 295977 | **0.015** | 6059 | 344535 | **0.018** | 2825 | 492076 | **0.006** |
| Alloy 3 | 9888 | 317768 | **0.031** | 13471 | 372526 | **0.036** | 6116 | 539941 | **0.011** |
| Alloy 4 | 18953 | 342251 | **0.055** | 25733 | 404089 | **0.064** | 11564 | 594328 | **0.019** |

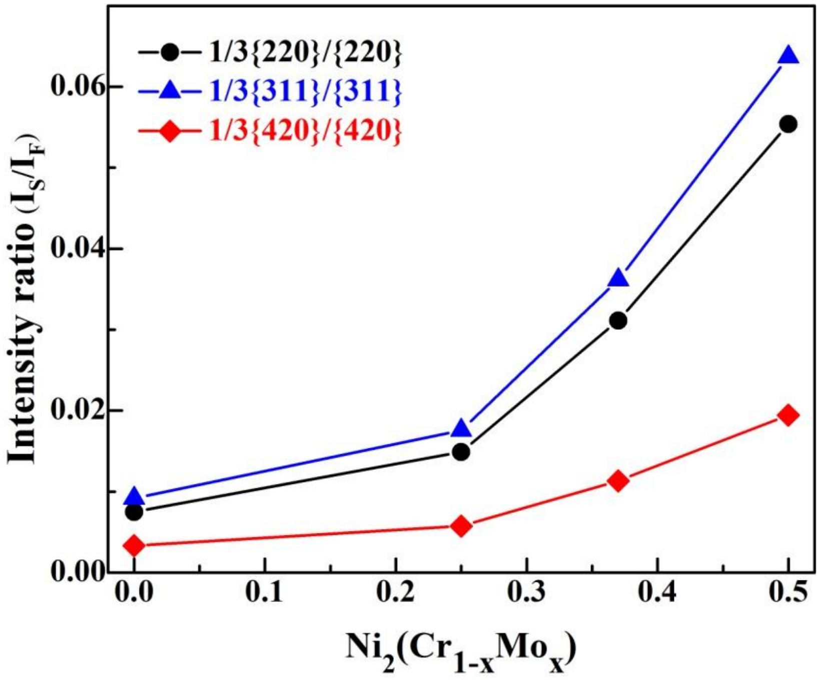

**Figure 2.3:** Ratios of intensities of superlattice to fundamental reflections as a function of Mo concentration in x-ray diffraction.

### 2.2.2. Electron Diffraction:

In this section, selected area electron diffraction patterns have been simulated which are important to identify different variants of the ordered $N_2M$ phase. From the structure factor table (Table 2.5), it is clear that {220}*, {113}* and {024}* reciprocal vectors each would get divided into three parts owing to the emergence of superlattice reflections arising from the ordered structure. Specific variants would show superlattice reflections in specific directions in the reciprocal lattice. These specific reflections have been used to simulate electron diffraction patterns using which one can identify different variants of the $N_2M$ phase unambiguously. Fig. 2.4 gives a set of such simulated diffraction patterns for <001>, <112> and <013> zone axes [69]. It is clear from fig. 2.4 that electron diffraction analyses with minimum three zone axes are essential to establish the existence of all 6 variants of the ordered phase. While both <001> and <013> zone axes can reveal only two variants in each diffraction patterns, three variants of the ordered phase can be identified in each diffraction patterns belonging to <112> zone axes.

### 2.2.3. Neutron diffraction:

Neutron diffraction follows the same mathematical foundation as discussed earlier for x-ray diffraction. The same mathematical equations given in appendix I can be used for calculating the peak intensities of fundamental and superlattice reflections in neutron diffraction by substituting atomic scattering factors by suitable scattering terms of the elements. Neutron interacts with atoms via nuclear forces which are of very short range (i.e. ~ $10^{-15}$ meters) and their interaction is measured in terms of scattering length. In addition, interaction of neutron with the nucleus of atoms can be treated as a point scattering as wavelengths of neutrons are much larger compared to the size of the nucleus. Due to this fact, the scattering amplitude of neutron is independent of scattering angle (unlike x-ray scattering, where scattering amplitude decreases with the

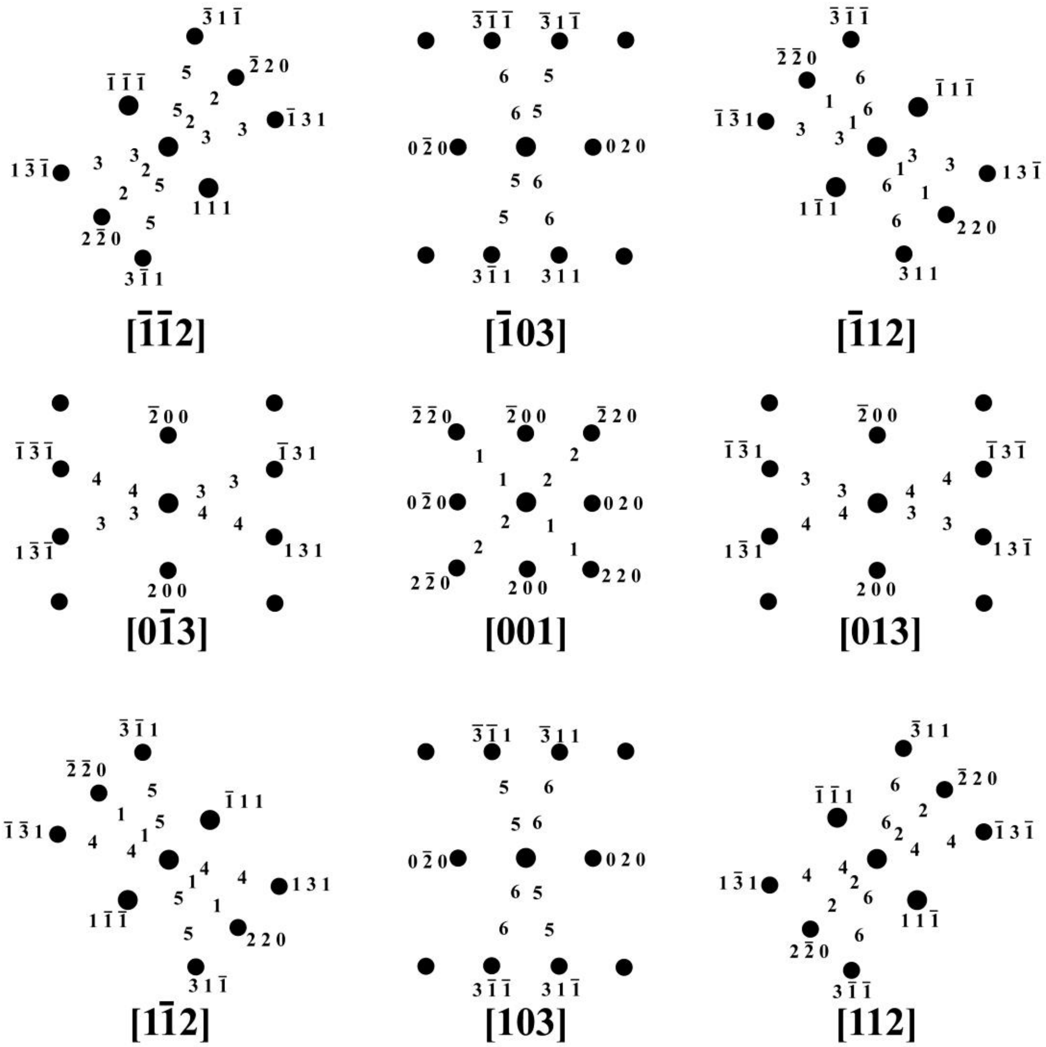

**Figure 2.4:** Simulated electron diffraction patterns of a few zones corresponding to a part of [001] stereographic projection which could be utilized for identifying different variants of the $N_2M$ phase. The numbers 1 to 6 refer to the different variants as well as the positions of the superlattice reflections corresponding to them [69]. Different zones have been underlined.

increase of scattering angle). Following the equations given in appendix I, the intensities of fundamental and superlattice peaks have been theoretically estimated for alloys investigated using scattering lengths of Ni, Cr and Mo atoms [71] and are given in table 2.8. It is clear from the table 2.8 that the ratio of intensities of superlattice to fundamental reflections is higher as compared with that for x-ray diffraction and is also strongly dependent on alloy composition.

However, ratios of intensities decrease with the increase of Mo concentration as shown in fig. 2.5.

**Table 2.8:** Theoretically estimated intensities of fundamental and superlattice reflections of alloys under investigation for neutron diffraction.

| Alloy Description | $I_S$ | $I_F$ | $I_S/I_F$ | $I_S$ | $I_F$ | $I_S/I_F$ | $I_S$ | $I_F$ | $I_S/I_F$ |
|---|---|---|---|---|---|---|---|---|---|
| | ⅓ $(220)_{fcc}$ | $(220)_{fcc}$ | | ⅓ $(311)_{fcc}$ | $(311)_{fcc}$ | | ⅓ $(420)_{fcc}$ | $(420)_{fcc}$ | |
| Alloy 1 | 515874 | 800642 | **0.125** | 2079251 | 64457 | **0.114** | 91578 | 47181 | **0.023** |
| Alloy 2 | 432323 | 670971 | **0.117** | 1742497 | 50424 | **0.107** | 71641 | 36909 | **0.021** |
| Alloy 3 | 445198 | 690953 | **0.099** | 1794390 | 44299 | **0.091** | 62939 | 32426 | **0.018** |
| Alloy 4 | 459359 | 712930 | **0.083** | 1851466 | 38111 | **0.076** | 54148 | 27897 | **0.015** |

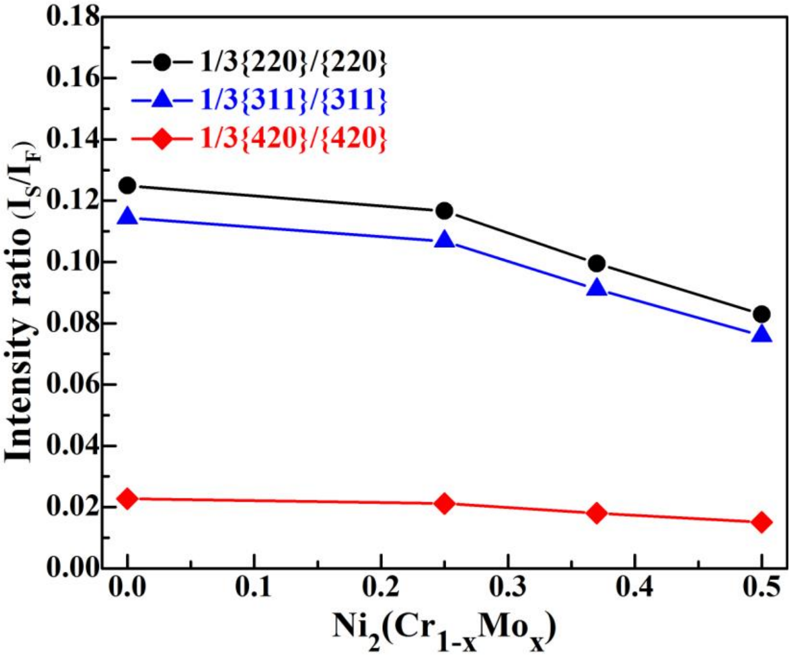

**Figure 2.5:** Ratios of intensities of superlattice to fundamental reflections as a function of Mo concentration in neutron diffraction.

This means that superlattice reflections would be visible in neutron diffraction patterns. This has been shown later in Section 7.2 that superlattice reflections appear strongly in neutron diffraction while they remains undetected in x-ray diffraction.

## 2.3. Basic Crystallographic features of competing structures:

The other phases which compete with $DO_{2h}^{25}$ structure in Ni-Cr-Mo alloys are $DO_{22}$ and $D1_a$ having $N_3M$ and $N_4M$ stoichiometry, respectively [13]. All these ordered structures share a common feature that they are produced by atomic ordering on {4 2 0} set of planes of fcc lattice [32]. For instance, periodic occupation of every 3rd, 4th and 5th layer of {4 2 0} atomic planes by M atoms, respectively, produces $DO_{2h}^{25}$, $DO_{22}$ and $D1_a$ ordered structures as shown in fig. 2.6. Fig. 2.6 also shows their respective unit cells and primitive unit cells drawn by broken green lines and solid red lines in the respective projection maps of atoms on a (0 0 1) plane of different ordered structures viewed along [0 0 1] direction. It is clear from fig. 2.6a that a layered

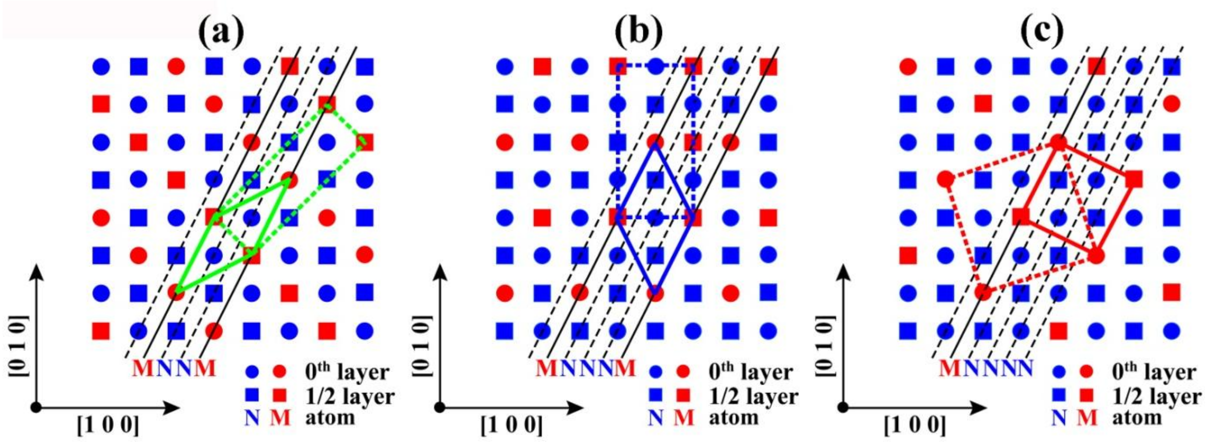

M-

**Figure 2.6:** [0 0 1] projection view of atomic arrangements in two adjacent (0 0 2) planes of fcc lattice. Unit cells and primitive unit cells of different structures are shown by broken lines and solid lines, respectively. Layered stacking sequences are shown in figs. (a) for $N_2M$ structure; (b) for $N_3M$ structure; and (c) $N_4M$ stacking on {4 2 0} planes corresponding to $DO_{2h}^{25}$, $DO_{22}$ and $D1_a$ structures, respectively [32].

repetition of N and M atoms on {4 2 0} planes as -N-N-M- type produce $\mathrm{DO}_{2h}^{25}$ superstructure which is shown in fig. 2.1. Arrangement of N and M atoms by periodically repeating ordering sequence of -N- N-N-M- type on {4 2 0} planes of fcc lattice (Fig. 2.6b) produce a body-centered tetragonal $DO_{22}$ structure which is shown in fig. 2.7a. It can be seen in fig. 2.7b that the $DO_{22}$ structure can be derived from the cubic $L1_2$ structure by successively shearing every (001) plane of the $L1_2$ structure by the displacement vector ½<110] (The asymmetrical notation means that permutations are possible on the first two indices while the third is fixed). In the $DO_{22}$ structure N atoms occupy corner and body center positions while the other atomic positions are occupied by M atoms. Unit cell of $DO_{22}$ structure (space group I4/mmm) contains 6 N atoms and 2 M atoms with coordinates of the atoms as follow:

N: $0,\frac{1}{2},0;\ \frac{1}{2},\frac{1}{2},0;\ 0,\frac{1}{2},\frac{1}{4};\ \frac{1}{2},0,\frac{1}{4};0,\frac{1}{2},\frac{3}{4};\ \frac{1}{2},0,\frac{3}{4}$

M: $0,0,0;\ \frac{1}{2},\frac{1}{2},\frac{1}{2}$

The tetragonal c-axis of the $D0_{22}$ unit cell can align itself along any one of the three axes of the fcc unit cell, resulting in the formation of three mutually independent orthogonal variants called transformation variants [72].

The orientation relationship of the ordered γ″ variants ($D0_{22}$ structure) with the parent fcc matrix is $(001)_{D0_{22}}$ // $\{001\}_{fcc}$, and $[001]_{D0_{22}}$ // $<001>_{fcc}$ . Since the axial ratio is very close to 2 (c/a ~2.05), the $D0_{22}$ structure can be regarded as a superstructure forming from the disordered fcc (A1) structure [73].

The arrangement of N and M atoms by periodically repeating ordering sequence of -N-N-N-N-M- type on {4 2 0} planes of fcc lattice (Fig. 2.6c) produces body central tetragonal $D1_a$ structure which is shown in fig. 2.8 [32]. The unit cell of the fcc structure drawn by dashed lines is also shown w.r.t. unit cell of $D1_a$ structure. The unit cell, which is shown schematically in fig. 2.8, contains 8 N atoms and 2 M atoms and the corresponding space group is I 4/m. The coordinates of these atoms are as follows:

$$N\colon \frac{1}{10},\frac{3}{10},\frac{5}{10};\ \frac{2}{10},\frac{6}{10},1;\ \frac{3}{10},\frac{9}{10},\frac{5}{10};\ \frac{4}{10},\frac{2}{10},1;\ \frac{6}{10},\frac{8}{10},1;\ \frac{7}{10},\frac{1}{10},\frac{5}{10};\ \frac{8}{10},\frac{4}{10},1;\ \frac{9}{10},\frac{7}{10},\frac{5}{10}$$

$$M\colon\ 0,0,0;\ \frac{1}{2},\frac{1}{2},\frac{1}{2}$$

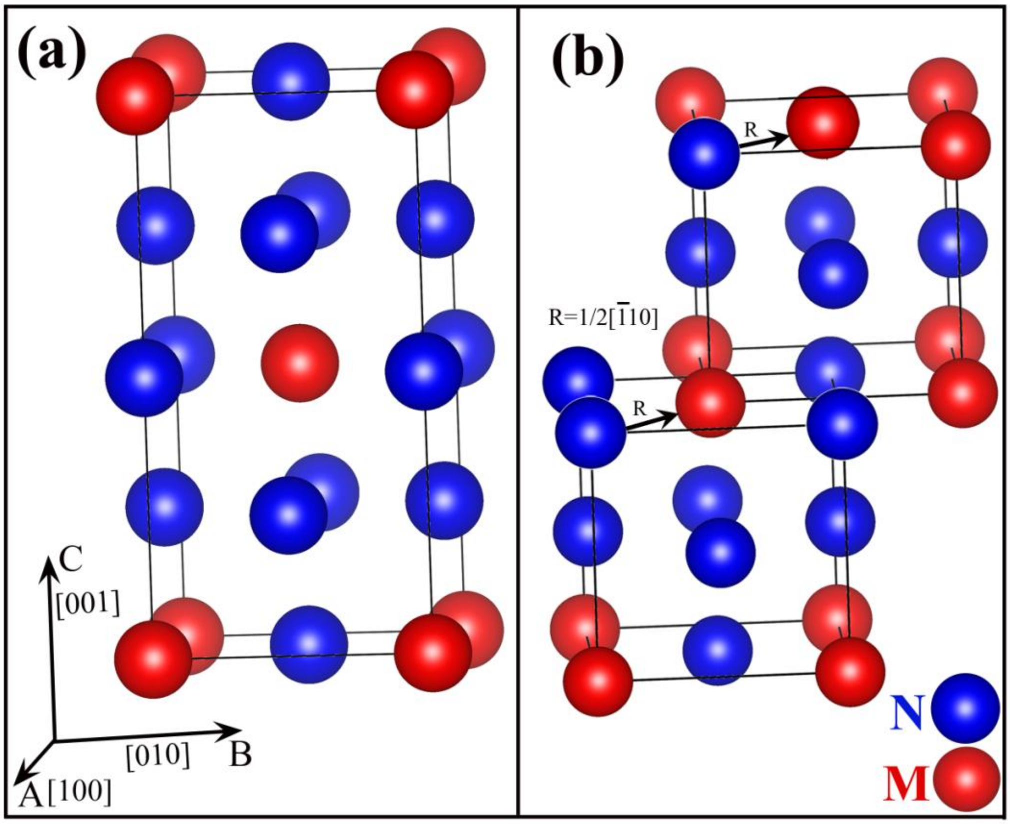

**Figure 2.7:** (a) Unit cell of $DO_{22}$ phase ($N_3M$ stoichiometry). (b) Generation of the $DO_{22}$ structure from the $L1_2$ structure by the operation of a periodic 1/2[$\bar{1}$10] shear on every other (0 0 1) plane of the latter.

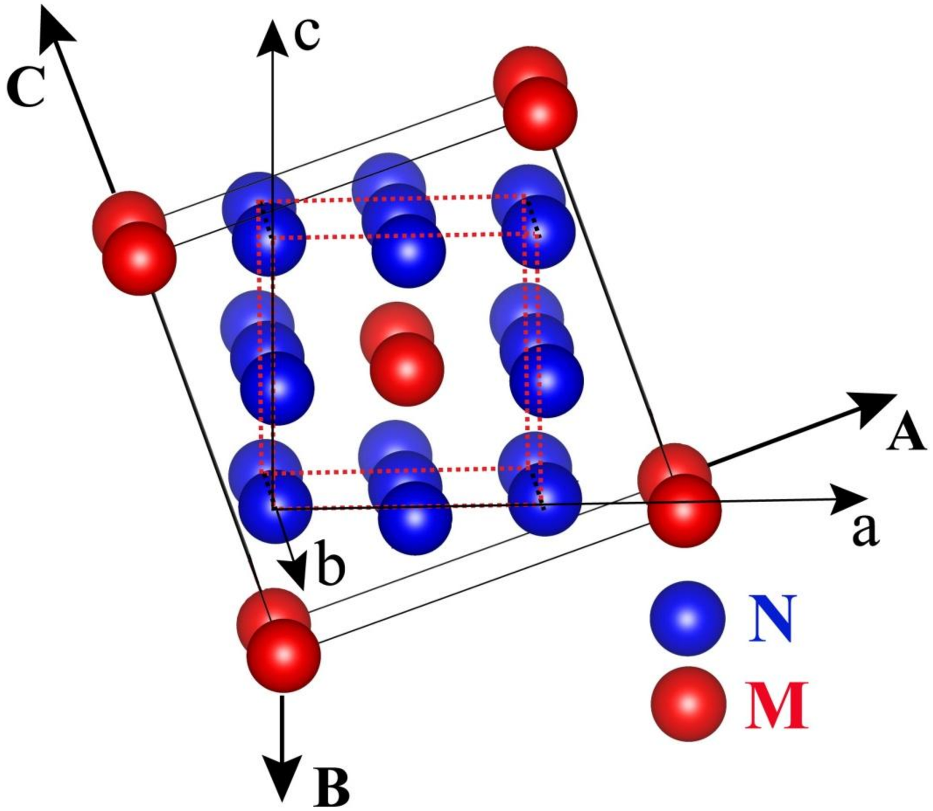

**Figure 2.8:** Unit cell of $D1_a$ phase of $N_4M$ stoichiometry (drawn with solid lines) shown with respect to fcc a lattice (drawn by broken lines) [32].

### 2.4. Atomic architecture in the Short-range order:

Short-range order (SRO) in Ni-Mo and Ni-Cr-Mo alloys has been characterized by the appearance of diffuse diffraction intensity maxima at {1 ½ 0} positions in electron diffraction [13, 32, 38, 39, 74-76]. Two models, namely, “Microdomain model” and “Static Concentration Wave (SCW) model” have been employed to explain the origin of diffuse diffraction intensity at these positions. The “Microdomain model” is based upon the concept of existence of microdomains of long-range ordered (LRO) structures, while the “Static Concentration Wave (SCW) model” is based upon concentration waves concept conceptualised to represent stacking of atomic species on lattice planes. In the microdomain model, {1 ½ 0} SRO state has been attributed to the presence of microdomains of LRO structures which need not correspond to the structures of equilibrium phases [31]. In this model, imperfectly ordered microdomains of $DO_{22}$ structure are suggested to be responsible for the appearance of diffuse intensity at {1 ½ 0} spots and its absence at {1 0 0} positions [31]. Moreover, evidence of diffuse reflections at superlattice positions of $DO_{2h}^{25}$ order and $D1_a$ - type of order in {1 ½ 0} SRO state lead the researchers to conclude that SRO state is actually comprise of a mixture of microdomains or sub-unit cell clusters of $DO_{2h}^{25}$, $DO_{22}$ and $D1_a$ structures [31]. The experimental evidences and Monte-Carlo simulation studies by Hata et el. [76-78] and Kulkarni et al. [79] support this model as they observe the existence of microdomains of $DO_{2h}^{25}$, $DO_{22}$ and D1a structural units in the {1 ½ 0} SRO state of $Ni_3Mo$ and $Ni_4Mo$ alloys.

The SCW model is based upon the concept of concentration waves which is first emphasize as an important tool for understanding transformation reactions in metallic solid solutions in the works of Hillert [54] and Cahn [55, 57] and later develop and generalize by de Fontaine, Cook and Hilliard [58-60, 80]. This approach is based on the discrete lattice methods used extensively by Krivoglaz [81] and Khachaturyan [82] which is generally applicable to the early stages of continuous transformations. In the discrete lattice formalism, continuum theory of Cahn describing spinodal decomposition appears as a limiting case at the long wavelength limits. The mathematical formalism of diffusion equations given by Cook et al. [59] explain the time evolution of quasiperiodic concentration waves in the context of both long-wavelength limits (Spinodal decomposition) and short-wavelength limits (Spinodal ordering). Cook et al. [59] correct the oversimplification of Cahn continuum theory [55, 56] by formulating diffusion equations in discrete lattice formalism. According to Cook et al. [59] the time evolution of the amplitude of concentration waves, for a given wave vector, is governed by following expression:

$A(k) = A^{o}(k)*\exp[\alpha(k)*t]$ ………………………………..(2.4)

Where, $A^{o}(k)$ is the amplitude of wave with wave vector, k, at t = 0 and α(k) is the amplification factor for given wave vector, k.

The amplification factor which appeared in equation 2.4 exhibits isotropic behavior in the continuum approximation of Cahn [55, 56], while shows anisotropic behavior in the discrete formalism of Cook et al. [59] (Fig. 2.9). It was clear from fig. 2.9 that in continuum approximation amplification factor remains finite in the longer wavelength spectrum of concentration waves until the wavelength reaches six times interplannar spacing beyond which it deviates from the normal behavior and diverge for waves having wavelength of the order of interplannar spacing. In the discrete lattice formalism the maximum amplification occur for wave

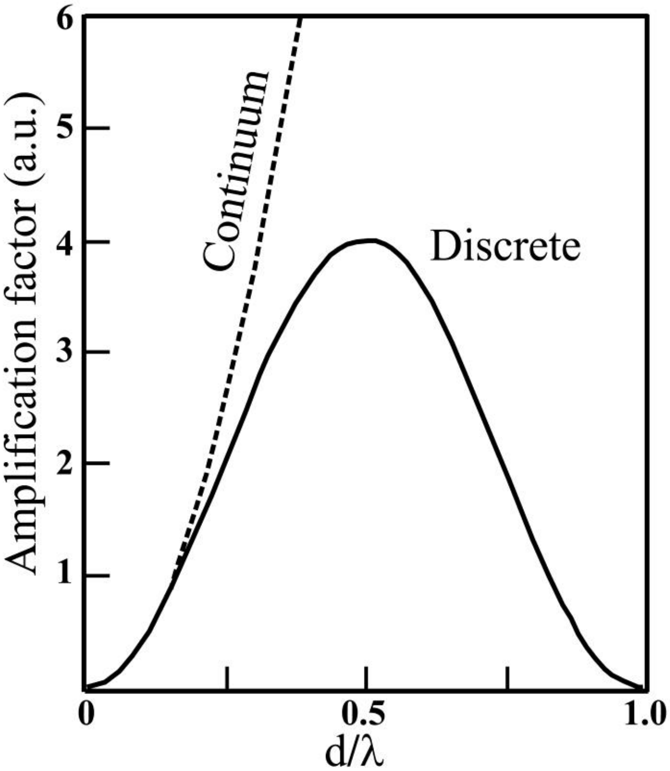

**Figure 2.9:** Amplification of concentration waves in the continuum approximation and discrete lattice formalism [59].

vectors having wavelengths of the order of interplannar spacing while remains lowest for waves having wavelengths longer than interplannar spacing.

The picture thus emerges as: a solid solution can be described by a spectrum of concentration waves of different wavelengths and amplitudes, defining the distribution of atoms over the lattice, which are represented by Fourier components of the concentration waves [80]. Out of this spectrum of concentration waves, only waves having positive values of $\alpha(k)$ grow spontaneously, while waves having negative values of $\alpha(k)$ decay [59]. The localization of the components of concentration waves at specific points in the first Brillouin zone is particularly useful for understanding the various diffuse scattering effects which accompany clustering and ordering. The amplitude of scattering at a location in the reciprocal lattice is proportional to the amplitude of the corresponding Fourier component of the composition function describing the heterogeneities in real space [80].

On the basis of the appearance of intensity maxima at {1 ½ 0} positions these concentration waves suggest to be characterized by wave vectors ending at {1 ½ 0} positions in <1 ½ 0> directions [80]. These concentration waves are suggested to contain $N_2M_2$ atomic arrangement [13] based on a hypothetical structure proposed by Khachaturyan [83]. These $N_2M_2$ type SCW are considered to be made up of -N-N-M-M- sequence of atoms stacked on {4 2 0} planes of the fcc lattice, which give rise to diffuse diffraction intensity maxima at {1 ½ 0} positions in the reciprocal space [13, 80]. A [0 0 1] view planes of a fcc lattice containing N and M atoms stacked in $N_2M_2$ manner is shown in fig. 2.10a, where one molecule size subunit cell is drawn by solid lines [13, 83]. The concentration wave corresponding to $N_2M_2$ structure is also shown in fig. 2.10b. Due to same geometrical appearance of subunit cell of the $N_2M_2$ stacking with that outlined for the $DO_{22}$ structure (see fig. 2.6b) suggest it to be call as imperfectly ordered subunit cell of $DO_{22}$ structure.

The specialty of the ordering process in the <1 ½ 0> family of alloys is that minima in the second derivative of free energy, F″, are exhibited at {1 ½ 0} points which are different from the superlattice positions of corresponding LRO structures. This minimization of F″ at these {1 ½ 0} positions occurred due to the absolute minimum of pair interaction function, V(k), (Fourier transform of pair interaction in real space) as symmetry elements intersect at these points [80]. According to this scheme SRO state forms by the amplification of concentration waves with wave vectors terminating at {1 ½ 0} special points, as the system becomes unstable with respect to such concentration waves, when it is brought below a critical temperature defined as the ordering spinodal. The preferential formation of waves with wave vectors ending

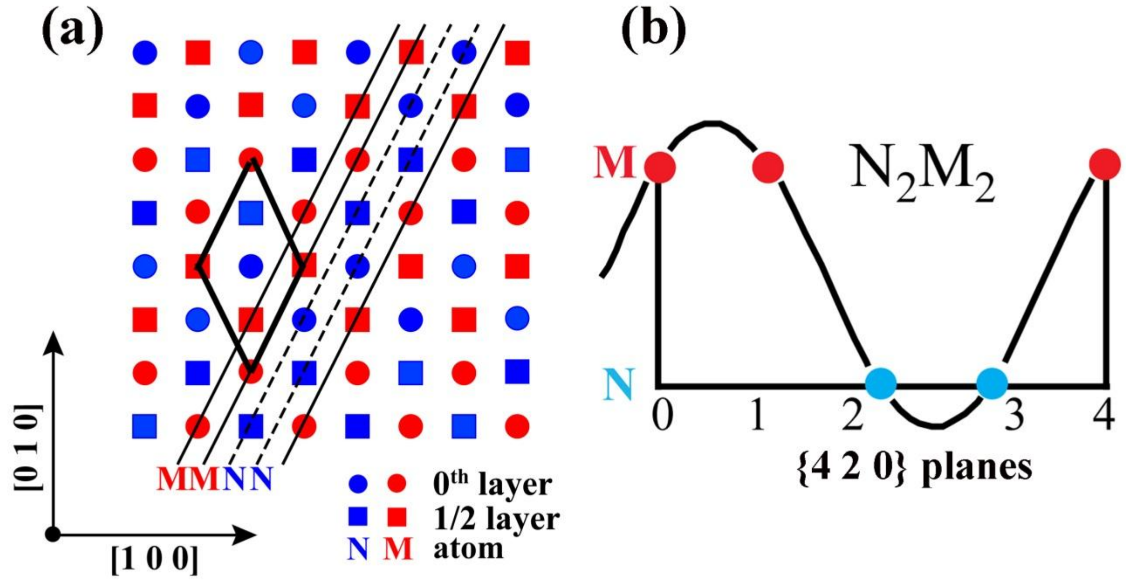

**Figure 2.10:** (a) [0 0 1] projection depicting atomic arrangements of $N_2M_2$ generated by a [1 ½ 0] concentration wave. One molecule size subunit cell is drawn by a solid line. The corresponding concentration wave representing $N_2M_2$ structure is also shown in fig. (b).

at {1 ½ 0} positions is favor by maximum amplification factor of these waves than that corresponding to other k-vectors of corresponding LRO structures [80]. A schematic representation of different LRO structures, in terms of their concentration waves, is shown in fig. 2.11. Fig. 2.12 shows the positions of superlattice reflections in the fourier spectra of different LRO structures belonging to (1 ½ 0) family. It was clear from Fig. 2.12 that the superlattice reflections corresponding to ordered structures divide wave vector ending at {4 2 0} positions in proportions which is decided by the position of M planes in the layered sequence of N planes. de Fontaine [80] have also showed that the spinodal temperature of the {1 ½ 0} waves is higher than that of all other concentration waves corresponding to LRO structures. Therefore, if by fast cooling the nucleation of the ordered phase is suppressed, the {1 ½ 0} waves will form and amplifies as soon as the temperature falls below their ordering spinodal $(T_S)$. At a temperature $T < T_S$, the driving force for amplification of the concentration wave amplitude would also be proportional to the supercooling $(T_S - T)$. Since the {1 ½ 0} waves possess the highest spinodal temperature, the driving force for their formation surpasses that of all other waves. Therefore, it is expected that {1 ½ 0} waves are preferentially formed and amplified even under conditions where the temperature is lower than the spinodal temperature of other waves.

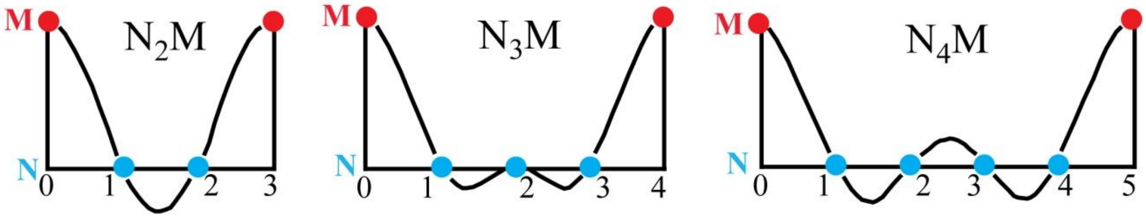

**Figure 2.11:** Concentration wave description of different long-range ordered structures [80].

In the SCW model long-range ordered structures of $DO_{2h}^{25}$, $DO_{22}$ and $D1_a$ types are generated by superimposition of different SCWs, e.g. superimposition of mutually perpendicular <1 ½ 0> SCWs of $N_2M_2$ type produces microdomains of $DO_{2h}^{25}$ and $D1_a$ structural units (Fig. 2.13). Similarly the microdomain of $DO_{22}$ structural unit is formed by the superimposition of <1 ½ 0> SCW with <1 0 0> wave as depicted in fig. 2.13. Thus, the formalism of SCW offered an easy interpretation of SRO and LRO as the atomic arrangements are describe in terms of superposition of simple co-sinusoidal waves of various amplitudes and wavelengths along specific crystallographic directions [80].

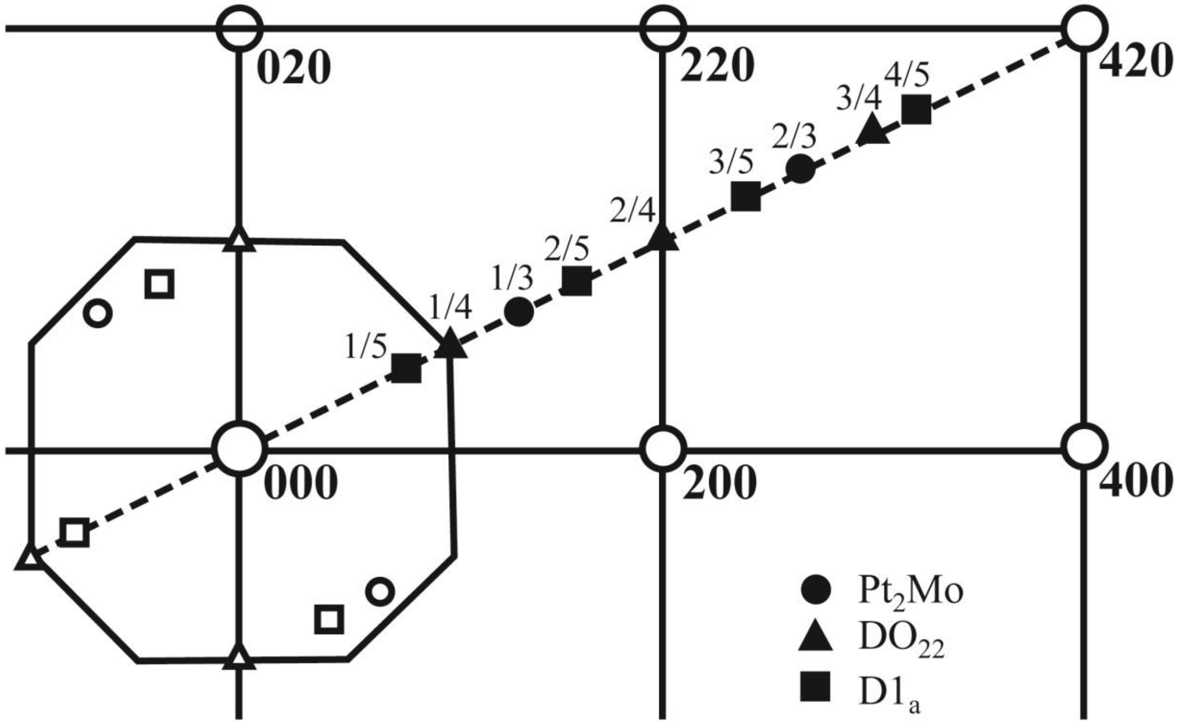

**Figure 2.12:** Fourier spectra of single variants of different long range order structures belonging to (1 ½ 0) family (filled symbols). Open symbols represent superlattice reflections of different ordered structures in the 1st Brillouin zone [80].

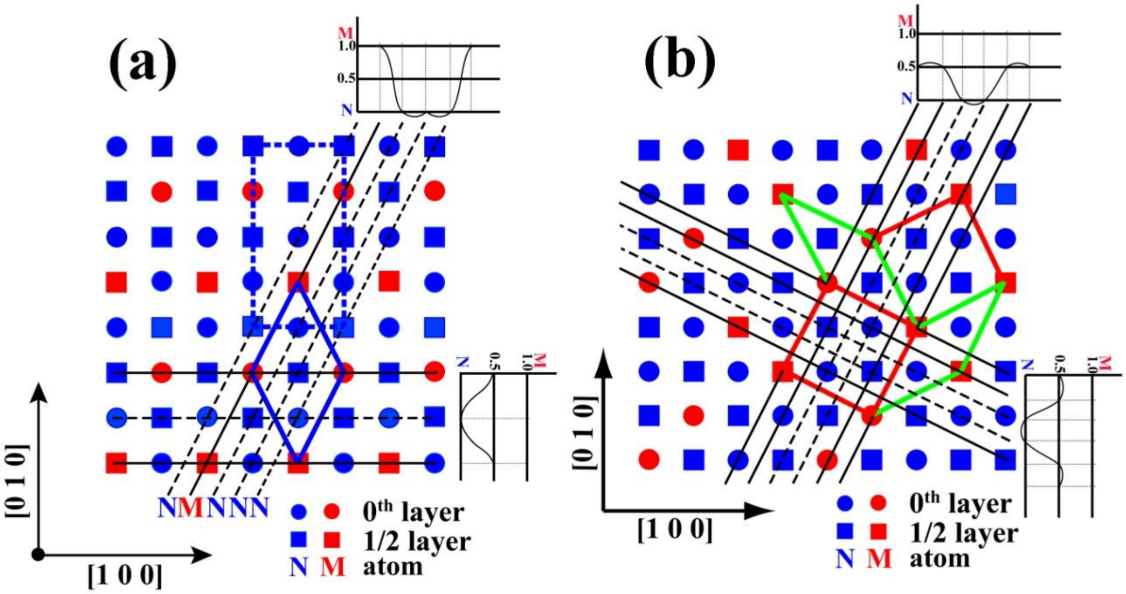

**Figure 2.13:** [0 0 1] projection depicting atomic arrangements in fcc lattice. (a) One molecule size microdomain of $DO_{22}$ structure is generated by superimposition of [1 ½ 0] and [1 0 0] concentration waves [13]. (b) Superimposition of two perpendicular <1 ½ 0> concentration waves. This structure comprises of an arrangement of two variants of each subunit cell corresponding to the $D1_a$ (square-shaped) and the $DO_{2h}^{25}$ (diamond-shaped) structures [13].

# CHAPTER 3

# ALLOY PREPARATION AND EXPERIMENTAL METHODS

## 3.1. Alloy Preparation:

### 3.1.1. Vacuum Arc Melting:

Synthetic alloys of $Ni_2(Cr_{1-x}Mo_x)$ stoichiomtery with x = 0, 0.25, 0.37 and 0.5, each weighing about 450 g, were prepared in an arc melting furnace under high purity argon atmosphere with a non-consumable tungsten electrode and a water cooled hearth. These alloys were selected in order to retain them in single γ phase field at 1200°C as per the Ni-Cr-Mo phase diagram given by Rideout et al. [23]. Fig. 3.1 shows the position of these alloys by solid circles on a tie line connecting $Ni_2Mo$ and $Ni_2Cr$ compositions. Alloys were produced from elemental charge of pure nickel, chromium and molybdenum each of 99.99 % purity. All the buttons were re-melted 5-6 times in order to attain chemical homogeneity of alloying elements in the buttons. In order to break the cast microstructure, these alloys were homogenized by soaking them at 1300 °C for about 40 h, under flowing high purity argon gas atmosphere followed by furnace cooling. Compositions of the homogenized alloys were verified by wavelength dispersive X-ray fluorescence analysis (WD-XRF) as well as by an average of multiple-point analysis using energy dispersive X-ray (EDX) spectroscopy. Compositions of alloys were found to be in agreement with the nominal composition of the alloy and are given in table 3.1. The multiple-point compositional analysis also verified homogeneity of the chemical species in the alloys. Alloy buttons were hot rolled in multiple passes at about 950 °C to reduce buttons thickness from 10.0 mm to 6.0 mm.

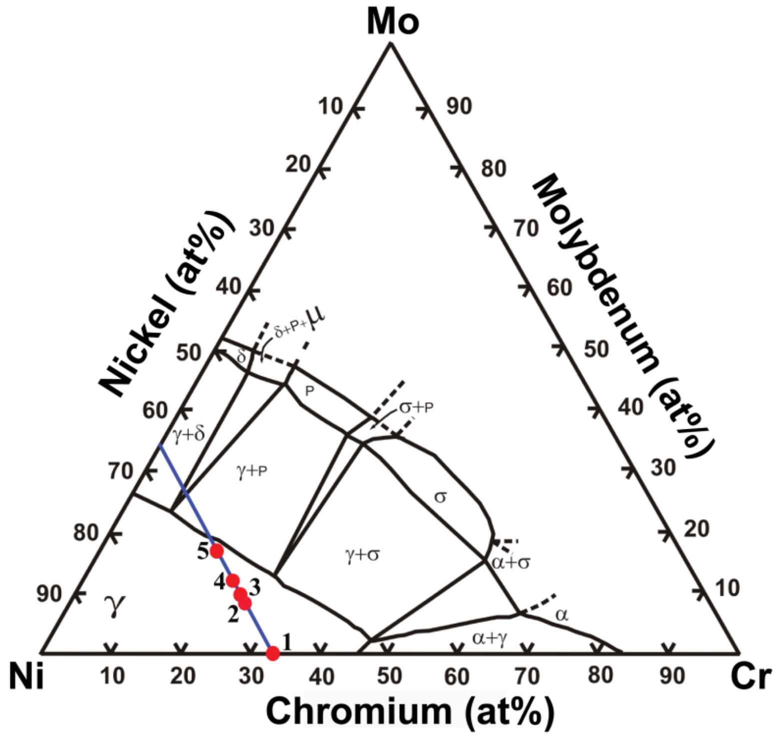

**Figure 3.1:** Ternary phase diagram for Ni-Cr-Mo alloys at 1200°C calculated by Rideout et al. [23].

### 3.1.2. Spat-quenching:

Cubes of about 2.8×2.8×2.8 $mm^3$ size were machined out from the homogenized alloys to prepare alloy samples in splat-quenched state. For splat-quenching, the cubic samples were melted with induction heating and then rapidly solidified to thin foils of about 80 μm thicknesses by pneumatically driven copper punches at a cooling rate of approximately $10^6$ K/sec [84]. Compositions of the splat-quenched samples were found to be in agreement with the respective alloy compositions prepared by cast melting route.

## 3.2. Heat Treatments:

Thin slices cut out from the homogenized bulk samples were sealed in quartz capsules under a helium gas atmosphere at about 160 mm of Hg pressure. The presence of helium gas ensured a rapid cooling rate during the water quenching treatment. Samples of all the alloys were solution treated at 1150°C for about 2h followed by water quenching (at cooling rate ~ $10^3$ K/sec [85]). Solution treated and water quenched samples were aged at different temperatures ranging from 500°C to 760°C, for time periods varied from few minutes to several hundreds of hour. Heat treatments were followed by quenching the sample by breaking the quartz capsule inside water. Identical ageing treatments were also used for splat-quenched samples in order to compare microstructural changes in samples with different initial microstructural states.

**Table 3.1:** Compositions of Ni-Cr-Mo alloys chosen for present study.

| **Sample Description** | **Alloy compositions in atomic % (weight %)** | | | | | | | | |
| --- | --- | --- | --- | --- | --- | --- | --- | --- | --- |
| | ***Theoretical*** | | | ***Experimentally determined composition*** | | | | | |
| | | | | **WDXFS** | | | **EDS** | | |
| | **Ni** | **Cr** | **Mo** | **Ni** | **Cr** | **Mo** | **Ni** | **Cr** | **Mo** |
| **Alloy 1** | 66.7 (69.3) | 33.3 (30.7) | - | 68.0 (69.3) | 32.0 (30.7) | - | 65.5 (68.2) | 34.5 (31.8) | - |
| **Alloy 2** | 66.7 (65.1) | 25.0 (21.6) | 8.3 (13.3) | 65.9 (64.2) | 25.2 (21.8) | 8.8 (14.1) | 64.5 (62.3) | 25.2 (21.6) | 10.3 (16.2) |
| **Alloy 3** | 66.7 (63.2) | 21.0 (17.6) | 12.3 (19.1) | 67.3 (63.7) | 20.2 (17.0) | 12.5 (19.4) | 64.2 (60.0) | 20.8 (17.2) | 15.0 (22.8) |
| **Alloy 4** | 66.7 (61.4) | 16.7 (13.6) | 16.7 (25.1) | 67.3 (61.7) | 15.6 (12.7) | 17.1 (25.6) | 67.3 (61.8) | 15.9 (12.9) | 16.8 (25.2) |

### 3.3. Specimen Preparation for Optical Microscopy, Microhardness and X-ray Diffraction studies:

Specimens for optical microscopy (OM) were prepared by first grinding on successive grades of silicon carbide paper up to 1200 grade, followed by final polishing on a wheel with diamond paste to mirror finish. These specimens were then electrochemically etched with a supersaturated solution of oxalic acid in water at a voltage in the range 10-15 volts to reveal grain boundaries in the microstructures. This procedure ensured that all features were revealed to the best resolution of microscope without any scratches. Samples prepared for optical microscopy were used directly for x-ray diffraction investigations for phase identification and lattice parameter measurements as well as microhardness testing.

### 3.4. Microhardness testing:

Microhardness testing was used to understand the effect of systematic substitution of Cr atoms by Mo atoms in stoichiometric $Ni_2(Cr_{1-x}Mo_x)$ alloys on the hardness properties of the alloys. Samples of about 5-7 mm thickness were used for microhardness investigations using a Vicker's microhardness tester. A constant load of 1 kg was used to measure microhardness at room temperature at 20 different locations. The standard deviation in the measured data set was calculated by measuring the deviations of the measured values from the average.

### 3.5. X-ray Diffraction:

X-ray diffraction (XRD) studies were carried out to confirm the crystallinity of the splat-quenched samples as well as to map the progress of ordering transformation in different $Ni_2(Cr_{1-x}Mo_x)$ alloys. These studies were carried out on a Bruker make D8 Discover diffractometer in Bragg-Brentano geometry employing Cu-$K_\alpha$ radiation source operated at 40 kV and 40 mA. Diffraction data was recorded using a Lynx-eye position sensitive detector which offers high detection efficiency of x-ray photons at lower acquisition times. Following details of the x-ray optics were used for diffraction experiments:

| | |
|---|---|
| Radiation | Cu $K_\alpha$ |
| Goniometer radius | 430 mm |
| Filter | Ni (0.012 mm) |
| Soller slit | 2.5° axial divergence |
| Detector slit | 8 mm |
| $2\theta$ range | 40° to 100° |
| Step size | 0.02° |
| Scan rate | 2 sec per step |

The measured sets of diffraction data was used for lattice parameter determination using Rietveld refinement procedures. The $2\theta$ scale of the diffractometer was calibrated with standard corundum sample and the diffractometer optics was optimally aligned to produce best instrumental resolution. NIST standard $CeO_2$ powder was used to determine the resolution of the instrument.

### 3.6. Optical and Transmission Electron Microscopy:

An Olympus make optical microscope using bright field as well as polarized light microscopy was used to characterize features such as grain size, inter and intra boundary precipitation.

Transmission electron microscopy (TEM) investigations were carried out in a Philips CM30 transmission electron microscope equipped with an EDAX make Genesis EDX system and operating at 300 kV. Thin foil specimens for TEM investigation were made by first mechanically grinding the samples to a thickness of about 0.1 to 0.2 mm. Disc samples of 3 mm diameter were then punched out from the thin foils. Electron transparent foils for TEM investigation were prepared by electrolytical polishing using an electrolyte containing 1 part of perchloric acid and 4 parts of ethanol by a Tenupol twin jet polishing instrument at about –35 to –30 °C with DC voltage from 20 - 25 Volts.

Standard TEM techniques such as bright-field (BF) and dark-field (DF) imaging and selected area electron diffraction (SAED) were employed for microstructural characterization. Fuji image plates were used for recording diffraction patterns employing long-time exposure (1-2 min.) due to weak and diffuse nature of {1 ½ 0} reflections. SAED patterns with different zone axes of <0 0 1>, <1 1 2> and <0 1 3> were used to identify the different variants of ordered $N_2M$ phase. Variants of ordered domains were imaged in the DF mode by selectively using superlattice reflections of the ordered phase. An attempt was made to qualitatively understand the ordering kinetics on the basis of intensity saturation rate of superlattice reflections with different ageing times. Following precautions were taken while quantifying the intensity of these reflections: (i) all measurements were done in the <1 0 0> zone axis; (ii) a fixed exposure time was used for recording the diffraction pattern after ensuring a nearly same total electron current density on the viewing screen; (iii) using the same objective aperture (Ø = 10 μm). The intensity profile of superlattice reflections was first determined along a line passing through the pre-defined centers of diffraction spots. Thickness and interaction volumes corrections were further incorporated by proportionately enhancing the intensities of transmitted beams to match their full-width at half-maxima. Diffraction intensities were then normalized by its transmitted intensity to quantify intensities at different ageing times.

### 3.7. 3-Dimensional Atom Probe:

3-dimensional atom probe (3D-AP) is an analytical microscope capable of revealing chemical distribution of atomic species in 3-dimensional space nearly at the atomic resolution in the reconstructed volume [86-89]. 3D-AP method offers the possibility to determine the chemical composition of sub-nanometer regions arbitrarily selected from the reconstructed volume. In the present work, a three-dimensional atom probe was used to carry out a high resolution microchemical analysis.

3-dimensional atom probe is a combination of two parts, a field ion microscope (FIM)

[90, 91] and a time-of-flight (TOF) mass spectrometer [92, 93]. In the field ion microscopy a needle-like conducting sharp sample is used to produce image of microstructural features in the apex region of the needle. A small amount of an inert gas, usually He or Ne, is usually admitted in the FIM chamber which acts as imaging gas. A high tension DC voltage, $U_{DC}$, is applied to the needle sample maintained at cryogenic temperature (70K). The application of cryogenic temperature reduces the transverse velocity of the imaging gas atoms and improves the imaging resolution. The high field in the proximity of tip sample causes polarization of imaging gas atoms which are drawn towards the surface of the tip. In the presence of intense electric field, image gas atoms become field ionized by the tunneling of electrons from imaging gas atoms through the surface potential barrier into a vacant energy levels in the specimen. This creates positively charged gas ions near the surface which fly away from the specimen towards the channel plate where the field ion image is formed on a fluorescence screen. In this way, a projection of the surface structures of the tip is formed at atomic resolution on the fluorescence screen. Usually a channel plate is placed in front of fluorescence screen which act as an image intensifier. The best imaging conditions are obtained by optimising channel plate and tip voltage. The electric field typically between 20-50 V/nm is required in the field ionization process [92, 94]. Such high field strengths are achieved by reducing the end radius of the tip to about 20-50 nm as electric field varies in inversely proportional manner with tip radius.

An atom probe experiment is started by removing the image gas from the experimental chamber. The surface atoms are then field evaporated by applying an additional voltage to the specimen in form of a series of high voltage pulses, $U_p$, of nanosecond rise time. The necessary field evaporation strength, F, is determined by the radius of curvature R of the sample and a total voltage, $U_{tot}$, between the sample and the counter electrode which is of the order $U_{tot}$= 2 -15 kV (see. Eq. 3.1). Here k is a shape factor which depends of the shaft angle of the sample whole value falls from k = 4 – 9 and $U_{tot} = U_{DC} + U_{p.}$ Different atomic species have different evaporation fields which are also dependent upon the charge state of evaporating ions. Critical evaporation field strengths F (V / nm) of the alloying elements Ni, Cr and Mo as a function of the charge state of each ion are given in table 3.2.

$$F = U_{tot} / k R \quad \ldots\ldots\ldots\ldots\ldots\ldots\ldots\ldots\ldots\ldots\ldots 3.1$$

**Table 3.2:** Critical evaporation field strengths of Ni, Cr and Mo atoms in different charge states.

| Element / Charge State | Evaporation Field strength (V/nm) | | |
|---|---|---|---|
| | +1 | +2 | +3 |
| Ni | 35 | 36 | 65 |
| Cr | 27 | 29 | 51 |
| Mo | 41 | 51 | 46 |

Ionized atoms removed from the surface of the samples are analyzed in the time of flight mass spectrometer according to equation 3.2.

$$M = m/n = 2eU_{tot} \left((t_{flight} - t_0)/L_{flight}\right)^2 \quad \ldots\ldots\ldots\ldots\ldots\ldots\ldots\ldots\ldots\ldots 3.2$$

Where, M is mass to charge ratio, e is the elementary charge and the flight time of an ion is the time between onset of the electric pulse, $t_0$, which triggers the field evaporation and the moment, $t_{flight}$, at which the ion has produced a signal at the end of the MCP, after it has completed the flight length, $L_{flight}$. This allows the chemical identification of the evaporated atom, and thus the element-specific 3D Reconstruction and analysis of the examined sample volume.

The 3D-AP detector consists of a microchannel plate (MCP) and an array of 100 multianodes with a parallel time recording system. The incident ions generate secondary electrons, which undergo rapid multiplication as they are accelerated through the channel plate. The cloud of electrons flies then towards the multianode detector and strikes against several anodes. The lateral arrangement of the evaporated ion can be precisely determined if at least three anodes are hit [86]. The calculation of the center of the charge-cloud yields the lateral position of the evaporated ion. Based upon the distance between the tubes of the MCP, only 60% of the evaporated ions are analyzed by the 3D-AP detector. In present study, 3D-AP experiments were performed on voltage pulsed CAMECA make tomographic atom probe (TAP) instrument [86]. The experiments were carried out in ultra-high vacuum $p < 10^{-6}$ Pa at a pulse-to-DC-voltage ratio of 0.2 employing a pulse repetition frequency of 1 kHz and a tip temperature of about 70 K. A schematic diagram of a voltage pulsed 3D-AP setup is shown in fig. 3.2. In each experiment about one million atoms were collected in an average sampling volume of about $10 \times 10 \times 200\ nm^3$.

After the completion of 3D-AP experiments, recorded mass spectra were analysed by identifying windows to different isotopes of Ni, Cr and Mo atoms. All isotopes of nickel atoms and chromium atoms were found in the $2^+$ charge state, while isotopes of molybdenum atoms were seen in both $2^+$ and $3^+$ charge states as shown in the fig. 3.3. Due to the peak overlapping of the $^{64}Ni^{2+}$ isotope with that of the $^{96}Mo^{3+}$ isotope, natural abundances of different isotopes were used to selectively fix atoms in the overlapping peaks. Despite it,

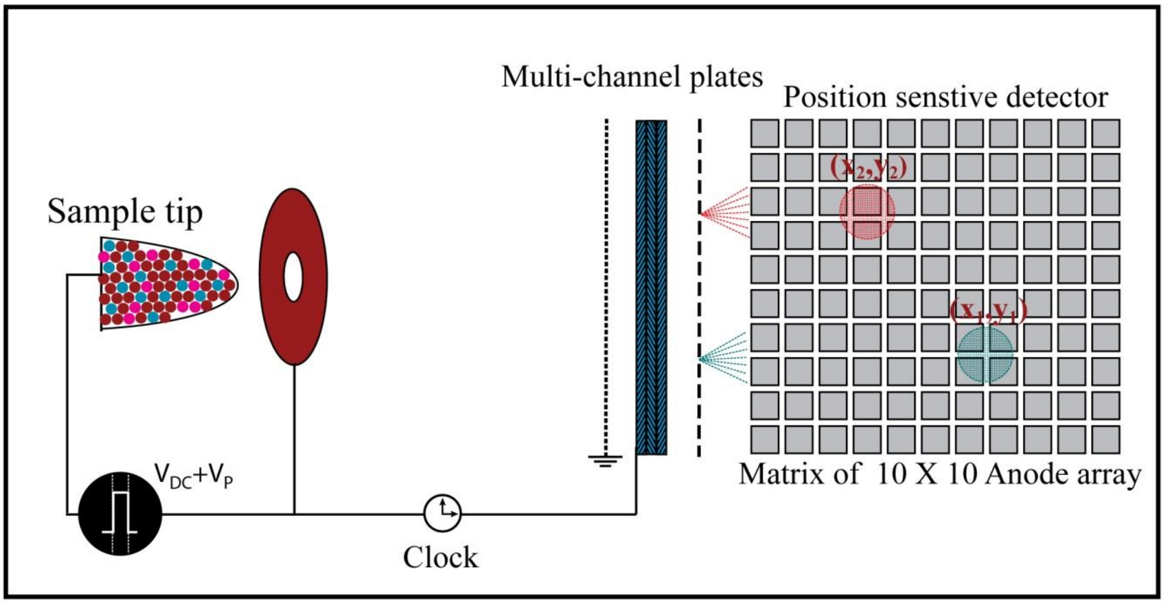

**Figure 3.2:** Schematic diagram of a voltage pulsed 3-dimensional atom probe.

error in the compositions of Ni and Mo atoms were expected due to intricate nature of assigning mass spectrum windows for the overlapped isotopes in the mass spectrum. However, contribution of this error was small as only the $^{96}Mo^{3+}$ peak overlapped with the $^{64}Ni^{2+}$ peak whose natural abundance was only 0.95%. The natural abundances of different were used to selectively fix atoms in the overlapping peaks. Despite it, error in the compositions of Ni and Mo atoms were expected due to intricate nature of assigning mass spectrum windows for the overlapped isotopes in the mass spectrum. However, contribution of this error was small as only the $^{96}Mo^{3+}$ peak overlapped with the $^{64}Ni^{2+}$ peak whose natural abundance was only 0.95%. The natural abundances of different isotopes for nickel, chromium and molybdenum atoms are given in table 3.3.

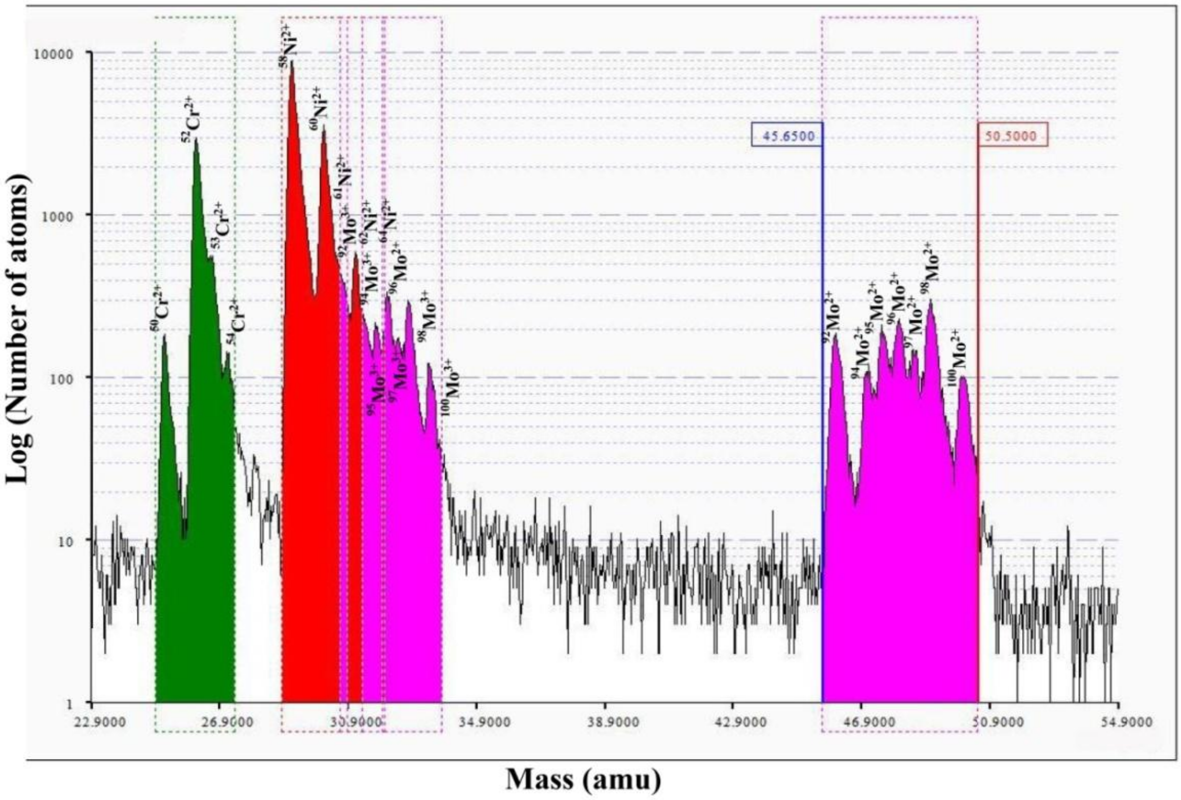

**Figure 3.3:** Mass spectrum of atoms evaporated from the apex of the sharp needle sample during 3D-AP experiment on $Ni_2(Cr_{0.63}Mo_{0.37})$ alloy.

**Table 3.3:** Natural abundances of different isotopes of nickel, chromium and molybdenum atoms

| Elements | Natural abundances of different Isotopes of atoms | | | | | | |
|---|---|---|---|---|---|---|---|
| Ni | $^{58}$Ni | $^{60}$Ni | $^{61}$Ni | $^{62}$Ni | $^{64}$Ni | | |
| | 67.8 | 26.4 | 1.16 | 3.71 | 0.95 | | |
| Cr | $^{50}$Cr | $^{52}$Cr | $^{53}$Cr | $^{54}$Cr | | | |
| | 4.35 | 83.8 | 9.5 | 2.36 | | | |
| Mo | $^{92}$Mo | $^{94}$Mo | $^{95}$Mo | $^{96}$Mo | $^{97}$Mo | $^{98}$Mo | $^{100}$Mo |
| | 14.8 | 9.1 | 15.9 | 16.7 | 9.5 | 24.4 | 9.6 |

**Statistical analysis of 3D-AP data:**

Atom probe data set inherently contains statistical noise due to reconstruction errors and unavoidable errors of the ion optics [86, 88]. The contribution of these statistical errors could be severe in the analysis of nano-sized concentration fluctuations in atom probe data set. Statistical analysis appears to be more suitable to discover these chemical heterogeneities as it separate non-statistical concentration fluctuations from the statistical noise. Statistical data mining tools like the repeated smoothing procedure (RSP) [95] and its advancement, the wavelength dependent filtering (WDF) [69, 96, 97] have been used in the past to quantitatively determine information of nano-sized chemical heterogeneities. Both RSP as well as WDF methods systematically reduce stochastic noise by moving average procedure involving averaging with immediate neighbouring values [95]. In both these methods wavelengths and amplitudes of concentration fluctuations are obtained by comparing the resulting variance of the measured concentration values $\sigma^2_{exp}(L)$ with the variance of a suitable statistic (random) distribution $\sigma^2_{ran}(L)$ [69, 95]. Reduced deviation parameter ($\Sigma^2$) defined in equation 3.3 is usually employed to measure significant deviation of variance for a random distribution. The two parameters viz. wavelength and amplitude represent size of chemical heterogeneity and their deviation from the average concentration.

$$\Sigma^2(\mathrm{L}) = \frac{\sigma^2_{\mathrm{exp}}(\mathrm{L}) - \sigma^2_{\mathrm{ran}}(\mathrm{L})}{\sigma^2_{\mathrm{ran}}(\mathrm{L})} \quad \ldots\ldots\ldots\ldots\ldots\ldots\ldots\ldots\ldots\ldots\ldots\ldots \quad 3.3$$

where, L is a measure of the size of chemical heterogeneities

**Concentration-based cluster analysis:** Chemical heterogeneities which often consist of a few atoms are called as clusters. For the identification of clusters there exist some methods based on different approaches. In this work, Ni-rich clusters were analyzed. For this purpose cluster search algorithm in the Tap3D program has been used. In this analysis, a spherical volume of radius $d_{max}$ = 1.1 nm over each atom in the reconstructed region moves and determines the concentration of the elements. In this case an atom defined as the center of a cluster when the concentration $C_i$ of element *i* exceeds a threshold value $C_x$ within the spherical volume. If two atoms identified as central atoms, they are referred to as a clustered, when the distance between them is less than the diameter of the spherical $d_{max}$.

**Concentration depth profile:** One of the most common representations of the analysis of atom probe data is the concentration depth profile. For this purpose, a cylinder with radius, R = 1-2 nm, oriented perpendicular to the interface between two phases (region of interest, ROI) will be placed. Along the longitudinal direction of the cylinder, the composition is analyzed as a function of the length (depth). In this case, the cylindrical volume along the longitudinal direction is divided in a sequence of blocks of a fixed depth and the mean concentration of each element is determined in different blocks. The fixed depth of a block is typically, $\Delta z$ = 0.5 nm. Using these parameters with a block containing $N_{at} \sim 100$ atoms, the statistical error, σ, in the measured concentration of element, $C_i$, will be about ± 0.1according to eq. 3.4. Usually to reduce the statistical errors larger volumes are analyzed ($N_{at} \sim 10^4$-$10^6$), whereby σ values assumes in the range of ± 0.01-0.05.

$$\sigma = (C_i(100-C_i)/N_{at})^{1/2} \qquad \ldots\ldots\ldots\ldots\ldots\ldots\ldots\ldots 3.4$$

### 3.8. Sample preparation for 3D-AP studies:

Sharp needles with apex radii of about 20-50 nm with uniform cross-section [92] are required for 3D-AP experiments. Different steps involved in the preparation of needle shape samples are as follows: Firstly, square shaped rods of 0.2 x 0.2 x 15 mm³ were cut out by electric discharge machining (EDM) of the bulk alloy. Corners of the square shaped wires were grounded by rounding them in between two pieces of emery papers of grit size 600. These samples were cleaned using ultrasonic bath by immersing them in an acetone solution to remove all impurities present on the surface of wires. After cleaning, these wires were fixed inside hollow cylindrical copper tubes. Two stage electropolishing were used to prepared sharp needle samples for 3D-AP investigations. In the first stage, samples were mounted on a special bench having a vertically movable table for holding a transparent glass beaker as shown in fig. 3.4. The glass cuvette was filled with a glycol solution topped with a thin layer

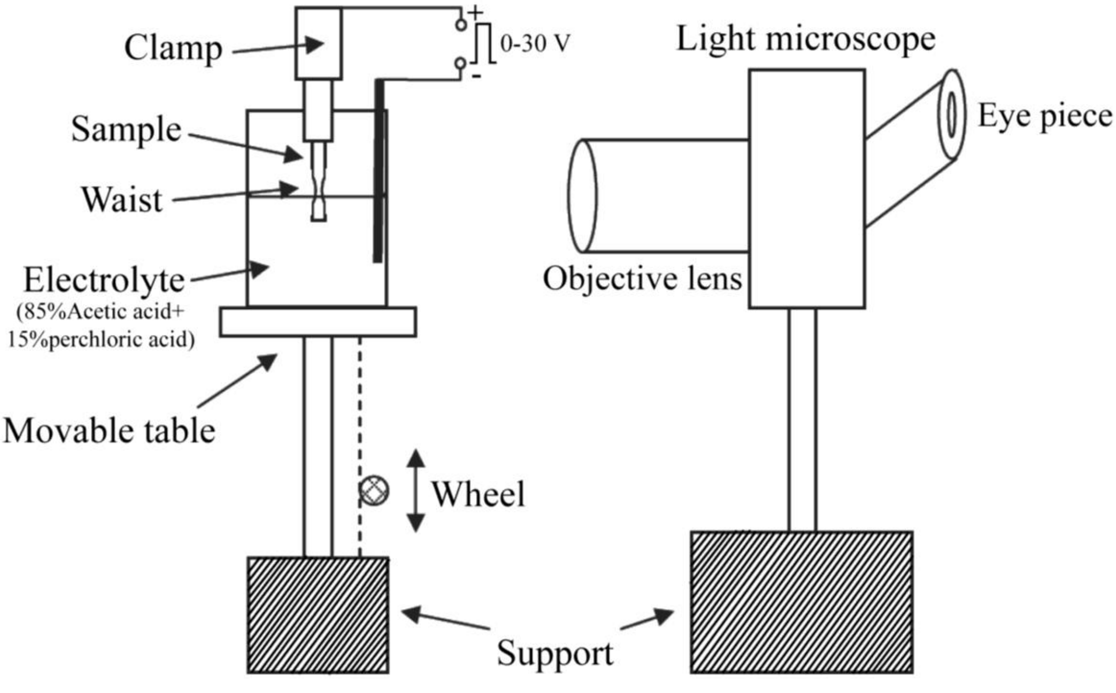

**Figure 3.4:** A schematic representation of the 1st stage of electropolishing for preparing wedge shape needle wires for 3-dimensional atom probe samples.

of an electrolyte (solution of 15% perchloric acid in acetic acid). Short voltage pulses of 0-30 volts were used to polish the sample to wedge shape geometry. A low magnification optical microscope placed in front of the cuvette was used to monitor the progress of electropolishing during the sample preparation. After the 1st step of polishing, wedge shaped needles were cleaned thoroughly in a methanol solution before using them for the 2nd stage polishing. In the 2nd stage, the wedge shaped needles were mounted on a horizontal table having a movable arm in the horizontal plane (Fig. 3.5). A small size Pt-ring was used for polishing the sample by forming a lens of an electrolyte (solution of 2% perchloric acid in 98% butoxyethanol). Short voltage pulses of 0-15 volts were used to carefully polish the sample to sharp needles of apex radii of about 20-50 nm as required for 3D-AP investigation. This step of polishing is also called as micropolishing. Once prepared, the final shape and size of apex radii of needle samples were measured in transmission electron microscope using a special sample holder for needle samples fixed in copper tubes. A TEM image of one such sample prepared by the two stage electropolishing method is shown in fig. 3.6.

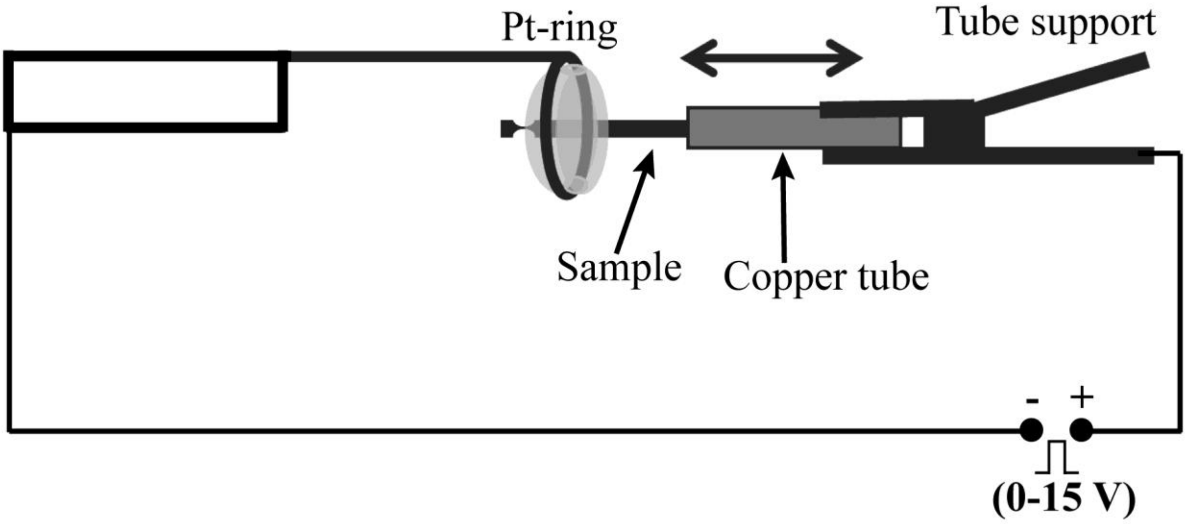

**Figure 3.5:** A schematic representation of 2nd stage of micropolishing for final tip preparation for 3-dimensional atom probe study.

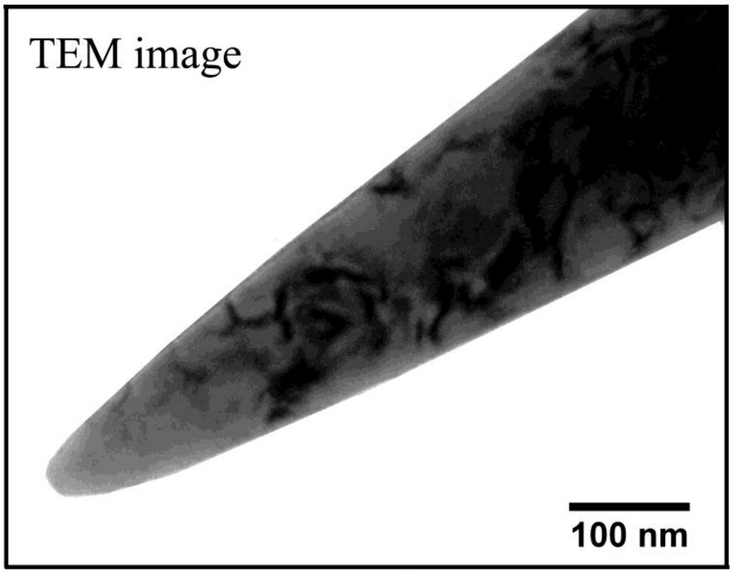

**Figure 3.6:** A bright field TEM micrograph of final tip for 3-dimensional atom probe study.

### 3.9. Differential Scanning Calorimetery:

Differential Scanning Calorimetery **(**DSC) was used to identify mechanisms of ordering transformation and to understand the role of Cr and Mo solutes on ordering kinetics in stoichiometric $Ni_2(Cr_{1-x}Mo_x)$ alloys. These studies were carried out during isochronal heating using a highly sensitive Mettler-Toledo make heat flux differential scanning calorimeter (DSC1/700). Thin slices of about 0.5 mm thickness having nearly similar weight, prepared by grinding and polishing samples to flat surfaces were used for DSC studies. These samples were solution treated at 1150°C for 2 h in a sealed quartz tube filled with helium gas followed by water quenching to produce them in a single γ phase. Heating of samples were carried out inside mini Pt-crucibles (70 μl), symmetrically located inside of a furnace, at programmed rates in an inert atmosphere of argon gas. The temperature of the sample was determined w.r.t. the furnace temperature measured with a Pt100 temperature sensor. However, since the temperature sensor was not in direct contact with the sample, a small temperature correction was necessary to correct the offset in the measured sample temperature. The melting points of different standard elements e.g. pure indium (156.6°C) and pure Zinc (419.6°C) metals were used to calibrate the sample temperature covering the intended temperature range of operation. Heat flow during heating of samples was determined by measuring temperature difference between sample crucible and empty crucible which acts as a reference side. A thermopiles assembly containing 56 nos. of thermocouples was used to determine temperature of the sample as well as of the reference crucibles. The entire assembly of thermopiles ensured higher accuracy of measurement and its sensitiveness to the weak thermal events (resolution – 0.04 μW and sensitivity – 11.9 at 135°C) . Heat flow calibration was carried out by comparing the measured value of enthalpy of fusion of pure indium with that reported in literature. A schematic diagram of a heat flux DSC used in present study is shown in fig. 3.7. In this set-up, the sample (S) and the reference (R) were connected by a low resistance heat flow path and the entire assembly was enclosed in a single furnace. Heating rates were varied from 2°C/min to 10°C/min for calorimetric studies. For each heating experiment, two consecutive heating cycles were used in identical experimental

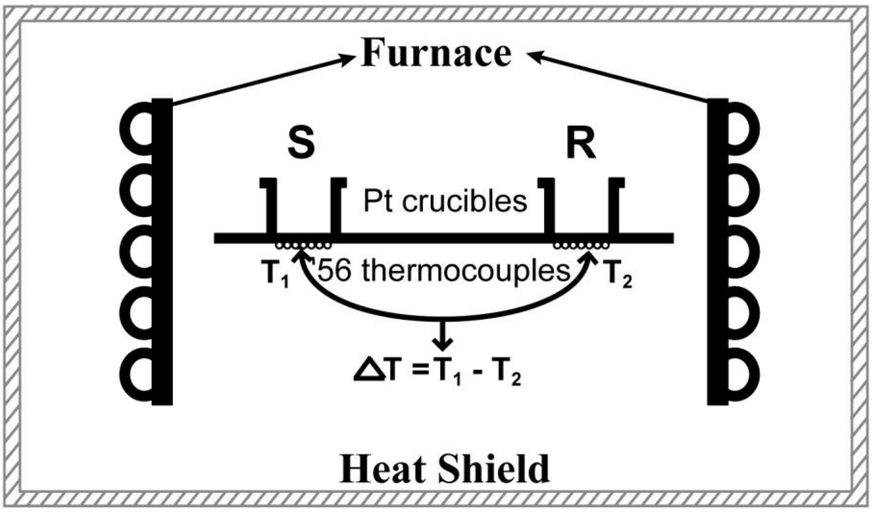

**Figure 3.7:** A schematic representation of heat flux differential scanning calorimeter. Crucible S and R represents sample and reference sides respectively.

conditions to delineate the instrumental effect from the thermograms. This was achieved by cooling the sample inside DSC at a rate of 40°C/min to lower temperature after completing 1st heating run. The baseline response of the instrument which is critically dependent upon the sample position inside the crucibles and positions of the crucibles inside the furnace was, therefore, correctly determined by this approach. However, this way of baseline correction was used only when the reaction peaks due to phase transformations were completed during the 1st heating run and nothing expected to happen during the 2nd heating run. Since the maximum operating temperature of this DSC was limited to 700°C, another differential scanning calorimeter (SETARAM make LABSYS DSC 16) capable of measuring reaction events at higher temperatures was also used for studies at temperatures above 700°C, though at a cost of less thermal sensitivity.

### 3.10. Resistivity measurement:

Square shaped wires of about 0.3 × 0.3 mm cross-section, 12-15 mm length and small coupons of about 5 × 5 mm cross-section and 1.0 mm thickness were cut out of the homogenized alloys. In house developed four probe resistivity measurement set up was used for measuring resistivity of samples during continuous as well as during isothermal heating. A schematic diagram of the resistivity measurement set-up used is shown in fig. 3.8. Four equidistance points were marked along the length of samples and copper wires of about 0.3 mm diameter were spot welded at these points. A constant current was passed through the sample from extreme two contacts while voltage drop was measured across two inner contacts of the sample. A highly stable and sensitive current source (Model No: 2400) and nano-voltmeter (Model No: 2182A) of Keithley make were used in the resistivity measurement setup. For each measured data point, effect of thermally induced voltage at contacts between wires and samples was corrected by averaging the voltage drop measured under reversed direction of the current flow. A resistive heating tubular furnace was used for heating the samples in the atmosphere of flowing high purity argon gas. The temperature of the furnace was controlled by regulating the current flowing through the furnace using a thyristor controlled by Eurotherm make PID temperature controller. The temperature of the furnace was calibrated on the basis of magnetic transition temperatures of pure nickel (T=357°C) and pure iron (769°C) [98]. Isochronal resistivity heating experiments were carried out at rates varying from 1°C/min to 10°C/min to deduce the transformation temperatures at a heating rate 0°C/min which was considered equivalent to transformation temperature under equilibrium condition. Isothermal experiments were carried out at temperatures ranging from 500°C to 680°C to determine incubation times for ordering transformation reactions. For isothermal experiments, samples were inserted inside the furnace only after it attained the required temperature. In addition, small coupons of samples were also placed closed to the wire samples during resistivity measurement to correlate resistivity changes with microstructural variation.

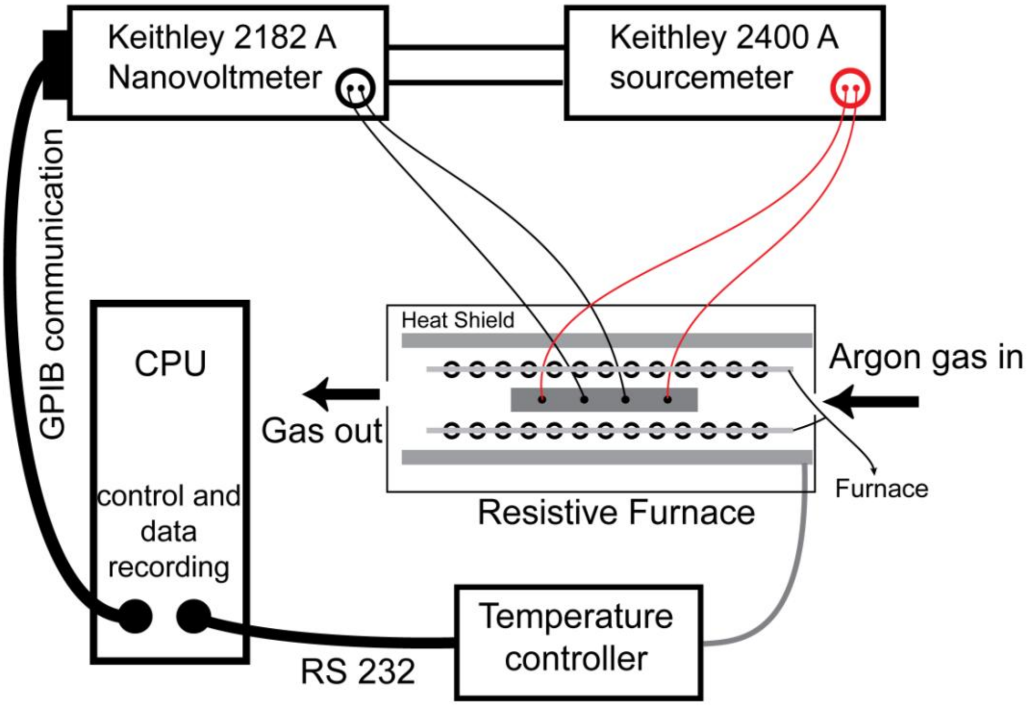

**Figure 3.8:** A schematic representation of in-house developed 4 probe high temperature resistivity measurement setup.

# CHAPTER 4

# CHARACTERIZATION OF SHORT-RANGE ORDER IN Ni-Cr-Mo ALLOYS

This chapter present the results of experimental investigations carried out to characterize the SRO in $Ni_2(Cr_{1-x}Mo_x)$ alloys subjected to various heat treatments to produce different microstructural states. Earlier investigations on Ni-Mo and Ni-Cr-Mo alloys (in the composition range 8–33 at% Mo) have revealed the existence of SRO by the appearance of diffuse diffraction intensity maxima at {1 ½ 0} positions in electron diffraction patterns [13, 31-35, 39, 49, 99]. As mentioned in Chapter 2, two models have been used to explain the appearance of diffuse diffraction intensity at {1 ½ 0} positions in these alloys. The 1st model ("SCW model") explains the appearance of diffuse diffraction intensity at {1 ½ 0} positions due to manifestation of an atomic arrangement of $N_2M_2$-type (where N = Ni and M = Mo) on {4 2 0} planes of the fcc lattice [13], while the 2nd model ("Microdomain model") correlate the origin of the appearance of {1 ½ 0} diffuse reflections with the existence of sub-unit cells of $D1_a$, $DO_{22}$ and $DO_{2h}^{25}$ structural units [78, 100]. A careful analysis of structural description of two models revealed that their atomic architecture inherently contains localized variation in chemical compositions. For instance, regions having local compositions of $N_2M_2$ would result in the "SCW model", while it would be of $N_3M$-type in the "Microdomain model". This can be seen in fig. 4.1 where structural descriptions of both "SCW model" and "Microdomain model" have schematically shown with the average composition of that localized region.

The SAED evidences in TEM were used to characterize the microstructure in terms of presence / absence of SRO, while 3-dimensional atom probe studies were used to characterize the distribution of constituent species nearly at the atomic scale. Further, analysis of 3D-AP data was used to identify the regions in the microstructure which were having compositions

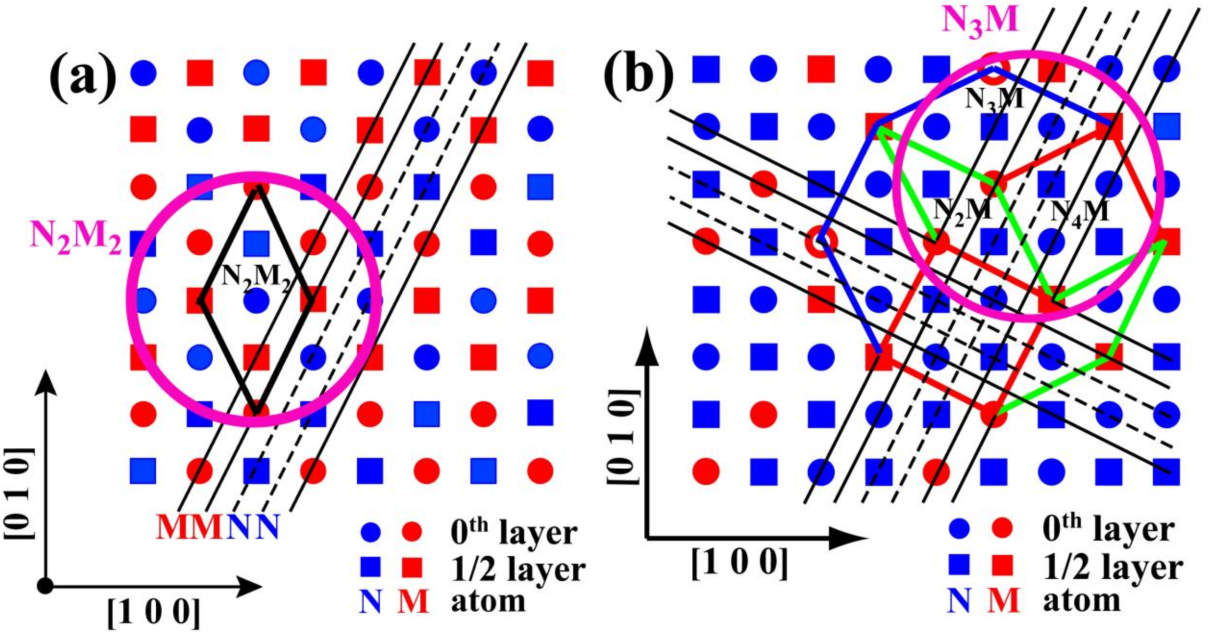

**Figure 4.1:** [0 0 1] projection depicting atomic arrangements; (a) $N_2M_2$ in static concentration wave model showing one molecule size subunit cell which is drawn by solid line; (b) Microdomain model showing subunit cells of $DO_{22}$ ($N_3M$), $DO^{25}_{2h}$ ($N_2M$) and $D1_a$ ($N_4M$) long-range ordered structures. Open symbols in fig. (b) are chemical defects incorporated to create subunit cell of $DO_{22}$ ($N_3M$) structure. The composition of the localized regions marked by a pink circle is also given in the figure.

different than the nominal alloy composition, which were termed as chemical heterogeneities. The knowledge of the chemical heterogeneities was used to correlate with the structural models of SRO suggested in the literature. Alloys samples in solution treated and water quenched (STWQ) and splat-quenched states were used to understand the effect of different heat treatment methods on the stability of SRO.

### 4.1. TEM investigations:

Alloys prepared by cast melting route exhibited equiaxed single phase microstructure with average grain size of about 0.5 mm. SAED patterns in <0 0 1>, <1 1 2> and <0 1 3> zone axes were used to determine the existence of SRO by identifying the positions of diffuse diffraction intensity maxima in the reciprocal space. TEM investigations of $Ni_2(Cr_{0.63}Mo_{0.37})$

and $Ni_2(Cr_{0.5}Mo_{0.5})$ alloys, in STWQ state, revealed diffuse intensity maxima at {1 ½ 0} and 1/3{2 2 0} positions (see arrow marks in the <1 1 2> zone axis of Fig. 4.2). Additional diffuse intensity maxima at 1/3{2 2 0} positions have been shown by Das et al. [31] in the {1½ 0} SRO state, who have attributed them to be due to the presence of another SRO belonging to an ordered structure. Das et al. [31] have further characterized this SRO state by the presence of diffuse intensity maxima at 1/3{1 1 3} positions, which were also observed in the present case (see electron diffraction patterns with <1 1 2> and <0 1 3> zone axes in figs. 4.2b and 4.2c). Since 1/3{2 2 0} as well as 1/3{1 1 3} positions in the reciprocal space are characteristic positions of the $DO_{2h}^{25}$ structure [27], it was not unreasonable to call it to be a

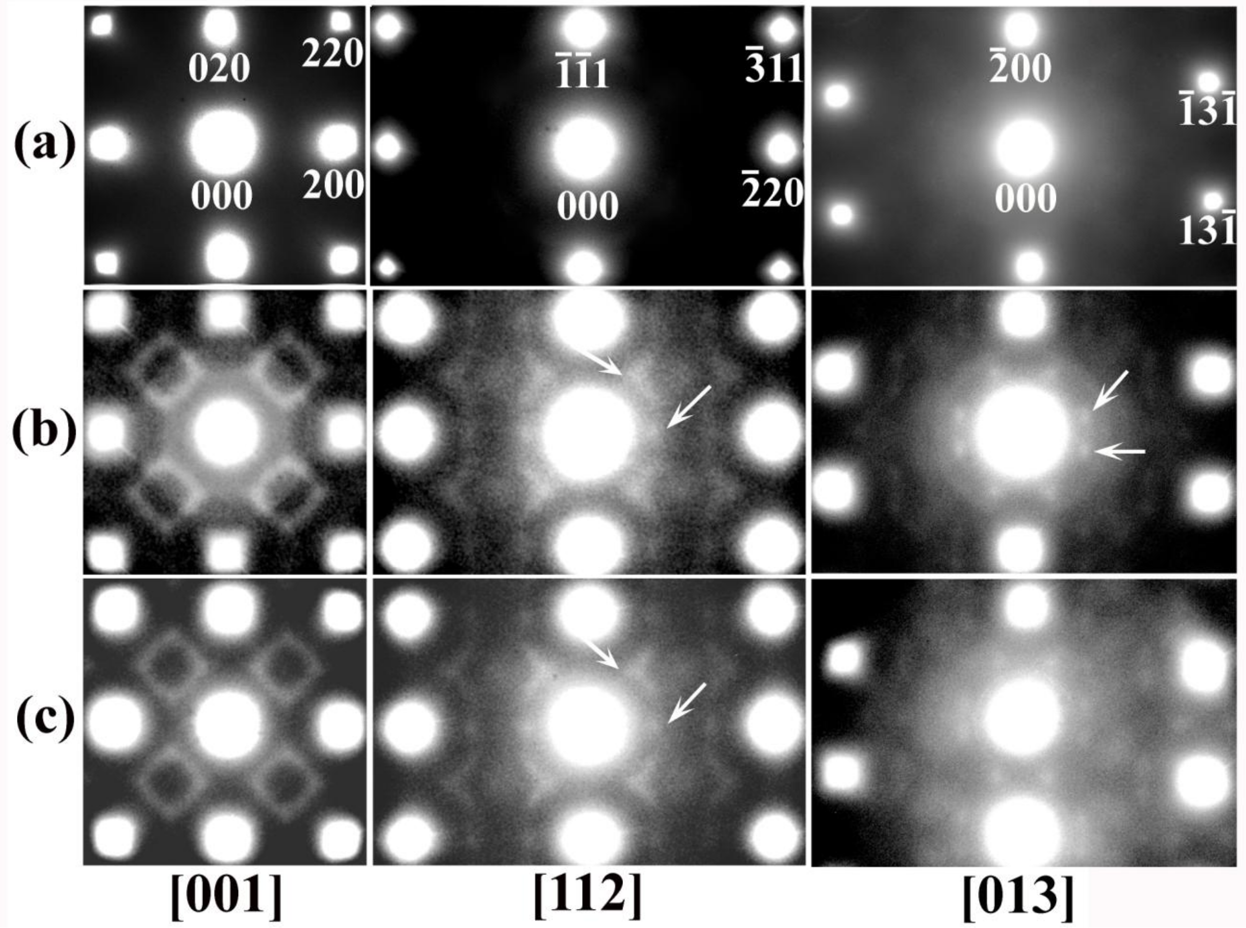

**Figure 4.2:** SAED patterns with [0 0 1], [1 1 2] and [0 1 3] zone axes obtained from (a) $Ni_2Cr$ (b) $Ni_2(Cr_{0.63}Mo_{0.37})$ and (c) $Ni_2(Cr_{0.5}Mo_{0.5})$ alloys in STWQ state. Presence of diffuse intensity maxima (marked by arrows) revealed the existence of short-range order.

SRO of the $DO_{2h}^{25}$ order, which was referred to as “1/3{2 2 0} SRO” in the present case. That diffuse intensity maxima due to the 1/3{2 2 0} SRO was not a consequence of the streaking effect of the existing {1 ½ 0} SRO was confirmed by the electron diffraction evidences in <0 1 3> zone axes in which reflections due to {1 ½ 0} SRO were absent (see spots marked by arrows in figs. 4.2b and 4.2c). Since 1/3{2 2 0} positions were close to {1 ½ 0} positions, their overlap of intensities gave rise to a characteristic nearly square-shaped intensity distribution in a <0 0 1> zone axes diffraction patterns (Fig. 4.2b and 4.2c). The qualification of diffuse reflections at 1/3{2 2 0} positions as SRO was also confirmed on the basis of resistivity change occurring during the intensification of these diffuse reflections. Nicholson et al. [101] have theoretically established that resistivity increases during the increase of SRO. Indeed, it was found experimentally that the resistivity increases during the intensification of 1/3{2 2 0} diffuse reflections which has been shown later in Section 5.2. However, their transformation in to sharp spots qualified it to call as superlattice reflections of LRO structure as resistivity decreases abruptly during increase of the intensity of sharp superlattice spots (shown later in Section 5.2). In contrast, electron diffraction patterns of $Ni_2Cr$ alloy in STWQ state did not reveal the presence of SRO (Fig. 4.2a). This was at variance with the evidence of diffuse intensity maxima at {1 ½ 0} positions in the diffuse neutron scattering study of solution treated $Ni_2Cr$ alloys [102]. The absence of SRO reflections in the electron diffraction patterns in the present investigation could be attributed to: (i) the size of SRO domains below the electron diffraction limit; and/or (ii) the nearly similar atomic scattering factors of Ni and Cr atoms. The existence of SRO was however supported by the mottled contrast observed in BF-TEM images (Fig. 4.3), which is known to be due to the presence of very fine particles or micro-domains of SRO in the matrix [39, 79]. Additional heat treatment at 525°C for 60 min. was used to further develop SRO in $Ni_2(Cr_{0.5}Mo_{0.5})$ alloy (Fig. 4.4). The SAED investigations on this sample revealed slight

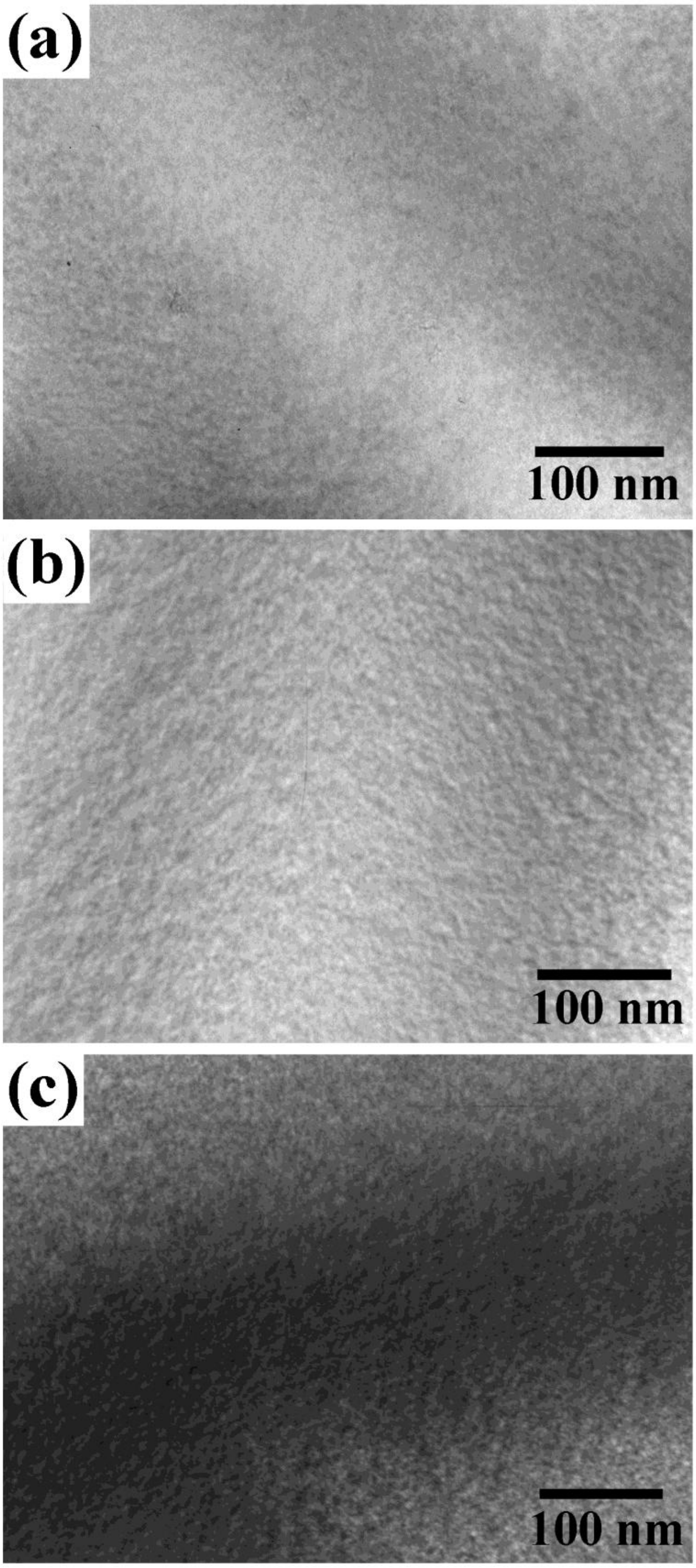

**Figure 4.3:** BF-TEM images obtained in <0 0 1> zone axis from; (a) $Ni_2Cr$; (b) $Ni_2(Cr_{0.63}Mo_{0.37})$; and (c) $Ni_2(Cr_{0.5}Mo_{0.5})$ alloys in STWQ state. The presence of mottled contrast supported the existence of short-range order.

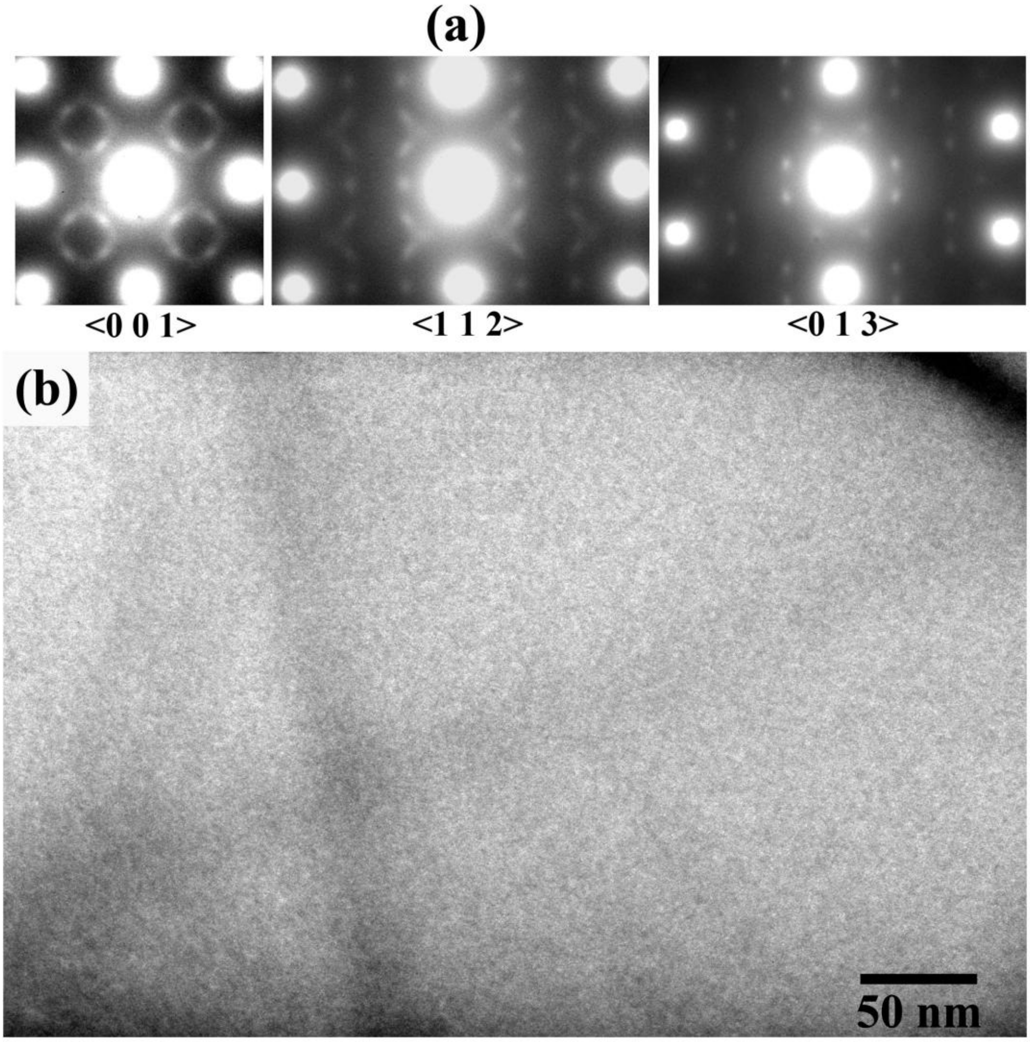

**Figure 4.4:** (a) SAED patterns with <0 0 1>, <1 1 2> and <0 1 3> zone axes from $Ni_2(Cr_{0.5}Mo_{0.5})$ alloy aged at 525°C for 60 min. (b) mottled contrast in BF-TEM image obtained in <0 1 3> zone axis.

enhancement of intensity at 1/3{2 2 0} positions and a decrease at {1 ½ 0} positions, though both reflections remained diffuse in nature as shown in fig. 4.4. Continued heating at this temperature would eventually form LRO phase as will be shown later in Section 5.4.

On the contrary, the formation of SRO in splat quenched $Ni_2(Cr_{0.63}Mo_{0.37})$ and $Ni_2(Cr_{0.5}Mo_{0.5})$ alloys was suppressed. This was obvious from SAED patterns and TEM images showing absence of the diffuse diffraction intensity in the [0 0 1] and [1 1 2] zone axes as well as mottled contrast in BF images (see figs. 4.5 and 4.6). An additional effect of splat quenching was significant reduction of the grain size in splat -quenched alloys as shown in fig. 4.6. Ageing treatment at 525°C for 120 min was used to understand the stability of microstructure in the disordered state of splat-quenched $Ni_2(Cr_{0.5}Mo_{0.5})$ alloy. SAED investigations on this sample revealed the appearance of characteristic diffuse diffraction intensity pattern similar to that seen in the solution treated state. This was suggested of preferential growth of SRO from a disordered state obtained by splat-quench processing of the alloy.

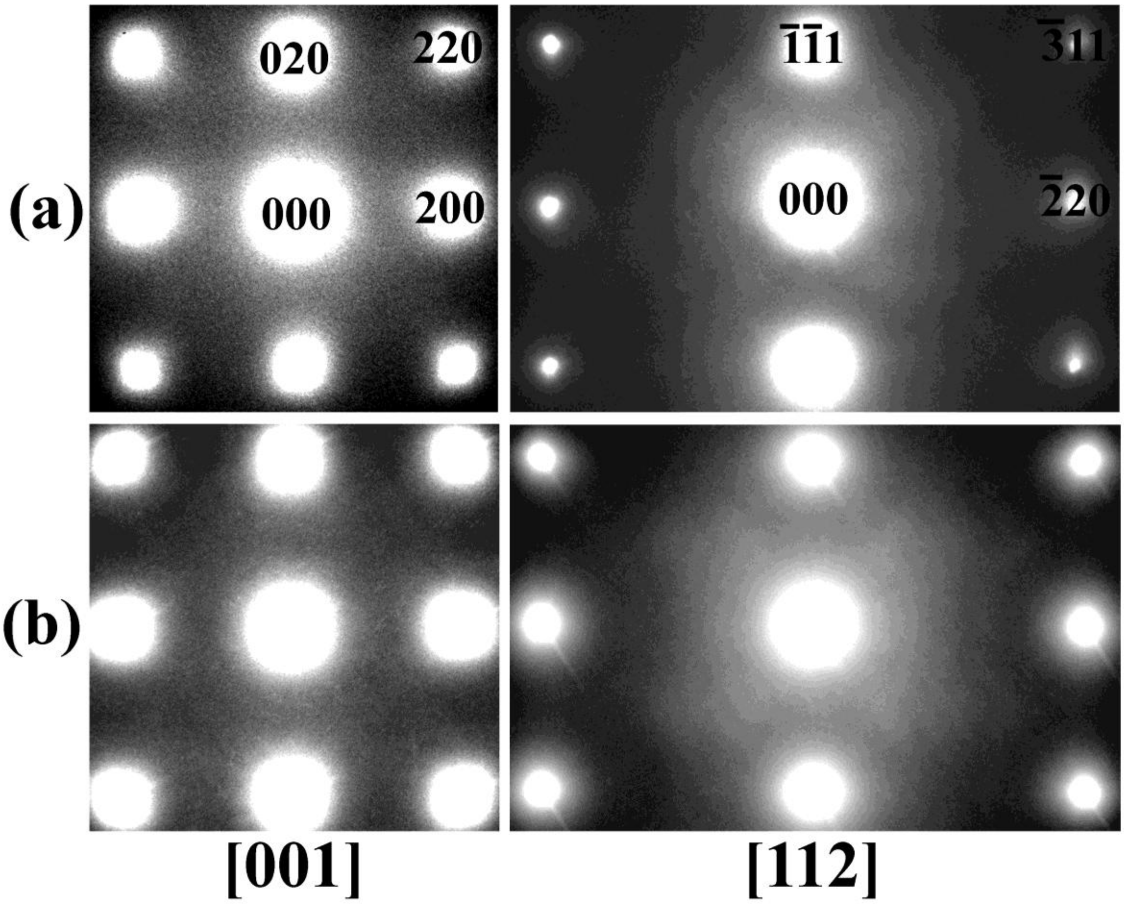

**Figure 4.5:** SAED patterns with [0 0 1] and [1 1 2] zone axes obtained from; (a) $Ni_2(Cr_{0.63}Mo_{0.37})$; and (b) $Ni_2(Cr_{0.5}Mo_{0.5})$ alloys in as-splat- quenched state. The absence of any diffuse intensity maxima confirmed the suppression of short-range

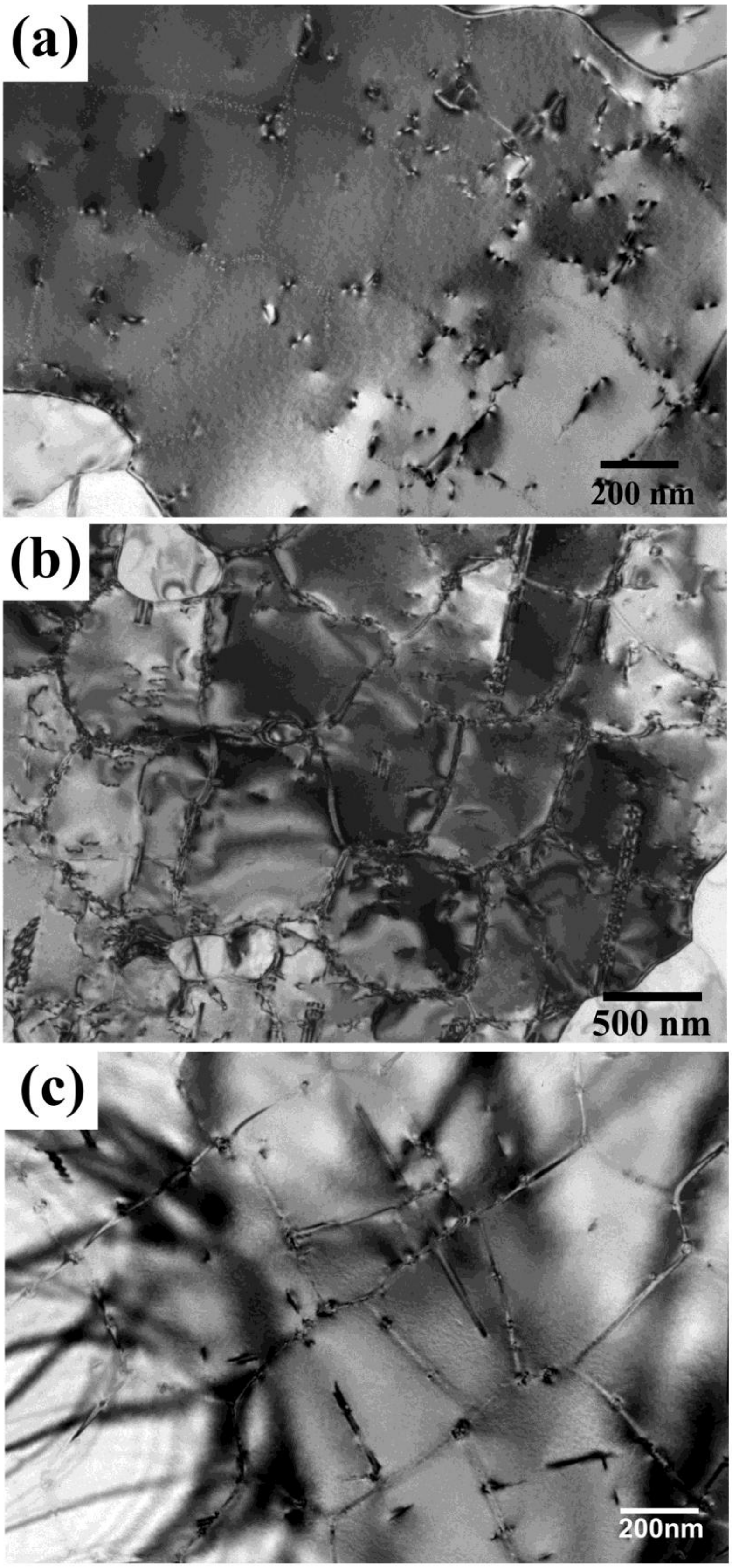

**Figure 4.6:** BF-TEM images obtained in <0 0 1> zone axis from; (a) $Ni_2Cr$; (b) $Ni_2(Cr_{0.63}Mo_{0.37})$; and (c) $Ni_2(Cr_{0.5}Mo_{0.5})$ alloys in as-splat quenched state. A smaller grain size in all alloys was evident in splat-quenched alloys.

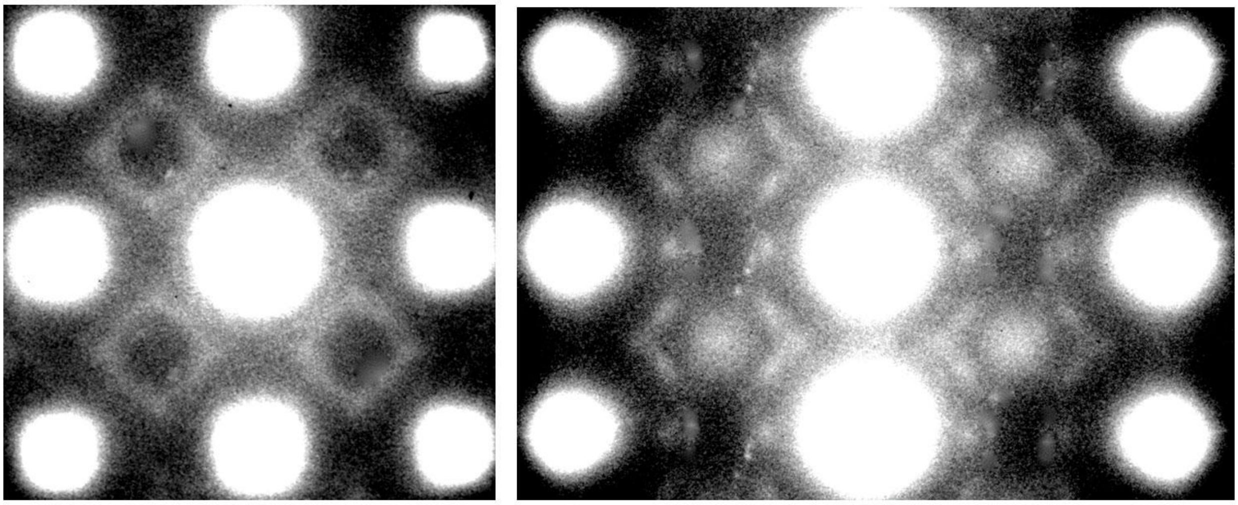

<001> <112>

**Figure 4.7:** SAED patterns with <0 0 1> and <1 1 2> zone axes from splat-quenched $Ni_2(Cr_{0.5}Mo_{0.5})$ alloy aged at 525°C for 120 min.

## 4.2. 3D-AP investigations:

3D-AP investigations were used to identify the nature of chemical heterogeneities prevailing in the microstructure of $Ni_2Cr$ and $Ni_2(Cr_{0.5}Mo_{0.5})$ alloys in the SRO state. These heterogeneities were characterized based upon a detailed statistical analysis of the multiple selected volumes of 3D-AP data using the wavelength dependent filtering (WDF) procedure [69] and the cluster search algorithm [103] (see Chapter 3). A comparison of chemical heterogeneities with the corresponding alloy in the absence of SRO was used to arrive at qualitative conclusions.

### 4.2.1. $Ni_2Cr$ alloy:

The atomic reconstruction maps of individual atomic species of $Ni_2Cr$ alloy in the splat-quenched and STWQ states are shown in fig. 4.8. The concentration depth profiles corresponding to the reconstruction maps are given below respective reconstruction maps. A visual inspection of the reconstructions maps was unable to reveal the existence of any chemical heterogeneity, though concentration depth profiles suggested a variation in the concentration of the individual species (see fig. 4.8). Concentration depth profiles corresponding to sampling volume of the splat-quenched sample revealed its average composition to be Ni-32.4at%Cr (Fig. 4.8a) which was close to nominal composition of the alloy, though in the STWQ sample average composition of the sampling volume was Ni-30.4at%Cr (Fig.4.8b). Marginally higher nickel concentration in the sampling volume of STWQ samples could possibly be due to slightly nickel rich region of the microstructure arrested in the 3D-AP experiment. This was suggested on the basis of composition of the sub-volume selected out of the reconstructed map of fig. 4.8b. Concentration depth analysis of sub-volume revealed its average composition of Ni-31.5at%Cr (Fig. 4.9) which was close to the nominal composition of the alloy, though fluctuations in the concentrations appeared much larger than those in fig.4.8b.

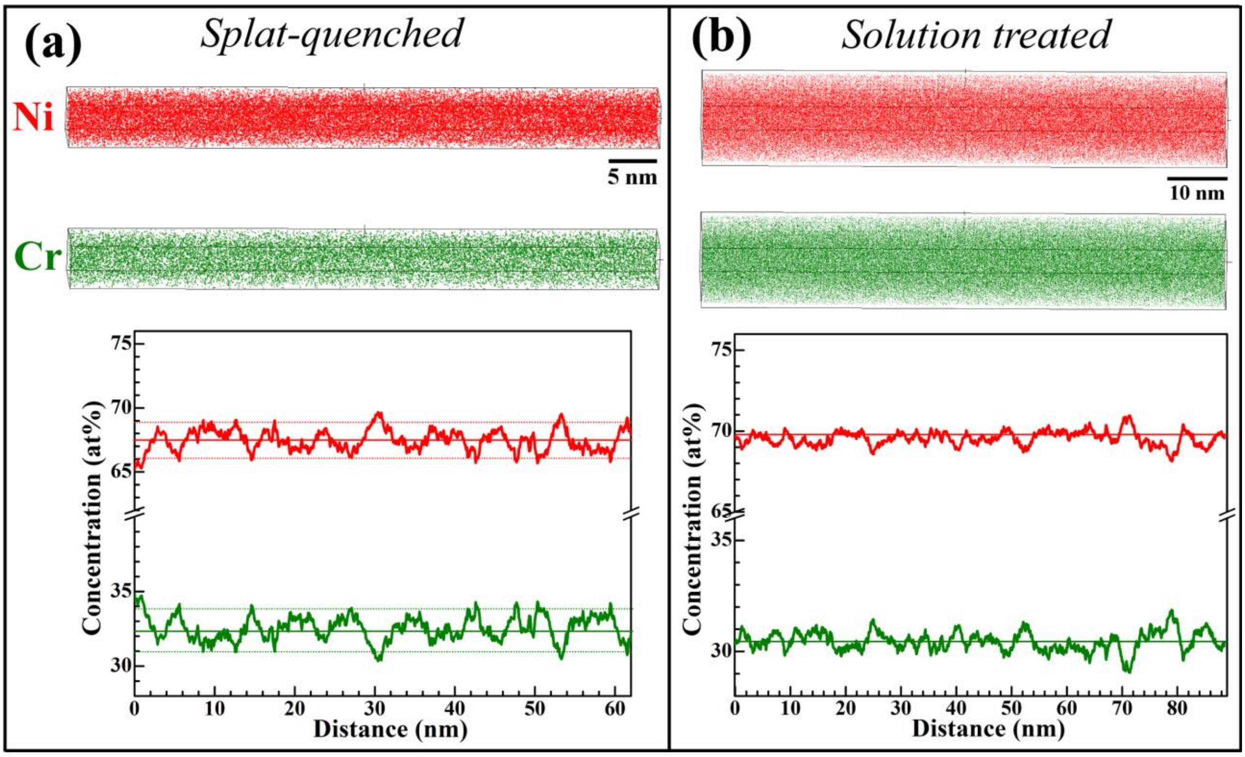

**Figure 4.8:** 3-dimensional reconstruction maps of nickel and chromium atoms in $Ni_2Cr$ alloy in; (a) splat-quenched state; and (b) solution treated state. Concentration depth profiles are given below the reconstruction maps.

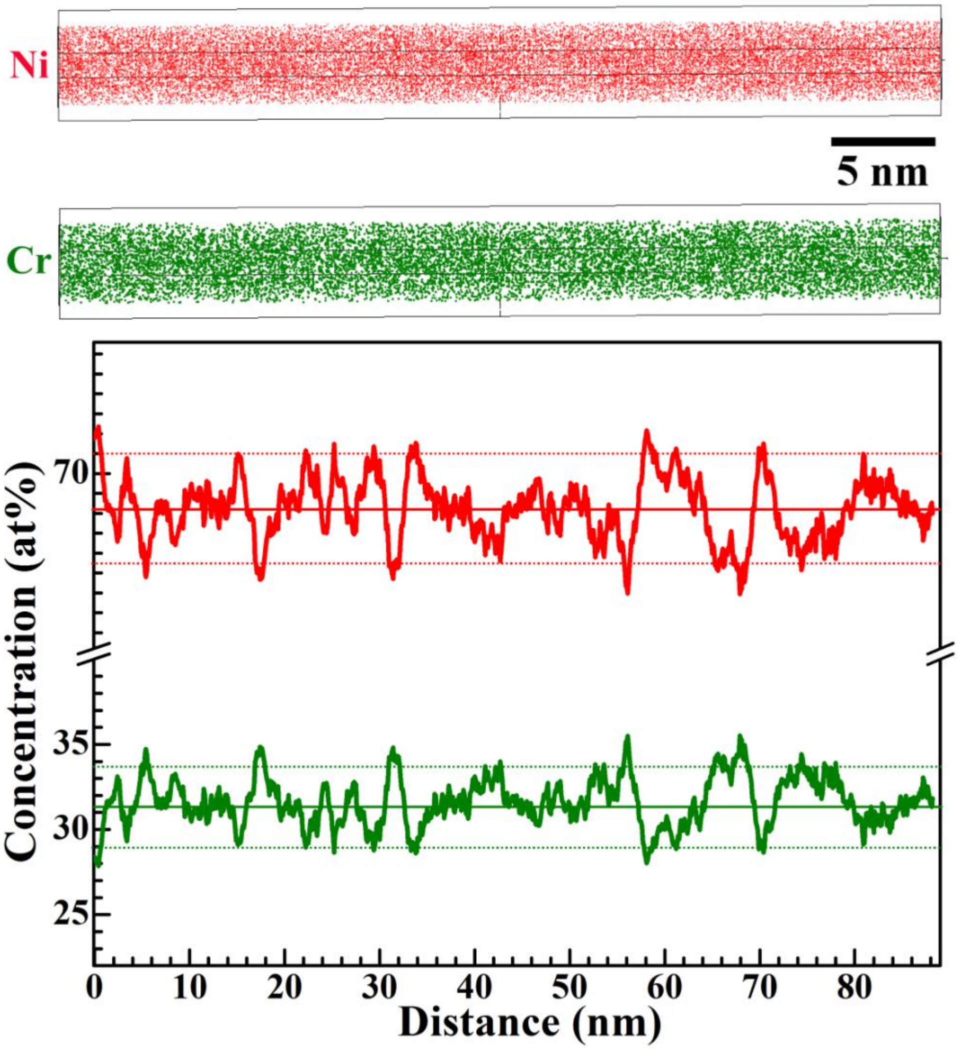

**Figure 4.9:** 3-dimensional reconstruction maps of nickel and chromium atoms in a sub-volume of fig. 4.8b. Concentration depth profiles are given below the reconstruction maps.

Cluster search method was used to identify chemical heterogeneities in above shown reconstructed volumes. Nickel concentration within threshold limits 47-57 at.% and 74-100 at.% were used to identify Ni-depleted and Ni-rich clusters, respectively, covering the composition range on either sides of the $Ni_2Cr$ stoichiometry. This analysis revealed that Ni-rich regions were predominantly present in the reconstructed volumes of both splat-quenched and STWQ samples (shown in fig. 4.10). The results of the cluster search analysis on the reconstructed volumes of splat-quenched and STWQ $Ni_2Cr$ alloy are presented as histograms in figs. 4.11a and 4.11b, respectively, showing number of atoms measured within clusters as a function of Ni concentration. It could be noticed that in the STWQ sample compositions of chemical heterogeneities were close to $Ni_3Cr$ type and were dominated by much larger number of atoms in comparison to those in the splat-quenched sample. Results of WDF analysis of atom probe data of the $Ni_2Cr$ alloy in both splat-quenched and STWQ states are shown in fig. 4.11c and 4.11d, respectively. Solid lines in fig. 4.11 represents the reduced deviation, $\Sigma^2$, plotted against the damping length (L) for Cr (the same for Ni is not shown as it is superimposed with that of Cr), whereas broken lines represent statistical errors associated with the $\Sigma^2$ [69, 95]. It was clear from the WDF analysis that both splat-quenched and STWQ samples contained non-random concentration fluctuations as both samples showed peaks in

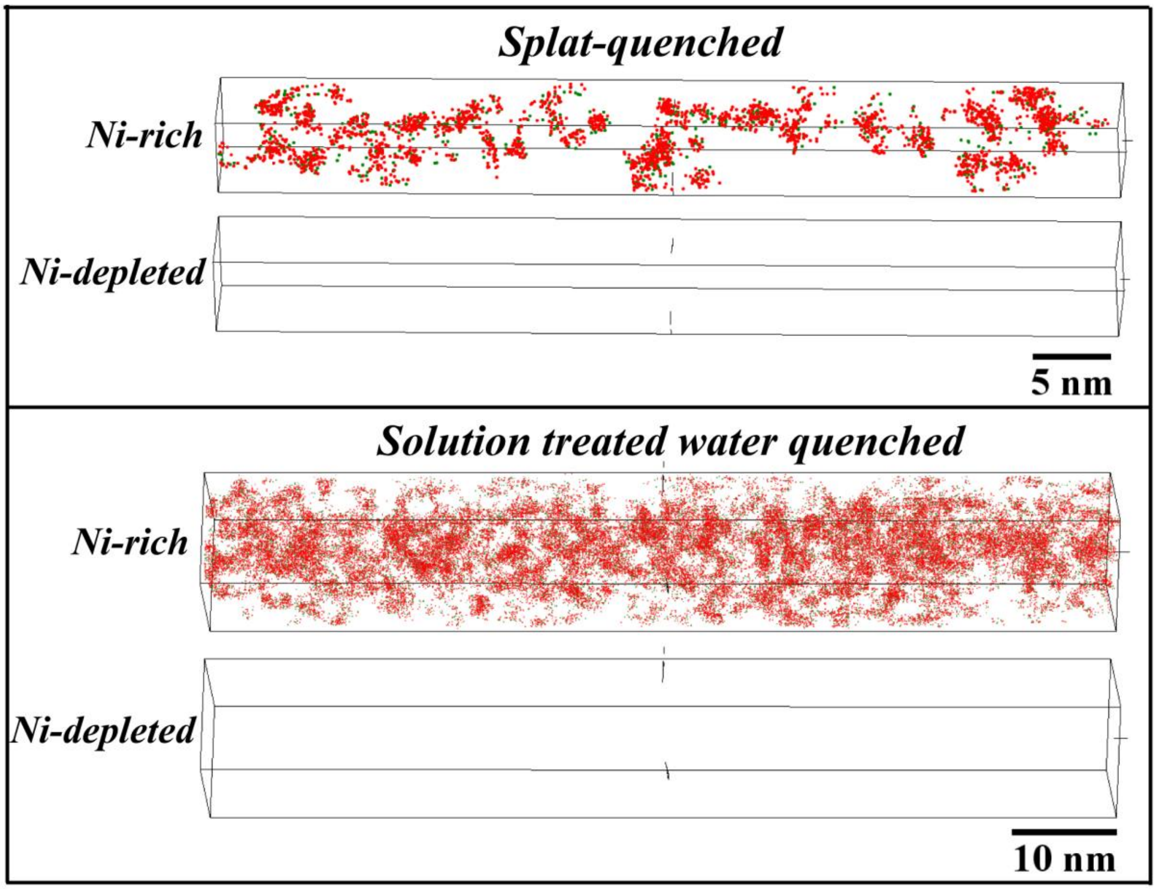

**Figure 4.10:** 3-dimensional reconstructions maps showing Ni-rich clusters in the splat-quenched and STWQ states of $Ni_2Cr$ alloy (See text for details).

the $\Sigma^2(L)$ that exceeded the statistical error limit. On the basis of this analysis, it could be concluded that the $Ni_2Cr$ alloy in splat-quenched state contained predominant concentration fluctuations of wavelength 3.8 nm having amplitude of 7.4 at% (see Chapter 4 for details on WDF method) around the average Cr concentration of 32.6 at% (Table 4.1). WDF analysis of the STWQ data revealed the presence of concentration fluctuations of different types - one having wavelength and amplitude of respectively 3.5 nm and 7.2 at%, and another having wavelength and amplitude of 7.4 nm and 5.5 at%. Observed two fluctuations were about average Cr concentrations of 31.7at% and 30.4 at%, respectively (Table 4.1).

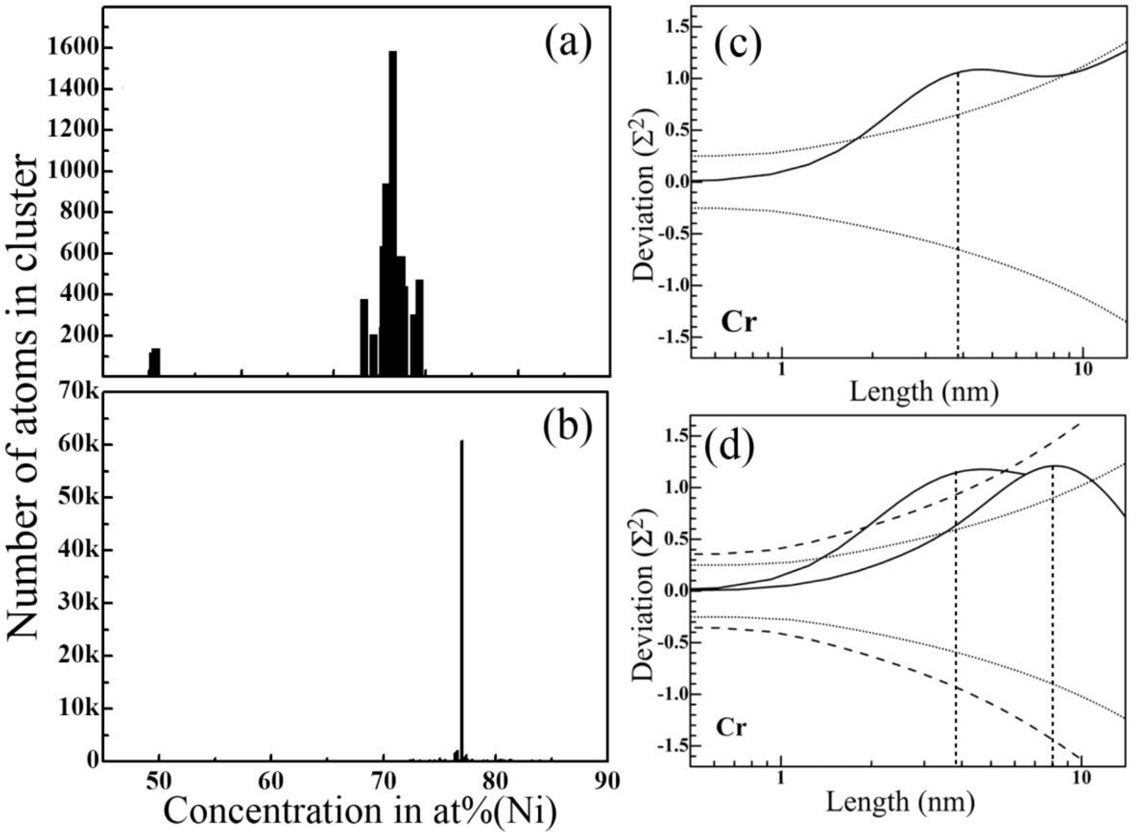

**Figure 4.11:** Cluster composition histograms showing the dominance of $Ni_3Cr$ compositions in; (a) splat-quenched; (b) STWQ state of the $Ni_2Cr$ alloy. WDF analysis of atom probe data to determine chemical heterogeneities in; (c) Splat-quenched state; (d) STWQ state of the $Ni_2Cr$ alloy, reduced deviation parameter is drawn by solid lines against the logarithm of the effective damping length of the Gaussian filter function [95]. Broken lines indicate the $2\sigma$ statistical errors.

**Table 4.1:** A tabular presentation of average concentrations of the alloying elements, the magnitude of concentrations fluctuations and the associated chemical heterogeneities in $Ni_2Cr$ and $Ni_2(Cr_{0.5}Mo_{0.5})$ alloys in different microstructural states.

| **Alloy** | **Thermal History** | **Average measured conc.** | **WDF analysis for Compositional Fluctuations** | | | |
|---|---|---|---|---|---|---|
| | | | **Average Wavelength, L (in nm)** | **Conc. Deviation, ΔC (Element)** | **Fluctuation range** | **Heterogeneity compositions** |
| $Ni_2Cr$ | Splat-quenched | Ni-32.6at%Cr | 3.8 | ± 7.4 (Cr) | 25.2 – 40.0 (Cr) | $Ni_{0.6}Cr_{0.4}$ , $Ni_{0.75}Cr_{0.25}$ |
| | Solution treated water quenched | Ni-31.7at%Cr | 3.5 | ± 7.2 (Cr) | 24.5 – 38.9 (Cr) | $Ni_{0.61}Cr_{0.39}$, $Ni_{0.75}Cr_{0.25}$ |
| | | Ni-30.4at%Cr | 7.4 | ± 5.5 (Cr) | 24.9 – 35.9 (Cr) | $Ni_{0.64}Cr_{0.36}$, $Ni_{0.75}Cr_{0.25}$ |
| $Ni_2(Cr_{0.5}Mo_{0.5})$ | Splat-quenched | Ni-16.1at%Cr-19.6at%Mo | 5.7 | ± 6.0 (Cr) | 10.1 – 22.1 (Cr) | $Ni_{0.74}(Cr+Mo)_{0.26}$,<br>$Ni_{0.54}(Cr+Mo)_{0.46}$ |
| | | | | ± 4.1 (Mo) | 15.5 – 23.7 (Mo) | |
| | Solution treated water quenched | Ni-16.6at%Cr-19.0at%Mo | 8.0 | ± 4.7 (Cr) | 11.9 – 21.3 (Cr) | $Ni_{0.74}(Cr+Mo)_{0.26}$,<br>$Ni_{0.55}(Cr+Mo)_{0.45}$ |
| | | | | ± 4.6 (Mo) | 14.4 – 23.6 (Mo) | |
| | Aged-525°C-60 min | Ni-16.3at%Cr-20.6at%Mo | 9.2 | ± 3.5 (Cr) | 12.8 – 19.8 (Cr) | $Ni_{0.71}(Cr+Mo)_{0.29}$,<br>$Ni_{0.55}(Cr+Mo)_{0.45}$ |
| | | | | ± 4.4 (Mo) | 16.2 – 25.0 (Mo) | |

### 4.2.2. $Ni_2(Cr_{0.5}Mo_{0.5})$ alloy:

3D-AP investigations of the $Ni_2(Cr_{0.5}Mo_{0.5})$ alloy was carried out in three microstructural conditions: (i) splat-quenched state; (ii)STWQ state; and (iii) STWQ samples aged at 525°C for 60 min. Investigation on aged sample was used to identify the effect of the growth of SRO (see fig. 4.4a) on chemical heterogeneities already prevailing in the microstructure of the alloy. Atomic reconstruction maps of individual atomic species from samples of $Ni_2(Cr_{0.5}Mo_{0.5})$ alloy in all three microstructural states are shown in fig. 4.12. Concentration depth profiles corresponding to reconstruction maps are given below the respective reconstruction maps. Similar to $Ni_2Cr$ alloy, a visual inspection of the reconstructions maps was unable to reveal the existence of any chemical heterogeneity, though concentration depth profiles suggested a variation in the compositions of the individual species. A marginally higher molybdenum concentration alloy was found in the reconstruction map of $Ni_2(Cr_{0.5}Mo_{0.5})$ alloy in all three microstructural states.

Cluster search analysis with nickel concentration within threshold limits of 47-57 at.% and 74-100 at.% were used to identify Ni-depleted and Ni-rich clusters, respectively, covering the composition range on either sides of the $Ni_2(Cr_{0.5}Mo_{0.5})$ stoichiometry. Cluster search analysis revealed the presence of both Ni-depleted as well as Ni-rich clusters in reconstruction volumes of all samples (Figs. 4.13), though Ni-depleted clusters appeared to dominate the reconstruction maps in all three cases. Fig. 4.13 also revealed that Ni-depleted clusters appeared more profoundly in the aged state than in splat-quenched state of the alloy, while Ni-rich clusters remained unaffected. The cluster composition histogram shown in fig. 4.14 confirmed this behaviour by the presence of large number of Ni-depleted clusters of bigger sizes in the aged state compared to that seen in splat-quenched state. This figure also revealed that the Ni-depleted clusters peaked about Ni-55at% (Cr,Mo) composition. WDF analyses of atom probe data from the three states are shown in fig. 4.14 (d, e and f). This

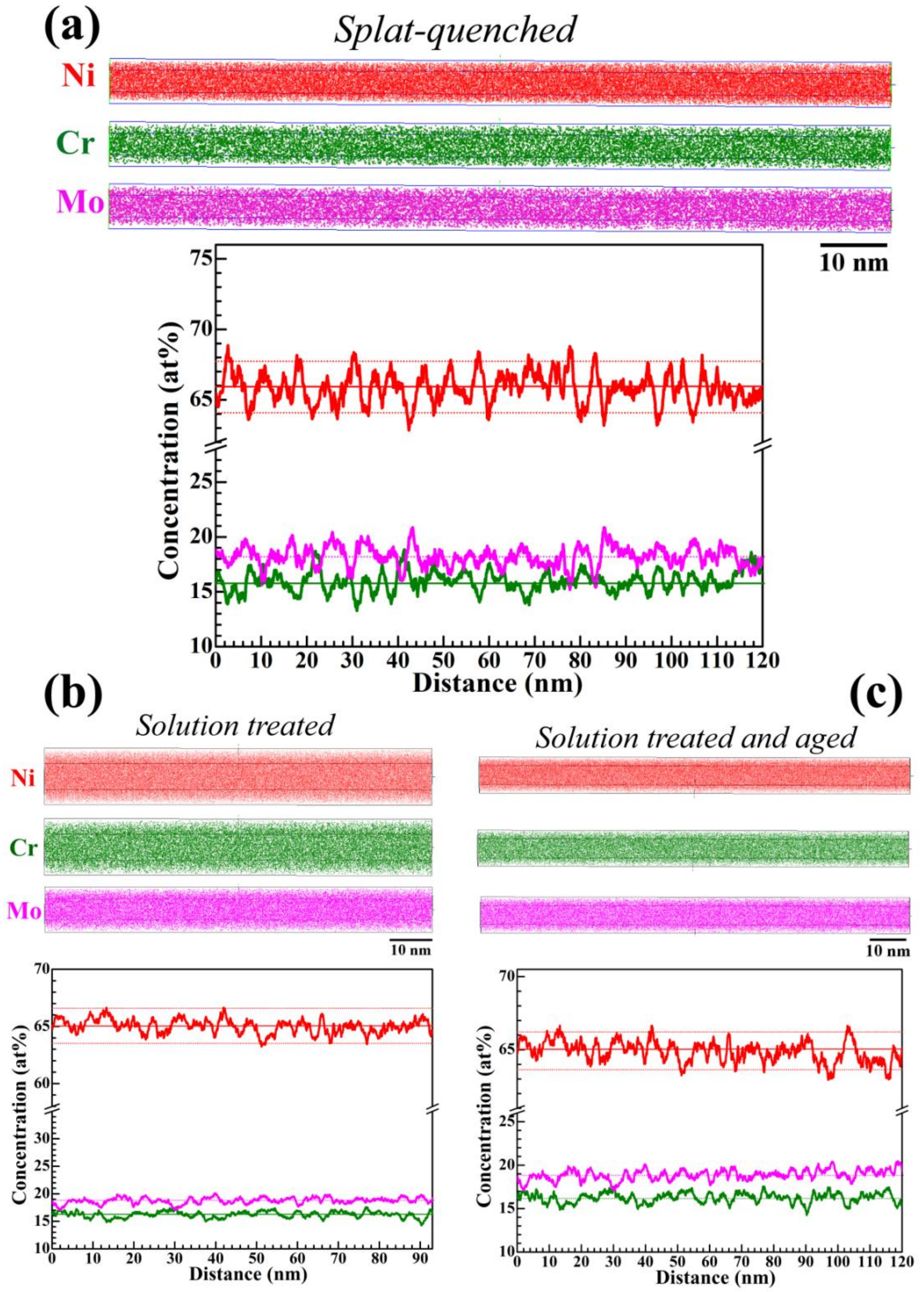

**Figure 4.12:** 3-dimensional reconstruction maps of nickel, chromium and molybdenum atoms in $Ni_2(Cr_{0.5}Mo_{0.5})$ alloy in; (a) splat-quenched state; (b) solution treated state; and (c) solution treated and aged state. Concentration depth profiles are given below the reconstruction maps.

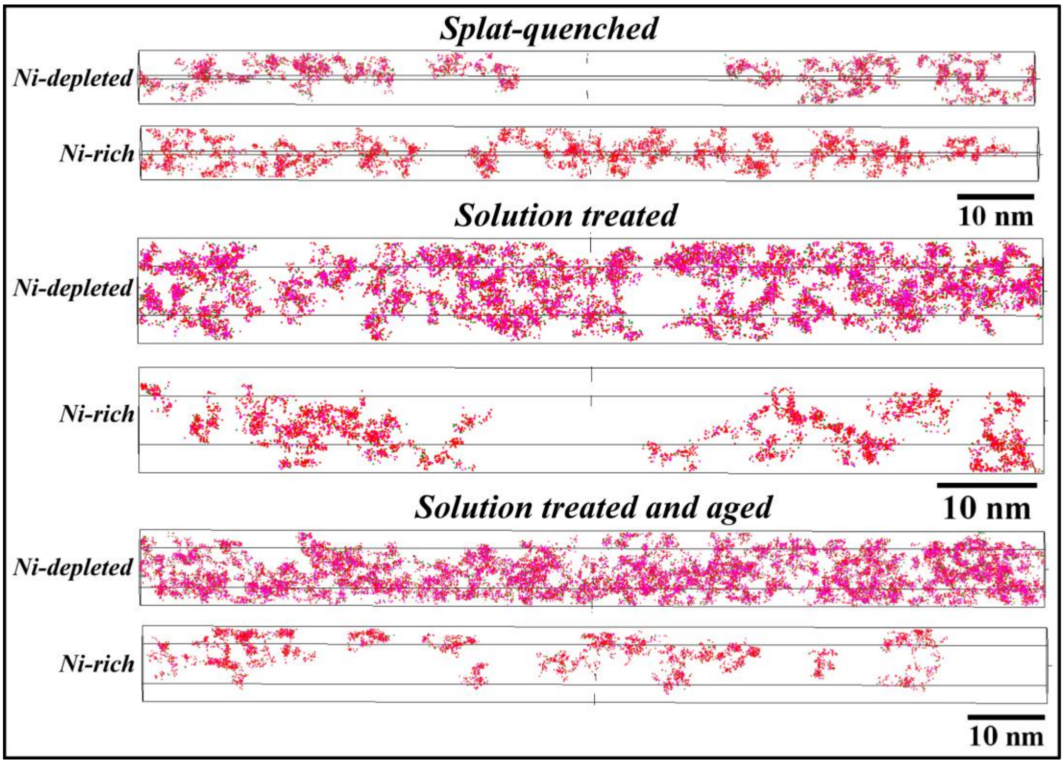

**Figure 4.13:** 3-dimensional reconstruction maps showing Ni-rich and Ni-depleted clusters in $Ni_2(Cr_{0.5}Mo_{0.5})$ alloy in splat-quenched state; STWQ state; and solution treated sample aged at 525°C for 60 min (see text for details).

analysis revealed the predominant existence of concentration fluctuations in Ni, Cr and Mo atoms in the splat-quenched state (Fig. 4.12d). These chemical fluctuations were characterized by wavelengths of about 5.0 nm, 4.8 nm and 6.6 nm with concentration amplitudes of 3.6 at% Ni (65.1 at%), 6.0 at% Cr (16.1 at%) and 4.1 at% Mo (18.8 at%), respectively, (Table 4.1), where the average concentrations are mentioned in the parentheses. On the other hand STWQ sample (Fig. 4.12e) exhibited $\Sigma^2$ maximum corresponding to predominant wavelengths of 5.6 nm, 9.1 nm and 6.9 nm with concentration amplitudes of 3.6 at% Ni (64.4 at%), 4.7 at% Cr (16.6 at%) and 4.6 at% Mo (19.0 at%), respectively. These analyses established the existence of non-random concentration fluctuations in the distributions of Ni, Cr and Mo elements in both the states. Similar kinds of concentration fluctuation were also found in the WDF analysis of the aged alloy as shown in fig. 4.12f. The concentration fluctuations were having wavelengths of about 4.4 nm, 9.2 nm and 9.3 nm with

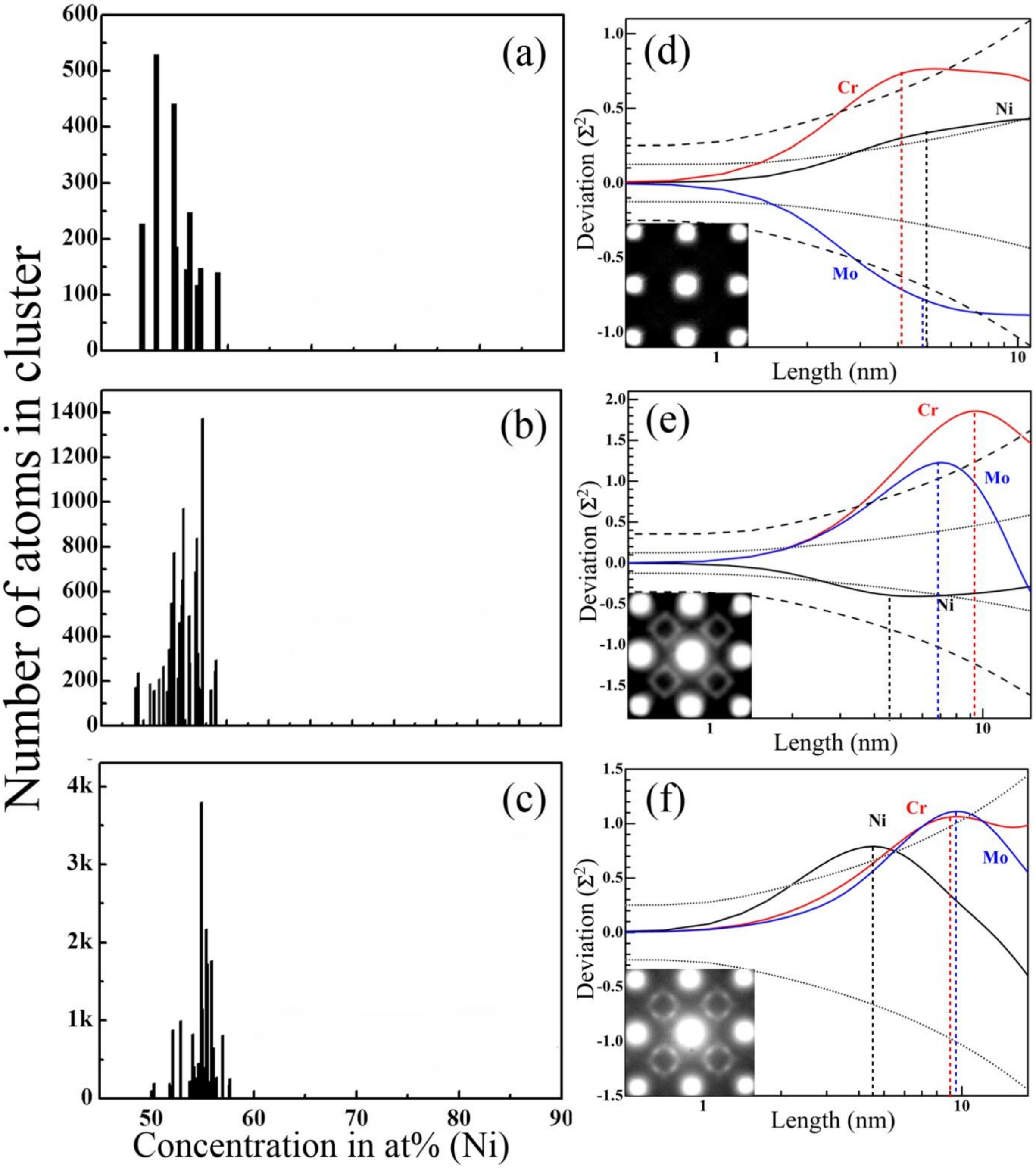

**Figure 4.14:** Cluster composition histograms showing the dominance of $Ni_{0.55}(Cr,Mo)_{0.45}$ compositions in; (a) splat-quenched state; (b) STWQ state; and (c) solution treated sample aged at 525°C for 60 min of $Ni_2(Cr_{0.5}Mo_{0.5})$ alloy. WDF analysis of atom probe data to identify chemical heterogeneities in; (d) splat-quenched state; (e) STWQ state; and (f) solution treated sample aged at 525°C for 60 min of $Ni_2(Cr_{0.5}Mo_{0.5})$ alloy, reduced deviation parameter is drawn by solid lines against the logarithm of the effective damping length of the Gaussian filter function [95]. Broken lines indicate the 2σ statistical errors.

amplitudes of 5.6 at% Ni (63.1 at%), 3.5 at% Cr (16.3 at%) and 4.4 at% Mo (20.6 at%), respectively.

Results of the WDF analysis on $Ni_2Cr$ and $Ni_2(Cr_{0.5}Mo_{0.5})$ alloys in different states of the microstructure are listed in table 4.1. This information was used to determine the possible compositions of the chemical heterogeneities. In splat-quenched state of $Ni_2Cr$ alloy, compositions of heterogeneities were Ni-25 at% Cr and Ni-40 at% Cr, whereas in the STWQ state the heterogeneities had compositions of Ni-24.9 at% Cr and Ni-35.9 at% Cr. In the $Ni_2(Cr_{0.5}Mo_{0.5})$ alloy, compositions of the heterogeneities were determined to be about 54.0 at% Ni and 74 at% Ni in all three states of the microstructure (Table 4.1). On the basis of the WDF analysis on both $Ni_2Cr$ and $Ni_2(Cr_{0.5}Mo_{0.5})$ alloys, it could be concluded that: (i) nearly similar type of chemical heterogeneities were present in both splat-quenched and in STWQ microstructures of the two alloys; (ii) STWQ state strengthened the chemical heterogeneities as evidenced by the increase in size of concentration fluctuations in the latter (Table 4.1).

## **4.3. Discussion:**

Binary Ni-Mo alloy of stoichiometric $Ni_2Mo$ composition exhibits diffuse intensity maxima at {1 ½ 0} positions in the SRO state [75]. Results shown above have demonstrated that addition of Cr to binary $Ni_2Mo$ alloy (i.e., in $Ni_2(Cr_{0.63}Mo_{0.37})$ and $Ni_2Cr_{0.5}Mo_{0.5}$ alloys) caused the appearance of additional diffuse reflections at 1/3{2 2 0} positions which corresponded to the ordered $Ni_2(Cr,Mo)$ phase. A similar effect of appearance of additional diffuse reflections apart from that at {1 ½ 0} positions have been mentioned in many other binary Ni-Mo alloys after the addition of ternary elements [37, 38]. For example, Kulkarni et al. [37] have observed diffuse reflections of $DO_{22}$ structure after the addition of Al to $Ni_3Mo$ alloy, while addition of Ta or W to $Ni_3Mo$ alloy have been found to result in the appearance of diffuse reflections of $DO_{2h}^{25}$ structure [38]. Martin and Williams[38] have suggested that accelerated ordering kinetics can be attributed to the formation of nuclei of ordered structures which appear as additional diffuse reflections in the {1 ½ 0} SRO state. The suppression of {1 ½ 0} and 1/3{2 2 0} reflections in splat-quenched $Ni_2(Cr_{0.5}Mo_{0.5})$ alloy (Fig. 4.5) ruled out the possibility of formation of nuclei of ordered domains during quenching. It has been mentioned earlier in chapter 2 that {1 ½ 0} SRO and the ordered structures ($DO_{22}$, $D1_a$ and $DO_{2h}^{25}$) can be described by static concentration waves of different wave vectors which characterize atomic arrangements on {4 2 0} planes of the fcc lattice. Out of this spectrum of waves, concentration waves with wave vectors ending at {1 ½ 0} positions grow preferentially due to largest driving force available for their amplification [80]. On this basis, preferential appearance of diffuse reflections at {1 ½ 0} positions could be argued from a completely disordered state. However, simultaneous appearance of diffuse reflections at {1 ½ 0} and 1/3{2 2 0} positions during ageing of the splat-quenched alloy (Fig. 4.7) revealed their association, which could be explained on the basis of existing structural models.

Since the "Microdomain model" replicates only the appearance of diffuse reflections at {1 ½ 0} positions [77-79, 100], it appeared to be unsuitable to explain the origin of additional diffuse intensity at 1/3{2 2 0} positions. On the contrary, a careful examination of the "SCW model" revealed that its $N_2M_2$ stacking inherently contained $N_2M$ atomic stacking necessary for the formation of $DO_{2h}^{25}$ structure (see fig. 4.14a). A schematic representation of $N_2M_2$ stacking showing the existence of subunit cell of ordered $N_2M$ structure (drawn by green lines) and subunit cell of imperfectly ordered $DO_{22}$ structure (drawn by black lines) are shown in fig. 4.15a. Further, it has been mentioned earlier (Chapter 2) that single <1 ½ 0> SCW creates subunit cell of imperfectly ordered $DO_{22}$ structure, while superimposition of two perpendicular <1 ½ 0> SCWs create subunit cells of $DO_{2h}^{25}$ ($N_2M$-type) and $D1_a$ ($N_4M$-type) structural units. In this scheme atomic arrangements of the "Microdomain model" could be created by incorporating chemical defect at suitable lattice sites, thus, creating subunit cell of $DO_{22}$ structure ($N_3M$-type) as shown in fig. 4.15b. This means that the "SCW model"

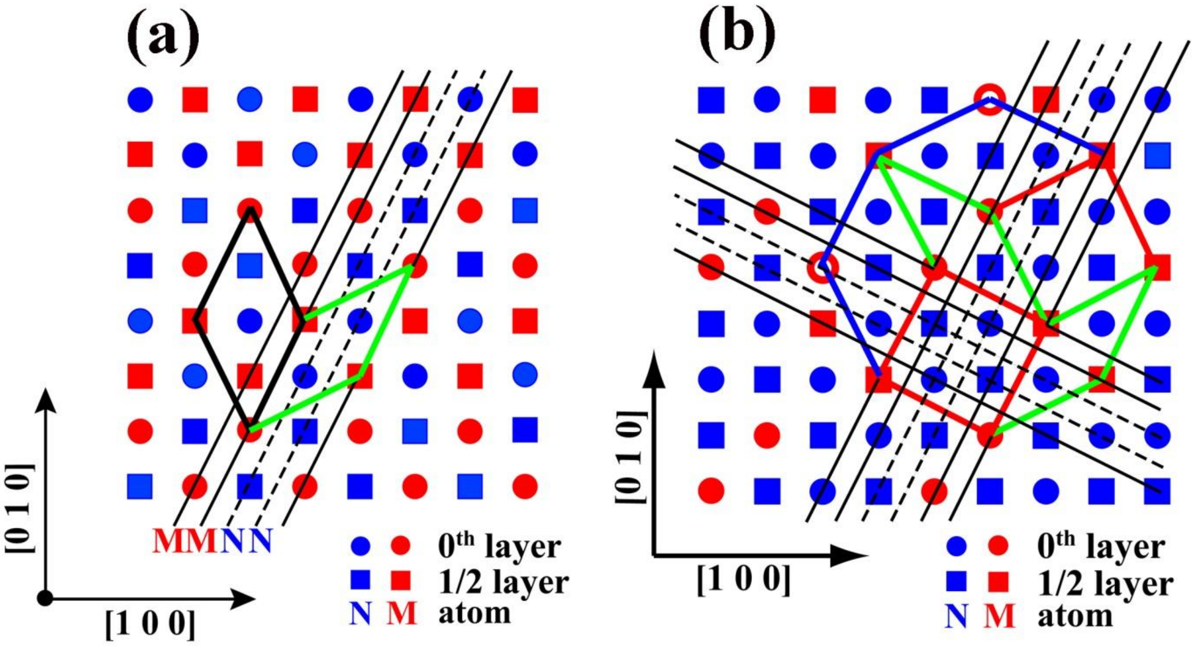

**Figure 4.15:** [0 0 1] projection depicting atomic arrangements; (a) $N_2M_2$ generated by [1 ½ 0] concentration wave, one molecule size subunit cells are drawn by solid lines; (b) superimposition of two perpendicular <1 ½ 0> concentration waves containing imperfection marked by open circles. This arrangement generates SRO state as suggested by cluster model.

could be suggested as a basic building block for the “Microdomain model”. Simultaneous appearance of the diffuse intensity maxima at {1 ½ 0} and 1/3{2 2 0} positions appeared to be consistent with this geometrical predictions of the presence of subunit cells of $\mathrm{DO}_{2h}^{25}$ phase in the “SCW model”. Experimental evidence of the existence of chemical heterogeneities having compositions close to $N_2M_2$-type also supported this model of SRO. On the contrary, presence of the diffuse intensity maxima at {1 ½ 0} positions in $Ni_2Cr$ alloy [102] appeared to be consistent with “Microdomain model”, which was supported by the existence of chemical heterogeneities having chemical composition close to $N_3M$-type. Thus, it could be suggested that partial replacement of Mo by Cr atoms in stoichiometric $Ni_2Mo$ alloys could have favoured the formation of SRO by single <1 ½ 0> SCW in contrast to binary Ni-Mo alloys where the SRO was established due to a mixture of $\mathrm{DO}_{22}$, $\mathrm{D1}_a$ and $\mathrm{DO}_{2h}^{25}$ subunit cells [64, 77, 78, 100, 104].

On the basis of this study it could be concluded that, though the short-range order state in many Ni-Mo and Ni-Cr-Mo alloys has been characterized by the appearance of diffuse reflections at {1 ½ 0} positions, additional diffuse diffraction intensity at 1/3{2 2 0} positions appeared $Ni_2(Cr_{1-x}Mo_x)$ alloys containing Mo concentration ≥ 0.37. Different models suggested in literature appeared to explain the pattern of diffuse reflections in different $Ni_2(Cr_{1-x}Mo_x)$ alloys. The “Microdomain model” which has successfully explain the origin of diffuse reflections at {1 ½ 0} positions in binary Ni-Mo alloys appeared to valid in $Ni_2Cr$ alloy. However, “SCW model” of $N_2M_2$ type could explain reasonably well the origin of additional diffuse reflections at 1/3{2 2 0} positions due to the inherent presence of atomic stacking of $N_2M$ type required for the formation of ordered $Ni_2(Cr,Mo)$ phase.

# CHAPTER 5

# ROLE OF Cr AND Mo SOLUTES ON THE EVOLUTION OF ORDERED NI$_2$(Cr,Mo) PHASE

This chapter describes the results of microhardness testing, four probe resistivity measurement, differential scanning calorimetry studies and transmission electron microscopy investigations undertaken to study the effects of Cr and Mo solutes on the formation and kinetics of ordered $Ni_2(Cr,Mo)$ phase in $Ni_2(Cr_{1-x}Mo_x)$ alloys.

## 5.1. Effect of Cr and Mo on Microhardness:

Room temperature microhardness of $Ni_2(Cr_{1-x}Mo_x)$ alloys in the solution treated state is

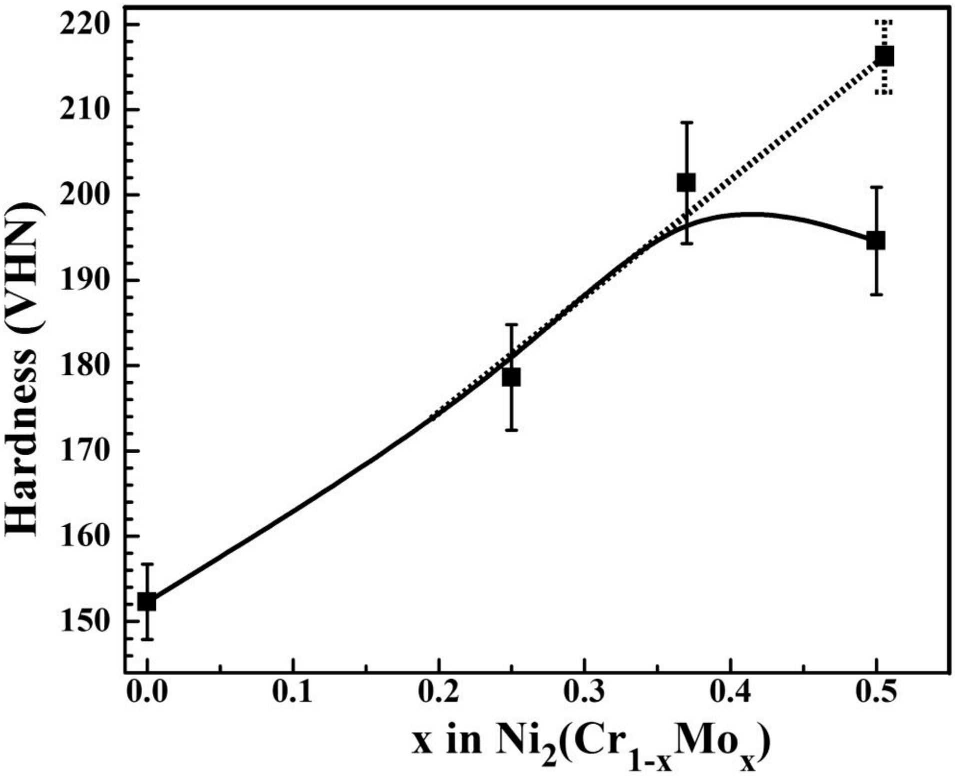

**Figure 5.1:** Microhardness as a function of Mo-content in stoichiometric $Ni_2(Cr_{1-x}Mo_x)$ alloys in solution treated and water quenched states. A dashed line showing the hardness expected for $Ni_2(Cr_{0.5}Mo_{0.5})$ alloy simply due to solid solution strengthening (size) effect of Mo. The error bars correspond to standard deviation of data points.

shown in fig. 5.1. It was interesting to note that the hardness first increased linearly with composition from $Ni_2Cr$ up to $Ni_2(Cr_{0.63}Mo_{0.37})$ alloys followed by a decrease in $Ni_2(Cr_{0.5}Mo_{0.5})$ alloy. This was surprising because replacement of Cr by Mo in $Ni_2Cr$ alloys was expected to impart solid solution strengthening due to relatively bigger atomic size of the latter as observed in alloys with compositions up to $Ni_2(Cr_{0.63}Mo_{0.37})$. Softening of the alloy beyond $Ni_2(Cr_{0.63}Mo_{0.37})$ composition suggested the influence of additional factors on the hardness of $Ni_2(Cr_{0.5}Mo_{0.5})$ alloy, which is explained later in the Section 5.5.2.

## 5.2. Resistivity behaviour during order evolution:

Isochronal resistivity measurements were carried out on different $Ni_2(Cr_{1-x}Mo_x)$ alloys in the solution treated and water quenched state to understand different stages involved in the evolution of the ordered phase. Isochronal resistivity profiles obtained during heating (5 °C/min) are shown in fig. 5.2. On the basis of the appearance of resistivity profiles, alloys could be grouped into two categories, namely, (a) category I comprising $Ni_2Cr$ and $Ni_2(Cr_{0.75}Mo_{0.25})$ alloys (Fig. 5.2a), and, (b) category II comprising $Ni_2(Cr_{0.63}Mo_{0.37})$ and

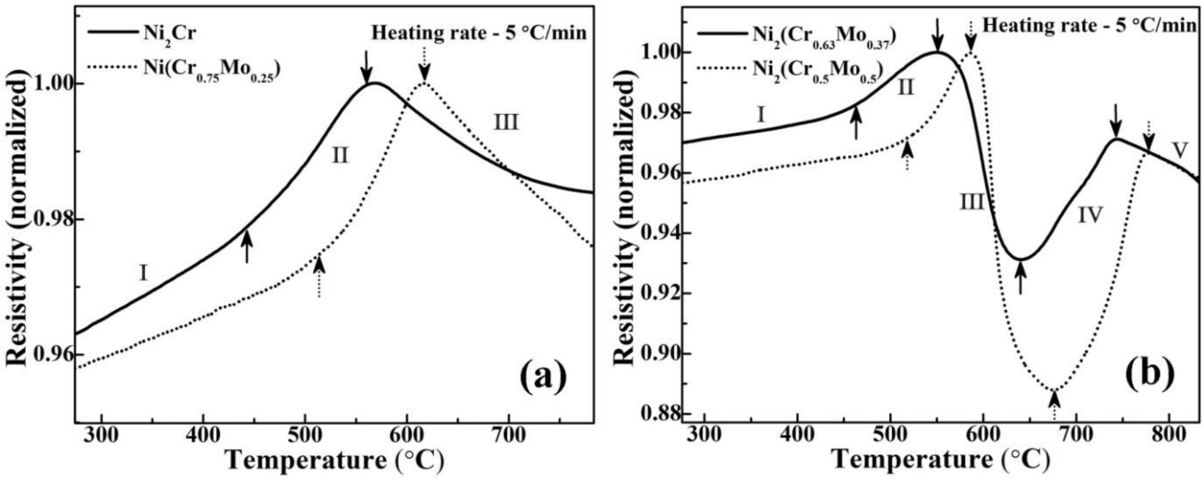

**Figure 5.2:** Isochronal resistivity profiles obtained during controlled heating of alloys at 5 °C/min from room temperature up to 900 °C; (a) for $Ni_2Cr$ and $Ni_2(Cr_{0.75}Mo_{0.25})$ alloys; and (b) for $Ni_2(Cr_{0.63}Mo_{0.37})$ and $Ni_2(Cr_{0.5}Mo_{0.5})$ alloys. The arrows marked in the figures demarcate different regimes of resistivity profiles.

$Ni_2(Cr_{0.5}Mo_{0.5})$ alloys (Fig. 5.2b). Different regimes of resistivity profiles are separated by arrows marked in respective figures. In fig. 5.2a, resistivity initially increased linearly with temperature (Regime I), followed by an increase at a higher rate till it reached a maximum, $T_{max1}$ (Regime II). Beyond the resistivity maximum, it decreased with temperature (Regime III) but always remained higher than that at the beginning of the experiment. $Ni_2Cr$ and $Ni_2(Cr_{0.75}Mo_{0.25})$ alloys exhibited resistivity maxima at temperatures about 571 °C and 620 °C , respectively. Resistivity profiles in category II alloys (Fig. 5.2b) were initially similar (Regimes I and II) to that in category I alloys (Fig. 5.2a), albeit with faster kinetics. However, in fig. 5.2b, the resistivity maxima was followed by a sharp drop (Regime III) that continued much below the initial value until it reached a minimum value at a temperature, $T = T_{min}$, beyond which it increased again to a second maximum which appeared at a temperature, T =

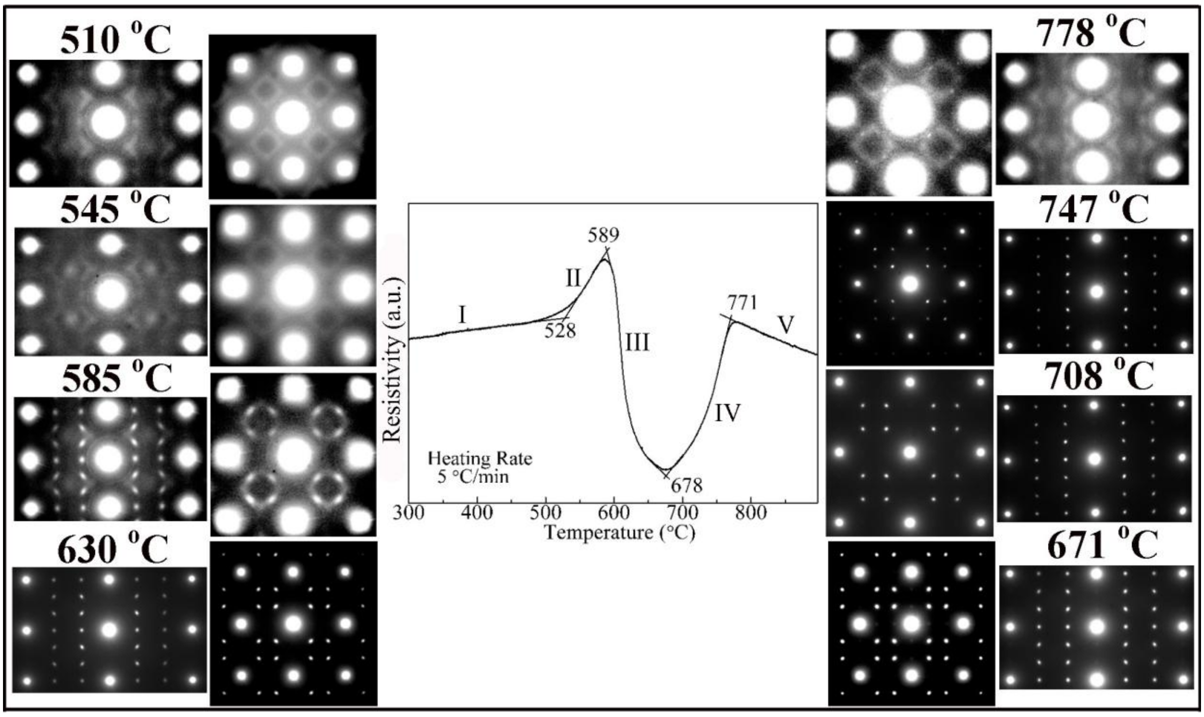

**Figure 5.3:** Microstructural correlation at different stages of the resistivity profile during heating run of $Ni_2(Cr_{0.5}Mo_{0.5})$ alloy. Central figure represents the resistivity profile during isochronal run and the figures around it represents the corresponding SAED patterns in <0 0 1> and <1 1 2> zone axes.

$T_{max2}$ (Regime IV). Continued heating beyond regime IV resulted in further decrease of resistivity but at a lower rate (Regime V). Since the SRO formation is reported to result in increase of the resistance of alloy while the LRO formation results in decrease [43, 45, 48], temperatures $T_{max1}$, $T_{min}$, and $T_{max2}$ could be correlated to the SRO to LRO transition ($T_{SRO\rightarrow LRO}$), the maximum ordering temperature ($T_{LRO\_max}$), and the LRO to SRO transition temperatures ($T_{LRO\rightarrow SRO}$), respectively. It was interesting to note that respective characteristic temperatures for $Ni_2(Cr_{0.5}Mo_{0.5})$ alloy appeared at higher temperatures compared to those for the $Ni_2(Cr_{0.63}Mo_{0.37})$ alloy (Fig. 5.2b). In order to correlate resistivity characteristics directly with microstructural changes that occurred during different regimes of resistivity profiles, samples of the $Ni_2(Cr_{0.5}Mo_{0.5})$ alloy were quenched at pre-determined temperatures corresponding to different regimes of the resistivity profile (Fig. 5.3). The selected area electron diffraction evidences with <0 0 1> and <1 1 2> zone axes were used to interpret microstructural changes happening in different resistivity regimes. The temperatures from which these specimens were quenched are mentioned by the side of each pattern. The intensity distribution of superlattice reflections in specimens heated up to 510°C was seen to be nearly the same as that of solution treated specimen (Fig. 5.2c) and this indicated that the short range ordered state was stable up to this temperature. The stability of microstructure up to this temperature was reflected in the nearly flat resistivity plot in regime I. SAED patterns from samples heated at temperatures between 510°C and 545°C (in the regime II) revealed the presence of a diffuse reflections of nearly same intensity at {1 ½ 0} and 1/3{2 2 0} positions. The diffuse nature of diffraction intensity at the superlattice positions corresponding to the ordered $Ni_2(Cr,Mo)$ phase (i.e., 1/3{2 2 0} positions) suggested it to be a SRO of the ordered $Ni_2(Cr,Mo)$ phase (henceforth referred to be as 1/3{2 2 0} SRO). BF micrograph of the specimen quenched at 545°C revealed only a mottled contrast (Fig. 5.4a) and dark field imaging with diffuse reflections did not reveal any feature. In fact, in regime II

(Fig. 5.3) where the increase of resistivity with temperature was maximum, the intensity of {1 ½ 0} reflections became progressively weaker while the intensity of 1/3{2 2 0} reflections became stronger with increasing temperature. The presence of two types of SRO reflections (i.e., {1 ½ 0} and 1/3{2 2 0} in fig. 5.3) appeared to have contributed to sharp increase in resistivity which peaked at around 585 °C. Relatively strong superlattice reflections at 1/3{2 2 0} positions could be seen at this temperature. SAED patterns obtained from samples quenched at 630°C and 671°C temperatures (regime III) showed strong superlattice reflections corresponding to the LRO state (i.e., at 1/3{2 2 0} and equivalent positions only) and their intensity was maximum at 671°C (near to the lowest value of resistance in the regime III). Dark-field images taken with 1/3{2 2 0} reflections (Fig. 5.4) also confirmed that the size as well as the number density of ordered particles was maximum at 671°C. Beyond this temperature (regime IV), the resistance increased again with increase of temperature. Intensity of 1/3{2 2 0} superlattice reflections also exhibited a decreasing trend with increase of temperature as evidenced from samples heated up to 708°C and 747°C temperatures (Fig. 5.3). DF micrographs also confirmed that the size and number density of ordered domains had decreased (Fig. 5.4d) compared to those seen in specimen heated up to 671°C (Fig. 5.4c). From this observation it was concluded that the increase in the resistivity in regime IV was due to progressive dissolution of ordered precipitates formed in the regime III. SAED patterns taken from the end of regime IV and beginning of V (i.e.,778 °C) revealed the transformation of sharp intense spots at the 1/3{2 2 0} superlattice positions into diffuse spots with simultaneous appearance of {1 ½ 0} reflections and this pattern was very similar to that seen at 545°C. This indicated that at temperatures above 778 °C, the transformation was reverting back to the state seen in the solution treated case. A further resistivity decrease in regime V (Fig. 5.3) was due to further reduction in intensity of diffuse 1/3{2 2 0} reflections with increase of temperature [105].

A linear regression method was used to estimate equivalent isothermal transformation temperatures, namely $T_{max1}$, $T_{min}$ and $T_{max2}$, based upon their dependence on heating rates in non-isothermal studies. In this approach resistivity profiles were first determined at varying

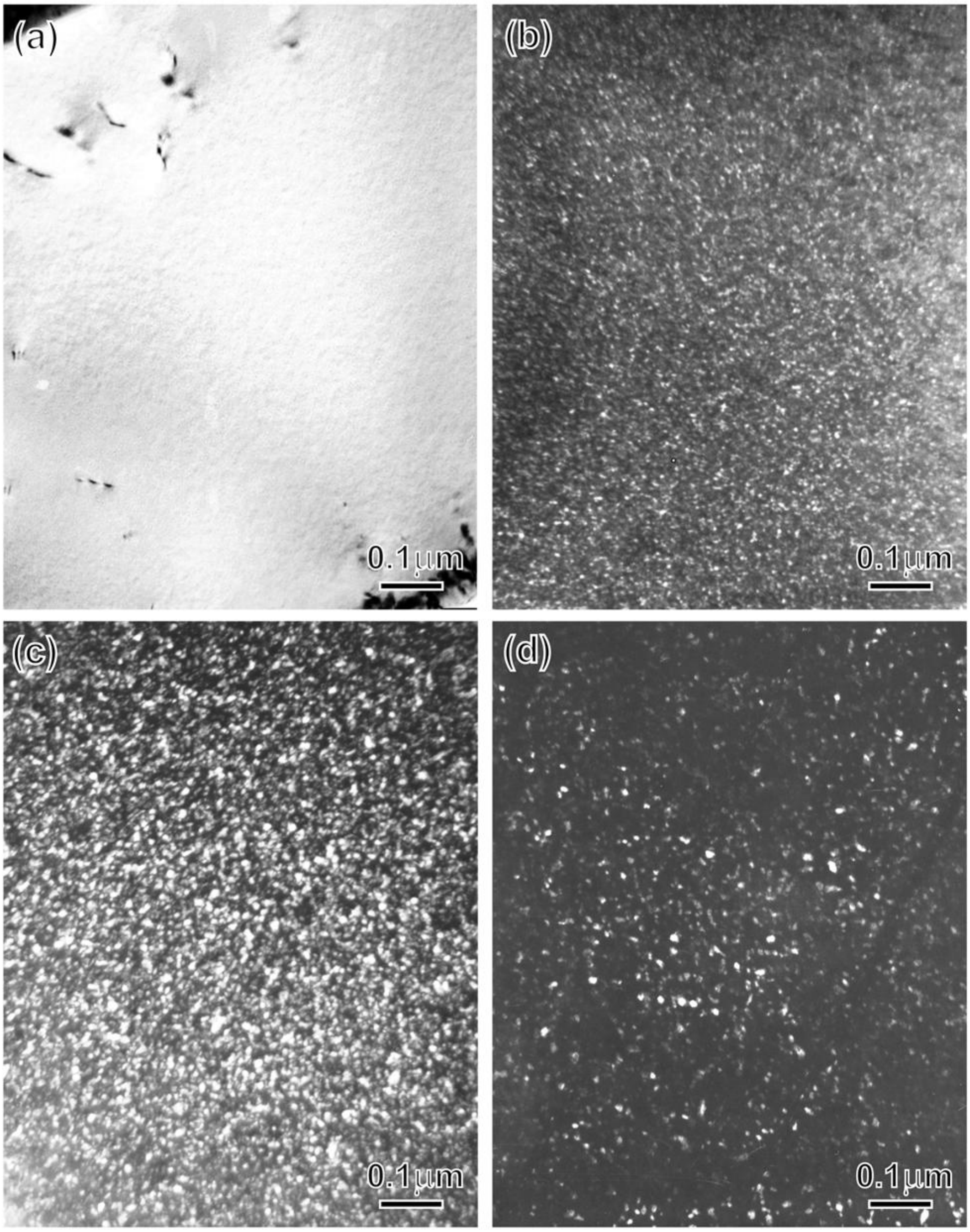

**Figure 5.4:** TEM images of resistivity quenched specimens at different temperatures: (a) BF with <0 0 1> at 545 °C (b) DF with LRO reflection in <0 0 1> at 630 °C (c) DF with LRO reflection in <0 0 1> at 671 °C (d) DF with LRO reflection in <0 0 1> at 747 °C.

heating rates (as shown in figs. 5.5a and 5.5c) for $Ni_2(Cr_{0.63}Mo_{0.37})$ and $Ni_2(Cr_{0.5}Mo_{0.5})$ alloys,

$$\alpha_{res} = \frac{1}{T}\frac{d\,{}^{\rho}\!/\!{}_{\rho_{max}}}{dT} \quad ..............................(5.1)$$

respectively. These resistivity profiles were used to calculate coefficient of thermal resistivity as defined below in equation 5.1 (Figs. 5.5b and 5.5d).

where, $\alpha_{res}$ is coefficient of thermal resistivity, T is temperature and $\rho$ and $\rho_{max}$ are instantaneous and the maximum value of the resistivity, respectively, in the measured plots. Intersections of the line $\alpha_{res} = 0$ with curves were taken as temperatures $T_{max1}$, $T_{min}$ and $T_{max2}$ in solution treated samples. These values were plotted as a function of heating rate (Fig. 5.6)

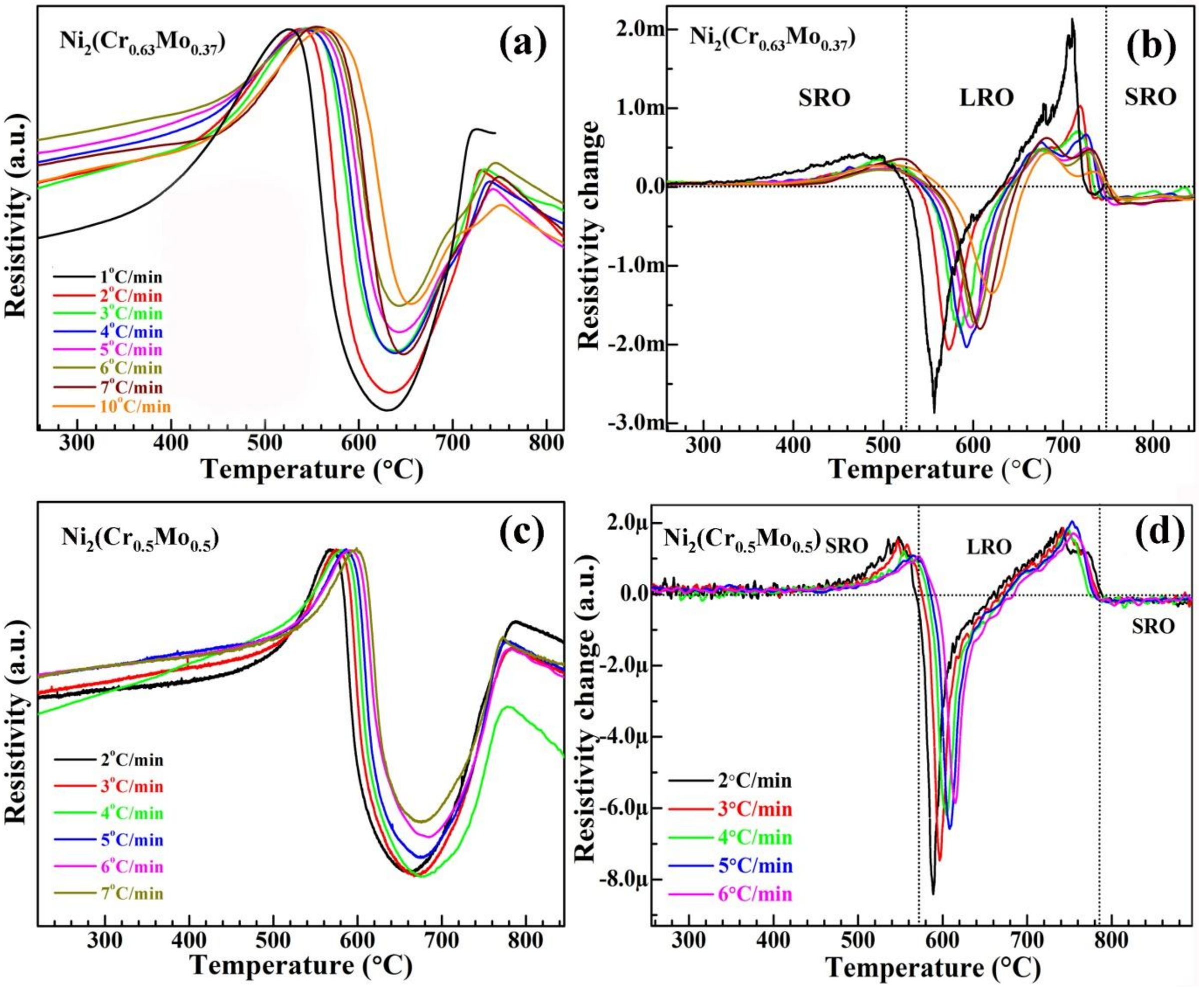

**Figure 5.5:** Resistivity and coefficient of thermal resistivity profiles during heating at different rates of $Ni_2(Cr_{0.63}Mo_{0.37})$ alloy in (a) and (b); and of $Ni_2(Cr_{0.5}Mo_{0.5})$ alloy in (c) and (d) respectively.

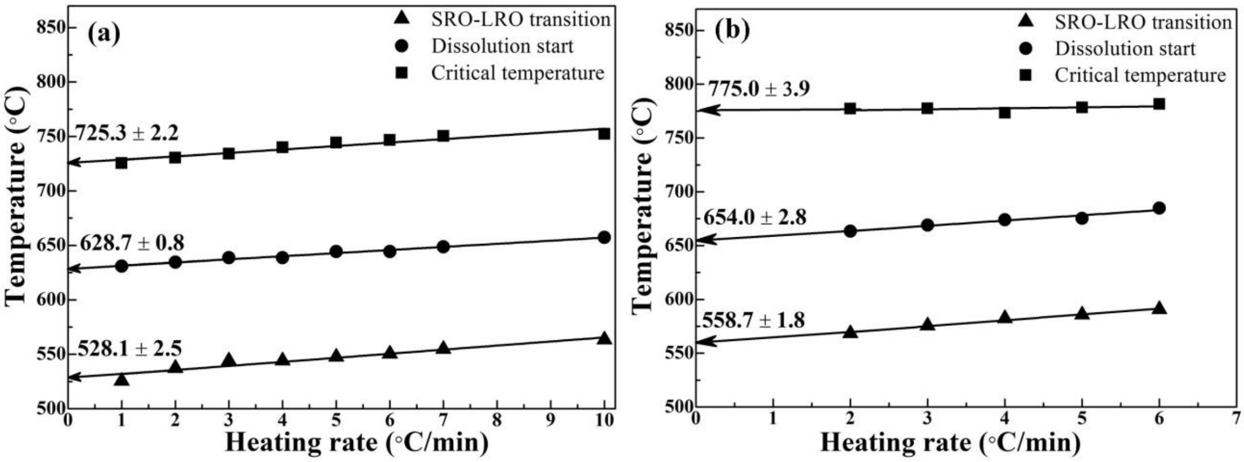

**Figure 5.6:** A linear regression plot of temperature versus heating rate to determine the isothermal transformation temperatures charactering different stages of order evolution in; (a) $Ni_2(Cr_{0.63}Mo_{0.37})$ alloy; and (b) $Ni_2(Cr_{0.5}Mo_{0.5})$ alloy.

and y-intercepts of extrapolations of respective linear fits were considered as $T_{max1}$, $T_{min}$ and $T_{max2}$ temperatures at zero heating rate in solution treated samples. It was found that $T_{max1}$, $T_{min}$ and $T_{max2}$ increased, respectively, from 528°C, 629°C and 725°C in the $Ni_2(Cr_{0.63}Mo_{0.37})$ alloy to 559°C, 654°C and 775°C in the $Ni_2(Cr_{0.5}Mo_{0.5})$ alloy. Resistivity studies on $Ni_2(Cr_{1-x}Mo_x)$ alloys, therefore, established that increase of Mo content from $Ni_2(Cr_{0.75}Mo_{0.25})$ to $Ni_2(Cr_{0.63}Mo_{0.37})$ composition significantly increased the overall ordering kinetics which will be discussed further in detail later in Section 5.5.3.

An attempt was made to qualitatively explain the progress of ordering during isochronal heating from the intensity of superlattice reflections in the diffraction patterns. This was done by determining the intensity of reflections at {1 ½ 0} and 1/3{2 2 0} positions from <0 0 1> SAED patterns of samples quenched at different stages of resistivity profile (Fig. 5.3), as explained in Section 3.6. Fig. 5.7 shows a plot of normalized intensities of superlattice spots as a function of temperature (heating rate 5°C/min). It was clear from this figure that intensities of LRO spots did not increase appreciably up to 585°C and thereafter it increased sharply to reach a maximum at 671°C, followed by a nearly equal decrease. Intensities of SRO spots also exhibited a decreasing trend in the temperature range from

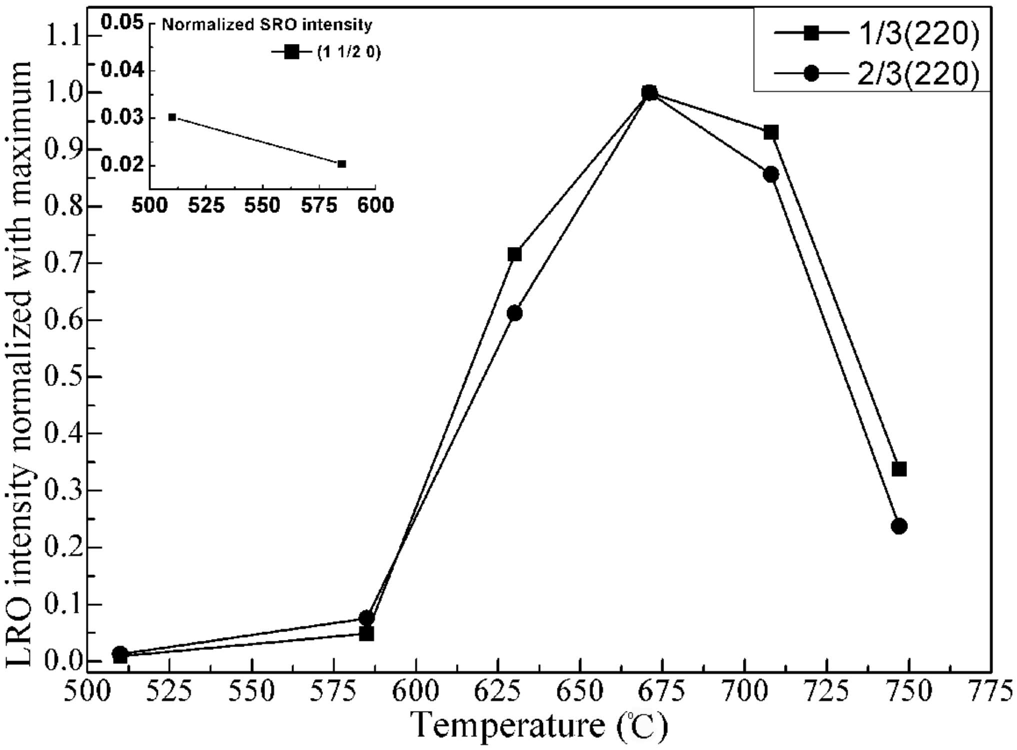

**Figure 5.7:** Intensity of the LRO and SRO spots obtained from SAED in <0 0 1> zone axis with temperature on resistivity quenched samples.

510°C to 585°C (shown as inset in fig. 5.7). These observations were consistent with the resistivity data.

### 5.3. Thermal analysis of order evolution:

Differential scanning calorimetric studies were carried out on $Ni_2(Cr_{1-x}Mo_x)$ alloys in the solution treated and water quenched state. Fig. 5.8 shows thermograms obtained during two consecutive heating cycles at a heating rate of 5°C/min These experiments were carried up to 675°C. During the 1st heating cycle, both $Ni_2Cr$ and $Ni_2(Cr_{0.75}Mo_{0.25})$ alloys exhibited the presence of exothermic peaks superimposed with a baseline shift which appeared at the end of peaks. The exothermic peak was stronger for the $Ni_2(Cr_{0.75}Mo_{0.25})$ alloy than that for the $Ni_2Cr$ alloy. These peaks were characterized by three temperatures, viz., onset temperature ($T_i$), peak temperature ($T_p$) and endset temperature ($T_f$), which were respectively 390°C, 532°C and 576°C, and 532°C, 579°C and 621°C for $Ni_2Cr$ and in $Ni_2(Cr_{0.75}Mo_{0.25})$ alloys.

This indicated a shift of all characteristic temperatures to higher values in $Ni_2(Cr_{0.75}Mo_{0.25})$ alloy. Exothermic peaks were absent during the 2nd heating cycle though the characteristic feature of baseline shift, which appeared during 1st heating cycle, was seen during the 2nd heating cycle as well, as marked by arrow in fig. 5.8a. Experiments with varying heating rates exhibited similar characteristic behaviour on both of these alloys. Since exothermic / endothermic peaks and a baseline shift in a DSC thermogram are characteristics of 1st order and 2nd order transformations respectively [106], it could be suggested that both 1st order as well as a 2nd order mechanisms were involved during the ordering reaction in $Ni_2Cr$ and $Ni_2(Cr_{0.75}Mo_{0.25})$ alloys. The observation of only baseline shift during the 2nd heating cycle suggested that a 2nd order transformation mode continued to operate in the absence of excess quenched-in defects which were eliminated during the 1st heating cycle. Further, as $Ni_2Cr$ alloy orders only below 571°C [12], it was not unreasonable to expect dissolution of ordered domains beyond this temperature during heating. Absence of any dissolution peak beyond 571°C in fig. 5.8a was suggested of sluggish ordering kinetics which inhibited the formation of ordered domains during heating. The sluggish nature of ordering was confirmed independently by isothermal ageing of the $Ni_2Cr$ alloy, which exhibited very fine ordered domains even after 500 h of ageing at 500°C (Fig. 5.8b). The appearance of superlattice reflections in the SAED pattern in < 1 1 2> zone axes (inset fig. 5.8b) confirmed the presence of the ordered phase. However, ordered particles remained very fine and could not be resolved in a DF image, though their presence was confirmed in a BF image by the appearance of mottled contrast characteristic of the presence of fine precipitates. On the basis of similar characteristics of calorimetry and resistivity results, a sluggish ordering was presumed to exist in $Ni_2(Cr_{0.75}Mo_{0.25})$ also.

Further increase of Mo-content to $Ni_2(Cr_{0.63}Mo_{0.37})$ and $Ni_2(Cr_{0.5}Mo_{0.5})$ compositions resulted in the appearance of two distinct exothermic peaks during the 1st heating cycle (Fig. 5.8c). The maximum temperatures (675°C) experienced by samples was well above the dissolution start temperature (i.e., 640°C) of ordered phase in $Ni_2(Cr_{0.63}Mo_{0.37})$ and marginally below (i.e., 680°C) in $Ni_2(Cr_{0.5}Mo_{0.5})$ alloys (deduced on the basis of resistivity

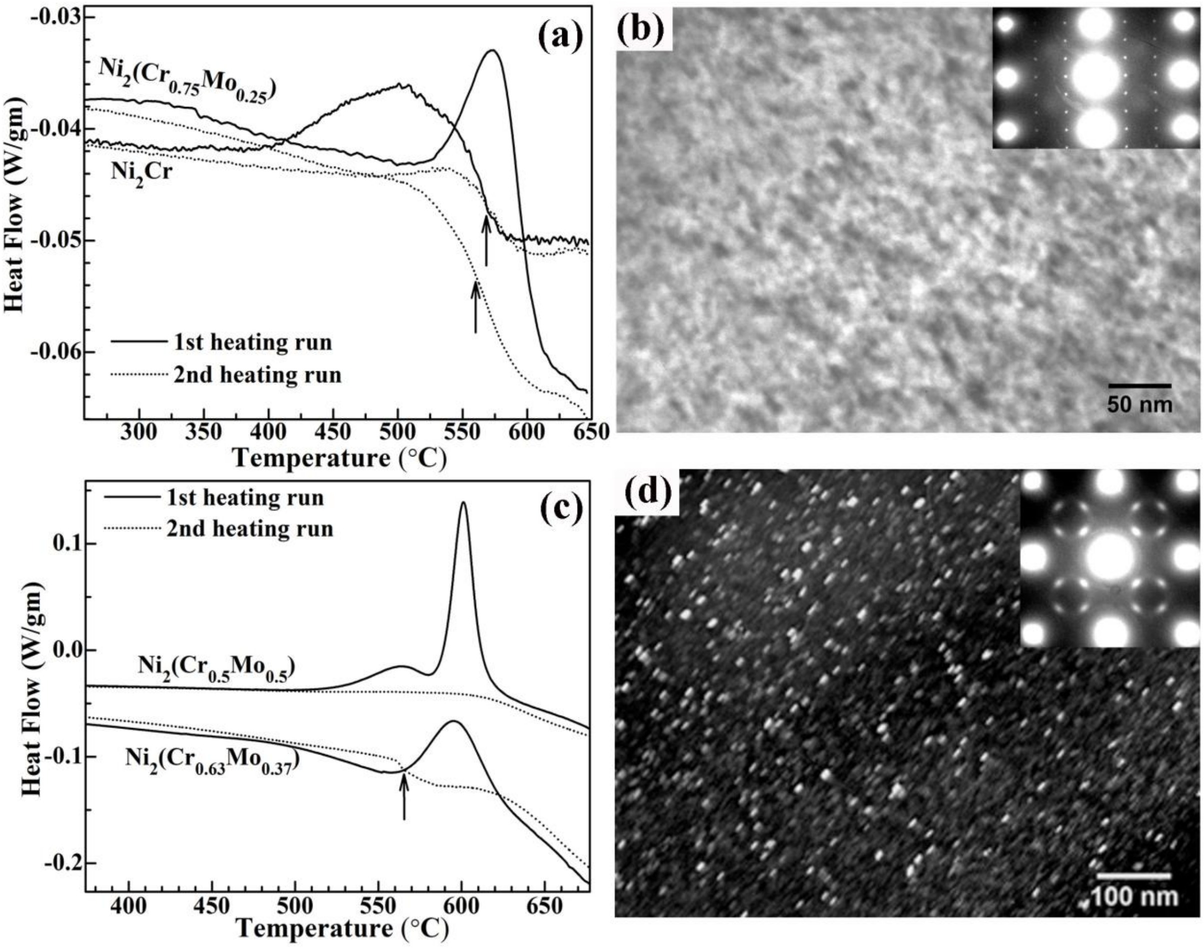

**Figure 5.8:** DSC thermograms of two consecutive heating cycles on: (a) $Ni_2Cr$ and $Ni_2(Cr_{0.75}Mo_{0.25})$ alloys revealing presence of exothermic peaks and baseline change; (c) $Ni_2(Cr_{0.63}Mo_{0.37})$ and $Ni_2(Cr_{0.5}Mo_{0.5})$ alloys revealing presence of two consecutive exothermic peaks and baseline change. TEM micrographs showing the presence of ordered $Ni_2(Cr,Mo)$ phase: (b) as mottled contrast in a BF image in $Ni_2Cr$ alloy after aging at 500°C for 500 h; and, (d) as particles in bright contrast in a DF image in $Ni_2(Cr_{0.5}Mo_{0.5})$ alloy after ageing at 525°C for 120 min. Corresponding SAED patterns in <1 1 2> and <0 0 1> zone axes, respectively, are shown as insets in respective micrographs.

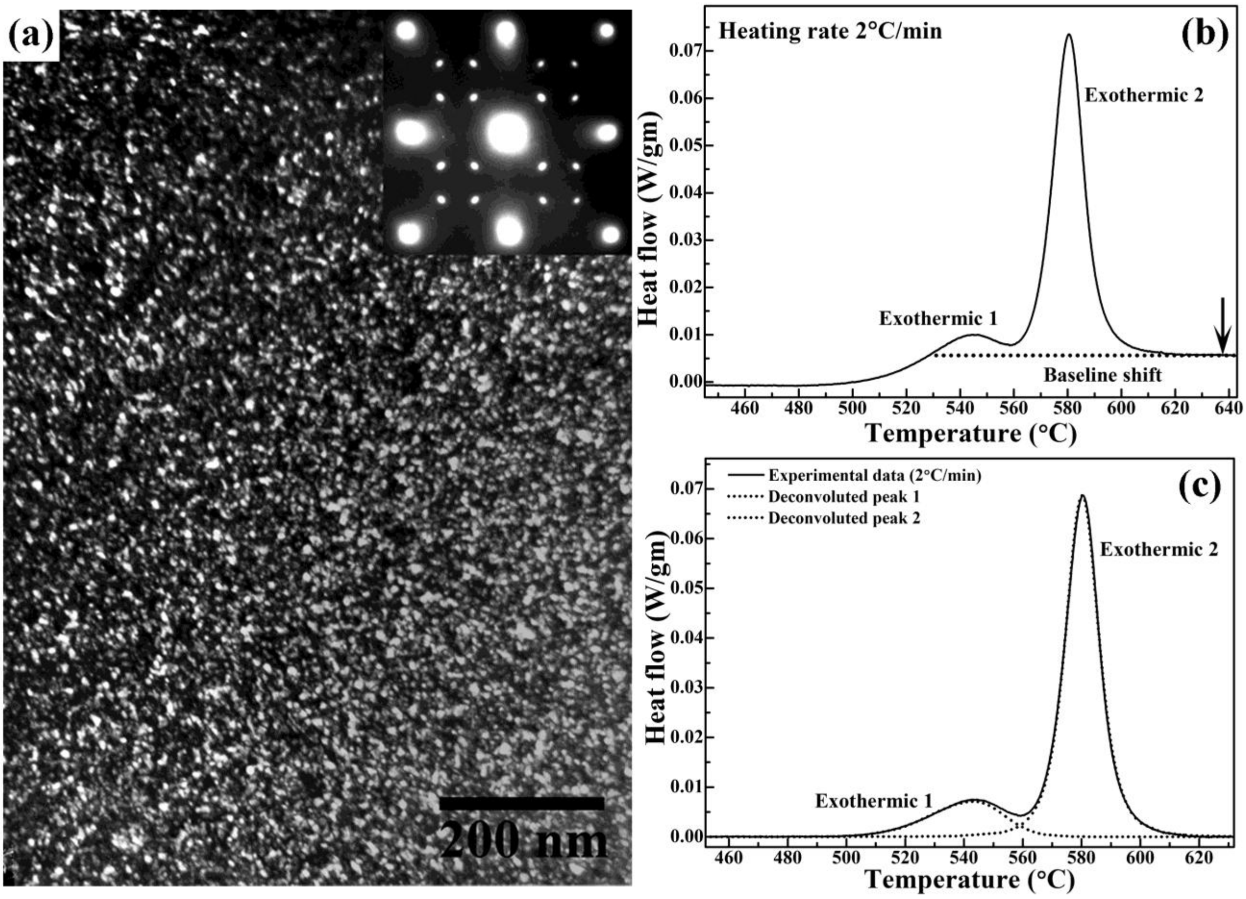

**Figure 5.9:** (a) DF-TEM micrograph of long range ordered phase showing the presence of well developed ordered domains in $Ni_2(Cr_{0.5}Mo_{0.5})$ alloy formed during heating at the end of 2nd exothermic peak in DSC (temperature marked by arrow in (b)). DSC thermograms of $Ni_2(Cr_{0.5}Mo_{0.5})$ alloy: (b) after baseline correction showing a baseline shift; (c) deconvoluted exothermic peaks obtained after removing baseline shift.

plots shown in fig. 5.2). This suggested a faster ordering kinetics in these alloys which was also confirmed by the formation of ordered domains within 2 h of ageing at 525°C in $Ni_2(Cr_{0.5}Mo_{0.5})$ alloy (Fig. 5.8d showing the presence of ordered domains in a DF micrograph). Both exothermic peaks appeared at higher temperatures in the $Ni_2(Cr_{0.5}Mo_{0.5})$ alloy than those in the $Ni_2(Cr_{0.63}Mo_{0.37})$ alloy. However, during the 2nd heating runs, both exothermic peaks disappeared in both the alloys. Further, in the $Ni_2(Cr_{0.63}Mo_{0.37})$ alloy, a shift in the baseline during the 2nd heating was observed at a temperature which corresponded to that of the endset temperature of the 1st exothermic peak during the 1st run (see fig. 5.8c drawn by broken line). This feature was seen at all heating rates employed. On the contrary, no such baseline shift was observed during the 2nd heating run on $Ni_2(Cr_{0.5}Mo_{0.5})$ alloys. This difference could be attributed to different initial microstructural states in the two alloys before the start of 2nd heating run. In the case of $Ni_2(Cr_{0.63}Mo_{0.37})$ alloy, temperature at the end of the 1stheating run (i.e., 675°C) was higher than the dissolution start temperatures of ordered phase (i.e. 640°C), which implied that ordered domains would have started dissolving by the end of the 1st run. The appeared baseline shift could thus be attributed to the formation of new ordered domains during the 2nd heating run. On the other hand in the $Ni_2(Cr_{0.5}Mo_{0.5})$ alloy, 675°C was below the dissolution start temperature (i.e., 680°C), no further ordering reaction could be observed, which was also supported by the absence of ordering events during the 2nd heating cycle (smooth thermogram) in fig. 5.8c. This was confirmed by the microscopic examination of $Ni_2(Cr_{0.5}Mo_{0.5})$ alloy interrupted after the finish of the 2nd exothermic peak which revealed the presence of well developed ordered domains (Fig. 5.9a). Thus the 2nd curve satisfied the criterion of perfect baseline only in $Ni_2(Cr_{0.5}Mo_{0.5})$ alloy. Subtracting this from the 1st heat flow curve revealed the existence of baseline shift after the 1st exothermic peak in this alloy also (Fig. 5.9b). Since a baseline shift after an exothermic peak could be associated to all the investigated $Ni_2(Cr_{1-x}Mo_x)$ alloys, it was logical to consider a 2nd order transformation as an intrinsic feature of ordering in Ni-Cr-Mo alloys. Deconvoluted peaks after removing baseline shift are shown in Fig. 5.9c, significance of each peak is discussed later in the following.

Isochronal DSC experiments clearly established the dependence of peak transformation temperatures on heating rates (Fig. 5.10), suggested of their kinetically driven nature. Activation energies associated with exothermic peaks were estimated using Kissinger [107, 108] and Augis-Bennett [109] methods. These methods were based on the hypothesis that the maximum transformation rate occurs at the peak temperature, $T_p$, such that $d^2X/dt^2 = 0$, where X = volume fraction of the transformed volume. The activation energy, Q, could then be

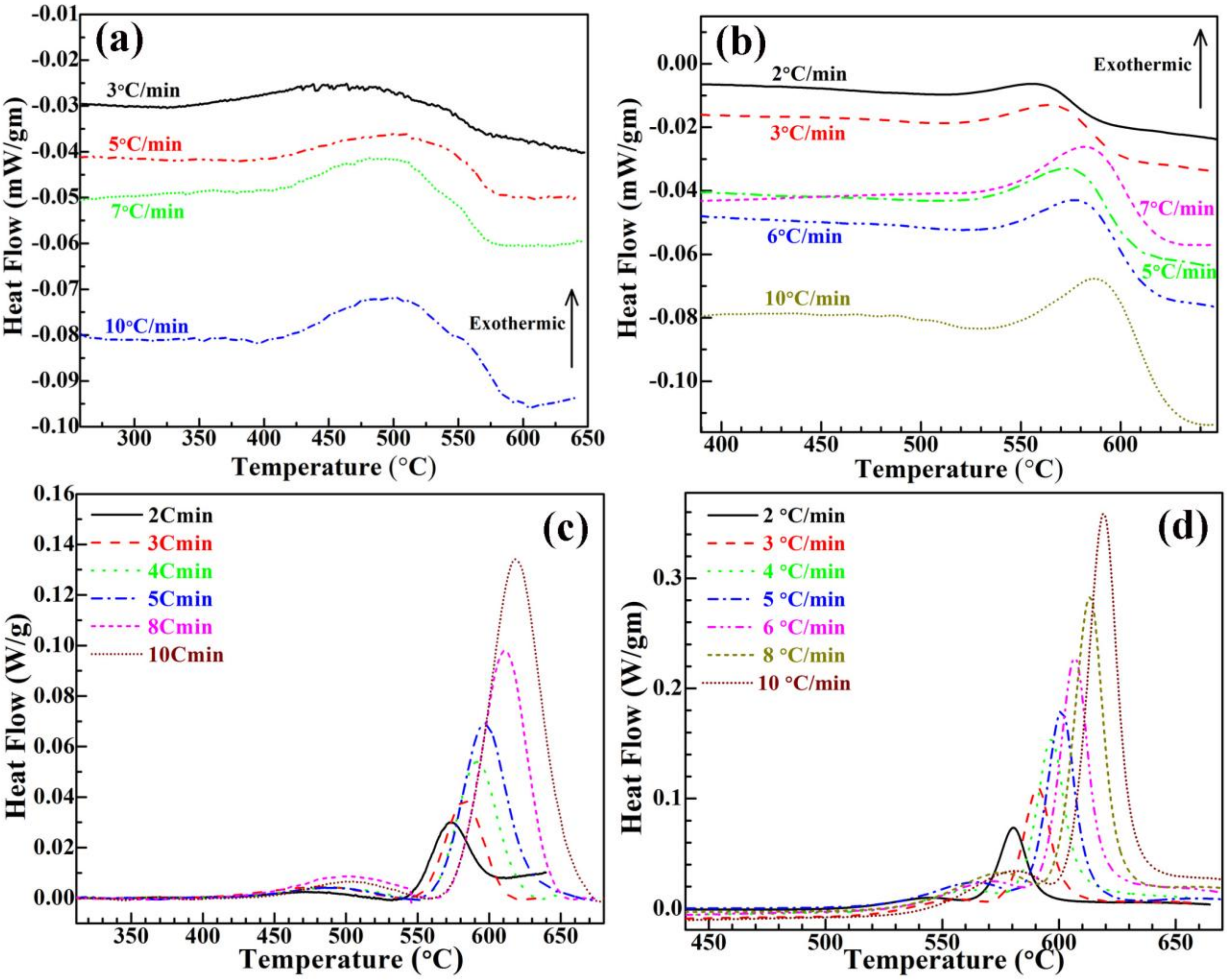

**Figure 5.10:** DSC thermograms obtained at different heating rates on (a) $Ni_2Cr$; (b) $Ni_2(Cr_{0.75}Mo_{0.25})$; (c) $Ni_2(Cr_{0.63}Mo_{0.37})$; and (d) $Ni_2(Cr_{0.5}Mo_{0.5})$ alloys. Note that the effect of baseline change was only removed for thermograms shown in figures (c) and (d).

calculated using the following expressions:

$$\frac{d(\ln[\beta/T_P^2])}{d(1/T_P)} = -\frac{Q}{R} \dots\dots \text{Kissinger} \dots\dots \quad (5.2)$$

$$\frac{d(\ln[\beta/(T_P - T_o)])}{d(1/T_P)} = -\frac{Q}{R} \dots\dots \text{Augis} - \text{Bennett} \dots\dots\dots \quad (5.3)$$

where, β is the heating rate, $T_o$ is ambient temperature and R is gas constant. From the slope of plots of $\ln[\beta/T_P^2]$ and $\ln[\beta/(T_P - T_o)]$ versus $1/T_P$ for different values of heating rates, value of the Q could be estimated.

Table 5.1 illustrates the effect of heating rates on characteristic temperatures, namely, $T_i$, $T_p$ and $T_f$, of exothermic peaks in $Ni_2(Cr_{0.75}Mo_{0.25})$ alloy and for the 1st peak in $Ni_2(Cr_{0.5}Mo_{0.5})$ alloy. Activation energies associated with these peaks were determined by the slope of a linear fit according to equations (5.2) and (5.3) (Fig. 5.11) and are tabulated in table 5.2. It was clear from table 5.2 that average activation energies for the 1st exothermic peak in $Ni_2(Cr_{0.75}Mo_{0.25})$ and $Ni_2(Cr_{0.63}Mo_{0.37})$ alloys were about 298 ± 15.8 kJ/mol and 295 ± 10.5 kJ/mol, respectively, which were almost similar. This implied that the processes responsible for formation of ordered phase in two alloys were same and remained unaffected by the increase of Mo-content. The increase of Mo-content to $Ni_2(Cr_{0.5}Mo_{0.5})$ composition, however, decreased its activation energy to about 247 ± 9.8 kJ/mol and increased the ordering kinetics as observed in fig. 5.8. On the contrary, the activation energy value associated with the 2nd exothermic peak increased from 206 ± 2.9 kJ/mol (in $Ni_2(Cr_{0.63}Mo_{0.37})$) to 255 ± 4.6 kJ/mol alloy in $Ni_2(Cr_{0.5}Mo_{0.5})$ alloy.

**Table 5.1:** Characteristic temperatures of exothermic peaks as a function of heating rate in $Ni_2(Cr_{0.75}Mo_{0.25})$ and $Ni_2(Cr_{0.5}Mo_{0.5})$ alloys.

| **Heating rate** | **$Ni_2(Cr_{0.75}Mo_{0.25})$** | | | **$Ni_2(Cr_{0.5}Mo_{0.5})$** | | |
|---|---|---|---|---|---|---|
| **(°C/min)** | **Start temp ($T_i$)** | **Peak temp ($T_p$)** | **Finish temp ($T_f$)** | **Start temp ($T_i$)** | **Peak temp ($T_p$)** | **Finish temp ($T_f$)** |
| 2 | 521.6 | 563.7 | 590.1 | 512.9 | 543.9 | 564.1 |
| 3 | 526.7 | 569.96 | 598.6 | 521.5 | 554.6 | 572.7 |
| 4 | - | - | - | 529.6 | 559.2 | 576.6 |
| 5 | 532.3 | 578.6 | 606.5 | - | - | - |
| 6 | 539.7 | 584.0 | 614.3 | 538.4 | 568.5 | 585.1 |
| 7 | 542.1 | 588.5 | 620.0 | 539.1 | 575.1 | 595.3 |
| 10 | 543.5 | 593.6 | 623.2 | 547.8 | 578.7 | 602.3 |

**Table 5.2:** Activation energy values obtained by two different approaches in $Ni_2(Cr_{1-x}Mo_x)$ alloys.

| **Methods** | **Activation energy in kJ/mol$^{-1}$** | | | | |
|---|---|---|---|---|---|
| | **$Ni_2(Cr_{0.75}Mo_{0.25})$** | **$Ni_2(Cr_{0.63}Mo_{0.37})$** | | **$Ni_2(Cr_{0.5}Mo_{0.5})$** | |
| | | **1st Peak** | **2nd Peak** | **1st Peak** | **2nd Peak** |
| **Kissinger** | 296.3 ± 15.8 | 293.5 ± 10.5 | 204.5 ± 2.8 | 247.5 ± 9.7 | 253.0 ± 4.6 |
| **Augis-Bennett** | 299.6 ± 15.8 | 295.7 ± 10.5 | 207.9 ± 2.9 | 245.5 ± 9.8 | 256.9 ± 4.6 |
| **Average** | 298 ± 15.8 | 294.6 ± 10.5 | 206.2 ± 2.9 | 246.5 ± 9.8 | 255.0 ± 4.6 |

## 5.4. Microstructural Characterization:

### 5.4.1. $Ni_2(Cr_{0.5}Mo_{0.5})$ alloys:

Owing to faster ordering kinetics of $Ni_2(Cr_{0.5}Mo_{0.5})$ alloys, a detailed study of microstructural changes occurring during isothermal ageing treatments were employed on this alloy to understand the mechanisms of ordering.

**Ageing at 525°C and 625°C:**

The order evolution was mapped by ageing at these temperatures for different periods of time. Electron diffraction of aged samples revealed a gradual decrease of intensity at {1 ½ 0} positions with concurrent increase at 1/3{2 2 0} and 1/3{1 1 3} positions (see fig. 5.12). The time at which distinct LRO reflections appeared was considered to be the onset of the formation of LRO. Ageing time between 60 min to 120 min was required for distinct appearance of the LRO at 525°C, while it appeared within 3 min at 625°C. This suggested of accelerated ordering transformation at 625°C compared with that at 525°C. Variations in the normalized intensity of 1/3{2 2 0} superlattice reflections with ageing time was used to understand kinetics behaviour of order evolution at 625°C. It is clear from fig. 5.12i that the intensity of superlattice reflections increased sharply up to about 30 min followed by a

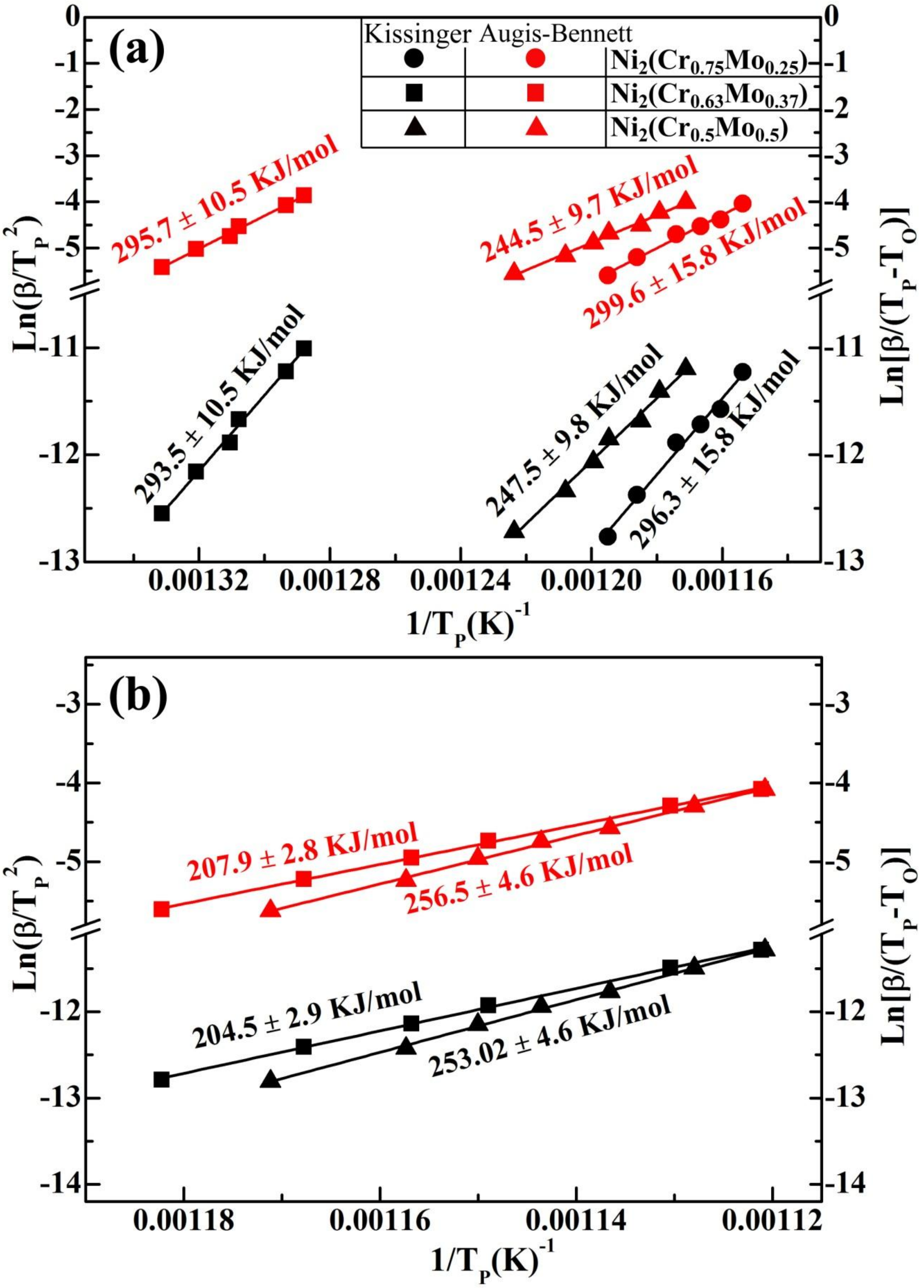

**Figure 5.11:** Activation energy analysis using Kissinger [107, 108] and Augis-Bennett [109] methods of exothermic peaks obtained on $Ni_2(Cr_{0.75}Mo_{0.25})$, $Ni_2(Cr_{0.63}Mo_{0.37})$ and $Ni_2(Cr_{0.5}Mo_{0.5})$ alloys corresponding to: (a) 1st exothermic peak and (b) 2nd exothermic peak.

gradual increase suggesting of an approaching intensity plateau. Intensity of superlattice reflections, in general, would be a function of: (i) volume fraction, (ii) order parameter of ordered domains; and (iii) atomic scattering factors. In the present case, since the same alloy after different ageing times was investigated, difference due to atomic scattering factors could be ignored. Further, the order parameter could be assumed to be nearly one as the alloy started exhibiting intense superlattice reflections within 5 min (Fig. 5.12f). It was, therefore, reasonable to presume that the superlattice reflection intensity was mainly governed by the volume fraction of ordered domains. A sharp increase in the intensity up to 30 min (Fig. 5.12i), thus, indicated that volume fraction of ordered domains increased sharply in this period beyond which it grew marginally. This was indirectly confirmed by measuring ordered domain sizes from DF images. Fig. 5.13a shows DF images of ordered particles obtained with superlattice reflections of two perpendicular ordered variants, marked by a circle in SAED, after ageing at 625°C for different time periods. Ordered domain sizes were measured using the freeware ImageJ software [110]. Fig. 5.13b shows the plot of domain sizes obtained after ageing treatment for different times. This plot confirmed a marginal increase of precipitates sizes from about 2.3 ± 0.5 nm to 3.2 ± 1.0 nm from ageing time of 60 min to 180 min. Thus, it could be concluded that the formation and growth of new domains dominated the ordering process up to about 30 minutes of ageing.

A sluggish ordering kinetics at 525°C could also be confirmed by microscopic investigation of prolonged aged (1070 h) $Ni_2(Cr_{0.5}Mo_{0.5})$ alloy. This ageing treatment induced few nanometer sized ordered domains in the matrix as can be seen in fig. 5.14. It has been mentioned earlier in Chapter 2 that ordered $Ni_2(Cr,Mo)$ phase forms with six orientation variants, each one of which have equal probability to precipitate in the alloy. This tendency was confirmed on an investigated alloy by mapping all variants of ordered domains (Fig. 5.14) using superlattice reflection in [013], [001] and [103] zone axes in the sampling area.

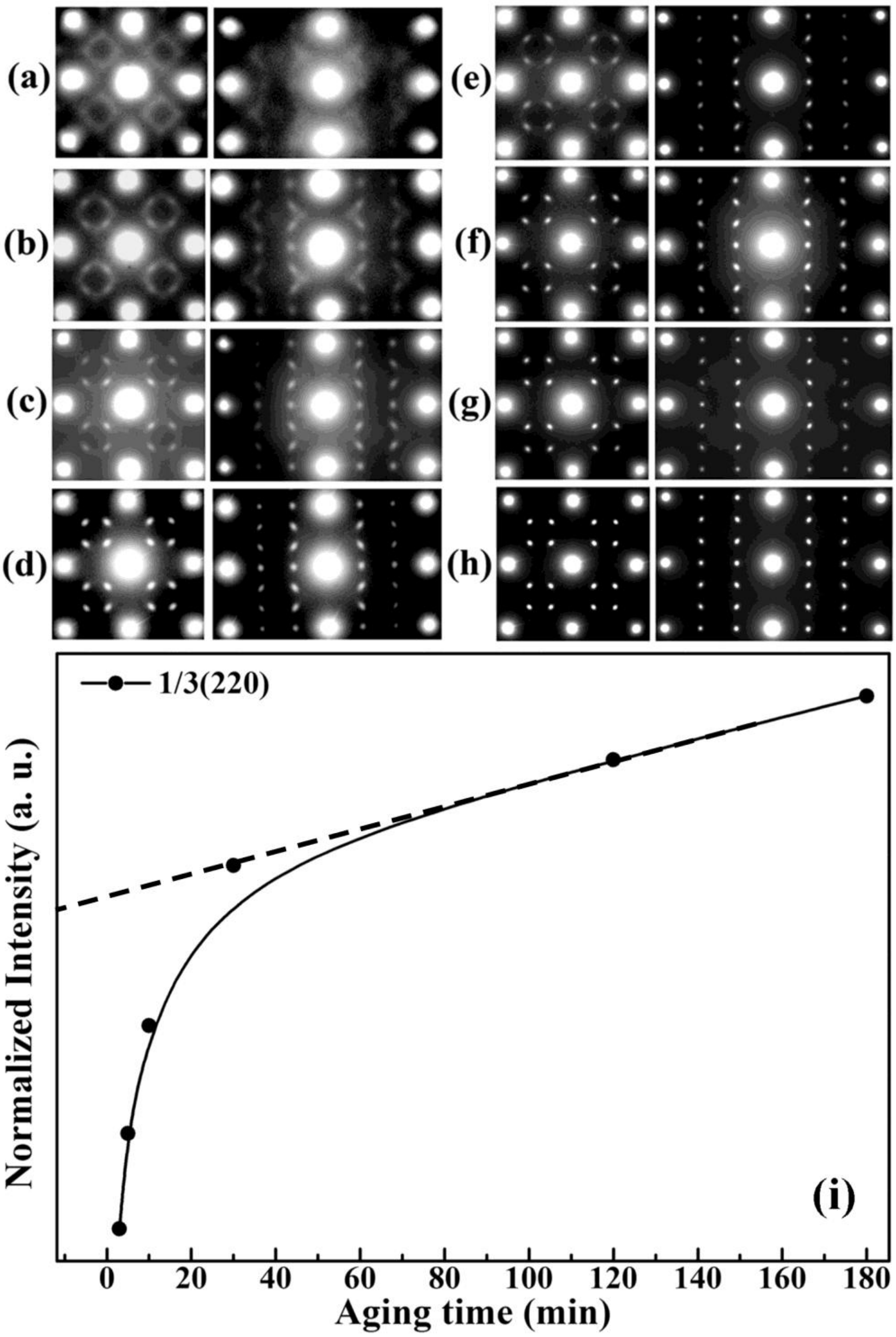

**Figure 5.12:** SAED patterns with <0 0 1> and <1 1 2> zone axes from $Ni_2(Cr_{0.5}Mo_{0.5})$ alloy after ageing for: (a) 30 min, (b) 60 min, (c) 120 min and (d) 180 min at 525°C; and, (e) 3 min, (f) 5 min, (g) 10 min, and (h) 30 min at 625°C. Fig. 5.12i shows the variation of superlattice intensity with aging time at 625°C normalized with respect to transmitted beam (see text for details). The intensity increased sharply up-to 30 min followed by a gradual increase. The broken line depicts extrapolated intensity variation expected at lower ageing times.

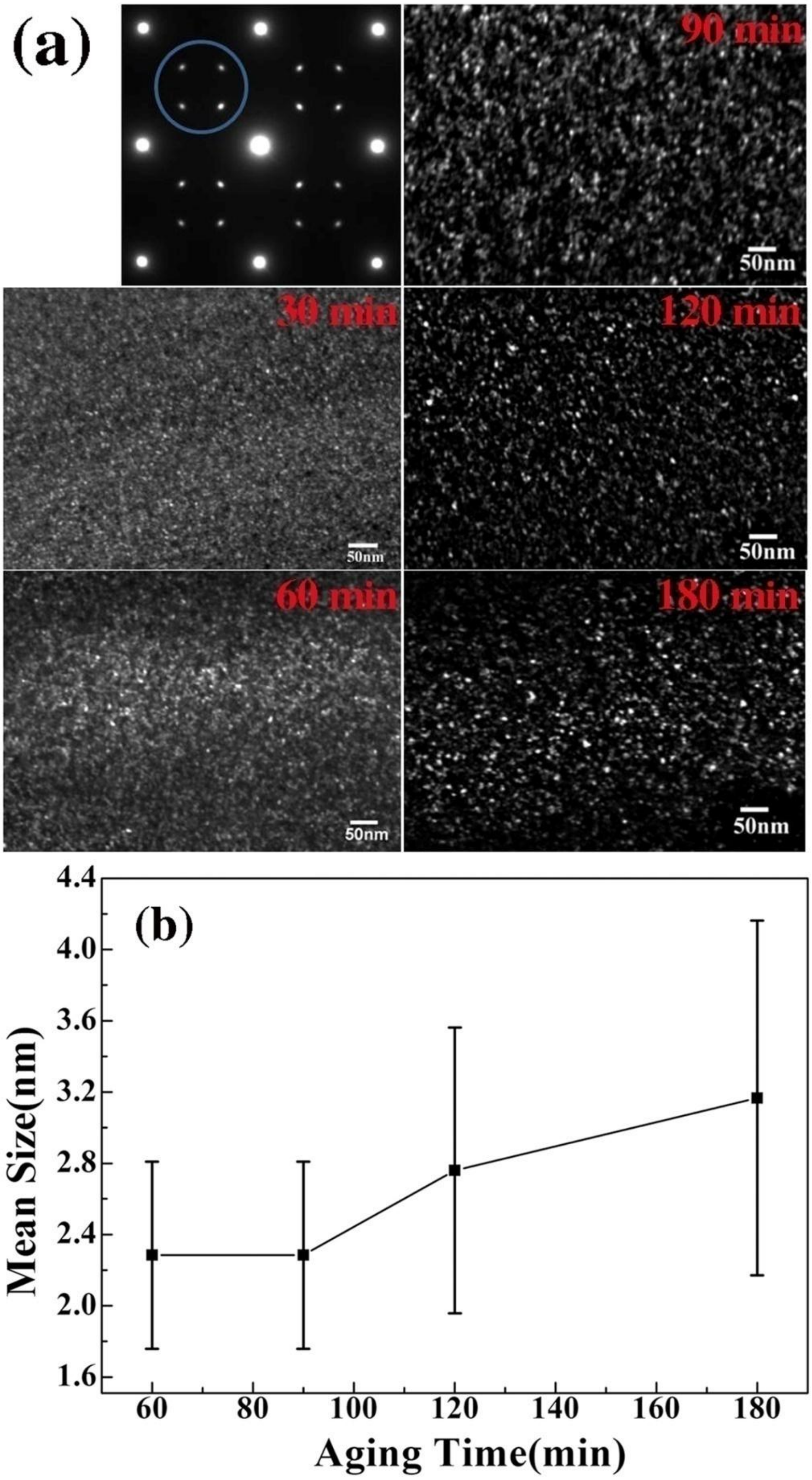

**Figure 5.13:** (a) DF-TEM micrographs showing the presence of fine LRO domains in $Ni_2(Cr_{0.5}Mo_{0.5})$ alloy aged for different periods of time at 625 °C. (b) a plot of particles size obtained using the ImageJ freeware software [110] showing a marginal increase in their sizes during ageing. The error bars correspond to standard deviation of data points.

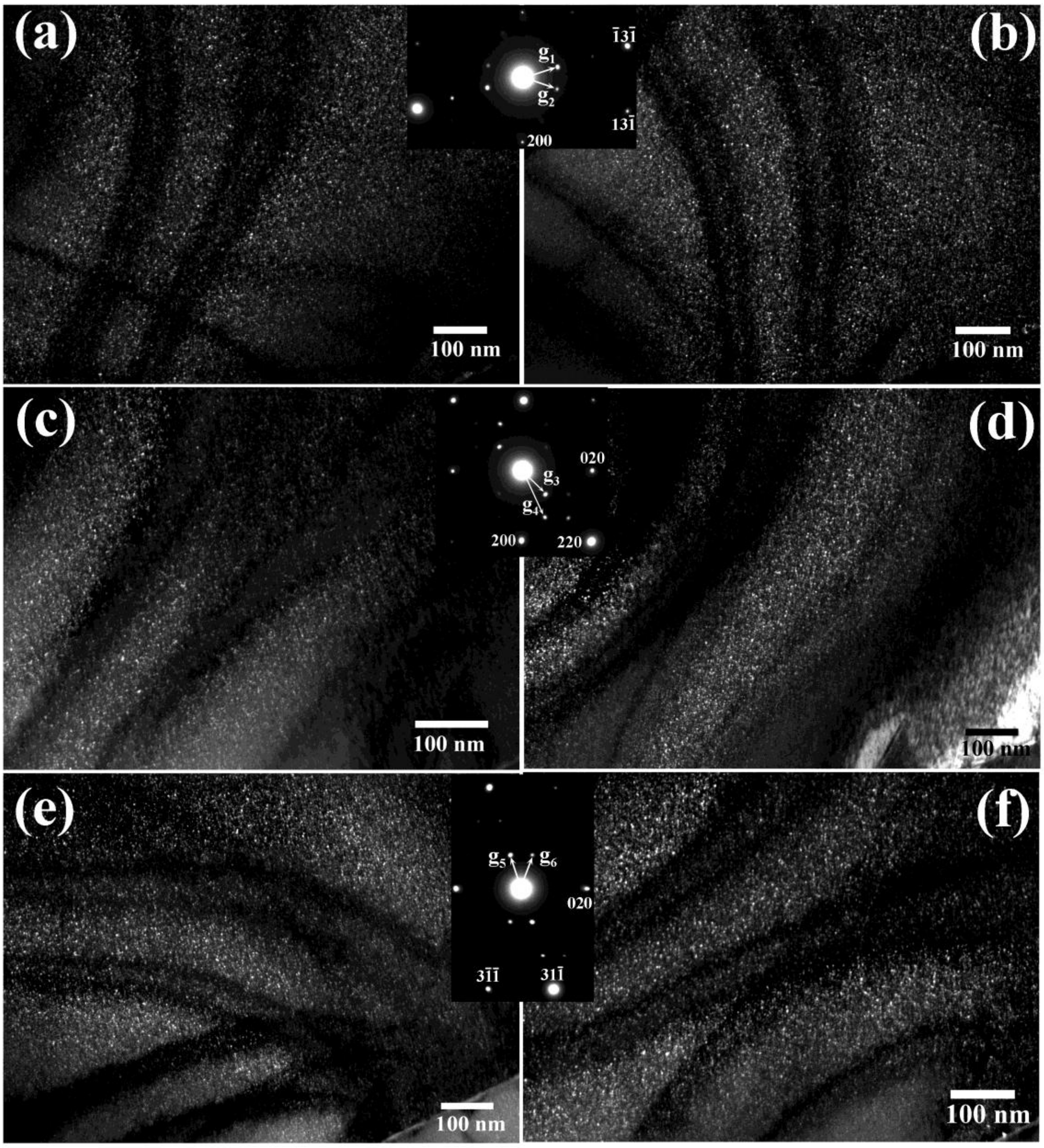

**Figure 5.14:** DF-TEM micrographs showing all six variants of the ordered $Ni_2(Cr,Mo)$ phase imaged with different superlattice reflections marked by respective g-vectors. (a) and (b) corresponded to $g_1$ and $g_2$ vectors in [0 1 3] zone axis; (c) and (d) corresponded to $g_3$ and $g_4$ vectors in [0 0 1] zone axis; (e) and (f) corresponded to $g_5$ and $g_6$ vectors in [1 0 3] zone axis.

### Ageing at 680°C:

In order to understand the effect of higher ageing temperature on ordering kinetics, $Ni_2(Cr_{0.5}Mo_{0.5})$ alloys were aged at 680°C for different times of 5 h, 20 h and 100 h. Microscopic examination of these alloys revealed comparatively larger domains than those observed at lower ageing temperature. At this temperature even a smaller ageing time of 5 h was sufficient to develop domains of about 25-30 nm sizes and their sizes grew further after 20 h of ageing as could be seen in fig. 5.15. A further increase of ageing to 100 h had almost completely transformed the matrix into ordered domains and their sizes were found to peak at about 50 nm (Fig. 5.16). Their sizes were calculated by determining major and minor axes of an ellipse fitted to the particles imaged in DF-TEM using *ImageJ* software, assuming ellipsoidal disk shape morphology of the ordered $Ni_2(Cr,Mo)$ domains as found by Kumar and Vasudevan [39]. Figs. 5.17a and b shows a DF-TEM image of the ordered domains and outlines of particles corresponding to DF-TEM image obtained after fitting ellipsoidal shape to domains, respectively. Particle sizes were found by size-frequency histograms of major and minor axes of ellipsoidal particles. It was found that their size distribution was best represented by lognormal distribution having peak value at about 46.3 nm and 30.3 nm for major and minor axes, respectively (Figs. 5.17c and 5.17d).

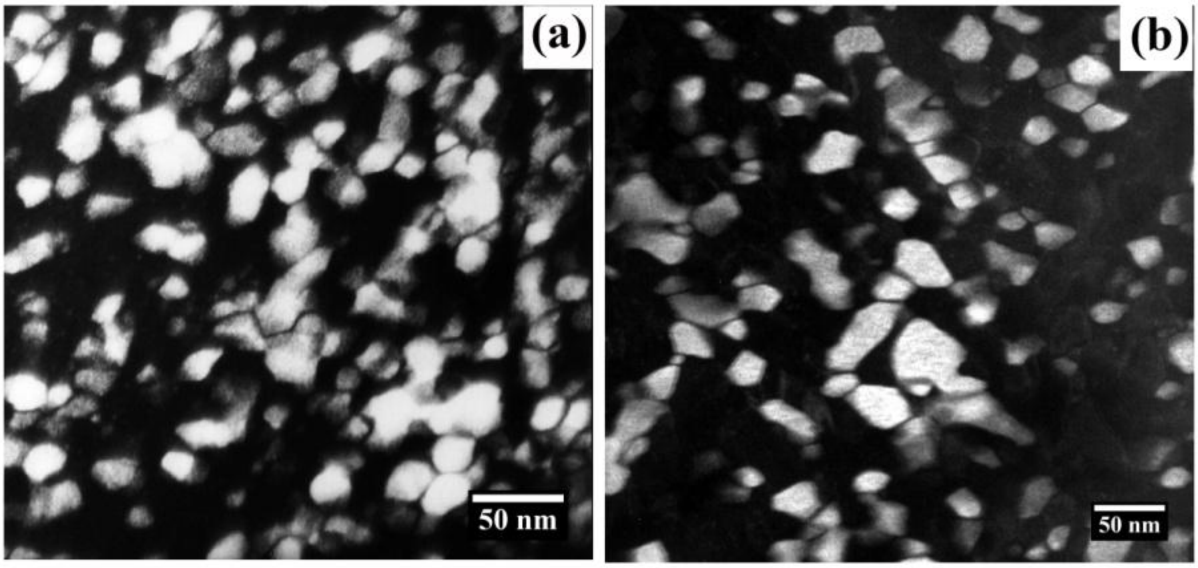

**Figure 5.15:** DF-TEM micrographs showing one variant of the ordered domains imaged with superlattice reflection in <0 0 1> zone axis in $Ni_2(Cr_{0.5}Mo_{0.5})$ alloy aged at 680°C for (a) 5 h; and (b) 20 h.

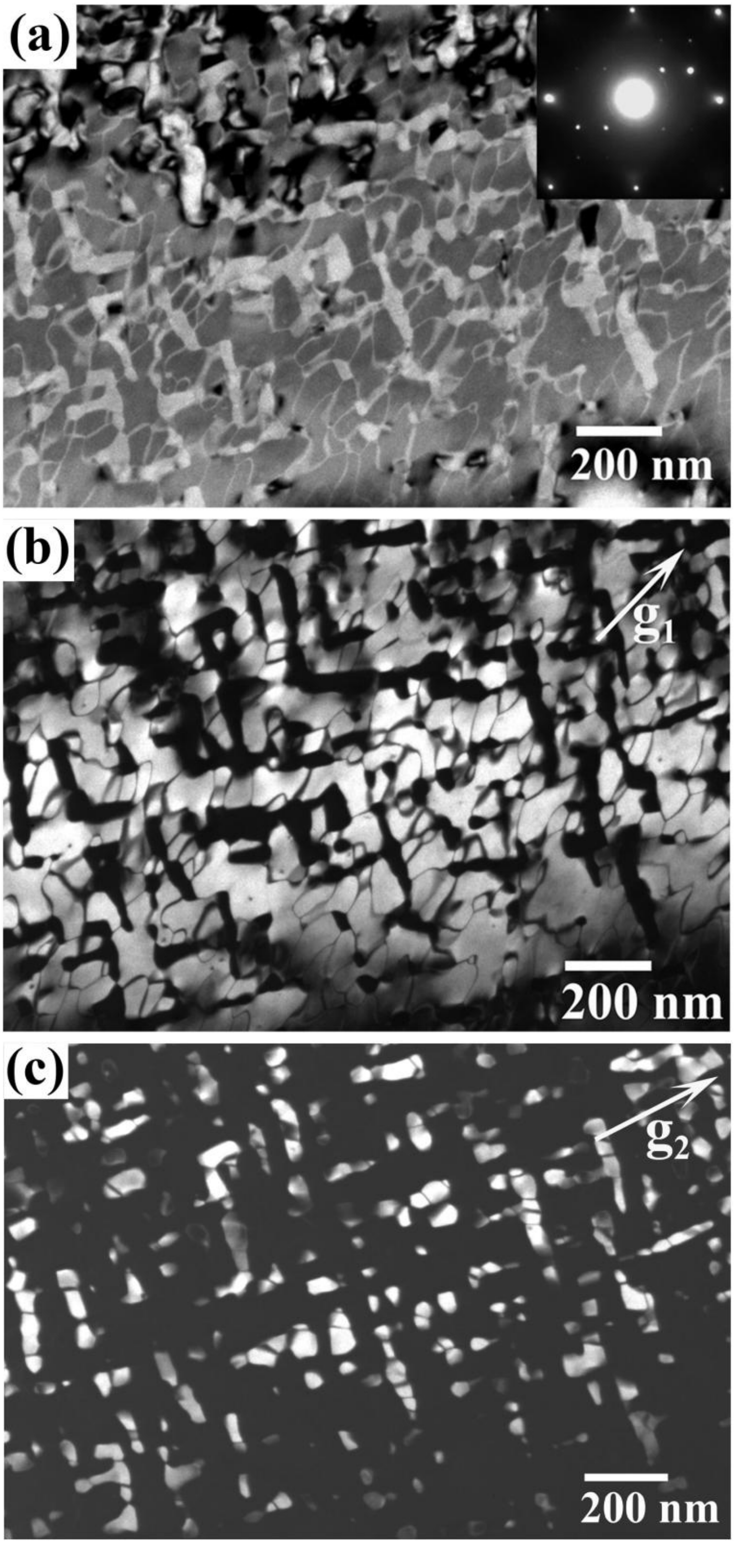

**Figure 5.16:** TEM micrographs showing ordered domains in $Ni_2(Cr_{0.5}Mo_{0.5})$ alloy aged at 680°C for 100 h imaged in different modes; (a) BF image obtained in <0 0 1> direction and corresponding SAED pattern in the inset; (b) DF image with one variant of ordered domain imaged with $g_1$-vector; (c) DF image with one variant of ordered domain imaged with $g_2$-vector.

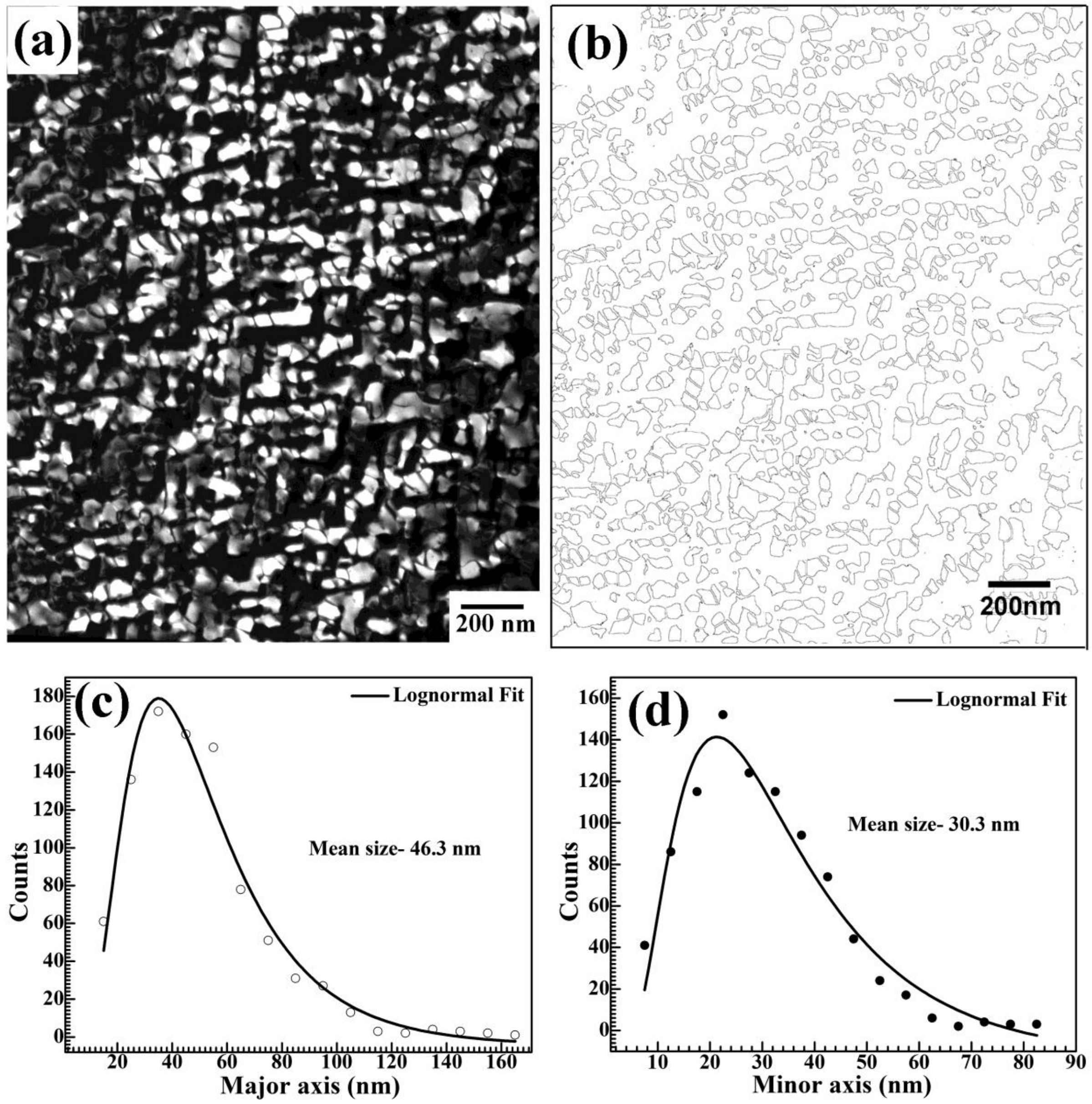

**Figure 5.17:** (a) DF-TEM micrograph showing ordered domains in $Ni_2(Cr_{0.5}Mo_{0.5})$ alloy aged at 680°C for 100 h; (b) processed image showing outlines of the precipitates corresponding to image (a) for particle size analysis in ImageJ. Lognormal fit to the particles size distribution obtained by fitting ellipsoidal shape to: (c) major axis; (d) minor axis.

### **Ageing at 750°C and 760°C:**

Ageing of $Ni_2(Cr_{0.5}Mo_{0.5})$ alloys at 750°C for 30 min produced sharp superlattice reflections of the ordered $Ni_2(Cr,Mo)$ phase (see SAED pattern in fig. 5.18a). DF-TEM images taken with these superlattice reflections confirmed the existence of well developed ordered domains of ellipsoidal shape in the matrix (Fig. 5.18a). On the contrary, superlattice reflections were absent in this alloy aged at 760°C for 30 min. However, this ageing treatment produced a microstructural state that exhibited diffuse diffraction intensity pattern quite similar to that observed in the solution treated and water quenched state. The presence of SRO was also evident by mottled contrast in BF image (Fig. 5.18b). However, this was surprising as ageing temperature of 760°C was below the critical order-disorder temperature ($T_C$ = 775°C) of this alloy. The absence / presence of ordered phase at 760°C / 750°C suggested that a minimum undercooling of about 25°C below the critical order-disorder temperature was necessary for the formation of ordered phase in this alloy. This undercooling effect was due to the positive contribution of coherency free energy of the ordered phase to the overall free energy [111].

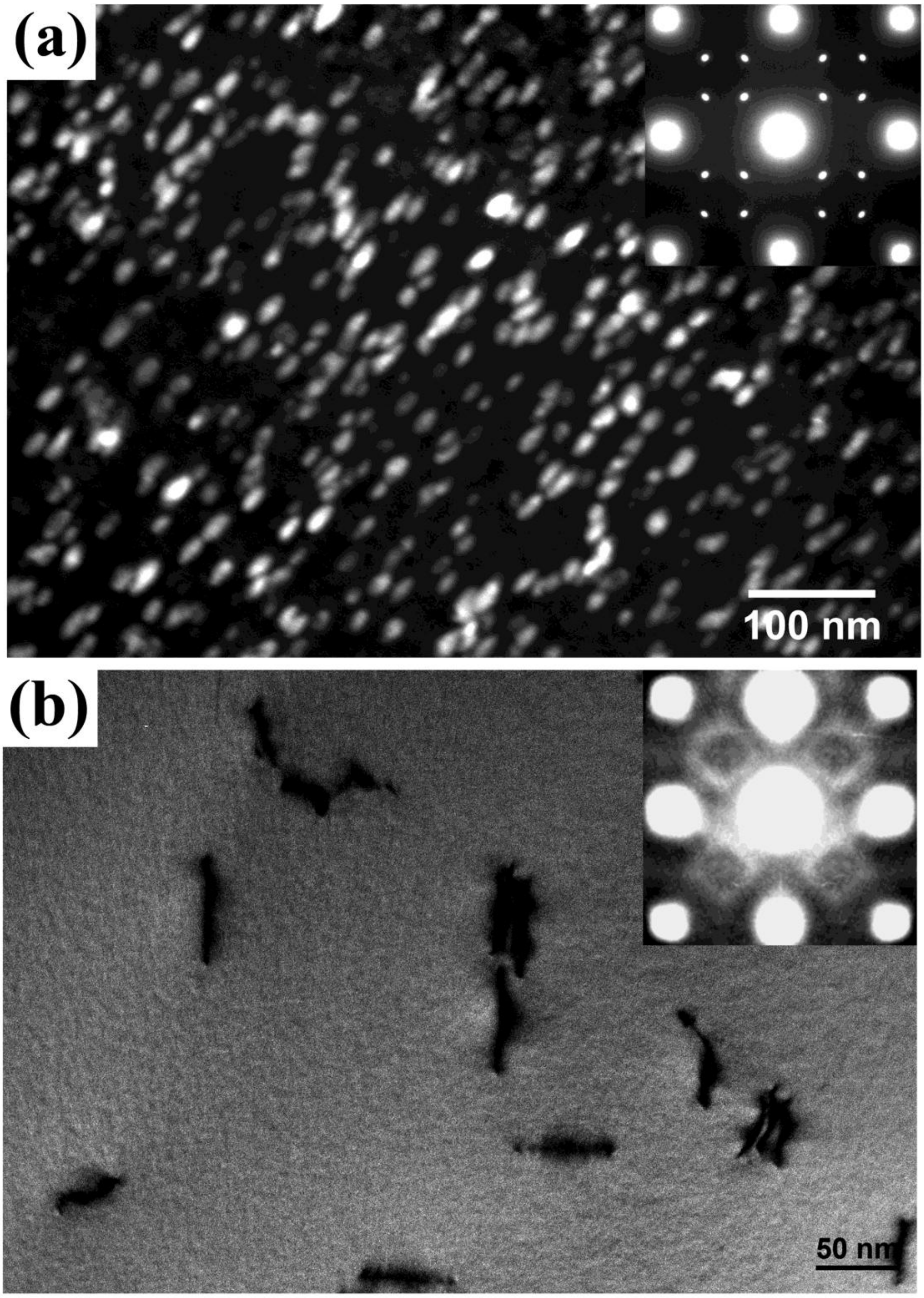

**Figure 5.18:** TEM micrographs of a $Ni_2(Cr_{0.5}Mo_{0.5})$ alloy and the corresponding SAED pattern along <0 0 1> zone axis in the inset after ageing at: (a) 750 °C / 10 min, DF micrograph revealing presence of well developed ordered domains; and (b) 760 °C / 30 min, a BF micrograph showing the presence of only SRO, no long-range order is visible.

### 5.4.2. $Ni_2(Cr_{0.63}Mo_{0.37})$ alloys:

Samples of $Ni_2(Cr_{0.63}Mo_{0.37})$ alloys were used to investigate microstructural changes at ageing temperatures of 525°C , 680°C, 695°C and 715°C and to compare them with those in $Ni_2(Cr_{0.5}Mo_{0.5})$ alloys.

**Ageing at 525°C:**

The ageing treatment at 525°C for 1070 h produced a high number density of few nano-meter sized ordered domains in the matrix as shown in fig. 5.19. DF-TEM micrographs of two perpendicular ordered variants imaged with superlattice reflections in <0 0 1> zone axis confirmed their nearly equal probability of the formation (Fig. 5.19). A microstructural comparison of this alloy with that developed in $Ni_2(Cr_{0.5}Mo_{0.5})$ alloy after same ageing treatment revealed a nearly similar microstructure state in both the alloys. On the basis of it nearly similar ordering kinetics at 525°C was suggested in both $Ni_2(Cr_{0.63}Mo_{0.37})$ and $Ni_2(Cr_{0.5}Mo_{0.5})$ alloys.

**Ageing at 680°C:**

The ageing treatment at 680°C for 100 h produced almost fully transformed ordered matrix. This was concluded on the basis of ordered domains imaged with superlattice reflections of two perpendicular ordered variants in <0 0 1> zone axis of SAED pattern (Fig. 5.20). This ageing treatment produced microstructure characterized by well defined ellipsoidal shape ordered domains (see fig. 5.20). The sizes of ordered domains were determined by adopting a methodology earlier used in Section 5.4.1 for $Ni_2(Cr_{0.5}Mo_{0.5})$ alloy. Fig. 5.21a and b shows a DF-TEM image of the ordered domains and outlines of particles corresponding to DF-TEM image obtained after fitting ellipsoidal shape to domains, respectively. In this case also, particle size distribution was found by size-frequency histogram of major and minor axes of ellipsoidal particles. It was found that their size distribution was best represented by a lognormal distribution for the major axis of the ellipse having a peak value at 23.9 nm and a normal distribution for minor axis having peak value at 11.8 nm (5.21c and 5.21d).

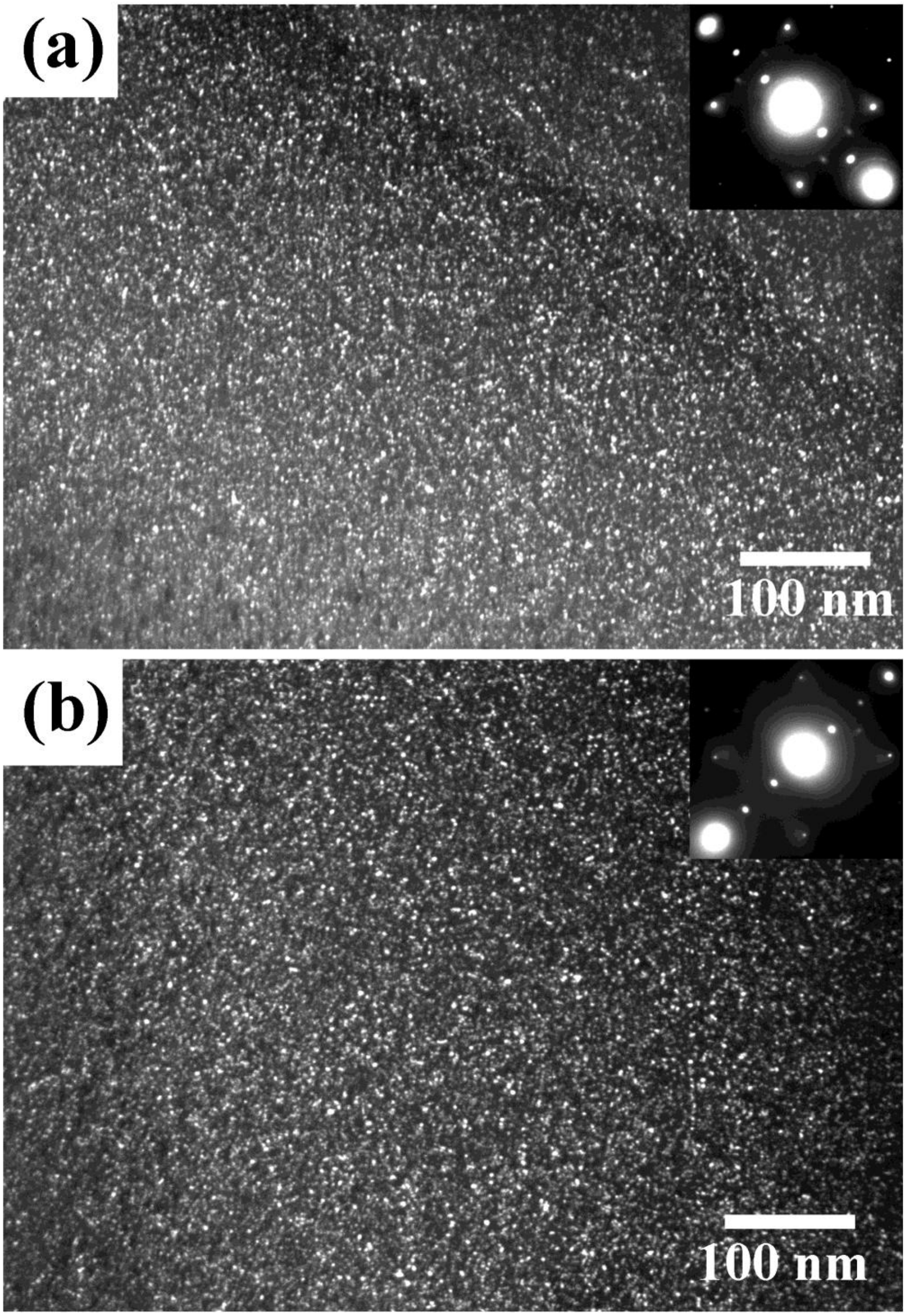

**Figure 5.19:** DF-TEM micrographs showing two variants of ordered $Ni_2(Cr,Mo)$ domains formed in $Ni_2(Cr_{0.63}Mo_{0.37})$ alloy during ageing at 525°C for 1070 h. The ordered domains were imaged with excited superlattice reflections in the <0 0 1> SAED patterns shown as insets in respective DF images.

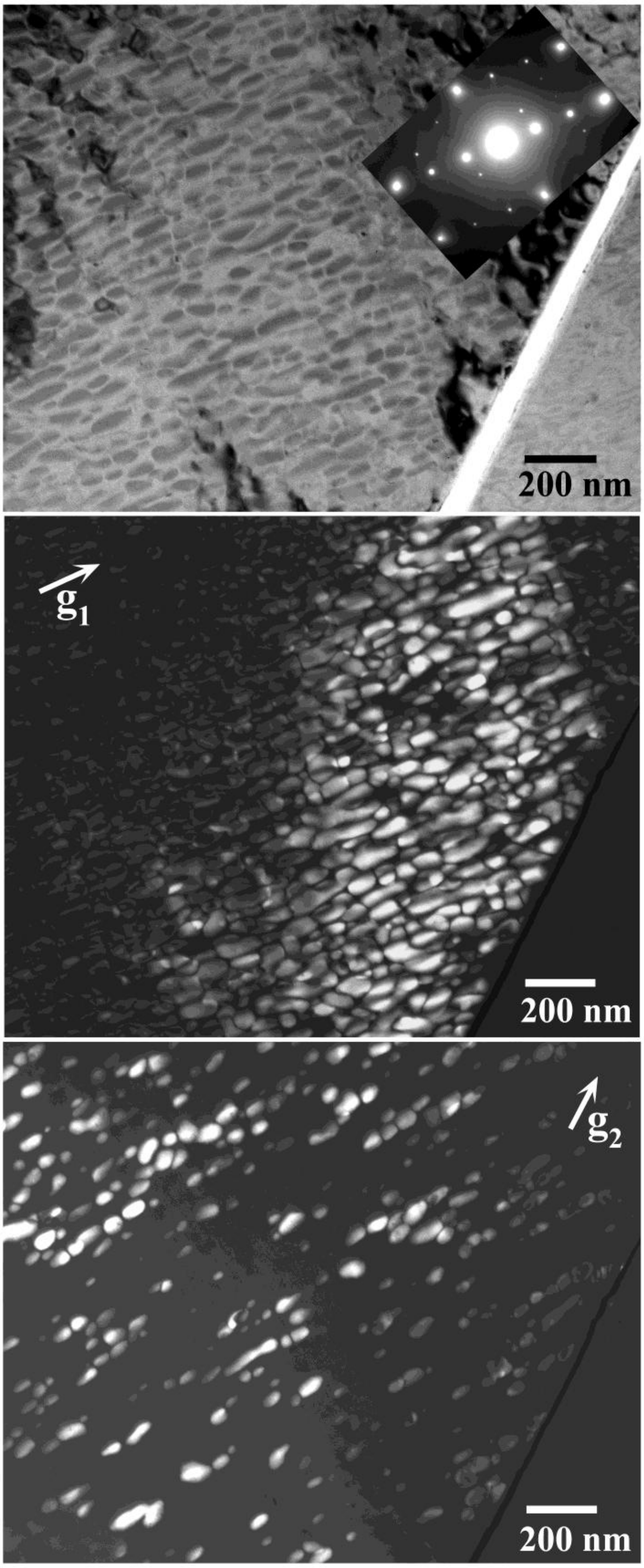

**Figure 5.20:** TEM micrographs showing ordered domains in $Ni_2(Cr_{0.63}Mo_{0.37})$ alloy aged at 680°C for 100 h imaged in different modes; (a) BF image obtained in <0 1 3> direction and corresponding SAED pattern in the inset; (b) DF image with one variant of ordered domain imaged with $g_1$-vector; (c) DF image with one variant of ordered domain imaged with $g_2$-vector.

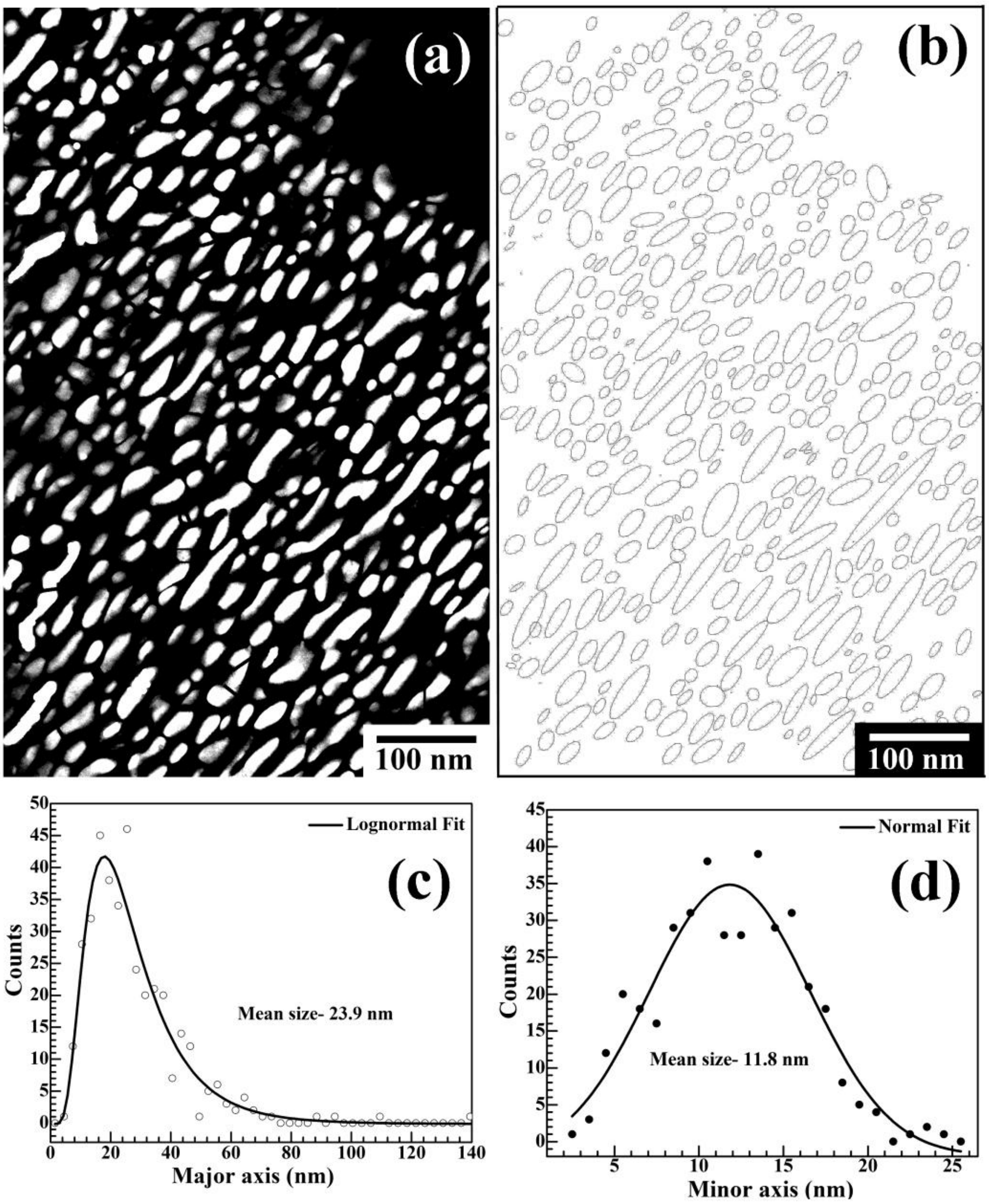

**Figure 5.21:** (a) DF-TEM micrograph showing ordered domains in $Ni_2(Cr_{0.63}Mo_{0.37})$ alloy aged at 680°C for 100 h; (b) processed image showing outlines of the precipitates corresponding to image (a) for particle size analysis in ImageJ. Lognormal and normal fit to the particles size distribution obtained by fitting ellipsoidal shape to: (c) major axis; (d) minor axis.

### Ageing at 695°C and 715°C:

It has been earlier mentioned in Section 5.2 that critical order-disorder temperature ($T_C$) of the $Ni_2(Cr_{0.63}Mo_{0.37})$ alloy is 720°C. Ageing at a temperatures difference of about 5°C and 25°C below $T_C$ were selected to study the effect of ageing temperatures on the tendency of

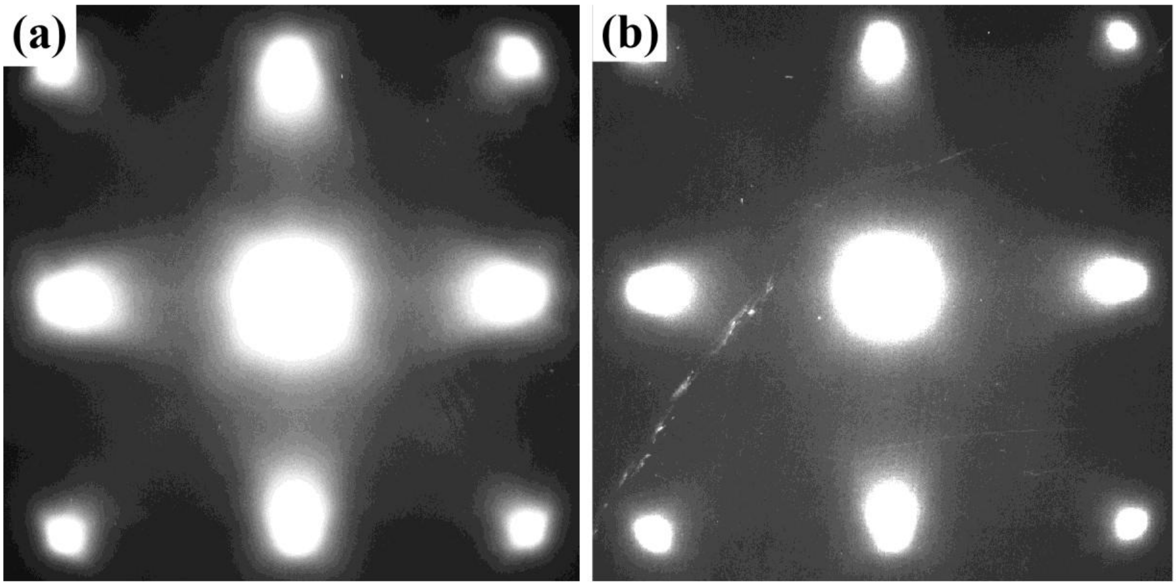

**Figure 5.22:** SAED patterns in <0 0 1> zone axis obtained with $Ni_2(Cr_{0.63}Mo_{0.37})$ alloy aged at; (a) 695°C for 30 min; and (b) 715°C for 30 min. The absence of superlattice reflections confirmed absence of LRO in both the states.

the formation of the LRO phase. Samples of $Ni_2(Cr_{0.63}Mo_{0.37})$ alloy were aged at 695°C and 715°C for about 30 min. Microscopic investigations revealed absence of superlattice reflections of the LRO phase in both the cases (Fig. 5.22). The absence of LRO at 695°C confirmed that undercooling of 25°C was insufficient to form the ordered phase in the alloy. However, presence of ordered domains at 680°C, which was 40°C below the $T_C$, revealed that this much of undercooling was necessary for the formation of ordered phase in this alloy.

## 5.5. Discussion:

On the basis of results presented above, it could be suggested that $Ni_2(Cr_{1-x},Mo_x)$ alloys undergo ordering transformation via a continuous mode through the {1 ½ 0} SRO state. The order developed with a gradual increase of 1/3{2 2 0} SRO at the expense of {1 ½ 0} SRO until the formation of LRO. Likewise, at temperatures above the critical ordering temperature, the LRO phase transformed into disordered phase through an intermediate SRO. Increase of Mo in these alloys affected ordering kinetics as evidenced by accelerated ordering kinetics in $Ni_2(Cr_{0.63},Mo_{0.37})$ and $Ni_2(Cr_{0.5},Mo_{0.5})$ alloys. Further, increase of $T_C$ of the

$Ni_2(Cr,Mo)$ phase with increasing Mo concentration suggested a shift of phase fields of the ordered phase. This behaviour could be explained more lucidly on the basis of stability of different phase fields encountered by alloy during order evolution.

During order evolution, alloys encountered three phase fields, namely, ordered phase (LRO), SRO and crystalline disordered phase as depicted schematically in fig. 5.23. These phase fields were separated by phase boundaries. That a phase boundary, as shown by broken lines, separating the crystalline disordered phase from SRO exists was concluded on the basis of attainment of complete disorder in splat-quenched state (shown earlier in Chapter 4). The SRO region was separated from the LRO by an "*equilibrium phase boundary*", which represented the limit above/below which the ordered phase must dissolve / form. However, due to coherency strain of the ordered phase, this limit would suppress to temperatures below the equilibrium phase boundary and is called "*coherent phase boundary*" [111]. The coherent phase boundary necessitates the requirement of undercooling for the formation of ordered phase. Below this boundary ordered phase would form via a nucleation and growth mode. At still lower temperatures continuous ordering would override the nucleation and growth process due to the build-up of concentration waves of large amplitudes, which become unbound at the instability limit [80]. This limit is called "*coherent instability boundary*" [53]. Below this boundary the order phase would evolve by a continuous ordering mechanism.

The kinetics of ordering transformation in different phase fields would be dependent upon the thermal history (shown in Chapter 6) as well as composition of alloys, as they would decide the kinetics of transformation mechanisms. Usually, annealing at temperatures below the coherent instability boundary would grow 1/3{2 2 0} SRO until the formation of the LRO after a certain incubation period. This period would decrease with increase of Mo content as well as with the ageing temperature. For instance, annealing of $Ni_2Cr$ alloy for 500

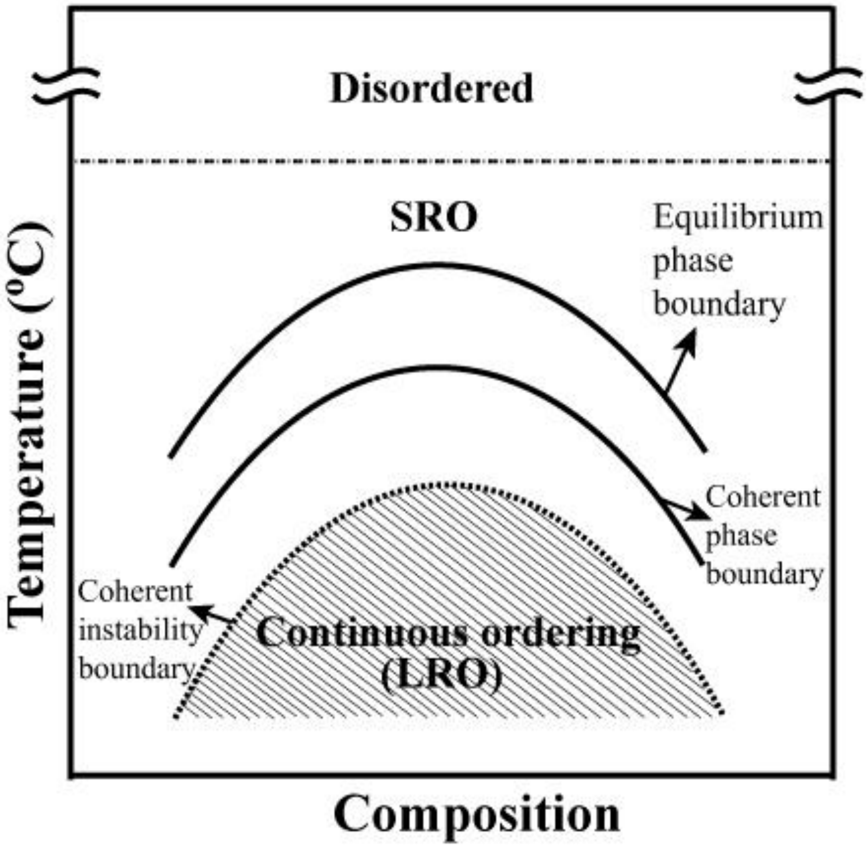

**Figure 5.23:** Schematic representation of different phase fields encountered by alloys during order evolution.

h at 500 °C produced very fine ordered domains which could not be resolved in a BF image (Fig. 5.8b). On the other hand, in $Ni_2(Cr_{0.5},Mo_{0.5})$ alloys, nanometer size ordered domains appeared within 2 h of ageing at 525°C (Fig. 5.8d) and the incubation time reduced further (up to few minutes) at higher ageing temperatures (Fig. 5.12e). Due to large incubation times associated with the formation of LRO in $Ni_2Cr$ and $Ni_2(Cr_{0.75},Mo_{0.25})$ alloys [12], the 1/3{2 2 0} SRO remained in a metastable state during isochronal heating, while smaller incubation times in $Ni_2(Cr_{0.63},Mo_{0.37})$ and $Ni_2(Cr_{0.5},Mo_{0.5})$ alloys allowed the formation of LRO. Apparently different ordering kinetics in category I and category II alloys could, therefore, be attributed to the dominance of different mechanisms in alloys containing varying Mo-content which has been discussed in the following.

### 5.5.1. Mechanisms of ordering transformations:

In $Ni_2Cr$ and $Ni_2(Cr_{0.75},Mo_{0.25})$ alloys, SRO to LRO transformation did not complete during isochronal heating and alloys remained predominantly in the 1/3{2 2 0} SRO state up to $T_C$. Earlier studies have established that the $T_C$ in the $Ni_2Cr$ alloy is 572 ± 5°C [12] above which SRO exists up to 650°C [102]. This confirmed that the resistivity maximum which appeared at 571°C in $Ni_2Cr$ alloy (Fig. 5.2a) corresponded to its $T_C$ and a decrease of resistivity beyond it could be attributed to the formation of {1 ½ 0} SRO. For temperatures, $T < T_C$, the existing {1 ½ 0} SRO exhibited a tendency to transform into LRO via the evolution of 1/3{2 2 0} SRO by a mechanism involving atomic rearrangements as evidenced by appearance of an exothermic peak in temperature regime II (see fig. 5.24a). Likewise, atomic rearrangements could be associated with the evolution of 1/3{2 2 0} SRO in $Ni_2(Cr_{0.75}Mo_{0.25})$ alloy, though the addition of Mo shifted $T_C$ to a higher value (620°C), suggesting of increased stability of the ordered $Ni_2(Cr,Mo)$ phase with Mo addition. The 1/3{2 2 0} SRO evolved via a 1st order continuous mode as confirmed by the appearance of exothermic peak in the region II of figs. 5.24a and b. For temperatures, $T > T_C$, {1 ½ 0} SRO could be suggested to form by a 2nd order transformation mode which was argued on the basis of the baseline shift at the end of exothermic peaks (Fig. 5.24a and b), which coincided with the temperature exhibiting resistivity maxima (i.e., at $T = T_C$). During isochronal heating, due to the sluggish ordering kinetics, the SRO (either 1/3{2 2 0} or {1 ½ 0}) had barely reached its maximum attainable value which caused the appearance of baseline shift at $T_C$ in consecutive heating cycles. This was independently confirmed by the calorimetric experiment of a sample aged at 585°C (marginally above $T_C$) for 50 h, which was devoid of any baseline shift in the entire temperature range (see inset of fig. 5.24a). The absence of baseline shift in the aged alloy where the {1 ½ 0} SRO was allowed to reach its maximum value, thus, confirmed that the formation of {1 ½ 0} SRO in the solution treated samples could have occurred via a 2nd order

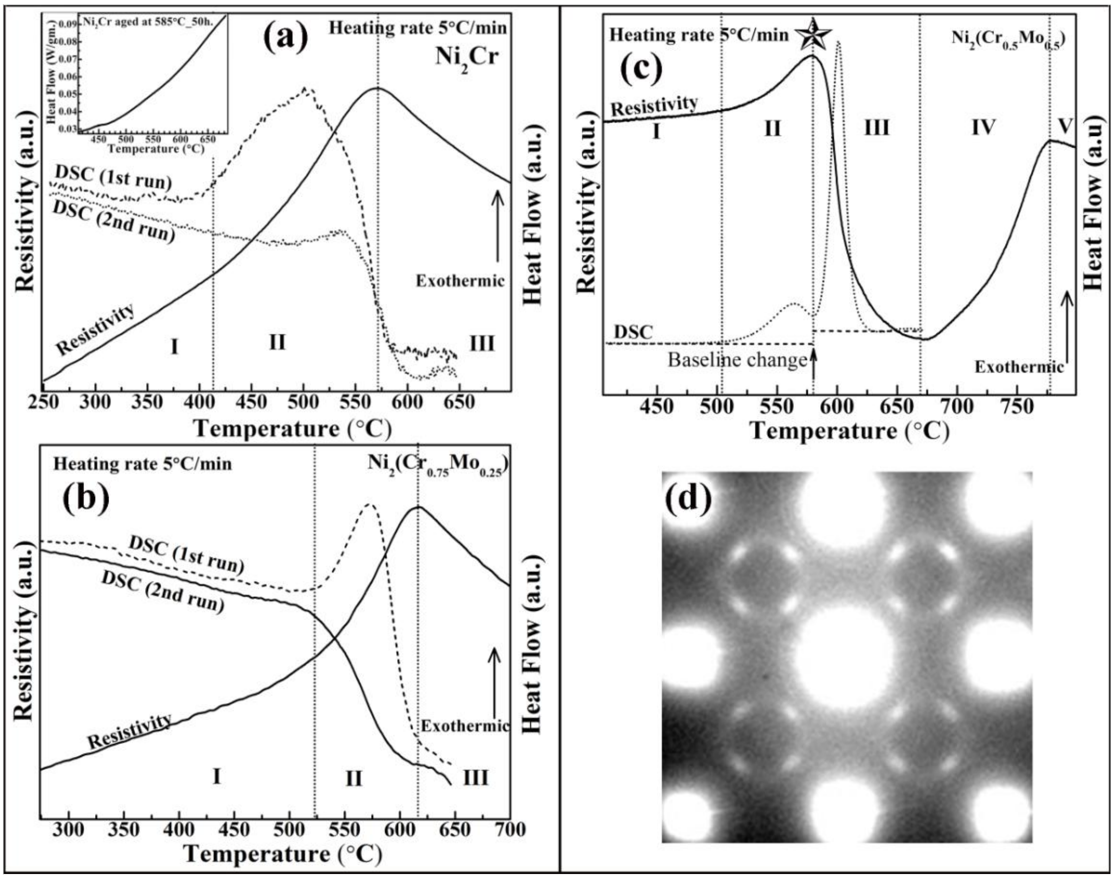

**Figure 5.24:** (a) to (c) Superimposed resistivity and DSC plots obtained during heating of: (a) $Ni_2Cr$; (b) $Ni_2(Cr_{0.75}Mo_{0.25})$ and (c) $Ni_2(Cr_{0.5}Mo_{0.5})$ alloys. In all cases baseline shift appeared at a temperature corresponding to the resistivity maxima separating regime II from III (shown by a dotted line). The inset in (a) shows the suppression of baseline change in a $Ni_2Cr$ alloy aged at 585 °C for 50 h (see text for details). (d) a <001> zone axes SAED pattern of the $Ni_2(Cr_{0.5}Mo_{0.5})$ alloy, arrested at a temperature marked by a star in (c) during heating, showing distinct LRO reflections and near extinction of SRO intensity.

transformation mode. Symmetry considerations of the {1 ½ 0} SRO structure also supported its formation by a 2nd order transformation mode, since $N_2M_2$ structure responsible for the appearance of {1 ½ 0} SRO [13, 112, 113] satisfies all the three Landau-Lifshitz-symmetry rules of a 2nd order transformation [13, 80].

A similar ordering tendency was observed in $Ni_2(Cr_{0.63},Mo_{0.37})$ and $Ni_2(Cr_{0.5},Mo_{0.5})$ alloys for $T < T_C$, though the 1/3{2 2 0} SRO could transform into LRO due to faster ordering kinetics in these alloys (see Fig. 5.24c for $Ni_2(Cr_{0.5},Mo_{0.5})$ alloy). This was confirmed by the presence of sharp 1/3{2 2 0} reflections and near extinction of {1 ½ 0} reflections in electron diffraction patterns of samples arrested at the end of 1st exothermic peak (Fig. 5.24d). Similar to category I alloys, for $T < T_C$, growth of the 1/3{2 2 0} SRO occurred via a 1st order continuous mode as evidenced by the appearance of an exothermic peak in temperature regime II in fig. 5.24c. However, the 1/3{2 2 0} SRO to LRO transformation involved a 2nd order mode as evidenced by a baseline shift immediately after the finish of 1st exothermic peak (see temperature regime II in fig. 5.24c). This analysis, thus, confirmed that the temperature at a baseline shift (marked by an arrow in fig. 5.24c) corresponded to the formation of LRO which occurred initially via the evolution of 1/3 {2 2 0} SRO involving a 1st order mechanism (continuous ordering) followed by a 2nd order mode during later stages of transformation pertaining to the elimination of {1 ½ 0} SRO. Thus, combined use of resistivity and DSC experiments confirmed the involvement of a 2nd order transformation mode during the completion of continuous ordering reaction. The operation of a 2nd order transformation mode could also be explained on the basis of static concentration waves (SCW's) model usually employed to explain the origin of {1 ½ 0} SRO in these alloys [13]. It has been shown earlier in Section 4.3 that $N_2M_2$-type SCWs responsible for the appearance of {1 ½ 0} SRO inherently contain atomic stacking of $N_2M$-type necessary to create the ordered $Ni_2(Cr,Mo)$ phase. The inherent presence of $N_2M$ stacking in $N_2M_2$ type SCWs resulted in the evolution of 1/3{2 2 0} SRO concomitantly with {1 ½ 0} SRO. However, evolution of 1/3{2 2 0} SRO continued till the $N_2M_2$ SCWs remained stable and the $N_2M$-structure reached a critical size to generate nuclei of the $Ni_2(Cr,Mo)$ phase. This was possible as no off-stoichiometric $N_2M_2$ structure would be stable at lower temperatures and it would undergo secondary ordering to generate stoichiometric ordered structure [114].

The accelerated ordering kinetics in these alloys also favoured the easy growth of ordered domains as evidenced by strong exothermic peak coinciding with sharp resistivity fall in regime III (Fig. 5.24c). The sharp resistivity fall has been known to occur during the growth of LRO domains as shown earlier in Section 5.2 and the presence of exothermic peak confirmed it to occur via a 1st order transformation mode. Above this stage, LRO domains started to dissolve as evidenced by sharp resistivity increase in regime IV. However, their dissolution did not transform the alloy into a disordered state as construed on the basis of slow resistivity decrease in regime V (Fig. 5.24c), which would have otherwise increased in a disordered state. In fact, dissolution of the LRO occurred in conjunction with the formation of {1 ½ 0} SRO as demonstrated earlier (see fig. 5.3). Thus the temperature separating regime IV from V represented the dissolution temperature of the LRO phase in alloys pertaining to category II. Similar to category I alloys, formation of the {1 ½ 0} SRO in regime V during the dissolution of LRO would also involve a 2nd order transformation mode. An independent high temperature DSC study on a $Ni_2(Cr_{0.5}Mo_{0.5})$ alloy confirmed it by the appearance of baseline shift immediately after the dissolution peak (endothermic peak) of ordered phase (as shown in fig. 5.25). Thus, both 1st order and 2nd order reactions could be suggested to contribute during the dissolution of ordered phase in category II alloys.

### 5.5.2. Effect of Mo addition on ordered phase boundaries:

The dissolution temperature of the ordered phase is reported to increase from 571 °C in $Ni_2Cr$ alloy to 672 °C in $Ni_2(Cr_{0.75}Mo_{0.25})$ alloy [14]. A further increase of dissolution temperature from 720 °C in $Ni_2(Cr_{0.63}Mo_{0.37})$ to 775°C in $Ni_2(Cr_{0.5}Mo_{0.5})$ alloys (see fig. 5.6) established an increased stability of the ordered phase with increase of Mo. This increased stability could be attributed to increased hybridization strength of d-d orbitals with increase in Mo content in these alloys, which has been demonstrated in a recent theoretical study [65]. Increase of Mo-contents in $Ni_2(Cr_{1-x}Mo_x)$ alloys could also affect the coherent phase boundary of the ordered phase provided coherency free energy change by this effect. Coherent phase boundary is a characteristic feature caused by the positive contribution of coherency free energy to the total

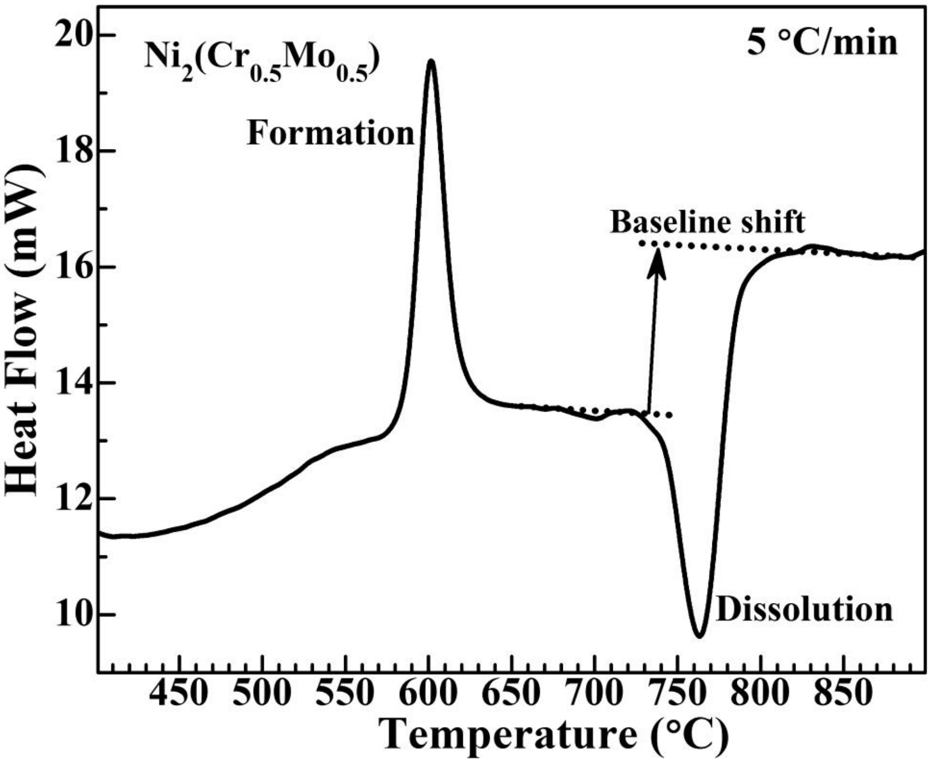

**Figure 5.25:** DSC thermogram of solution treated and water quenched $Ni_2(Cr_{0.5}Mo_{0.5})$ alloy revealing presence of exothermic peak (formation of ordered phase) and endothermic peak corresponding to the dissolution of ordered phase during isochronal heating. A baseline shift at the end of the dissolution peak is marked by arrow in the figure.

free energy and signifies the requirement of a certain amount of undercooling below an equilibrium phase boundary for the nucleation process [111]. According to Karmazin et al. [12, 14], an undercooling of about 37°C below the equilibrium phase boundary is necessary for the formation of ordered phase in binary Ni-Cr and ternary Ni-Cr-Mo alloys having varying amount of Ni and Cr for a fixed Cr/Mo ratio of 3. However, the present work suggested an undercooling of about 25°C in $Ni_2(Cr_{0.5}Mo_{0.5})$ alloy as evidenced by the presence / absence of LRO at 750°C / 760°C (Fig. 5.18). Therefore, it was not unreasonable to conclude that replacement of Cr by Mo in $Ni_2(Cr_{0.5}Mo_{0.5})$ alloy reduced the necessary undercooling for the formation of LRO. In other words, it could be construed that the replacement of about half of Cr by Mo atoms in $Ni_2(Cr_{0.5}Mo_{0.5})$ alloy brought the coherent phase boundary more closer to the equilibrium phase boundary than that in $Ni_2Cr$ and

$Ni_2(Cr_{0.75}Mo_{0.25})$ alloys. For ordering transformations, the coherency free energy varies as $E\times\eta^2$, where E, is elastics modulus, and η is order parameter [57]. The elastic modulus is a measure of bond strength between atomic species which can change with the change of Mo amount in $Ni_2(Cr_{1-x}Mo_x)$ alloys. A recent study by Hu et al. [65] has established that elastic modulus of $Ni_2Cr$ increases with Mo addition up to $Ni_2(Cr_{0.75}Mo_{0.25})$, while reported a decrease in $Ni_2(Cr_{0.5}Mo_{0.5})$ alloy. This difference has been attributed to partial change in the nature of atomic bonding from covalent character in alloys up to $Ni_2(Cr_{0.75}Mo_{0.25})$ compositions to metallic type in $Ni_2(Cr_{0.5}Mo_{0.5})$ alloy. Hu et al. [65] attributed this change to the disappearance of the band gap at the Fermi level of free electron density of states. The observed linear increase of hardness from $Ni_2Cr$ to $Ni_2(Cr_{0.63}Mo_{0.37})$ alloy and a decrease beyond it (Fig. 5.1) was consistent with this change in the nature of atomic bonding from covalent to metallic type. This decrease in the elastic modulus, in turn, lowered the elastic free energy contribution, which manifested in shifting the coherent phase boundary closer to equilibrium phase boundary in $Ni_2(Cr_{0.5}Mo_{0.5})$ alloy. Since the hardness continued to increase linearly up to the $Ni_2(Cr_{0.63}Mo_{0.37})$ composition, it could be argued that the covalent nature of bonding dominated up to this composition. Thus, it was not unreasonable to assume the existence of coherent phase boundary at a temperature about 37°C below the equilibrium phase boundary in $Ni_2(Cr_{0.63}Mo_{0.37})$ alloy.

Based upon above evidences, order evolution in $Ni_2(Cr_{1-x}Mo_x)$ alloys can be summarized as depicted schematically in fig. 5.26. It could be seen from fig. 5.26 that the equilibrium phase boundary moved in a non-linear manner to higher temperatures with increased amount of Mo in these alloys. The coherent phase boundary also exhibited a similar trend with a temperature offset of about 37 °C up to $Ni_2(Cr_{0.63}Mo_{0.37})$ alloy, which reduced to 25 °C in $Ni_2(Cr_{0.5}Mo_{0.5})$ alloy. This revealed a smaller undercooling requirement for the formation of LRO in $Ni_2(Cr_{0.5}Mo_{0.5})$ alloy compared with other alloys where larger undercooling was required. The instability boundary existed below the coherent phase boundary by a temperature of about 50°C which will be shown in Section 6.1. A clear confirmation of the existence of the coherent phase boundary in category II alloys and difficult to demarcate it from the instability boundary in category I alloys could be seen as depicted in fig. 5.26. Below the instability boundary, the ordered phase would form by a continuous ordering mode as shown in the shaded region of fig. 5.26. The presence of well defined coherent and instability boundaries were the direct consequence of enhanced ordering kinetics in category II based alloys. The sequence of ordering transformation in $Ni_2(Cr_{1-x}Mo_x)$ alloys could, thus, be generalized as follows: (1) evolution of SRO from the disordered phase; (2)

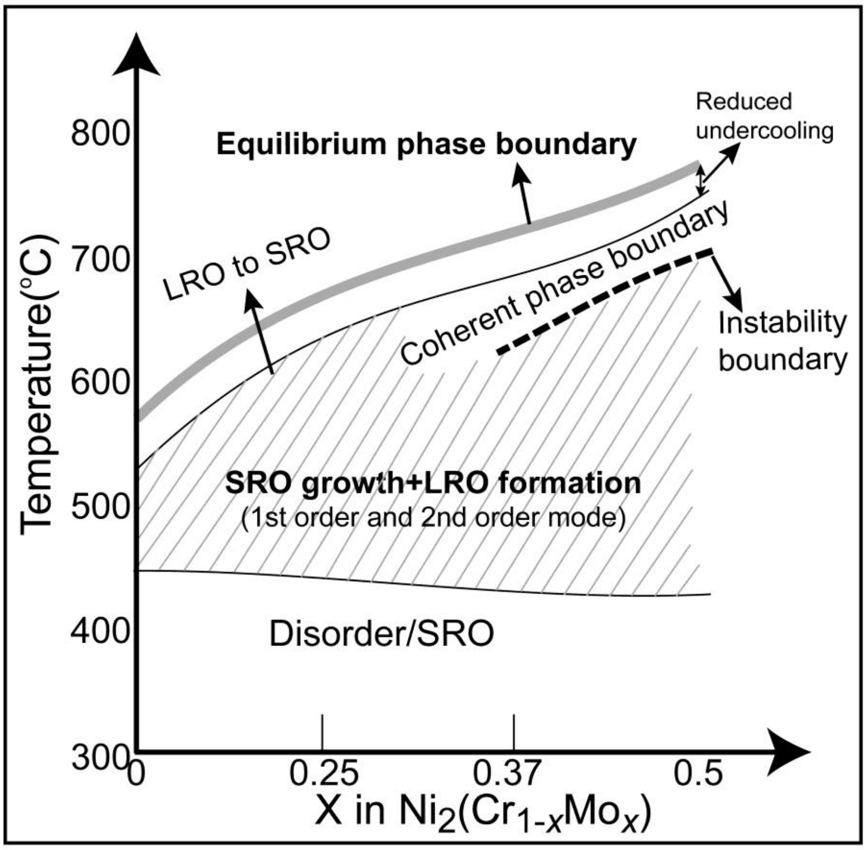

**Figure 5.26:** A schematic representation of micromechanisms of order evolution in $Ni_2(Cr_{1-x}Mo_x)$ alloys. LRO to SRO transition takes place via $2^{nd}$ order mode at the crossing of thick line in the figure while all other transitions take place via a $1^{st}$ order mode. The $2^{nd}$ order mode also operates within the shaded region of the figure during the formation of LRO from SRO involving continuous ordering transformation.

transformation of the SRO to LRO; (3) growth of the LRO; (4) dissolution of the LRO; and (5) evolution of SRO during the dissolution of LRO (Fig. 5.26). While a transformation mechanism of 1st order type would contribute to steps (2), (3) and (4), a 2nd order transformation mode would also contribute during steps (1), (2) and (5).

### 5.5.3. Role of Cr and Mo solutes on ordering kinetics:

Attempts were made to identify atomic species controlling the ordering reactions by comparing activation energies determined by kinetic analysis with the reported literature. Usually in solid state diffusion, activation energies for lattice diffusion of substitutional solutes fall close to self-diffusion values of solvent atoms but a variance is expected when there is a difference in the atomic sizes. A larger misfit of solutes in a host lattice decreases the activation energy when the solute atom is large and vice-versa [115, 116]. For instance, nearly similar atomic radii of Cr and Ni atoms, the activation energy for the self-diffusion of Ni is 275 kJ/mol [117] while that of Cr in pure Ni is 272 kJ/mol [118]. However, activation energy for the Cr diffusion increases to 290 kJ/mol in Ni-30at%Cr [118]. This suggested of additional factors like atomic bonding responsible for the higher activation energies in concentrated alloys. Janotti et al. [115] and Kramer et al. [116] have reported that increased bonding directionality increases activation energies for solutes diffusion when solute and host atoms have similar radii. On the basis of this argument it could be argued that increased activation energy for Cr diffusion in Ni-30at%Cr alloys would have resulted from the increased the bonding directionality between solute-host atoms.

On the other hand, there is limited data available on the activation energy of Mo in Ni-alloys. The activation energy for the diffusion of Mo in Ni is about 268 kJ/mol [119]. Due to the absence of appropriate activation energy data of Mo diffusion in Ni-Cr alloys, the effect of Mo addition on its activation energy in $Ni_2(Cr_{1-x}Mo_x)$ alloys was deduced on the basis of following understanding: (i) Mo atoms substitute Cr atoms in the alloy; (ii) for a given Ni-Cr-

Mo alloy, Ni-Mo bonds are relatively stronger than Ni-Cr bonds [65]; (iii) strengths Ni-Cr bonds increases while that of Ni-Mo bonds decreases with further substitution of Cr by Mo [65]. It was, therefore, not unreasonable to assume that the activation energy for the diffusion of Mo in Ni-Cr-Mo alloys would decrease with the increase in Mo.

In the present study, the experimentally obtained activation energies of about 294-300 kJ/mol were in agreement with that for lattice diffusion of Cr in binary Ni-Cr alloys [118]. This confirmed that diffusion of the Cr governed the formation of the ordered phase during continuous ordering transformation (1st exothermic peak) in alloys having $Ni_2(Cr_{0.75}Mo_{0.25})$ to $Ni_2(Cr_{0.63}Mo_{0.37})$ compositions. This is in agreement with the strong hybridization of d-d orbitals of Ni-Mo bonds allowing easy diffusion of Cr atoms due to their weaker hybridization with Ni atoms [65]. However, a significant drop of activation energy to 247 kJ/mol in $Ni_2(Cr_{0.5}Mo_{0.5})$ alloys suggested that Mo diffusion promoted the formation ordered phase beyond $Ni_2(Cr_{0.63}Mo_{0.37})$ composition. This was possible since substitution of Cr by Mo atoms have a tendency to decrease the strength of Ni-Mo bonds and increase that of Ni-Cr bonds till they become nearly same at $Ni_2(Cr_{0.5}Mo_{0.5})$ composition [65]. In addition, the nature of bonding also changes its character from covalent type (strong bond) in $Ni_2(Cr_{0.63}Mo_{0.37})$ alloy to metallic type in $Ni_2(Cr_{0.5}Mo_{0.5})$ alloy [65]. It is therefore not unreasonable to conclude that the delocalized nature of metallic bonding combined with nearly similar strengths of Ni-Cr and Ni-Mo bonds promoted the diffusion of both Cr as well as Mo in $Ni_2(Cr_{0.5}Mo_{0.5})$ alloys.

Activation energies for 2nd peak (observed for category II alloys) corresponding to $Ni_2(Cr_{0.63}Mo_{0.37})$ and $Ni_2(Cr_{0.5}Mo_{0.5})$ alloys were 206 kJ/mol and 255 kJ/mol, respectively (Table 5.2). Though, the activation energies for the formation as well as growth (respectively 1st and 2nd peaks of fig. 5.24c) of ordered domains in $Ni_2(Cr_{0.5}Mo_{0.5})$ alloy were nearly same, activation energy for growth in the $Ni_2(Cr_{0.63}Mo_{0.37})$ alloy (2nd peak of fig. 5.8c) was significantly lower than that for the formation (1st peak of fig. 5.8c). Nearly similar activation energies for the two processes in the $Ni_2(Cr_{0.5}Mo_{0.5})$ alloy confirmed that the lattice diffusion of both Cr and Mo solutes contributed during the continuous ordering as well as growth stages. In contrast, in the $Ni_2(Cr_{0.63}Mo_{0.37})$ alloy, significantly lower activation energy for the second peak suggested of little role of lattice diffusion of Cr and Mo in Ni during the growth process. Since the investigated alloy had quite a larger grain size, the effect of grain boundary diffusion could also be ignored. Incidentally, this activation energy value was close to the diffusion of Cr as well as Ni in pure Cr [120]. The lower activation energy for diffusion of solutes in Cr could be attributed to its low energy required for the formation of vacancies [120]. On these lines it could be argued that the diffusion of Mo in Cr would also result in such smaller value of activation energy, which was supported by the fact that bigger Mo atoms would require relatively smaller energy to reach at Cr vacancy. Such a mechanism would lead to the enrichment of Mo in the ordered $Ni_2(Cr,Mo)$ domains, which has been shown in a recent study [29]. It would be shown later in Section 7.3 that compositions of ordered domains were indeed enriched with Mo which supported the above postulate.

On the basis of the present work, following conclusions can be made.

1. The order evolution may involve one or more of following steps depending upon alloy composition, thermal history and ageing temperature:
    - i. evolution of the SRO from the disordered phase;
    - ii. transformation of the SRO to LRO;
    - iii. growth of the LRO;
    - iv. dissolution of the LRO; and
    - v. evolution of SRO during the dissolution of LRO.

2. Evolution of the ordered $Ni_2(Cr,Mo)$ phase occurred via a continuous ordering mechanism involving both 1st order and 2nd order transformation mode, while the growth/dissolution of ordered phase occurred via 1st order mode.
3. The 2nd order transformation mode operated during the transition of the alloy from short-range order to long-range order or vice-versa.
4. The ordering kinetics significantly increased with increase of Mo beyond $Ni_2(Cr_{0.63}Mo_{0.37})$ compositions.
5. Predominantly lattice diffusion of Cr atoms in the alloy contributed to the formation of ordered phase during continuous mode in all alloys except $Ni_2(Cr_{0.5}Mo_{0.5})$ which involved diffusion of both Cr and Mo atoms.
6. Coherent phase boundary moved close to equilibrium phase boundary in $Ni_2(Cr_{0.5}Mo_{0.5})$ alloy due to smaller contribution of coherency free energy.

# CHAPTER 6

# ORDER EVOLUTION IN THE ABSENCE OF SHORT-RANGE ORDER

This chapter describes the effect of SRO on the evolution of order during ageing in $Ni_2(Cr_{1-x}Mo_x)$ alloys investigated primarily by TEM and resistivity investigations.

## 6.1. Microstructural Characterization:

As mentioned in chapter 4, solution treated $Ni_2(Cr_{0.63}Mo_{0.37})$ and $Ni_2(Cr_{0.5}Mo_{0.5})$ alloys exhibited SRO characterized by the appearance of diffuse diffraction intensity maxima at {1 ½ 0} and 1/3{2 2 0} positions in the SAED patterns (Fig. 4.2). During ageing, this SRO gradually transformed into LRO of $Ni_2(Cr,Mo)$ phase, which occurred via a continuous ordering mode at lower ageing temperatures (Section 5.4). It was also shown in Section 4.1 that splat-quench processing of the alloys was able to suppress the formation of SRO (see figs. 4.5). Hence, a detailed study of order evolution during ageing was carried out on splat-quenched $Ni_2(Cr_{0.5}Mo_{0.5})$ alloy and compared with the solution treated samples to understand the effect of suppression of SRO on the evolution of order. $Ni_2Cr$ alloy was also used to compare the effect of suppression of SRO in splat-quenched state on the order evolution.

Samples of $Ni_2(Cr_{0.5}Mo_{0.5})$ alloy were aged for varied time periods spanning over few minutes to several hundred minutes at 525°C to 750°C temperatures, while up to 1000 h of ageing at 500°C was used on $Ni_2Cr$ alloy due to its sluggish ordering kinetics. SAED, DF and BF evidences were used to characterize the microstructural changes occurred during these ageing treatments.

## 6.1. Order evolution in splat-quenched $Ni_2(Cr_{0.5}Mo_{0.5})$ alloy:

Fig. 6.1 shows results of TEM investigations of samples of $Ni_2(Cr_{0.5}Mo_{0.5})$ alloy aged at 525°C and 625°C for varied time periods. SAED evidences in <0 0 1> and <1 1 > zone axes were used to study progress of ordering by monitoring diffraction intensity at positions corresponding to ordered $Ni_2$(Cr,Mo) phase as shown in fig. 6.1. The microscopy evidences of samples aged at both temperatures revealed a prior appearance of diffuse diffraction intensity pattern similar to that seen in the solution treated and water quenched state of the alloy. Continued ageing at 525°C though increase the diffraction intensity at characteristic SRO positions sharp reflections of the ordered phase could not be seen even after 300 min of ageing (see fig. 6.1). On the other hand, sharp reflections of the LRO appeared within 60 min

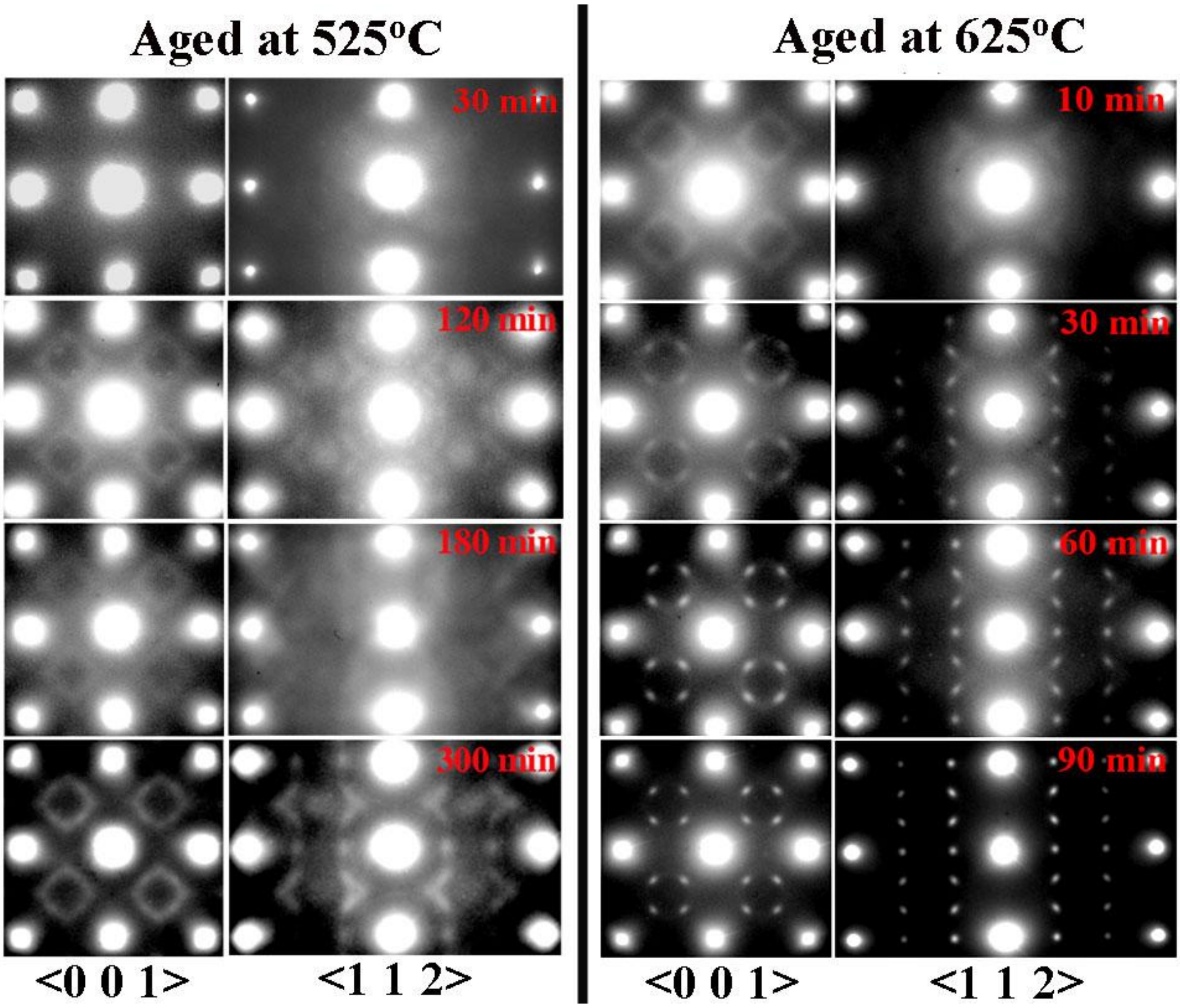

**Figure 6.1:** SAED patterns in <0 0 1> and <1 1 2> zone axes during ageing at 525°C and 625°C of splat-quenched $Ni_2(Cr_{0.5}Mo_{0.5})$ alloy. The continuous mode of transformation is evident in both states of alloy at both ageing temperatures by the gradual change of diffraction intensity pattern from diffuse nature to sharp reflections of ordered structure.

of ageing at 625°C (Fig. 6.1). The appearance of characteristic diffuse diffraction intensity pattern of SRO from a complete disordered state confirmed that SRO state was an intermediate ordering stage in the development of ordered $Ni_2$(Cr,Mo) phase.

Similar observation of initial appearance of SRO followed by its transformation to superlattice reflections of ordered $Ni_2$(Cr,Mo) phase was observed at 700°C and 750°C (Figs.

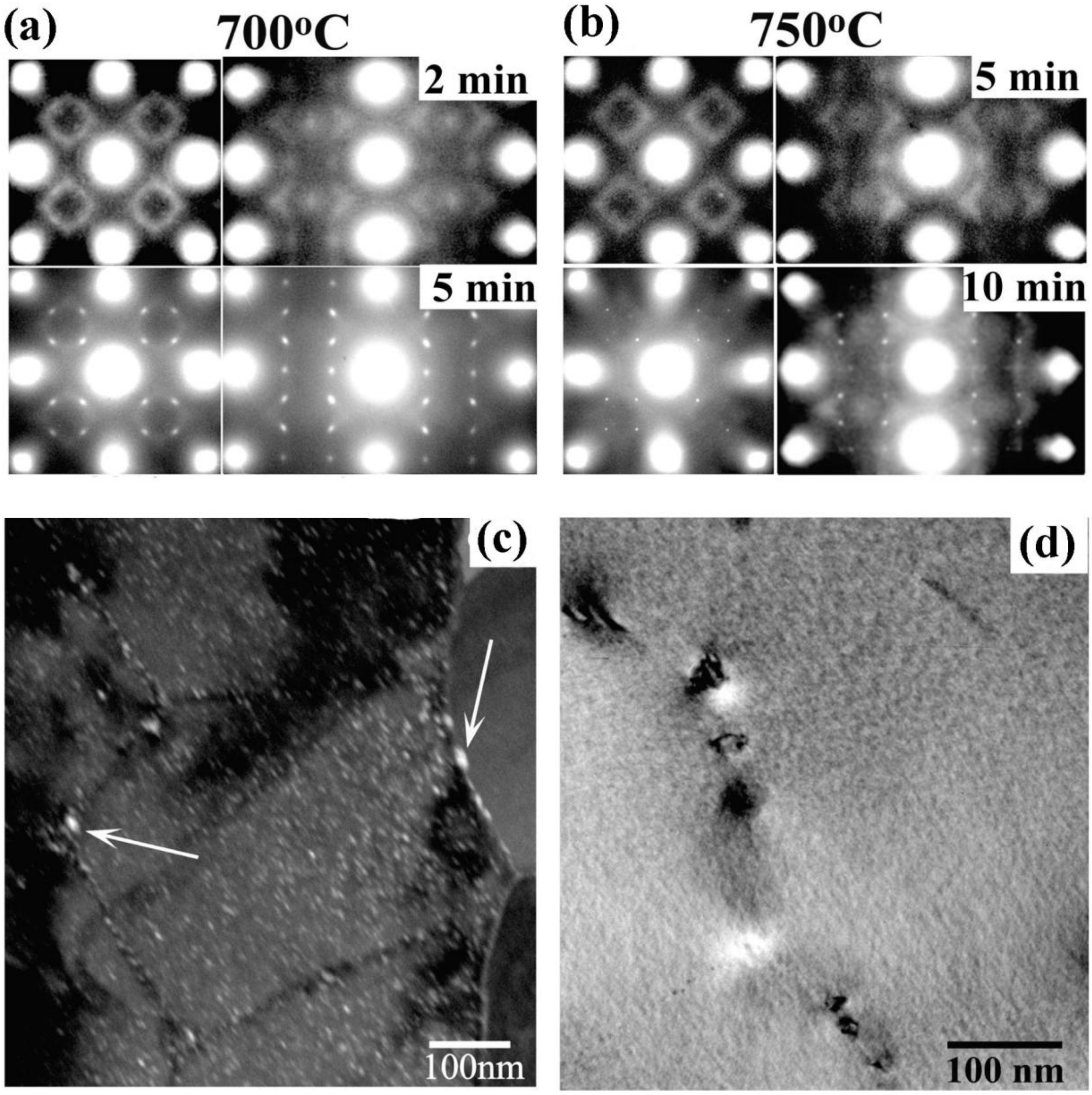

**Figure 6.2:** SAED patterns in <0 0 1> and <1 1 2> zone axes of splat-quenched $Ni_2(Cr_{0.5}Mo_{0.5})$ alloy during ageing at; (a) 700°C; and (b) at 750°C. (c) DF image showing presence of ordered domains in sample after 5 min of ageing at 700°C; (d) BF image of samples aged at 750°C for 10 min showing only mottled contrast.

6.2a and b). The sharp reflections of LRO developed within 5 min of ageing at 700°C which were superimposed over the traces of diffuse intensity of the SRO. DF-TEM imaging confirmed the formation of a few nanometer-sized ordered domains within 5 min of ageing at 700°C. These domains homogeneously distributed within grains, though, a few were seen at grain boundaries as well as marked by arrows in fig.6.2c. Similar observations were made at 750°C temperature after 10 min though their intensity was insufficient to reveal them in the DF-TEM images (Fig. 6.2b).The appearance of a mottled contrast in BF-TEM images confirmed the existence of fine precipitates in the matrix (Fig. 6.2d). The observation of appearance of sharp superlattice reflections of LRO superimposed over the diffuse diffraction intensity of SRO suggested that ordered domains might have formed via a nucleation and growth mechanism at both 700°C and 750°C. This was possible as these temperatures were close to the critical order-disorder temperature (775°C) of this alloy where large amplitude of concentration fluctuations can easily initiate the nucleation process for the nucleation and growth mechanisms.

A comparison of order evolution of the splat-quenched alloy with the solution treated $Ni_2(Cr_{0.5}Mo_{0.5})$ alloy at 525°C (compare figs. 6.1 and 5.12) revealed that LRO reflections appeared within 120 min of ageing in the solution treated sample, while LRO reflections were absent in the splat-quenched sample even after 300 min of ageing. Similarly, distinct LRO reflections appeared within 3 min and 60 min at 625°C in the solution treated sample and the splat-quenched samples, respectively (compare figs. 6.1 and 5.12). Increase of ageing temperature to 700°C resulted in the appearance of LRO reflections within 5 min in the splat-quenched samples (Fig. 6.2a), while well developed LRO reflections appeared within 2 min of ageing of the solution treated samples (Fig. 6.3a). The DF-TEM micrograph confirmed the formation of high density of ordered domains in the solution treated samples aged for 2 min at 700°C (Fig. 6.3b). Ageing at 750°C also revealed sluggish ordering kinetics in the splat-quenched alloy (compare figs. 6.2b and 5.18a). Ageing times required for the appearance of LRO reflections at different temperatures were used to plot incubation time versus ageing temperatures in the splat-quenched samples and solution treated and water quenched samples of $Ni_2(Cr_{0.5}Mo_{0.5})$ alloy as shown in fig. 6.4. This figure has clearly showed that kinetics of ordering transformation remained sluggish in absence of SRO in the splat-quenched samples.

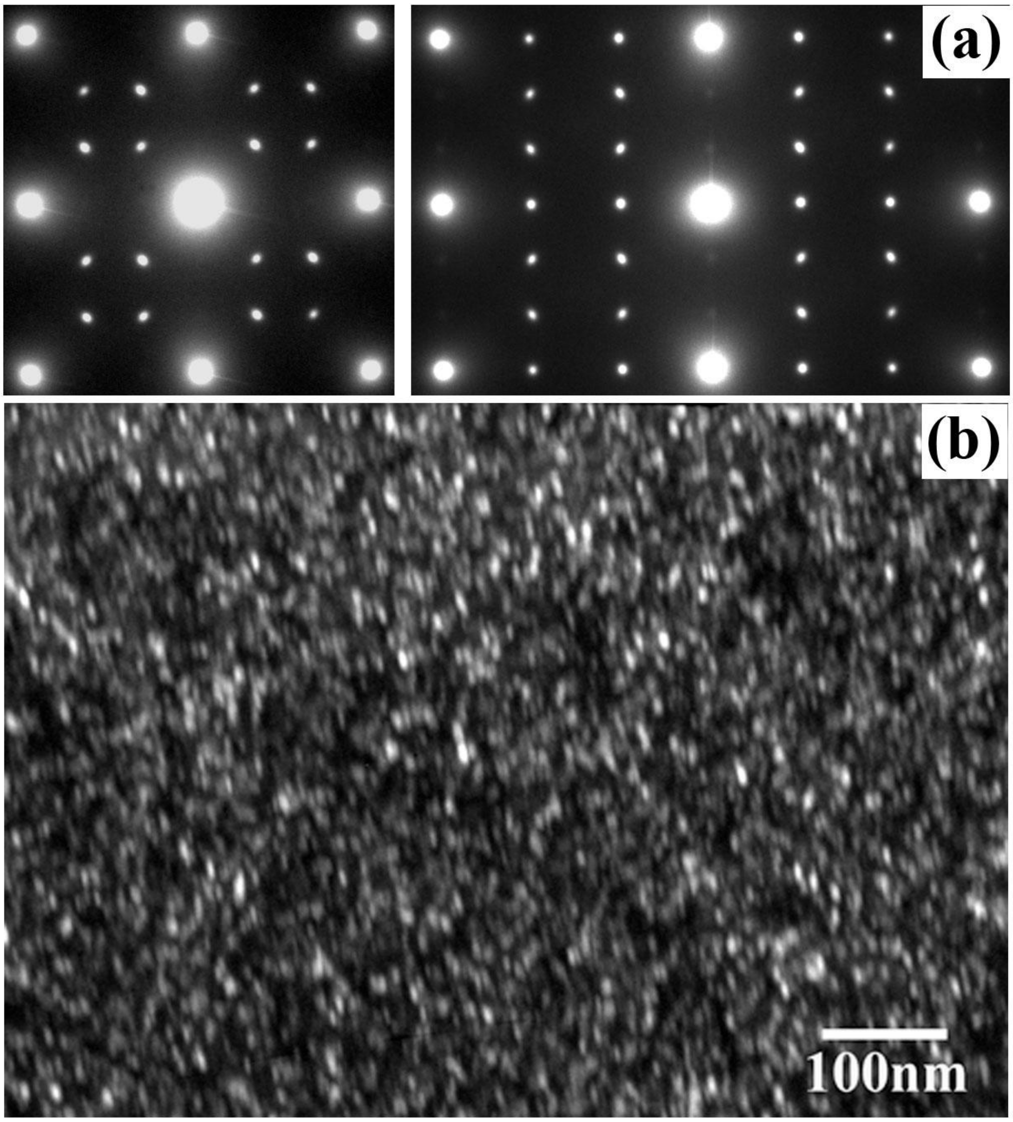

**Figure 6.3:** (a) SAED patterns in <0 0 1> and <1 1 2> zone axes of solution treated and water quenched $Ni_2(Cr_{0.5}Mo_{0.5})$ alloy aged at 700°C for 2 min. (b) DF-TEM micrograph showing presence of high density of ordered domains.

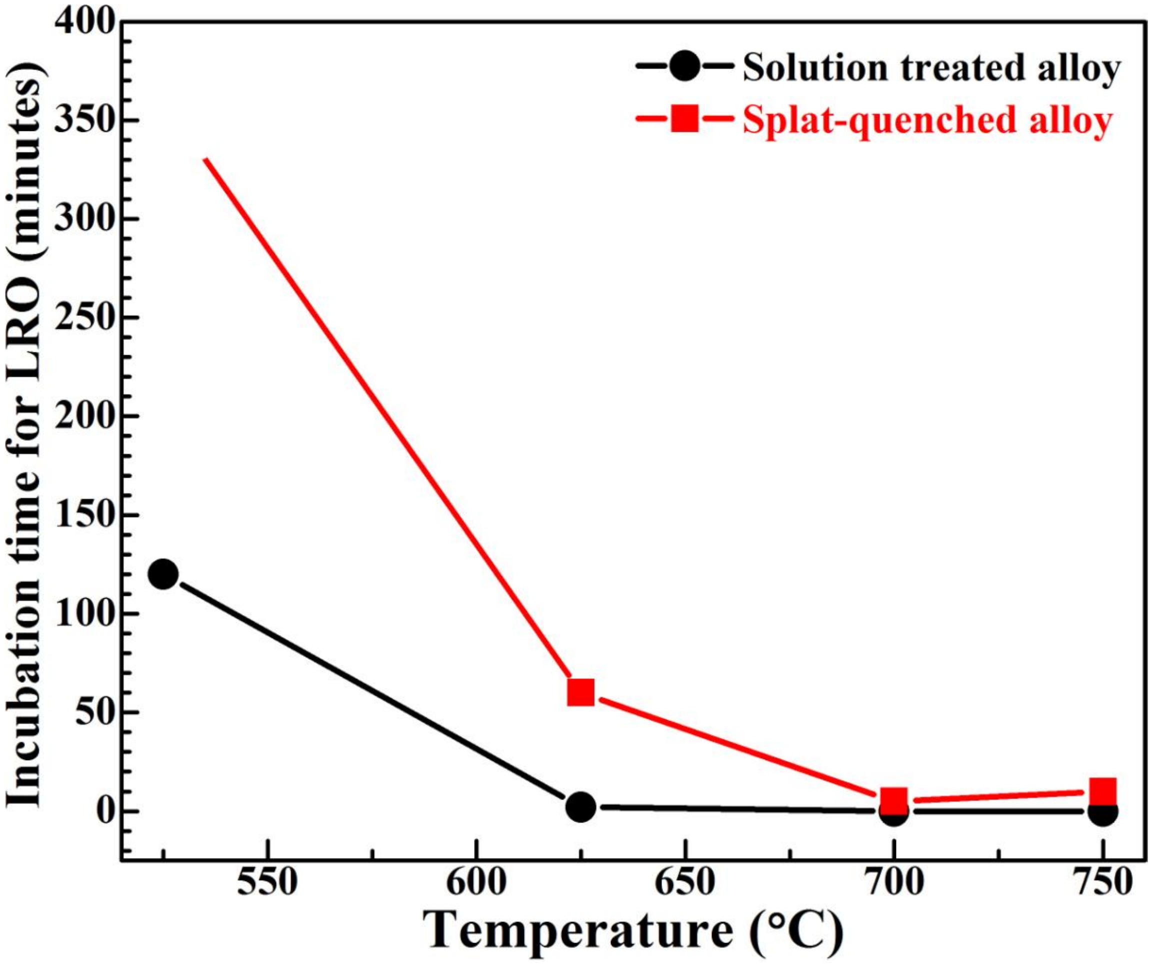

**Figure 6.4:** Incubation time for the formation of LRO at different ageing temperatures of the splat-quenched state and solution treated and water quenched state of $Ni_2(Cr_{0.5}Mo_{0.5})$ alloy.

## 6.2. Order evolution in $Ni_2Cr$ alloy:

Sharp reflections of the ordered phase appeared within 500 h of ageing at 500°C in the solution treated samples of $Ni_2Cr$ alloy (Fig. 6.5a). BF-TEM micrographs confirmed the presence of fine ordered domains by the characteristic mottled contrast as shown in fig. 6.5b. However, same ageing treatment on splat-quenched samples of $Ni_2Cr$ alloy was insufficient to produce LRO reflections, though sharp LRO reflections were seen after 1000 h of ageing as shown in SAED patterns with <1 1 2> zone axis in fig. 6.6.

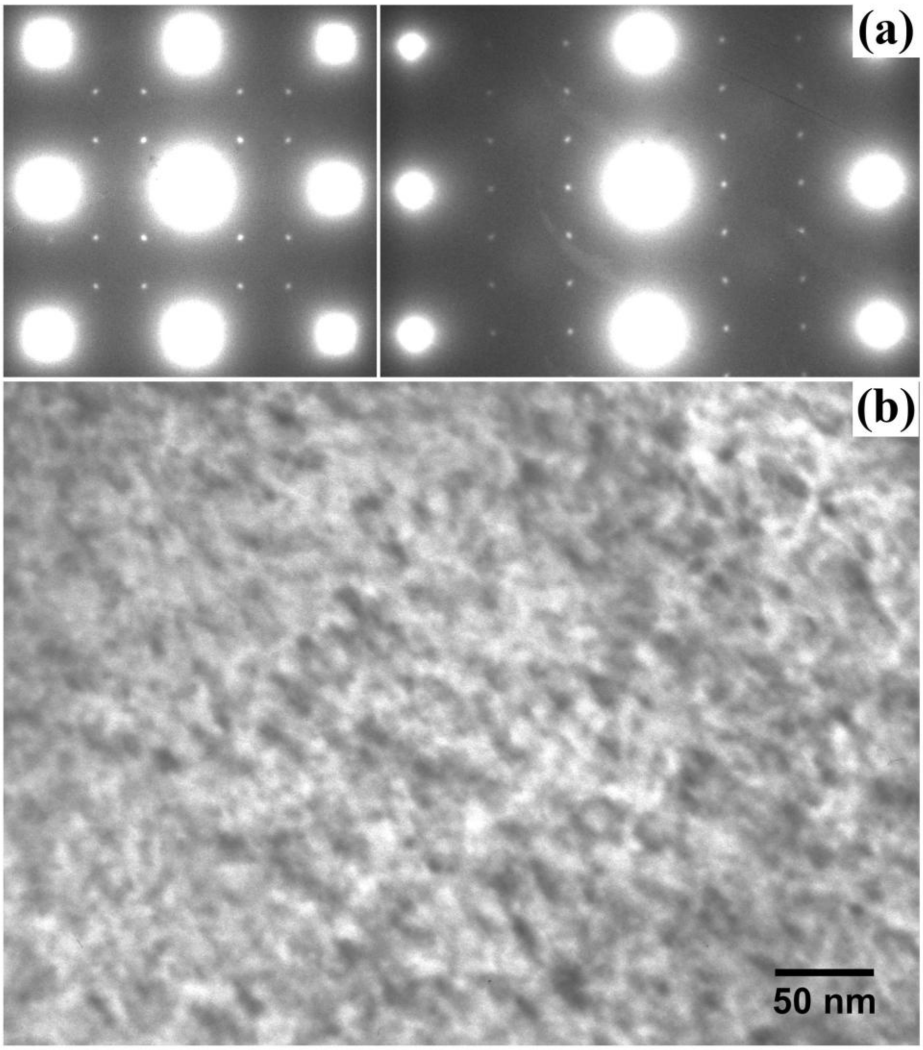

**Figure 6.5:** (a) SAED patterns in <0 0 1> and <1 1 2> zone axes of solution treated and water quenched $Ni_2Cr$ alloy aged at 500°C for 500 h, (b) BF-TEM micrograph showing mottled contrast due to the presence of fine ordered domains.

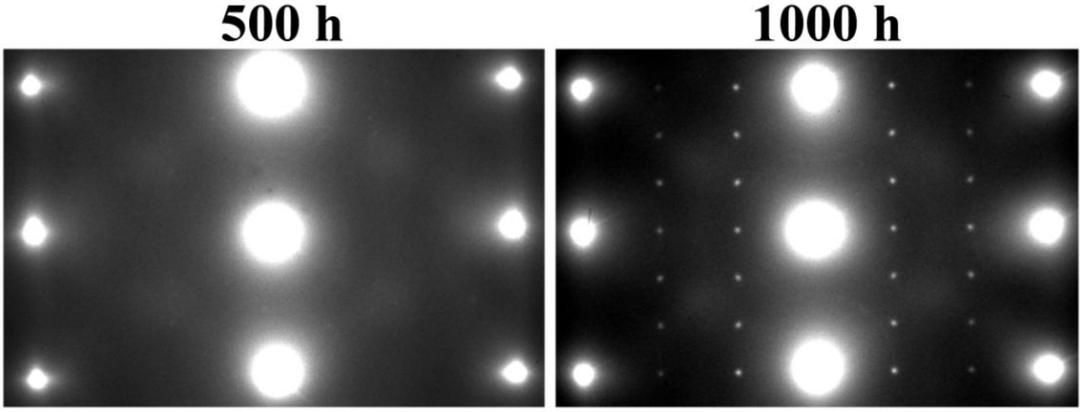

**Figure 6.6:** SAED patterns in <1 1 2> zone axes of splat-quenched $Ni_2Cr$ alloy aged at 500°C for 500 h and 1000 h.

## 6.2. Resistivity study of order evolution in $Ni_2(Cr_{0.5}Mo_{0.5})$ alloy:

Isothermal resistivity studies were also used to support the sluggish ordering kinetics in the absence of SRO. Isothermal resistivity experiments were carried out by inserting samples inside the furnace after it reached the desired temperatures. These studies were carried out over a temperature range of 525°C to 680°C. These experiments on splat-quenched as well as solution treated and water quenched samples showed a gradual increase of resistivity during initial ageing times followed by a decrease after attaining a maximum value, though the splat-quenched samples required longer time reach its maxima. The isothermal resistivity plots obtained on splat-quenched samples and solution treated water quenched samples of $Ni_2(Cr_{0.5}Mo_{0.5})$ alloy at 540°C are shown in fig. 6.7a. It was clear from fig. 6.7a that in the splat-quenched samples longer ageing time was required for the appearance of resistivity maximum. On the basis of microstructural understanding of order evolution at 525°C with time, described above, following conclusion could be made: (i) increase of SRO in the alloy appeared as gradual resistivity increase; (ii) formation and growth of LRO domains appeared as a continuous resistivity fall; (iii) time corresponding to resistivity maxima represented the onset of the appearance of sharp reflections from diffuse spots. On the basis of this understanding incubation times for the formation of LRO at different temperatures in both splat-quenched and solution treated water quenched samples of $Ni_2(Cr_{0.5}Mo_{0.5})$ alloy were determined and are plotted in fig. 6.7b. This figure clearly showed that the incubation time was larger in the splat-quench samples than solution treated water quenched samples of $Ni_2(Cr_{0.5}Mo_{0.5})$ alloy.

Thus, the important finding of this study was the sluggish ordering kinetics in the splat-quenched samples compared to solution treated samples of the same alloy. This was contrary to normally expected behaviour in the presence of high concentration of quenched-in defects. Rapid quenching of alloys from the liquid state was expected to produce excess quenched-in

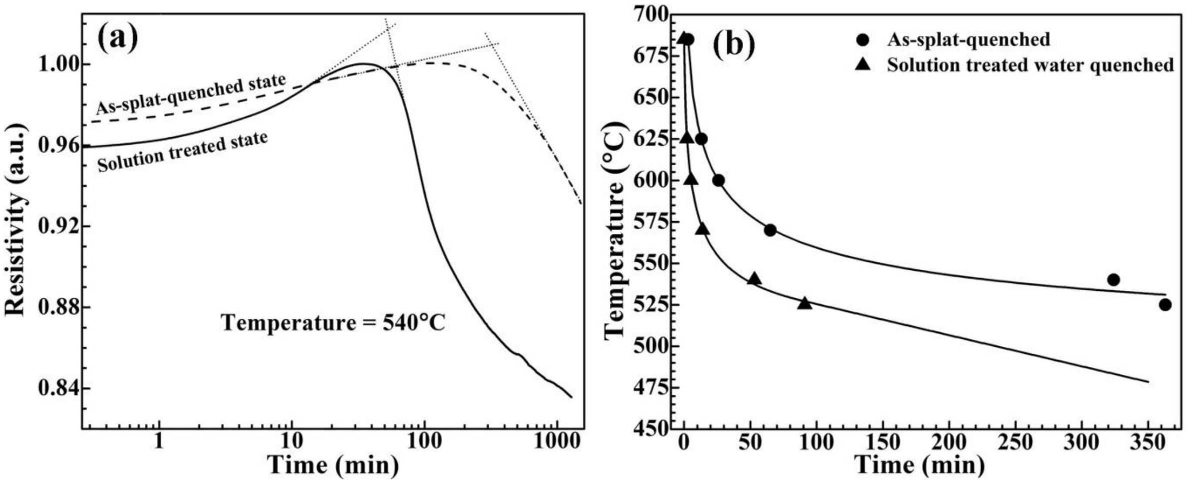

**Figure 6.7:** (a) Isothermal resistivity plots of splat-quenched and solution treated water quenched samples of $Ni_2(Cr_{0.5}Mo_{0.5})$ alloy aged at 540°C. (b) plots of incubation times for the formation of LRO phase in two different initial microstructural states of $Ni_2(Cr_{0.5}Mo_{0.5})$ alloy.

vacancies and lattice defects, which should have enhanced the rate of reaction due to increased mobility of diffusing species, see e.g., [64, 121, 122]. It will be shown in the discussion that ordering kinetics was strongly governed by pair interactions between constituent's species and a strong reduction of pair interactions by suppressing the SRO in the splat-quenched samples resulted in abnormal behaviour of sluggish ordering kinetics.

## 6.3. Discussion:

Present experimental investigations established a sluggish ordering kinetics in the splat-quenched samples of $Ni_2Cr$ and $Ni_2(Cr_{0.5}Mo_{0.5})$ alloys. Since the splat-quenched samples are known to contain higher quenched-in vacancies as compared to those quenched from a solid solution state, they were expected to exhibit faster ordering kinetics [64, 121, 122]. The curious observation of anomalous ordering kinetics in splat-quenched was understood in terms of driving force available for ordering as explained in the following.

According to Landau [123], the free energy change, $\Delta F$, during ordering can be expressed in terms of a generalized order parameter, $\eta$, given by the following expression:

$$\Delta F = A*\eta^2 + B*\eta^3 + C*\eta^4 + \ldots\ldots\ldots\ldots\ldots\ldots\ldots (6.1)$$

where, coefficients A, B and C depend up on wave vector, temperature, and alloy composition while $\eta$ is proportional to the concentration wave amplitude. Symmetry considerations and 2nd order nature of the <1 ½ 0> spinodal ordering dictates A to be negative, B = zero and C is positive at temperatures close to the instability temperature [74]. During initial stages of ordering, i.e., close to the disordered state (when $\eta \cong 0$) and for small wave amplitudes, the free energy change is governed by the first harmonic term in Eq. 6.1, as the contribution of higher order terms is negligible. For a given wave vector, *k*, the extent to which $\Delta F$ is minimized is thus determined primarily by A, which itself is governed by the pair-interaction function, *V*(k), as given in equation 6.2 by Mayer et al. [74]

$$A(k) = N_v[2*V(k) + k_BT/C_NC_M]/2\ldots\ldots\ldots\ldots (6.2)$$

Where, $N_v$ denotes the number of atoms per unit volume, $k_B$, is Boltzmann's constant, and $C_N$ and $C_M$ are atom fractions of the alloy constituents N and M. Since $k_BT/C_NC_M$ would always be positive, it is *V*(k) only that would be important in equation 6. 2 for the coefficient A(k) to be negative. The occurrence of the diffuse intensity maxima at {1 ½ 0} positions in the early stages of ordering therefore could be correlated with *V*(k) which has absolute minima at {1 ½ 0} positions [80]. The pair interaction function, thus, has an important role in stabilizing concentration waves during a second order reaction (i.e., SRO formation during spinodal ordering). The pair-interaction function in the initial ordering stages is also important in tailoring the order evolution sequences by changing individual pair interaction energies and such simulations have already been carried out in the past by Hata et al. [104] and Kulkarni [79]. Further, it has been established by Kulkarni that diffuse diffraction intensity map mimics the *V*(k) function in the initial ordering stages which depends upon wave vector and alloy composition [79]. The stabilization of only concentration waves with k = <1 ½ 0> and 1/3<2 2 0> in the present case thus confirmed the importance of their pair interaction functions during the evolution of order.

The driving force for ordering transformation in the smaller amplitude limit is also dependent upon the amplitude of the concentration waves which were evolving according to equation 6.1. The time evolution of concentration waves, $A_m$, for a given wave vector during a diffusion reaction at smaller length scale [59], can be described by equation 6.3 in the small amplitude limits.

$$A_m(k)= A_m^{\circ}(k)*\exp[\alpha(k)*t]\ldots\ldots\ldots\ldots\ldots\ldots\ldots\ldots.(6.3)$$

Where, $A_m^{\circ}$is the initial amplitude of concentration wave at t = 0, and $\alpha(k)$ is the amplification factor which is related to the second derivative of free energy [59]. This amplification factor, for a given Fourier component k, depends strongly on $V$(k) especially at temperatures relatively lower than the instability temperature as shown by Kulkarni [79]. As the amplitude of concentration waves for a given wave vector is also dependent upon the pair interaction functions, equation (6.2) can be used to determine the value of concentration waves amplitude at t = 0.

The pair interaction energies which have replicated the experimentally observed diffuse diffraction intensity patterns in $Ni_2Mo$ alloy [79], exhibited ordering behaviour similar to that in the investigated alloy system, were used in present study to understand the amplification of concentration waves having different k-vectors. The temporal evolution of the amplification of concentration waves was determined for wave vectors corresponding to disorder, LRO (1/3 <2 2 0>), and SRO (<1 ½ 0>) states on the basis of equations 6.1 to 6.3 and is shown in fig. 6.8 (see Appendix II for details). It was clear from fig. 6.8 that <1 ½ 0> wave exhibited the largest amplification among all which is in agreement with our experimental evidences as well as with earlier studies [124]. Fig. 6.8 also demonstrated that, in the early stages of ordering, both <1 ½ 0> and 1/3 <2 2 0> waves grew simultaneously nearly at the same rate, which supported the simultaneous appearance of diffuse diffraction intensity maxima at 1/3{2 2 0} and {1 ½ 0} positions (see fig. 6.1). On the other hand, wave amplification in the disordered state remained relatively a sluggish process as can be seen in fig. 6.8 and is followed by the amplification of <1 ½ 0> and 1/3 <2 2 0> waves after attaining certain amplitude equivalent to either of the <1 ½ 0> or 1/3 <2 2 0> waves. The weaker pair interaction function in the disordered state, in fact, had suppressed the initial amplitude of the concentration waves as evident in fig. 6.8 and resulted in a sluggish ordering kinetics. Continuation of ordering results in an increase in the amplitude of concentration waves. Once the amplitude of the concentration waves reached high values, the anharmonic terms in the free energy expansion modulate the harmonic effect by the emergence and preferred growth of higher order waves generally producing peaks at other superlattice positions [125]. This was consistent with present observations where SL reflections of the ordered phase appeared at positions different than those of the SRO as the transitory stages of ordering have to eventually make away for the equilibrium / metastable ordered phase.

The continuous nature of ordering transformation has a tendency to compete with a nucleation and growth mode at higher temperatures [114]. Observation of sharp superlattice reflections of the ordered phase appearing simultaneously with a diffuse diffraction intensity of the SRO state in splat-quenched samples at 700°C and 750°C was consistent with this competing nature. In the context of Landau model, this was possible since these ageing temperatures were close to the critical ordering temperature (775°C) where large amplitude of concentration fluctuations can easily initiate the nucleation process for the nucleation and growth mechanisms.

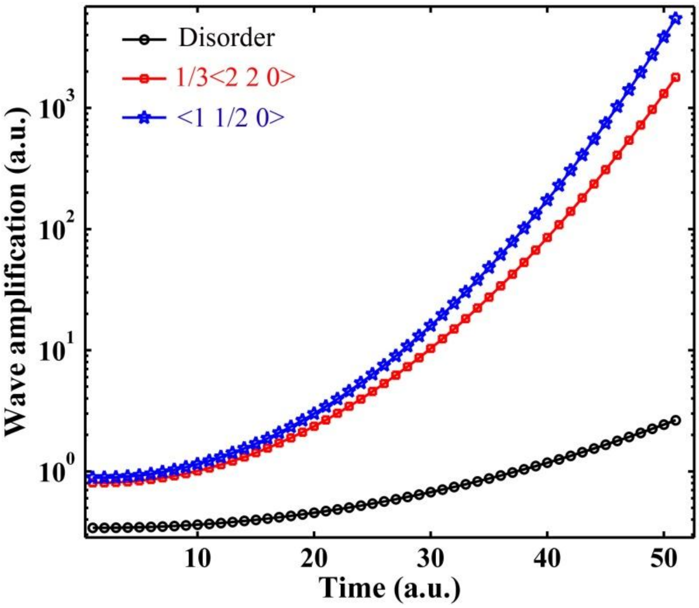

**Figure 6.8:** Amplification of concentration waves with wave-vectors corresponding to disorder; long-range order; and short-range order state (see text for details).

On the basis of results presented above it could be concluded that initial microstructure of the alloy play a crucial role in deciding ordering kinetics of $Ni_2$(Cr,Mo) phase in Ni-Cr-Mo alloys. Kinetics of ordering transformation could be made sluggish by suppressing SRO state in the initial microstructure. However, prior formation of SRO, even in the disordered state, was the prerequisite for the long-range ordered phase formation. This tendency appeared to be consistent with the maximum driving force for the amplification of {1 ½ 0} SRO which was the main governing factor for the initial evolution of SRO from a complete disordered state.

# CHAPTER 7

# COMPOSITIONAL STABILITY OF THE ORDERED $Ni_2(Cr,Mo)$ PHASE IN Ni-Cr-Mo ALLOYS

This chapter deals with identification of the compositions of the ordered $Ni_2(Cr,Mo)$ phase in Ni-Cr-Mo alloys. The $Ni_2(Cr,Mo)$ phase has been suggested to have different stability at different concentrations of Cr and Mo solutes [26, 65]. For instance, Chan et al. [26] have reported that formation energy of the $Ni_2Cr$ phase lowers by the substitution of about 80% Cr atoms by Mo atoms in the phase. A recent theoretical study on the stability of the $Ni_2(Cr,Mo)$ phase for varying Cr and Mo solute concentrations by Hu et al. [65] suggests that this phase has maximum stability at $Ni_2(Cr_{0.75}Mo_{0.25})$ composition while least stability at $Ni_2(Cr_{0.5}Mo_{0.5})$ composition. Thus, it could be construed that ordered $Ni_2(Cr,Mo)$ phase would prefer to form at those compositions which have least formation energy (highest stability). Two alloys, namely $Ni_2(Cr_{0.63}Mo_{0.37})$ and $Ni_2(Cr_{0.5}Mo_{0.5})$ alloys, were used for this study due to their tendency to transform disordered matrix phase phase into ordered phase within reasonable ageing times as shown in Section 5.4. Different experimental techniques of microhardness testing, x-ray and neutron diffraction and 3-dimensional atom probe investigation were used to analyze and interpret compositional stability of the ordered $Ni_2(Cr,Mo)$ phase.

## 7.1. Microhardness variation with order evolution:

Microhardness measurements of $Ni_2(Cr_{0.63}Mo_{0.37})$ and $Ni_2(Cr_{0.5}Mo_{0.5})$ alloys were carried out as a function of ageing times to understand the effect of ordered phase on the hardness properties. Ageing at 680°C for time periods between few minutes to hundreds of hours were used to develop different fractions of ordered phase in the microstructure of these alloys. It was found that hardness could reach its maximum value within a few hour of ageing at 680°C

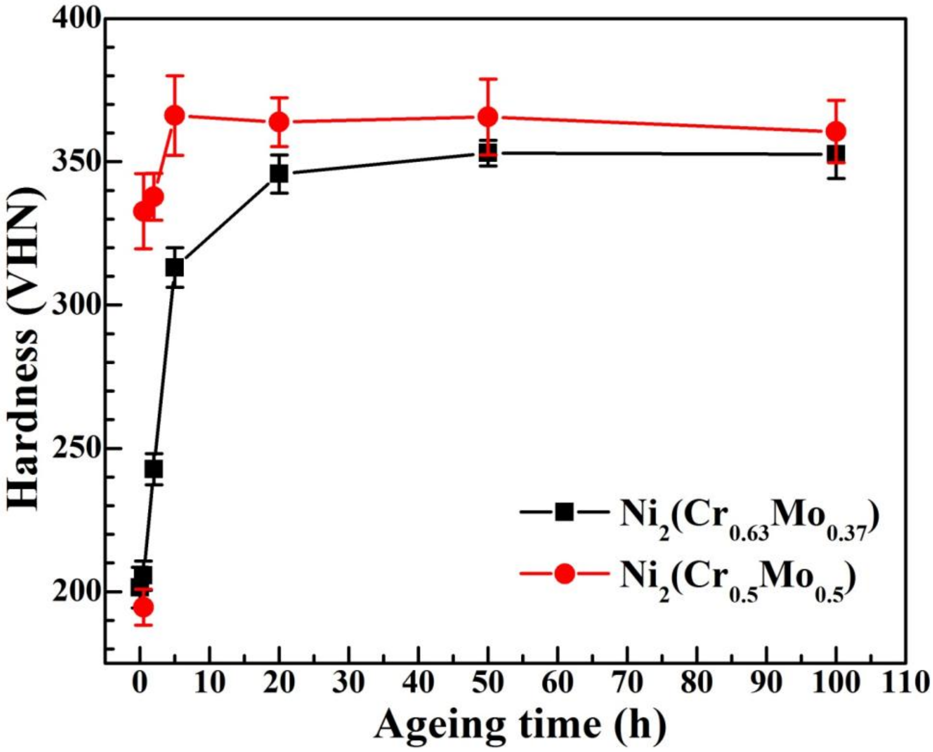

**Figure 7.1:** Microhardness change with ageing time at 680°C in $Ni_2(Cr_{0.63}Mo_{0.37})$ and $Ni_2(Cr_{0.5}Mo_{0.5})$ alloys.

in the $Ni_2(Cr_{0.5}Mo_{0.5})$ alloy, while much longer period was required to attain the maximum hardness in the $Ni_2(Cr_{0.63}Mo_{0.37})$ alloy (Fig. 7.1). However, both alloys exhibited hardness plateaus at about 350 VHN value during prolonged ageing. This appeared to be at variance with the work of Hu et al. [65] who have suggested a weaker atomic bonding in $Ni_2(Cr,Mo)$ phase at $Ni_2(Cr_{0.5}Mo_{0.5})$ composition, the formation of which could have resulted a smaller hardness value in $Ni_2(Cr_{0.5}Mo_{0.5})$ alloy. Almost similar hardness of $Ni_2(Cr_{0.63}Mo_{0.37})$ and $Ni_2(Cr_{0.5}Mo_{0.5})$ alloys, thus, suggested the possibility of formation of ordered phase with composition different than the alloy composition in $Ni_2(Cr_{0.5}Mo_{0.5})$ alloy, which could not be ruled out as $Ni_2(Cr_{0.5}Mo_{0.5})$ superstructure has least stability [65]. It will be shown in the subsequent sub-sections that ordered phase has preference to form with different compositions.

## 7.2. Lattice parameter instability during order evolution:

**7.2.1. X-ray diffraction:** X-ray diffraction (XRD) studies were carried out to understand lattice parameter instabilities in the ordered phase. This study was based upon the understanding that lattice parameter contraction occurs during ordering in Ni-Cr and Ni-Cr-Mo alloys [12, 14]. XRD plots of solution treated and water quenched $Ni_2(Cr_{1-x}Mo_x)$ alloys are the shown in fig. 7.2a. It was clear from the figure that diffraction peaks appeared at lower $2\theta$ values with the increase of Mo-content in the alloy, confirming an increase of lattice parameter with the increase of Mo. Values of lattice parameters determined from XRD analysis are plotted in fig. 7.2b. It was clear from fig. 7.2b that lattice parameter of the fcc phase in disordered $Ni_2(Cr_{1-x}Mo_x)$ alloys increased monotonically in a non-linear fashion from a minimum value of 3.567 Å (for the $Ni_2Cr$ alloy, which agreed with the finding of Karmazin et al. [12]) to a maximum value of 3.621Å in $Ni_2(Cr_{0.5}Mo_{0.5})$ alloy. Fig. 7.2b also showed that lattice parameter increased by about 1.6% in the $Ni_2(Cr_{0.5}Mo_{0.5})$ alloy relative to

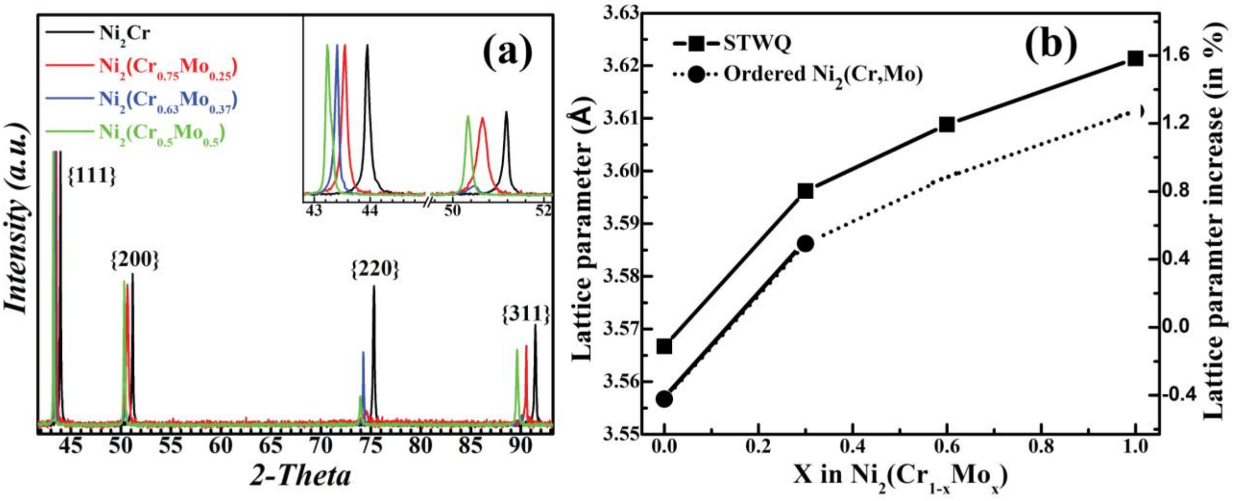

**Figure 7.2** (a) X-ray diffraction patterns of solution treated $Ni_2(Cr_{1-x}Mo_x)$ alloys, the inset in the figure clearly shows the shift of Bragg peaks to lower theta with the increase of Mo in the alloy; (b) lattice parameter of $Ni_2(Cr_{1-x}Mo_x)$ alloys in the solution treated state determined from fig. (a) by filled square symbols; same plot shows the reported lattice parameter values of the ordered phase in respective alloys by filled circles and extraplotted to other compositions which is shown by dotted lines.

that in the $Ni_2Cr$ alloy. Though, ordered $Ni_2(Cr,Mo)$ phase in all these alloys has a $DO_{2h}^{25}$ structure, no information is available in the literature on its lattice parameter values when both chromium and molybdenum present in the ordered phase. This information is available only for the binary $Ni_2Cr$ alloy system, where both first principle calculations and experimental studies have been used to determine the lattice parameter of the ordered $Ni_2Cr$ phase. Chan et al. [26] have computed lattice parameters of the ordered $Ni_2Cr$ phase as a=2.46 Å, b=7.36 Å and c=3.55 Å. Hirabayashi et al. [70] and Karmazin et al. [12] have used fundamental peaks position in the x-ray diffraction to determine cell parameters of the ordered $Ni_2Cr$ phase in terms of cubic lattice parameter, which they assume to represent c-parameter of its orthorhombic unit cell. Hirabayashi et al. [70] have further proposed a methodology to calculated a- and b-parameters of the orthorhombic unit cell on the basis of their geometrical relationship with the c-parameter. Whereas, Hirabayashi et al. [70] have reported the value of c-parameter to be 3.562 Å, Karmazin et al. [12] have found it to be 3.556 Å. A small difference in the values of lattice parameters reported by Karmazin et al. [12] and Hirabayashi et al. [70] could be due to different ageing times used by the two, which are about an order in difference. Karmazin et al. [12] have found that the increase of ageing time at 450°C reduces lattice parameter continuously until it reaches a plateau after several thousand hours of ageing. The ageing time of several thousand hours used by Karmazin et al. [12], thus, appears to be sufficient to produce invariant lattice parameter, while ageing time of 3200 h at 460°C used by Hirabayashi et al. [70] appears to insufficient for kinetically sluggish ordering transformation in the $Ni_2Cr$ alloy. A slightly larger value of the lattice parameter in the work of Hirabayashi et al. thus appears to be due incomplete ordering. Thus, c-parameter reported by Karmazin et al. [12] can be used to calculate other cell parameters of the ordered $Ni_2Cr$ phase using a methodology suggested by Hirabayashi et al. [70] and the calculated cell parameters are given in table 7.1.

Due to sluggish ordering kinetics of $Ni_2(Cr_{0.75}Mo_{0.25})$ alloy, lattice parameters of the ordered phase in this alloy were estimated on the basis of reported literature. For the ordered phase in $Ni_2(Cr_{0.75}Mo_{0.25})$ alloy, Karmazin et al. [14] have shown a lattice contraction of 0.01 Å in the c-parameter upon ordering. During the present study, lattice parameter of the fcc phase in disordered $Ni_2(Cr_{0.75}Mo_{0.25})$ alloy was 3.596 Å (Table 7.1). It was therefore not unreasonable to conclude that the value of the c-parameter of the ordered phase in $Ni_2(Cr_{0.75}Mo_{0.25})$ alloy would be 3.586 Å. Karmazin et al. [14] have also shown that contraction in the c-parameter due to ordering remains more or less same when about 25% of Cr atoms are replaced by Mo atoms in the $Ni_2Cr$ alloy. Extending this argument, it was assumed that other alloys containing higher amount of Mo atoms exhibited similar lattice contraction. On the basis of lattice parameters determined for the fcc phase in disordered $Ni_2(Cr_{0.63}Mo_{0.37})$ and $Ni_2(Cr_{0.5}Mo_{0.5})$ alloys, c-parameters of the ordered phase in these alloys could be estimated as given in table 7.1. A plot of c-parameter of ordered phase determined for different alloy compositions is shown in fig. 7.2b. On the basis of this fig. 7.2b, it could be concluded that the same ordered phase in alloys with different compositions exhibited different lattice parameters.

**Table 7.1:** Lattice Parameter values obtained for ordered $Ni_2(Cr,Mo)$ phase using methodology suggested by Hirabayashi et al. [70]

| State | Lattice Parameter (Å) | $Ni_2Cr$ | $Ni_2(Cr_{0.75}Mo_{0.25})$ | $Ni_2(Cr_{0.63}Mo_{0.37})$ | $Ni_2(Cr_{0.5}Mo_{0.5})$ |
|---|---|---|---|---|---|
| **Disorder** | **c** | 3.567 | 3.596 | 3.609 | 3.621 |
| **Order** | **a** | 2.515 | 2.536 | 2.545 | 2.554 |
| | **b** | 7.544 | 7.608 | 7.636 | 7.661 |
| | **c** | 3.556 | 3.586 | 3.599 | 3.611 |

In principle, progress of an ordering reaction is monitored by the appearance of superlattice peaks in diffraction patterns. However, structure factor considerations in the present case limited their detection in XRD experiments (Section 4.3). Therefore, peak shift due to lattice parameter contraction, broadening and splitting of the fundamental peaks during ordering was utilized to study the progress of ordering during isothermal ageing of $Ni_2(Cr_{0.63}Mo_{0.37})$ and $Ni_2(Cr_{0.5}Mo_{0.5})$ alloys at 680°C. Table 7.2 gives peak positions of the fundamental reflections of disordered phase and ordered phase in the $Ni_2(Cr_{0.5}Mo_{0.5})$ alloy computed according to lattice parameters given in table 7.1. It could be seen from table 7.2 that {1 1 1}, {2 0 0} and {2 2 2} peaks of the fcc structure would split into two peaks, while all other peaks would split into multiple peaks upon ordering. Due to minimum separation of

**Table 7.2** $2\theta$ positions of diffraction peaks in the disordered and ordered state of $Ni_2(Cr,Mo)$ alloy computed using lattice parameters given in table 7.1.

| **Positions of fundamental reflections** | | | | |
|---|---|---|---|---|
| **Disordered FCC, {h k l}** | | **Ordered Orthorhombic, (HKL)** | | **Separation ($2\theta$)** |
| **Reflections** | **$2\theta$** | **Reflections** | **$2\theta$** | |
| {1 1 1} | 43.456 | (1 0 1) | 43.449 | 0.004 |
| | | (0 3 1) | 43.453 | |
| | | | | |
| {2 0 0} | 50.614 | (1 3 0) | 50.605 | 0.009 |
| | | (0 0 2) | 50.614 | |
| | | | | |
| {2 2 0} | 74.391 | (2 0 0) | 74.37 | 0.012 |
| | | (0 6 0) | 74.382 | 0.001 |
| | | (1 3 2) | 74.383 | |
| | | | | |
| {3 1 1} | 90.287 | (2 3 1) | 90.266 | 0.008 |
| | | (1 6 1) | 90.274 | |
| | | (1 0 3) | 90.283 | 0.009 |
| | | (0 3 3) | 90.285 | 0.002 |
| | | | | |
| {2 2 2} | 95.531 | (2 0 2) | 95.511 | 0.011 |
| | | (0 6 2) | 95.522 | |

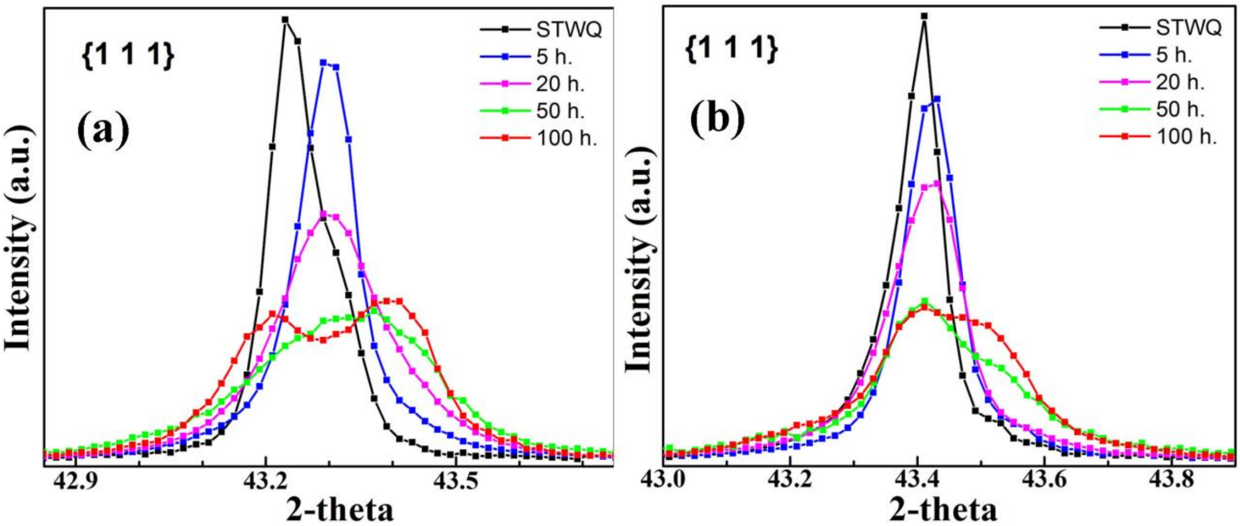

**Figure 7.3:** Peak broadening of {1 1 1} peak in x-ray diffraction with ageing time at 680°C in; (a) $Ni_2(Cr_{0.5}Mo_{0.5})$ alloy; and (b) $Ni_2(Cr_{0.63}Mo_{0.37})$ alloy. The peak splitting was evident at ageing times of 50 h and 100 h in both the alloys.

ordered phase reflections in the {1 1 1} peak, lattice parameter instabilities in the ordered phase would be easy to observe in XRD by monitoring peak broadening / splitting of {1 1 1} peak. This was also favoured by minimum instrumental broadening effect on the peak broadening of {1 1 1} peak which was the strongest peak in the diffraction pattern (see Appendix III for details on the instrumental broadening). In $Ni_2(Cr_{0.5}Mo_{0.5})$ alloy, this peak first broadened with ageing time until split into two peaks after 100 h of ageing (Fig. 7.3a). As TEM evidences shown earlier in Section 5.4 have established that nearly complete disordered matrix transformed into the ordered phase after 100 h of ageing of the $Ni_2(Cr_{0.5}Mo_{0.5})$ alloy, the observed twin peaks first could be suggested due to $(1\ 0\ 1)_o$ and $(0\ 3\ 1)_o$ reflections of the ordered phase. However, apparently larger separation between two peaks ($\Delta\theta_{observed}$=0.18°) than expected ($\Delta\theta_{theoretical}$=0.004°, see table 7.2) ruled out this possibility. In addition, continuous increase of peak separation with the progress of ordering also ruled out the possibility of appearance of twin peaks due to $(1\ 0\ 1)_o$ and $(0\ 3\ 1)_o$ reflections. It was therefore not unreasonable to deduce that the observed twin peaks in fully ordered state of $Ni_2(Cr_{0.5}Mo_{0.5})$ alloy corresponded to ordered structures having slightly different lattice parameters, which could be due to difference in their chemical compositions.

Likewise, {1 1 1} peak in the $Ni_2(Cr_{0.63}Mo_{0.37})$ alloy exhibited a similar broadening effect during initial stages ageing times, which ultimately showed a tendency to split into two peaks during prolonged ageing (fig. 7.3b), though well separated peaks, as seen in $Ni_2(Cr_{0.5}Mo_{0.5})$ alloy, did not appeared even after 100 h of ageing. Microstructural evidences on this alloy as shown earlier in Section 5.4 too revealed nearly complete transformation of the disordered matrix into the order structure within 100 h of ageing.

### 7.2.2. Neutron diffraction:

Neutron diffraction experiments were carried out on $Ni_2(Cr_{0.5}Mo_{0.5})$ alloy which was aged at 680°C for 100 h. Room temperature as well as high temperature in-situ experiments were used to monitor the changes in the superlattice peaks using neutron having de-Broglie wavelength of 1.3 Å. Room temperature neutron diffraction pattern is shown in fig.7.4 in

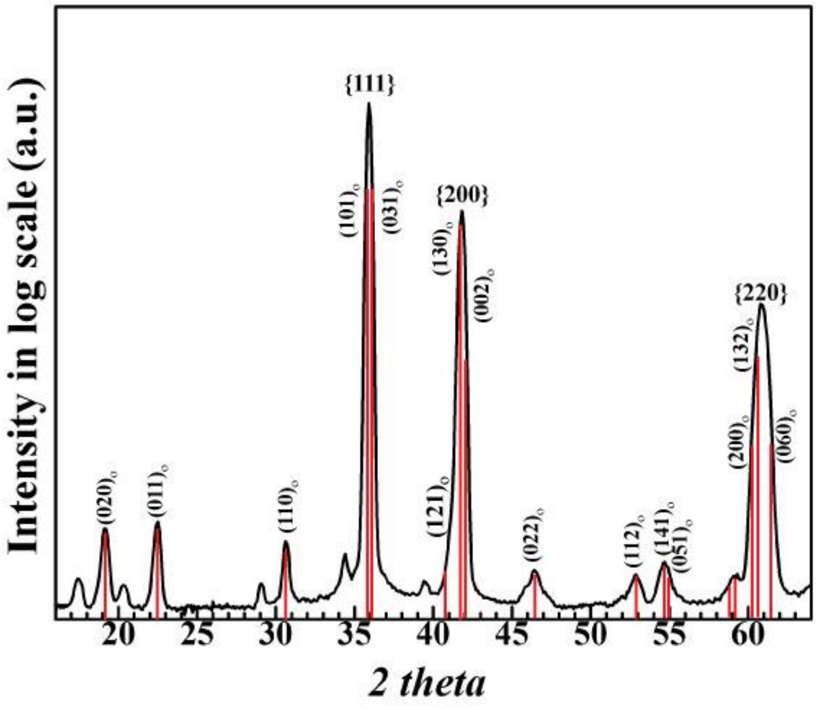

**Figure 7.4:** Room temperature neutron diffraction pattern from fully ordered $Ni_2(Cr_{0.5}Mo_{0.5})$ alloy (aged at 680°C for 100 h) showing diffraction peaks indexed w.r.t. fcc structure as well as in terms of ordered $Ni_2(Cr,Mo)$ phase reflections. Red lines correspond to the theoretical calculated position of the peaks.

which diffraction peaks were indexed both w.r.t. fcc structure as well as the orthorhombic structure. A sequence of neutron diffraction patterns obtained at different temperatures during in-situ heating is shown in fig.7.5 which clearly shows that the intensity of superlattice peaks undergo a gradual decay in a continuous manner until it disappeared completely at about 760°C temperature. Complete extinction of superlattice peaks at 760°C was in agreement with resistivity and TEM studies reported earlier. However, typical feature of peak splitting and broadening of fundamental peaks, as found in XRD (Fig. 7.3) could not be observed in neutron diffraction. The inability of neutron diffraction to reveal the peak splitting could be attributed to its higher instrumental broadening contribution. This became clear when FWHM of fundamental peaks observed by XRD were compared with those obtained by neutron diffraction in the solution treated state of $Ni_2(Cr_{0.5}Mo_{0.5})$ alloy (Fig. 7.6) – neutron diffraction

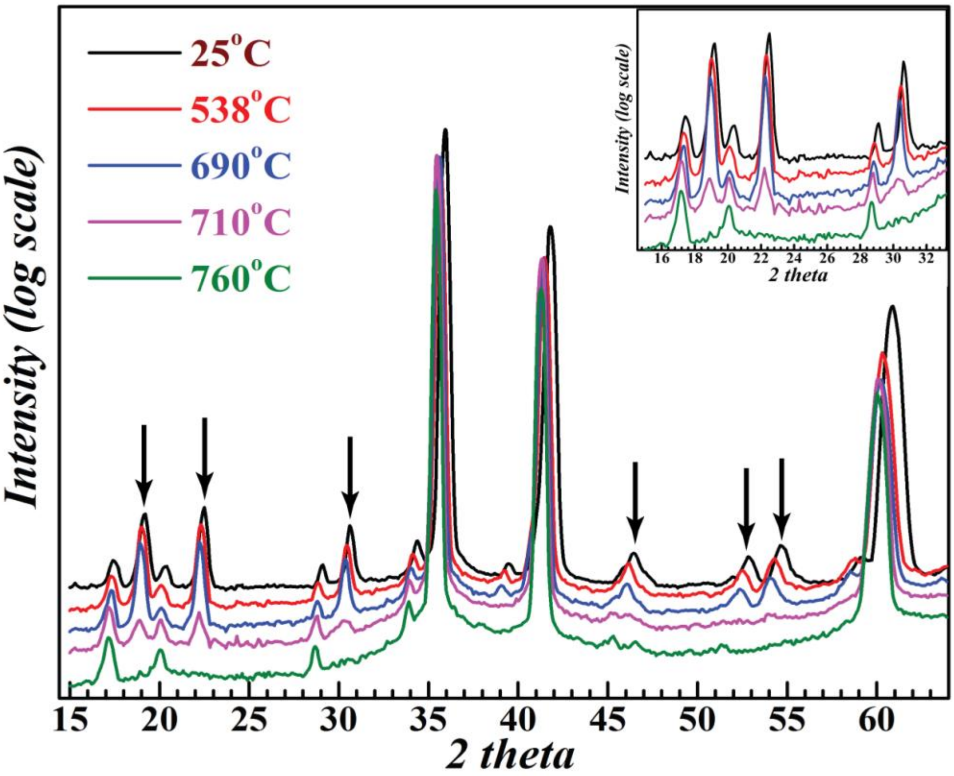

**Figure 7.5:** High temperature in-situ neutron diffraction patterns from fully ordered $Ni_2(Cr_{0.5}Mo_{0.5})$ alloy showing the disappearance of superlattice reflections (peaks marked by arrows) at 760°C.

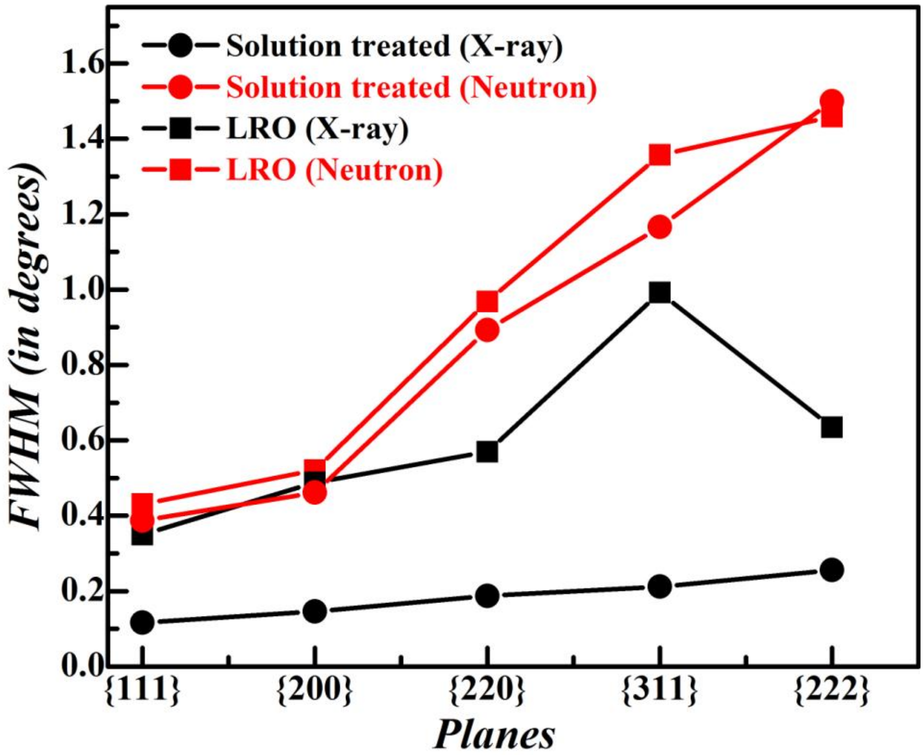

**Figure 7.6:** Full width at half maximum (FWHM) plots of different peaks in the solution treated and fully ordered (LRO) $Ni_2(Cr_{0.5}Mo_{0.5})$ alloy investigated by x-ray and neutron diffraction.

exhibited significantly higher broadening than by XRD. The amount of this broadening was in-fact higher than that caused by the change in microstructural state of the alloy due to the ordering transformation (compare FWHM in the disordered and ordered state of the alloy measured by XRD in fig. 7.6). This confirmed that large contribution of instrumental broadening in neutron diffraction was responsible for its inability to reveal peak splitting during ordering transformation. Nonetheless, the appearance of number of superlattice peaks of the ordered phase in neutron diffraction was advantageous for the determination of cell parameters of the ordered phase. Rietveld analysis of the diffraction data using Full-Prof freeware software [126] revealed cell parameters of the ordered structure to be, a = 2.546 Å, b = 7.604 Å and c = 3.606 Å. Cell parameters ‘a’ and ‘c’ determined from the neutron diffraction pattern were in agreement with that given in table 7.1, while slightly lower ‘b’ parameter suggested that the methodology of Hirabayashi et al. [70] slight over estimates the b-axis.

## 7.3. Compositional characterization of ordered domains using 3D-AP:

In order to determine the compositions of the ordered domains, 3D-AP investigations were carried on both $Ni_2(Cr_{0.63}Mo_{0.37})$ and $Ni_2(Cr_{0.5}Mo_{0.5})$ alloys which were aged at 680°C for 100 h. A prolonged ageing treatment of 100 h was selected for 3D-AP experiments as this ageing time (at 680°C) was sufficient to produce ordered domains at their equilibrium compositions. Sharp needles prepared for 3D-AP investigations were first investigated by Field Ion Microscopy (FIM) in the presence of neon gas to clean the surface and image the microstructural features present at the apex of the tip. A FIM image of ordered domains imaged as bright regions in a investigated sample of $Ni_2(Cr_{0.63}Mo_{0.37})$ composition is shown in fig. 7.7. Visible ellipsoidal shape of domains was consistent with ordered domains imaged with TEM (Fig. 5.20). The 3-dimensional reconstruction map of individual atomic species after assigning different peaks in the mass spectrum is shown in fig. 7.8. It was clear from this figure that the middle part of the reconstructed volume was depleted of chromium atoms

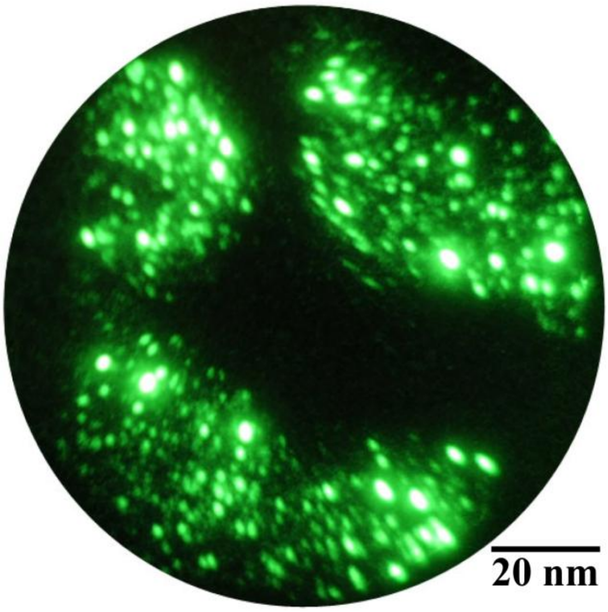

**Figure 7.7:** Field ion microscope image showing ordered domains as bright regions in the image obtained from $Ni_2(Cr_{0.63}Mo_{0.37})$ alloy aged at 680°C for 100h.

and enriched with molybdenum atoms while nickel distribution remained uniform throughout the whole reconstruction volume. This difference appeared clearly in the concentration depth profile shown in the same figure (below the reconstruction map). The concentration depth profile unambiguously established that ordered domains in the $Ni_2(Cr_{0.63}Mo_{0.37})$ alloy were either rich with Cr-atoms or Mo-atoms. The Cr-rich regions were found to have Ni-19.8at%Cr-13.4at%Mo and Ni-22.4at%Cr-10.8at%Mo compositions while the composition of Mo-rich region was Ni-13.1at%Cr-20.2at%Mo. Investigation of multiple samples too confirmed the existence of ordered domains with these compositions. This has been illustrated in fig. 7.9 where Cr-rich regions with composition close to Ni-19.8at%Cr-13.4at%Mo were seen at different parts of the reconstructed volume. The concentration depth profiles measured along selections through these regions (see square selections 1, 2 and 3) in reconstruction maps confirmed the existence of such regions as shown in the fig. 7.9. These concentration depth profiles also revealed the existence of regions having nickel concentration lower than that required for stoichiometric composition. These regions could, thus, be suggested to belong to the disordered matrix which could not transform into ordered phase due to smaller Ni-concentration left over in the region after ordering transformation. A magnified view of the reconstruction map of one such region exhibiting apparently lower nickel concentration (see the smallest selection in fig. 7.9) is shown in the same figure below the reconstruction maps of Ni, Cr and Mo atoms. Surprisingly, the reconstruction map drawn after including all constituent species had revealed a planar arrangement in the distribution of atomic species having interplannar spacing of about 1.8 Å. This distance was similar to the interplannar separation between (2 0 0) planes of the fcc lattice. However, absence of periodic variation in the concentration of individual atomic species in the concentration depth profile measured in the direction perpendicular to these planes (see figure below the small selection) supported the view of absence of any order in this region.

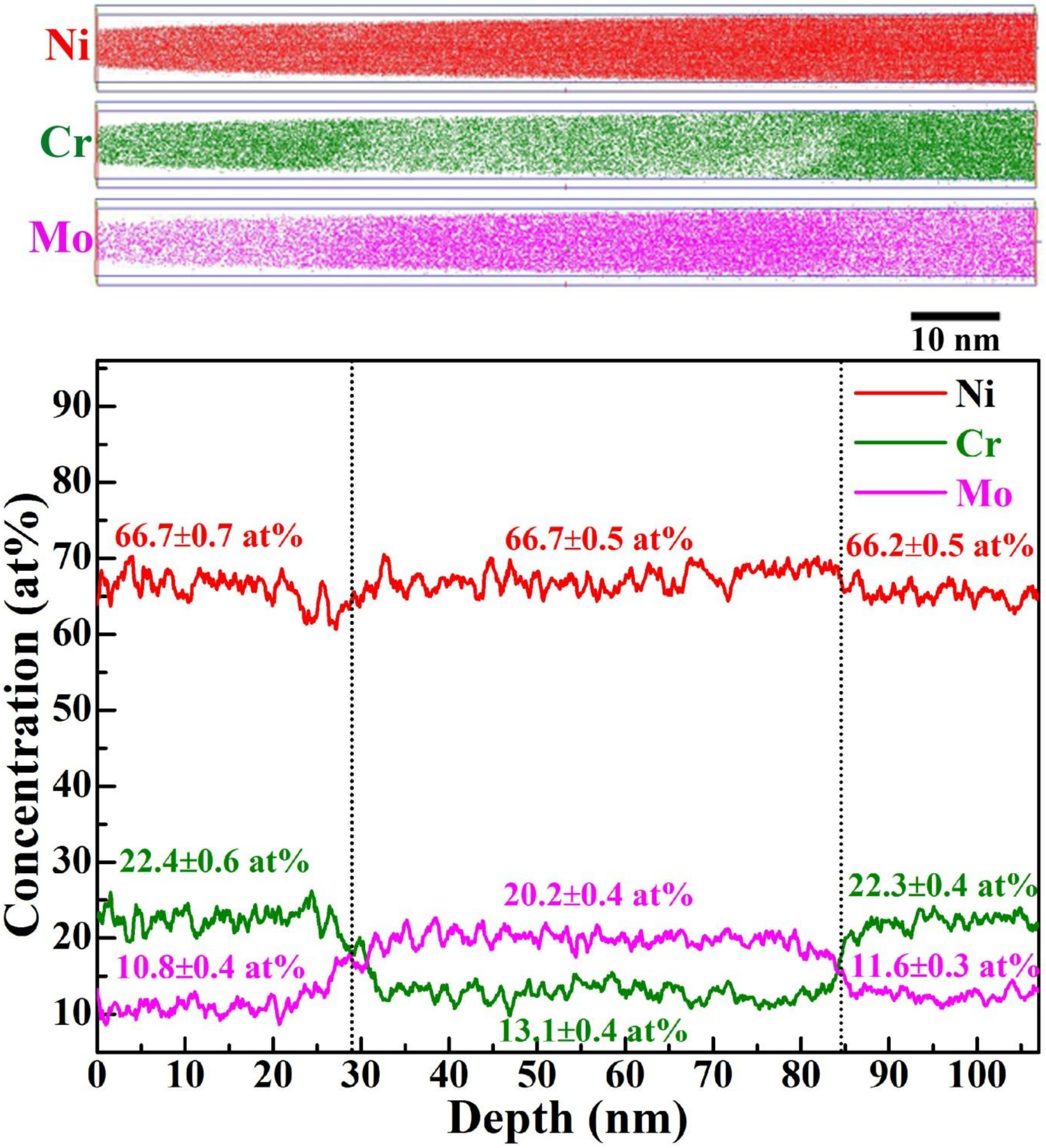

**Figure 7.8:** 3D-AP reconstruction map of Ni, Cr and Mo species in $Ni_2(Cr_{0.63}Mo_{0.37})$ alloy aged for 100 h at 680°C. The corresponding concentration profiles along the length of the reconstruction revealed the presence of Cr-rich and Mo-rich ordered domains.

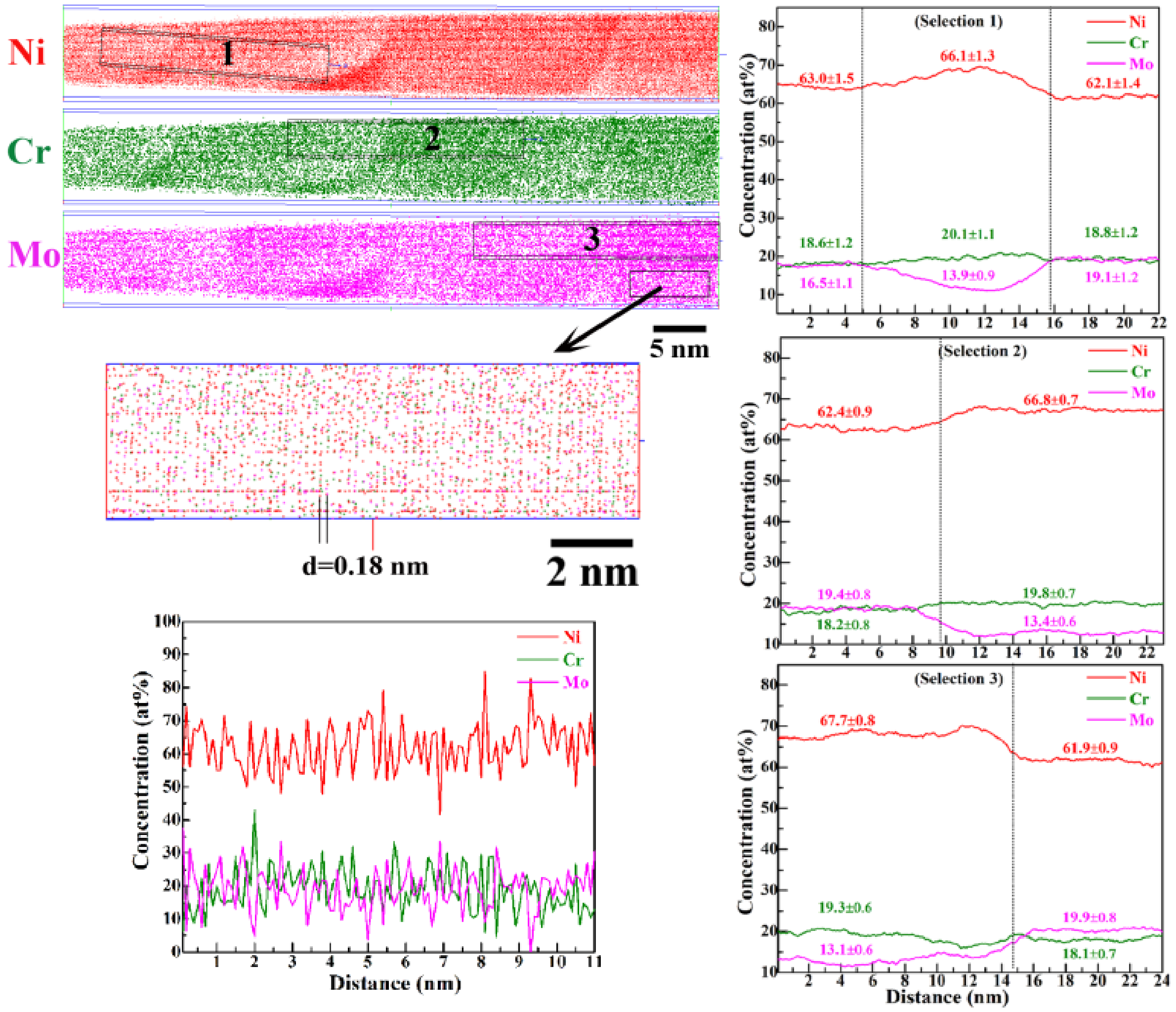

**Figure 7.9:** 3D-AP reconstruction map of Ni, Cr and Mo species in $Ni_2(Cr_{0.63}Mo_{0.37})$ alloy aged for 100 h at 680°C. Concentration depth profiles along different selections marked by 1, 2 and 3 in the reconstruction map are shown on the right hand side of the figure. The magnified section (below reconstruction maps) shows arrangement of {2 0 0} atomic planes. Below are the corresponding concentration depth profiles for Ni, Cr and Mo.

On similar lines, $Ni_2(Cr_{0.5}Mo_{0.5})$ alloy aged for 100 h at 680°C was studied. Fig. 7.10 shows ellipsoidal shaped bright regions in the FIM images of ordered domains in the $Ni_2(Cr_{0.5}Mo_{0.5})$ alloy. 3D-AP experiments were carried out on multiple samples as single experiment could not revealed different compositions due to larger domains sizes in this alloy. The 3D-AP investigation of one of the sample confirmed the presence of Mo-rich region having Ni-12.6at%Cr-20.6at%Mo composition (close to $Ni_2(Cr_{0.37}Mo_{0.63})$ stoichiometry) as revealed by

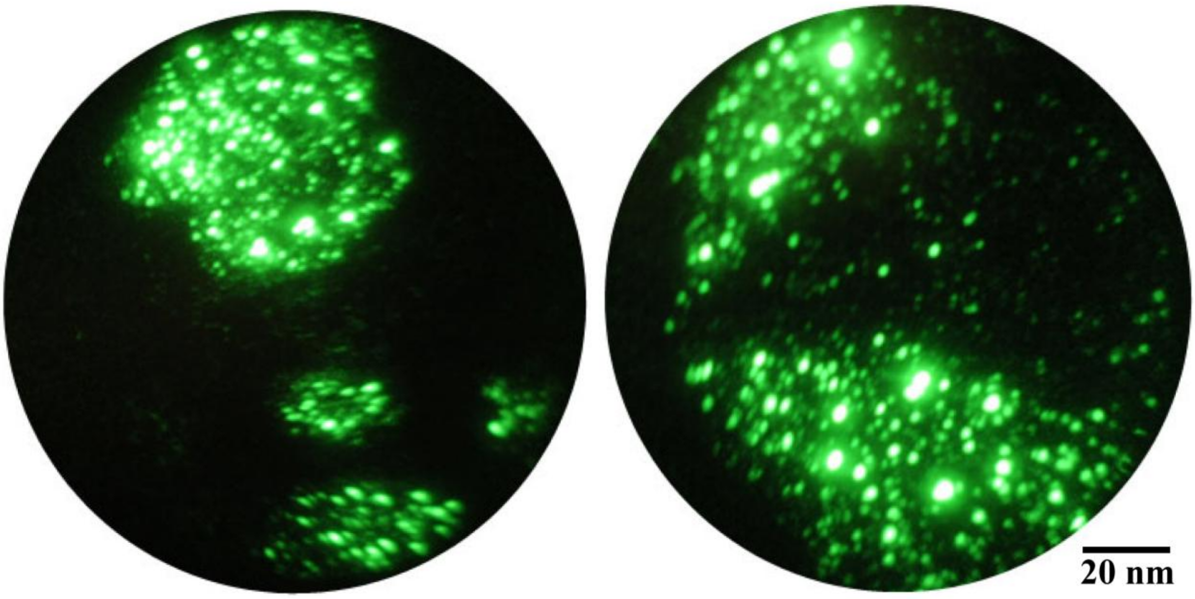

**Figure 7.10:** Field ion microscope images showing ordered domains as bright regions in the images obtained from different samples of $Ni_2(Cr_{0.5}Mo_{0.5})$ alloy aged at 680°C for 100h.

the concentration depth profile (Fig. 7.11a) corresponding to the reconstruction map shown in fig. 7.11b. Furthermore, fig. 7.11b revealed a planar arrangement in the distribution of nickel atoms which appeared more lucidly after taking out a small volume out of the reconstruction map (marked by a rectangle in fig. 7.11b). The enlarged view of this selection is shown as fig. 7.11c where planar arrangement of nickel atoms appeared more clearly having interplannar separation of about 3.6 Å. The concentration depth profile measured in a direction perpendicular to these planes established a periodic variation in the concentration of individual atomic species as shown in fig. 7.11d which supported the view that this region belonged to an ordered domain. It was clear from the concentration profiles that nickel concentration varied from maximum value of about 80 at% to a minimum value of about 50 at%, while Cr and Mo concentration varied in a fashion as shown in the figure 7.11d. This interplannar separation of about 3.6 Å was found to be in agreement with $(0\ 1\ 3)_o$ planes of the ordered structure (highlighted in the proposed structure for the $Ni_2(Cr_{0.37}Mo_{0.63})$ stoichiometry shown in fig. 7.11e). Calculated concentration profiles of individual constituents species in a direction perpendicular to $(0\ 1\ 3)_o$ planes is given in fig. 7.11e. A

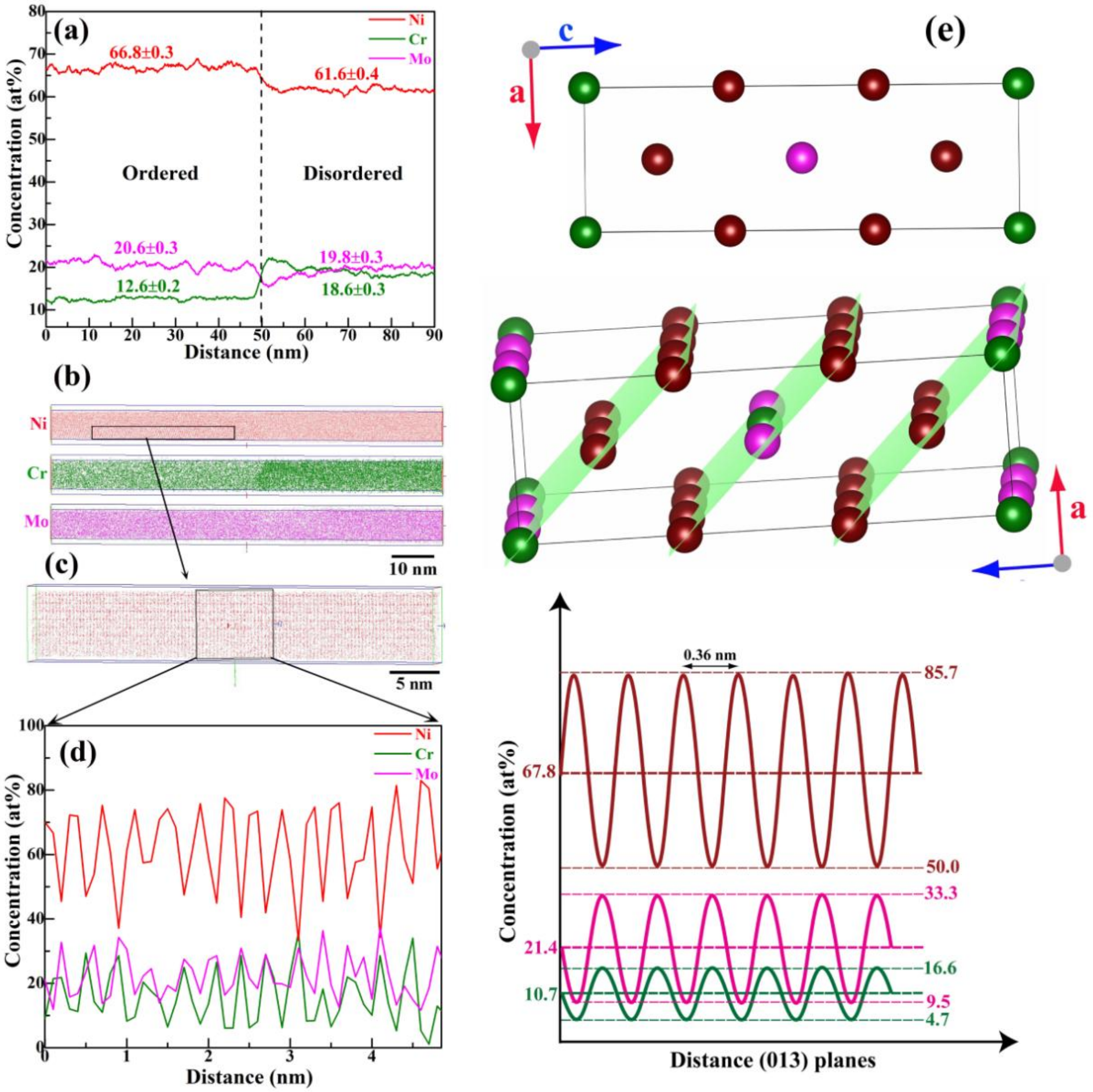

**Figure 7.11:** 3D-AP results of $Ni_2(Cr_{0.5}Mo_{0.5})$ alloy aged for 100 h at 680°C: (a) Concentration depth profile along the length of the atomic reconstruction maps shown in fig. (b); (c) enlarged view of small selection marked by a rectangle in fig. (b); and (d) shows a wave like concentration profiles of individual species corresponding to region marked by square selection in fig. (c). (e) shows unit cell of the ordered structure proposed for $Ni_2(Cr_{0.37}Mo_{0.63})$ composition with the calculated concentration depth profiles of individual species along [0 1 3] direction below the unit cell.

reasonably close agreement between the calculated concentration profiles with experimentally determined concentration profiles, further, suggested that the structure proposed in fig. 7.11e could represent the ordered structure of the $Ni_2(Cr_{0.37}Mo_{0.63})$ stoichiometry. In addition, fig. 7.11a also revealed region of about Ni-18.6at%Cr-19.8at%Mo composition in which nickel concentration was less than the stoichiometric composition. Karmazin et al. [14] have suggested that ordered $Ni_2(Cr,Mo)$ phase of stoichiometric composition can only tolerate small solute substitution on Ni sites, it was, therefore, not unreasonable to conclude that regions with significantly lower Ni-concentration corresponded to disordered regions.

Another sample revealed the existence of Mo-rich as well as Cr-rich regions of ordered domains (Fig. 7.12). Iso-concentration surfaces at 18.5at%Cr and 19.5at%Mo concentrations were used to delineate Cr-rich and Mo-rich regions in a reconstructed volume (see, Cr-rich region with green colour surface and Mo-rich region with pink colour surface inside of the reconstruction volume in fig. 7.12a). Individual selections of small volumes across these surfaces were made to determine compositions inside of the iso-concentration surfaces which are shown by selection 1 and selection 2 in fig. 7.12b. A concentration depth profile measured along z-axis of these selections confirmed the existence of Mo-rich ordered domains of Ni-13.6at%Cr-20.at%Mo composition (Fig. 7.12c) and Cr-rich ordered domains of Ni-20.0at%Cr-13.6at%Mo type (Fig. 7.12d). Measured compositions were quite close to stoichiometric $Ni_2(Cr_{0.37}Mo_{0.63})$ and $Ni_2(Cr_{0.63}Mo_{0.37})$ compositions, respectively, and the same could be suggested to exist in the ordered phase.

Apart from these two compositions, regions with equiatomic Cr and Mo solutes concentration were also seen in another investigated sample. However, concentration of nickel atoms appeared to be little lower than that required for stoichiometric composition. The reconstruction map of individual Ni, Cr and Mo atoms are shown in fig. 7.12. In this map

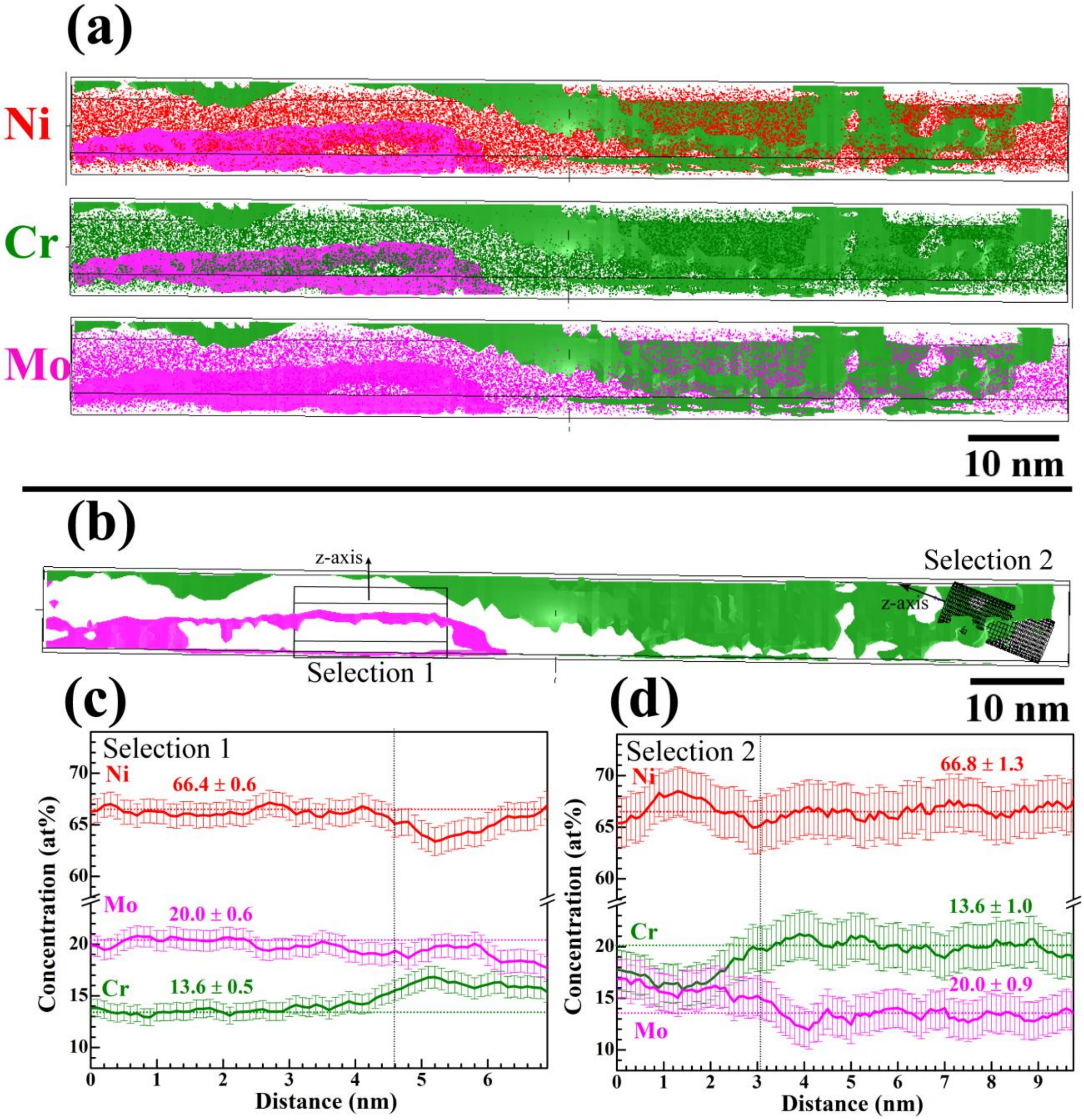

**Figure 7.12:** (a) Iso-concentration surfaces at 19.5at%Mo (shown with pink surface) and 18.5 at%Cr (shown with green surface) in 3-dimensional reconstruction maps of nickel, chromium and molybdenum atoms in the $Ni_2(Cr_{0.5}Mo_{0.5})$ alloy aged for 100 h at 680°C. (b) shows two selections made across iso-concentration surfaces of Cr and Mo atoms. Concentration depth profiles along the z-axis of the selections shown in the reconstruction maps are given below in figs. (c) and (d).

two different regions having nearly equiatomic Cr and Mo solute concentration were separated by a region which was enriched of Cr. This was found by drawing iso-concentration surface at 22at%Cr concentration which is shown by a green colour in the reconstruction map. A concentration depth profile measured along the length of a cylinder (radius 2.5 nm) which was drawn perpendicular to the iso-concentration surface revealed that this interface was enriched with Cr while depleted of nickel. The composition of the regions outside the iso-concentration surface was found to be Ni-18.7at%Cr-17.1at%Mo. These regions could be suggested to belong to ordered part of the domains and a slight enrichment of Cr solutes at the cost of nickel atoms could be due to the partial substitution of nickel sites by Cr atoms. Compositions of regions belonging to the ordered phase determined by 3D-AP studies in two alloys are given in table 7.3 with the nearest equivalent stoichiometric composition.

**Table 7.3:** Composition of the regions belonging to ordered domains determined by 3-dimensional atom probe experiments

| **S. No.** | **Compositions measured by 3D-AP experiments in** | | **Equivalent stoichiometric composition** |
|---|---|---|---|
| | ***Ni-21at%Cr-12.3at%Mo alloy*** | ***Ni-16.6at%Cr-16.6at%Mo alloy*** | |
| 1. | Ni-13.9at%Cr-20.2at%Mo | Ni-12.6at%Cr-20.6at%Mo | ~$Ni_2(Cr_{0.37}Mo_{0.63})$ |
| 2. | Ni-22.4at%Cr-13.9at%Mo | Ni-20.9at%Cr-12.0at%Mo | ~$Ni_2(Cr_{0.63}Mo_{0.37})$ |
| 3. | - | Ni-17.1at%Cr-18.7at%Mo | ~$Ni_{1.8}(Cr_{0.52}Mo_{0.48})$ |

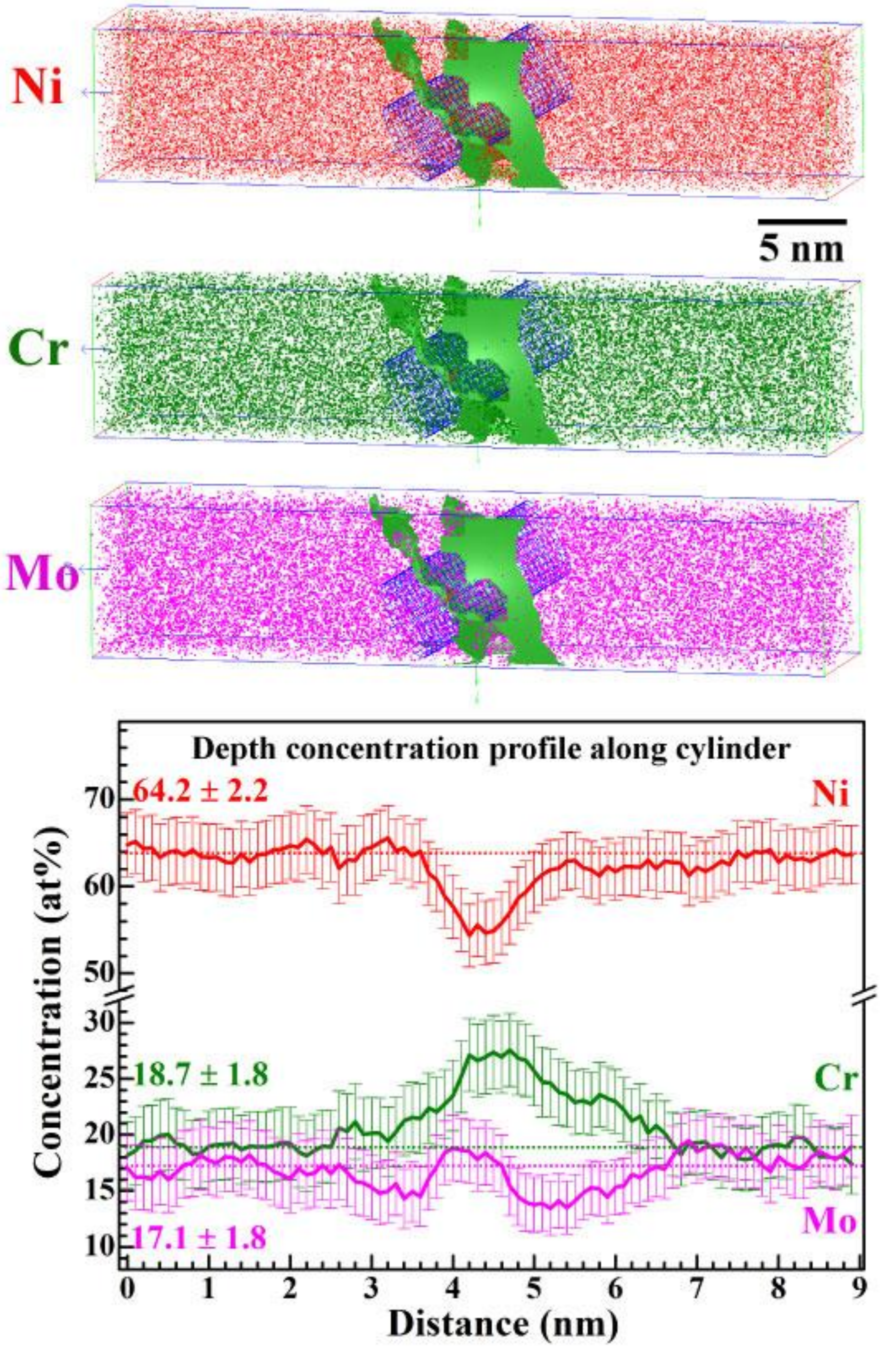

**Figure 7.13:** 3D-AP reconstruction map of Ni, Cr and Mo atoms in $Ni_2(Cr_{0.5}Mo_{0.5})$ alloy aged for 100 h at 680°C. Iso-concentration surface at 22at%Cr concentration is shown by green colour in the reconstruction maps. A concentration depth profile of individual species along the length of a cylinder located perpendicular to the iso-concentration surface is shown below the reconstruction maps.

### 7.4. Discussion:

Ni-Cr-Mo-base alloys containing different concentration of Cr and Mo solutes are known to form ordered $Ni_2(Cr,Mo)$ phase in them [10, 11, 14, 15, 27, 29, 39, 47, 61, 62, 65, 68, 70, 127-129]. The stability of this ordered phase has been shown to be affected by relative amount of Cr and Mo solutes in the $Ni_2(Cr,Mo)$ phase [26, 65]. In binary Ni-Cr alloys this phase has been found to have maximum stability at the stoichiometric $Ni_2Cr$ composition [12, 26]. The stability of this ordered phase has been further found to increase with the partial substitution of Cr by Mo atoms in stoichiometric $Ni_2(Cr,Mo)$ phase [26]. However, Karmazin et al. [14] have found that this phase would have higher stability at compositions different than the stoichiometry of the ordered phase, which they have suggested on the basis of phase boundary of ordered phase in Ni-Cr-Mo alloys having varying amount of Ni and Cr for a fixed Cr/Mo ratio of 3. On the basis of their study, they suggested that Mo atoms can substitute the lattice sites occupied by both Ni and Cr atoms in the ordered structure. This appears to be consistent with the composition of $Ni_2(Cr,Mo)$ precipitates (of about Ni-22.6at%Cr-12.9at%Mo) in commercial Ni-base alloy (Alloy C-22HS having composition Ni-24.7at%Cr-10.8at%Mo) experimentally determined by using energy-dispersive X-ray (EDX) studies in TEM.

The greater importance of this phase in many Ni-base alloys encouraged researcher to understand the stability of this ordered phase at different concentrations of Cr and Mo solutes. This can be seen in a recent theoretical investigation by Hu et al. [65] who have studied the formation energy of $Ni_2(Cr_{1-x}Mo_x)$ phase by systematically varying Cr and Mo solute concentration from $x = 0$ to 0.5. Hu et al. [65] have found that the formation energy decreases continuously with the increase of Mo until it reaches a minimum value at $Ni_2(Cr_{0.75}Mo_{0.25})$ composition beyond which it increases again and reaches a maximum value at $Ni_2(Cr_{0.5}Mo_{0.5})$ composition. On its basis they have suggested a least stability of the ordered phase at $Ni_2(Cr_{0.5}Mo_{0.5})$ composition.

Though, a higher stability of the ordered phase at $Ni_2(Cr_{0.75}Mo_{0.25})$ composition has been suggested by Hu et al. [65], existence of ordered phase at $Ni_2(Cr_{0.63}Mo_{0.37})$ stoichiometry in two different alloys supported its higher stability over $Ni_2(Cr_{0.75}Mo_{0.37})$ stoichiometry. In addition, the existence of composition close to $Ni_2(Cr_{0.37}Mo_{0.63})$ stoichiometry in the ordered regions of two different alloys established that ordered phase would have higher stability at $Ni_2(Cr_{0.63}Mo_{0.37})$ and $Ni_2(Cr_{0.37}Mo_{0.63})$ stoichiometric compositions. This has been depicted in fig. 7.14 which compares the formation energy of this ordered phase reported by different researchers at different compositions. Whereas, Chan et al. [26] calculated the formation energy of the ordered phase at three different stoichiometric compositions which were situated towards Mo-rich side (shown by filled circles) in fig. 7.14, the formation energy calculated by Hu et al. [65] filled the gaps towards Cr-rich side of the composition which are shown by red colour square symbols. However, existence of ordered phase at two similar compositions in two different alloys suggested that formation energy minima should appear at compositions marked by cyan colour square symbols in the same figure. In addition to it, the existence of ordered phase at equiatomic Cr and Mo solute concentration ($Ni_{1.8}(Cr_{0.52}Mo_{0.48})$) in $Ni_2(Cr_{0.5}Mo_{0.5})$ alloy, despite of the least stability of $Ni_2(Cr_{0.5}Mo_{0.5})$ phase, suggested that partial substitution of Mo atoms by Ni and Cr atoms in the $Ni_2(Cr_{0.5}Mo_{0.5})$ phase could have resulted in a change in its stability by changing its formation energy. This appeared to be consistent with the study of Karmazin et al. [14] who have found greater stability of the ordered phase at slightly off-stoichiometric composition. Existence of ordered domains with different compositions in the ordered microstructure of the alloy, thus, could be correlated with their slightly different lattice parameters. On this basis, it could be argued that the fundamental peaks characterizing the

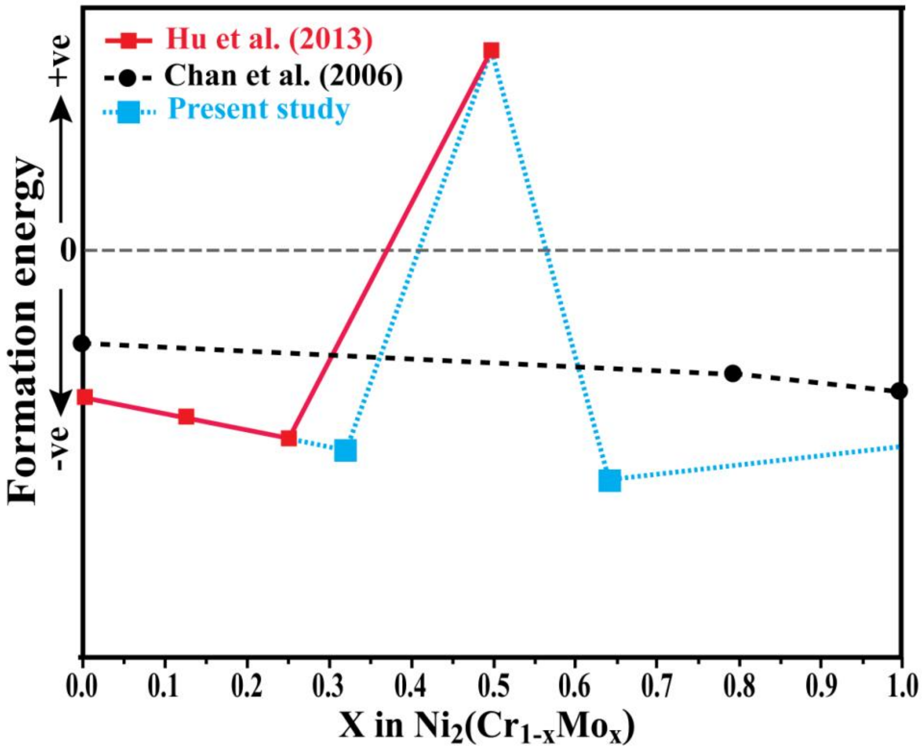

**Figure 7.14:** Formation energy of $Ni_2$(Cr,Mo) phase calculated by different researchers at different concentrations of Cr and Mo solutes. Same figure shows a modified plot drawn on the basis of experimental evidences obtained in the present study.

ordered microstructure (in x-ray diffraction) were the convolution effect of different peaks due to slightly different lattice parameters of the ordered domains. In-fact, the relative volume fraction of these ordered domains would decide the apparent splitting of the fundamental peaks. As ordered phase was identified with $Ni_2(Cr_{0.63}Mo_{0.37})$ and $Ni_2(Cr_{0.37}Mo_{0.63})$ compositions in $Ni_2(Cr_{0.63}Mo_{0.37})$ alloy, apparent broadening and splitting of {1 1 1} peak could be attributed to different lattice parameters of these ordered domains as shown in fig.7.2b, while additional composition of $Ni_{1.8}(Cr_{0.52}Mo_{0.48})$ would also contribute to the broadening and splitting of {1 1 1} peak in the $Ni_2(Cr_{0.5}Mo_{0.5})$ alloy. In $Ni_2(Cr_{0.63}Mo_{0.37})$ alloy, smaller Mo content in it would limit the maximum volume fraction of $Ni_2(Cr_{0.37}Mo_{0.63})$ ordered phase which could be the possible reason for apparently weaker splitting of {1 1 1} peak even after 100 h of ageing time. As the formation of Mo-rich ordered phase ($Ni_2(Cr_{0.37}Mo_{0.63})$) in $Ni_2(Cr_{0.63}Mo_{0.37})$ alloy would also create Mo-depleted regions, which could be suggested as possible reason for the appearance of convoluted peak towards higher $2\theta$ side after longer ageing times. On the contrary, composition of $Ni_2(Cr_{0.5}Mo_{0.5})$ alloy would allow the formation of equal volume fraction of ordered phase with $Ni_2(Cr_{0.37}Mo_{0.63})$ and $Ni_2(Cr_{0.63}Mo_{0.37})$ compositions, due to which peak splitting appeared clearly in this alloy after 100 h of ageing.

XRD and 3D-AP evidences, therefore, clearly established that the ordered phase in both $Ni_2(Cr_{0.63}Mo_{0.37})$ and $Ni_2(Cr_{0.5}Mo_{0.5})$ alloys had a tendency to phase separate into $Ni_2(Cr_{0.63}Mo_{0.37})$ and $Ni_2(Cr_{0.37}Mo_{0.63})$ compositions. This phase separation, however, happened after a prolonged ageing as shown by XRD experiments (Fig. 7.3) by splitting of the single {111} peak into a doublet (clearly visible after 100 h of ageing at 680°C). From the hardness data (Fig. 7), it was clear that the $Ni_2(Cr_{0.5}Mo_{0.5})$ alloy achieved maximum hardness within 5 h of ageing while that in the $Ni_2(Cr_{0.63}Mo_{0.37})$ alloy reached within 20 h, suggesting that the two alloys had reached nearly full order within these periods. Correlating the hardness and the XRD data, it was evident that at these times the respective alloys still exhibited single {111} XRD peak and only ageing beyond these periods exhibited continuous broadening and splitting of the XRD peaks while maintaining a plateau in their hardness values. Therefore, it was not unreasonable to assume that these alloys first formed ordered phase corresponding to alloy stoichiometry and phase separated later due to compositional instability. This deduction was on the lines of the assumption used in Figure 5.26, where stoichiometry of the ordered phase was considered to be that of respective alloy compositions because ordering temperatures were obtained during isochronal heating experiments. The equilibrium ordering temperature of the two alloys would in fact be different due to the presence of ordered phases of $Ni_2(Cr_{0.63}Mo_{0.37})$ and $Ni_2(Cr_{0.37}Mo_{0.63})$ stoichiometries and the actual value would depend upon their relative volume fractions and the interface separating them. Identification of these temperatures and mechanisms involved in separation of the ordered phases require detailed simulation studies, which is outside the scope of present work.

On the basis of the present work, following conclusions can be made.

1. $Ni_2(Cr,Mo)$ phase has more stability at $Ni_2(Cr_{0.63}Mo_{0.37})$ and $Ni_2(Cr_{0.37}Mo_{0.63})$ compositions.
2. During ordering, alloys form ordered phase with stoichiometry corresponding to respective alloy compositions and later during prolonged ageing tends to phase separate into $Ni_2(Cr_{0.63}Mo_{0.37})$ and $Ni_2(Cr_{0.37}Mo_{0.63})$ compositions.
3. X-ray diffraction is more suitable method to follow peak splitting of fundamental peaks over neuron diffraction during ordering transformation on the studied alloys.
4. Relative volume fraction of different compositions of ordered domains govern the peak splitting of fundamental peaks in x-ray diffraction during ordering transformation.

# CHAPTER 8

# SUMMARY AND CONCLUSIONS

In this dissertation, detailed investigation of the formation of ordered $Ni_2(Cr,Mo)$ phase has been carried out in $Ni_2(Cr_{1-x},Mo_x)$ alloys containing varying amounts of Cr and Mo solutes (x = 0 to 0.5). Complete order evolution path has been identified and micromechanisms involved in the order evolution have been proposed. On the basis of present study, following conclusions can be made.

- The order evolution in Ni-Cr-Mo alloys may involve one or more of following steps depending upon alloy composition, thermal history and ageing temperature:
    vi. evolution of the SRO from the disordered phase;
    vii. transformation of the SRO to LRO;
    viii. growth of the LRO;
    ix. dissolution of the LRO; and
    x. evolution of SRO during the dissolution of LRO.
- Evolution of the ordered $Ni_2(Cr,Mo)$ phase occurs via a continuous ordering mechanism involving both 1st order and 2nd order transformation mode, while the growth / dissolution of ordered phase occurred via 1st order mode. The 2nd order transformation mode operates during the transition of the alloy from short-range order to long-range order or vice-versa. Lattice diffusion of Cr atoms governs the formation of the ordered $Ni_2(Cr,Mo)$ phase during continuous ordering mode in Ni-Cr-Mo alloys having Mo/Cr ratios $\leq 0.33$ and by Cr as well Mo diffusion in alloys having Mo/Cr $> 0.33$.
- The ordering kinetics increases significantly with when diffusion of Mo atoms starts playing role in the ordering mechanism.

- Formation of the ordered $Ni_2(Cr,Mo)$ phase is always preceded by the appearance of SRO. However, suppression of the SRO significantly retards the ordering process. This has been attributed to significant changes in pair interactions that cause sluggish ordering kinetics. Thus, faster quenching methods or other means, which can suppress or reduce the initial SRO, offer means of retarding the evolution of the ordered $Ni_2(Cr,Mo)$ phase in Ni-Cr-Mo alloys.
- Different SROs observed in different alloys have been correlated to the presence of specific types of chemical heterogeneities. The {1 1/2 0} SRO observed in the $Ni_2Cr$ alloys predominantly contains $Ni_3Cr$ type heterogeneities while the $Ni_2(Cr_{0.5}Mo_{0.5})$ alloy that exhibits {1 ½ 0} SRO as well as 1/3{2 2 0} SRO contains predominant heterogeneities of $Ni_{0.55}(Cr,Mo)_{0.45}$ types.
- Compositional analysis of ordered $Ni_2(Cr,Mo)$ domains revealed their preference to stabilize at $Ni_2(Cr_{0.63}Mo_{0.37})$ (i.e., Cr-rich) and $Ni_2(Cr_{0.37}Mo_{0.63})$ (i.e., Mo-rich) compositions irrespective of alloy composition.

# *Future scope of work*

1. Determination of Warren-Cowley SRO parameters in splat-quenched and solution treated $Ni_2(Cr_{1-x}Mo_x)$ alloys using Extended X-ray absorption fine structure (EXAFS) studies can be suggested as one of possible work to quantitatively understand the changes in the atomistic architecture during the suppression of SRO in splat-quenched samples.
2. Evolution of Warren-Cowley SRO parameters in $Ni_2(Cr_{1-x}Mo_x)$ alloys during order evolution using in-situ heating EXAFS experiments can be proposed as another work.
3. Detailed calculations of the formation energy of $Ni_2(Cr_{1-x}Mo_x)$ phases with x varied from 0 to 1 can be suggested as one of the possible area in which thorough 1st principle calculation are required to understand the stability of the ordered phase at different Mo/Cr ratios.
4. In-situ heating high resolution synchrotron diffraction experiments on $Ni_2(Cr_{0.63}Mo_{0.37})$ and $Ni_2(Cr_{0.5}Mo_{0.5})$ alloys can be suggested for future work to understand lattice parameters instabilities in the ordered $Ni_2$(Cr,Mo) phase during order evolution.
5. Microstructural understanding of order evolution in $Ni_2(Cr_{1-x}Mo_x)$ alloys can be used as a guideline to evaluate the mechanical properties of these alloys.

# APPENDIX I

## *Calculation of Intensity of Reflections in XRD Patterns*

The intensity of a reflection in the X-ray diffraction is given by the formula [130]

$$I_S = I_o \times |F_S|^2 \times m \times LPF \qquad \text{....(A.I.1)}$$

Where $I_o$ = a constant depending upon the intensity of incident radiation, F is the structure factor for the reflection, m is the multiplicity factor and LPF is the Lorentz-polarization factor. The structure factor for fundamental and superlattice reflections for the $Pt_2Mo$ type structure has been derived in chapter 3 and is as follows:

$$F_f = 2(2f_N + f_M) \qquad \text{.... (A.I.2)}$$

$$F_s = 2S(f_N - f_M) \qquad \text{.... (A.I.3)}$$

where subscripts N and M represent atoms occupying different sublattices. In the case of $Ni_2(Cr,Mo)$ phase, N position are occupied by nickel atoms, M positions by either chromium or molybdenum and S is the order parameter for $Ni_2(Cr,Mo)$ phase. When more than one atom can occupy a particular sub lattice position, the atomic scattering factor is expressed as the weighted average depending upon the probability for each atom to occupy that site. Now the equations (A.I.2) and (A.I.3) simplify to

$$F_f = 2[2f_{Ni} + (xf_{Cr} + (1 - x)f_{Mo})] \qquad \text{.... (A.I.4)}$$

$$F_f = 2S[f_{Ni} - (xf_{Cr} + (1 - x)f_{Mo})] \qquad \text{.... (A.I.5)}$$

where, x is the concentration of Cr in the phase.

The Lorentz-Polarization factor (LPF) is defined as:

$$LPF = \frac{1 + \mathrm{Cos}^2(2\theta)}{8 \times \mathrm{Sin}^2(\theta) \times \mathrm{Cos}^2(\theta)} \qquad \text{....(A.I.6)}$$

**The atomic scattering Factor:**

The atomic scattering factor, f, is often assumed to be independent of wavelength of radiation. This is true only when the wavelength of incident radiation is much smaller than the wavelength of absorption edges corresponding to different electronic levels in the scattering atom which is the case in electron diffraction in transmission electron microscopes. In the case of x-ray diffraction, the wavelength of incident radiation is of the same order as the wavelength of absorption edges for some of the elements; the atomic scattering factor depends strongly on the photoelectric absorption and anomalous scattering [131].

The corrected atomic scattering factor is given by the formula

$f = f_o + f' + i f''$ …. (A.I.7)

where f is the normal scattering factor in the absence of corrections, $f'$ and $f''$ are the real and imaginary dispersion terms which account for the difference between the idealized case and the actual case. Substituting this value of f in the expression (A.1.4) and (A.1.5) and simplifying we get $F^2$ as

$$F_f^2 = 4\left[\{2(f_{Ni} + f'_{Ni}) + x(f_{Cr} + f'_{Cr}) + (1-x)(f_{Mo} + f'_{Mo})\}^2 + \left\{2f''_{Ni} + xf''_{Cr} + (1-x)f''_{Mo}\right\}^2\right]$$

…. (A.I.8)

and

$$F_s^2 = 4\left[\{(f_{Ni} + f'_{Ni}) - x(f_{Cr} + f'_{Cr}) - (1-x)(f_{Mo} + f'_{Mo})\}^2 + \left\{f''_{Ni} - xf''_{Cr} - (1-x)f''_{Mo}\right\}^2\right]$$

…. (A.I.9)

The atomic scattering factors of different elements of interest in present case have been computed using the values for $f_o$, $f'$ and $f''$ values taken from literature [132] for Cu-$K_\alpha$ radiations which are commonly used as monochromatic x-ray sources and are given in table A.I.1. The values $F_f^2$ and $F_s^2$ calculated using these atomic scattering factor values are given in table 2.7. The superlattice reflections that are normally used to follow/identify ordering in $Pt_2Mo$ structure are ⅓{2 2 0}, ⅓{1 1 3} and ⅓{4 2 0}. The ratio of intensity of superlattice to fundamental peaks corresponding to the same family of planes is used to determine whether the superlattice reflections will be visible and whether they can be used to detect order. These values are theoretically determined for different alloys investigated in present study and are given in table 2.7 in Chapter 2.

| **hkl** | $\frac{\sin\theta}{\lambda}$ | **Atomic scattering factor**<br>**Cu $K_\alpha$** | | |
|---|---|---|---|---|
| | | $\mathbf{f_{Ni}}$ | $\mathbf{f_{Cr}}$ | $\mathbf{f_{Mo}}$ |
| ⅓ (220) | 0.131 | 24.714 | 20.734 | 37.016 |
| (220) | 0.394 | 15.871 | 12.474 | 24.955 |
| ⅓ (311) | 0.154 | 23.973 | 20.022 | 35.907 |
| (311) | 0.461 | 13.937 | 10.917 | 22.832 |
| ⅓ (420) | 0.207 | 21.794 | 17.915 | 32.676 |
| (420) | 0.621 | 10.581 | 8.6444 | 19.211 |
| $\mathbf{f'}$ | - | -2.956 | -0.198 | -0.191 |
| $\mathbf{f''}$ | - | 0.509 | 2.443 | 2.735 |

# APPENDIX II

## *Calculation of wave amplification of concentration waves*

The time evolution of concentration waves, $A_m$, for a given wave vector during a diffusion reaction at smaller length scale [59], can be described by equation A.II.1 in the small amplitude limits.

$$A_m(k) = A_m^\circ(k)*\exp[\alpha(k)*t] \ldots\ldots\ldots\ldots\ldots\ldots\ldots\ldots \textit{(A.II.1)}$$

where, $A_m^\circ$ is the initial amplitude of concentration wave at t = 0, and $\alpha(k)$ is the amplification factor which is related to the second derivative of free energy [59]. This amplification factor, for a given Fourier component, k, depends strongly on $V(k)$ especially at temperatures relatively lower than the instability temperature as shown by Kulkarni [79] and can be known using equations 6.1 and 6.2 of Chapter 6. Similarly, equation 6.2 can be used to determine the concentration wave amplitude at t = 0. The value of function $V(k)$ required for computing equation 6.2 for a given wave-vector can be found using the equation A.II.2

$$V(k) = \sum_{i=1}^{10} S_i(k) \times v_i(k) \ldots\ldots\ldots\ldots\ldots\ldots\ldots\ldots \textit{(A.II.2)}$$

where, $S_i(k)$ are shell functions representing number of like atoms minus unlike atoms in the ith coordination shell and $v_i(k)$ are the average pair interaction energies in the ith coordination shell about a given atomic species and is defined as

$$v_i = E_{iAB} - 1/2\,(E_{iAA} + E_{iBB}) \ldots\ldots\ldots\ldots\ldots\ldots\ldots\ldots\ldots\ldots \textit{(A.II.3)}$$

where $E_{iAA}$, $E_{iBB}$ and $E_{iAB}$ being the energies of the AA, BB and AB pairs, respectively, for the ith coordination shell. A negative value of $v_i$ thus indicates preference for unlike ith nearest neighbour pairs.

Considering the importance of waves corresponding to disordered, {1 ½ 0} and {2/3 2/3 0} state in present case, shell functions and pair interaction energies found by Kulkarni et al.

[79] in $Ni_2Mo$ alloy (given in table A.II.1) have been used in present case to compute the temporal evolution of these waves according to equation A.II.1.

**Table A.II.1** Values of shell functions and pair interaction energies given by kulkarni et al. [79] in equiatomic binary alloy used in present case to compute temporal evolution of different concentration waves.

| S. No. | Shell No. | Shell Function ($S_i$) corresponding to wave-vectors | | | Pair interaction energies ($v_i$) |
|---|---|---|---|---|---|
| | | disordered | 1 ½ 0 | ⅔ ⅔ 0 | |
| 1 | <½ ½ 0> | 6 | -4 | -3 | -1 |
| 2 | <1 0 0> | 3 | 2 | 0 | 0.1923 |
| 3 | <1 ½ ½> | 12 | 8 | 6 | 0.4615 |
| 4 | <1 1 0> | 6 | -4 | -3 | -0.0769 |
| 5 | < 3/2 ½ 0> | 12 | -8 | 0 | 0.1154 |
| 6 | <1 1 1> | 4 | -8 | 2 | 0.0769 |
| 7 | <3/2 1 ½> | 24 | 16 | -12 | 0.0154 |
| 8 | <2 0 0> | 3 | 6 | 0 | 0 |
| 9 | <3/2 3/2 0> | 6 | -4 | 12 | 0.0385 |
| 10 | <2 ½ ½> | 12 | -8 | 6 | -0.0231 |

# APPENDIX III

## *Determination of instrument contribution towards peak broadening in XRD*

The contribution of the instrumental broadening on the diffraction peaks in the XRD patterns was obtained by measuring diffraction pattern on NIST standard $CeO_2$ powder using experimental conditions identical to actual experiments. The statistics of the measurement was improved by measuring diffraction patterns at a step of 0.01° with sufficient acquisition time in order to increase peak to background ratio. The instrumental contribution was then determined by measuring full width at half maxima of individual peaks in the diffraction pattern. Standard Caglioti relationship given by equation A.III.1 was used to fit the instrumental broadening (FWHM) response at different $\theta$ values and is shown by fig. A.III.1.

$$FWHM^2 = A\tan^2\theta + B\tan\theta + C \text{.................................... } A.III.1$$

It was clear from fig. A.II.1 that the contribution of instrumental broadening remained smaller for $\theta$ values less than 50° and increased at higher rate beyond it.

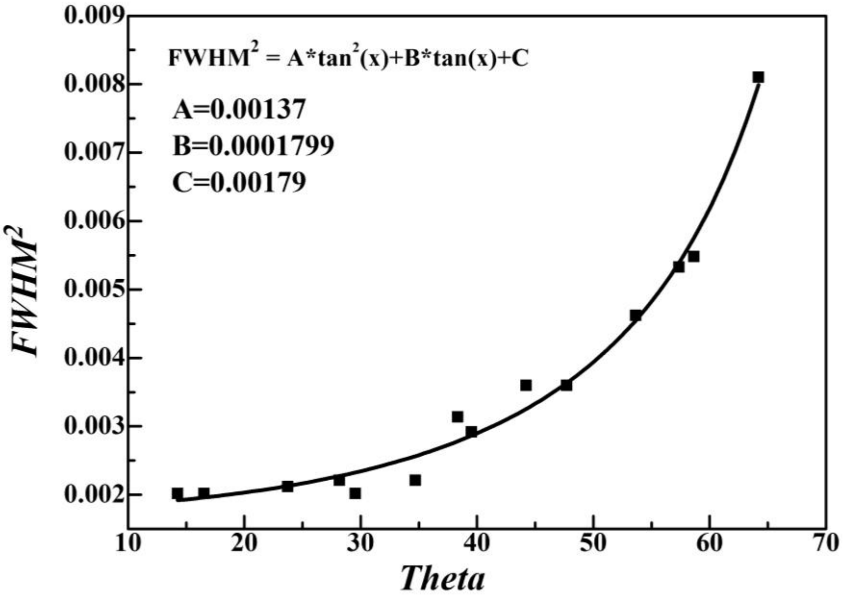

**Figure A.III.1:** Plot of instrumental broadening obtained with NIST standard $CeO_2$ powder.

## References:

[1] C.T. Sims, N.S. Stoloff, W.C. Hagel. Superalloys II, John Wiley and Sons, New York, 1987.

[2] M.J. Cieslak, T.J. Headley, A.D. Romig. The Welding Metallurgy of Hastelloy alloys C-4, C-22 and C-276, Metallurgical Transactions A 17A (1986) 2035-2047.

[3] E. Metcalfe, B. Nath. Some effects of the ordering transformation in Nimonic 80A on stress relaxation behaviour, Material Science and Engineering 67 (1984) 157-162.

[4] J.B. Singh, A. Verma, D.M. Jaiswal, N. Kumar, R.B. Patel, J.K. Chakravartty. Rejuvenation of service exposed ammonia cracker tubes of cast Alloy 625 and their re-use, Material Science and Engineering A 644 (2015) 254-267.

[5] P.S. Pao, S.J. Gill, C.R. Feng, D.J. Michel. Fatigue and fracture of a $Ni_2Cr$ ordered intermetallic alloy, Materials Science and Engineering A153 (1992) 532-537.

[6] K. Miyata, M. Igarashi. Effect of Ordering on Susceptibility to Hydrogen Embrittlement of a Ni-base Superalloy, Metallurgical and Materials Transactions A 23A (1992) 953-961.

[7] B.J. Berkowitz, C. Miller. The Effect of Ordering on the Hydrogen Embrittlement Susceptibility of $Ni_2Cr$, The Metallurgical Society of AMIE 11A (1980) 1877-1881.

[8] A. Marucco, B. Nath. Effects of ordering on the properties of Ni-Cr alloys, Journal of Material Science 23 (1988) 2107-2114.

[9] P. Nash. in Binary Alloy Phase Diagram. 2 ed., ASM International, OH, 1990.

[10] P.E.A. Turchi, L. Kaufman, Z.-K. Liu. Modeling of Ni–Cr–Mo based alloys: Part I—phase stability, Calphad 30 (2006) 70-87.

[11] H.J. Klein, C.R. Brooks, E.E. Stansbury. The Establishment of Long-Range Order in $Ni_2Cr$ Using Electron Microscopy, Physica Status Solidi (a) 38 (1970) 831-836.

[12] L. Karmazin. Lattice parameter studies of structure changes of Ni-Cr Alloys in the region of $Ni_2Cr$, Material Science and Engineering 54 (1982) 247–256.

[13] U.D. Kulkarni, S. Banerjee. Phase separation during the early stages of ordering in $Ni_3Mo$, Acta Metallurgica 36 (1988) 413–424.

[14] L. Karmazin, J. Krejci, J. Zeman. Gamma Phase and $Ni_2Cr$-type long-range order in Ni-rich Ni-Cr-Mo alloys, Materials Science and Engineering A 183 (1994) 103-109.

[15] H.C. Pai, M. Sundararaman, B.C. Maji, A. Biswas, M. Krishnan. Influence of Mo addition on the solvus temperature of $Ni_2(Cr,Mo)$ phase in $Ni_2(Cr,Mo)$ alloys, Journal of Alloys and Compounds 491 (2010) 159-164.

[16] Y. Chen, R. Hu, H. Kou, T. Zhang, J. Li. Precipitation of nanosized $DO_{22}$ superlattice with high thermal stability in an Ni–Cr–W superalloy, Scripta Materialia 76 (2014) 49–52.

[17] D.S. Bloom, N.J. Grant. An Investigation of the Systems Formed By Chromium, Molybdenum, and Nickel, Transactions of the AIME 200 (1954) 261-268.

[18] I. Class, H. Grafen, E. Scheil. Development of a corrosion resistant Ni-Cr-Mo Alloy and little harmful precipitation, Z. Metallk. 53 (1962) 283-293.

[19] E. Gozlan, M. Bamberger, S.F. Dirnfeld, B. Prinz, J. KIod. Topologically close-packed precipitations and phase diagrams of Ni-Mo-Cr and Ni-Mo-Fe and of Ni-Mo-Fe with constant additions of chromium, Materials Science and Engineering A141 (1991) 85-95.

[20] L. Kaufman, H. Nesor. Calculation of superalloy phase diagrams Part I, Metallurgical Transactions 5 (1974) 1617-1621.

[21] J.R. Mihalisin, C.G. Bieber, R.T. Grant. Sigma-Its occurrence, effect, and control in Nickel-base Superalloys, Transactions of the AIME 242 (1968) 2399-2414.

[22] M. Raghavan, R.R. Mueller, G.A. Vaughn, S. Floreen. Determination of Isothermal Sections of Nickel Rich Portion of Ni-Cr-Mo System by Analytical Electron Microscopy, Metallurgical and Materials Transactions A 15A (1984) 783-792.

[23] S. Rideout, W.D. Manly, E.L. Kamen, B.S. Lement, P.A. Beck. Intermediate Phase in ternary Alloy Systems of Transition Metals, Transactions of the AIME 191 (1951) 872-876.

[24] A.K. Jena, S.B. Rajendraprasad, K.P. Gupta. The Cr-Mo-Ni (Chromium-Molybdenum-Nickel) System, J. Alloy Phase Diagrams 5 (1989) 164-177.

[25] G.E. Gdowski. Survey of Degradation Modes of Four Nickel-Chromium-Molybdenum Alloys. In: UCRL-ID-108330 LRN-, (Ed.): Lawrence Livermore National Laboratory, 1991.

[26] K.S. Chan, Y. Pan, Y. Lee. Computation of Ni-Cr Phase Diagram via a Combined First-Principles Quantum Mechanical and CALPHAD Approach, Metallurgical and Materials Transactions A 37A (2006) 2039-2050.

[27] M. Sundararaman, L. Kumar, G.E. Prasad, P. Mukhopadhyay, S. Banerjee. Precipitation of an Intermetallic Phase with $Pt_2Mo$-Type Structure in Alloy 625, Metallurgical and Materials Transactions A 30A (1999) 41-52.

[28] M.K. Miller, I.M. Anderson, L.M. Pike, D.L. Klarstrom. Microstructural characterization of Haynes® 242™ alloy, Materials Science and Engineering A 327 (2002) 89–93.

[29] X.M. Li, J.W. Bai, P.P. Liu, Y.M. Zhu, X.S. Xie, Q. Zhan. Coherent $Ni_2$(Cr, Mo) precipitates in Ni–21Cr–17Mo superalloy, Journal of Alloys and Compounds 559 (2013) 81-86.

[30] Y. Ustinovshikov. Phase and structural transformations in the $Ni_{65}Mo_{20}Cr_{15}$ alloy at changing the temperature of heat treatment, Journal of Alloys and Compounds 588 (2014) 470-473.

[31] S.K. Das, P.R. Okamoto, P.M.J. Fisher, G. Thomas. Short range order in Ni-Mo, Au-Cr, Au-V and Au-Mn alloys, Acta Metallurgica 21 (1973) 913-928.

[32] P.R. Okamoto, G. Thomas. On Short Range Order and Micro-Domains in the $Ni_4Mo$ system, Acta Metallurgica 19 (1971) 825-841.

[33] E. Ruedl, P. Delavignette, S. Amelinckx. Electron diffraction and electron microscopic study of long and short-range order in $Ni_4Mo$ and of the substructure resulting from ordering, Physica Status Solidi 28 (1968) 305–328.

[34] T. Saburi, K. Komatsu, M. Yamamoto, S. Nenno, Y. Mizutani. Trans. Metall. Soc. AMIE 245 (1969) 2348.

[35] J.E. Spruiell, E.E. Stansbury. X-Ray Study of short-range order in Nickel alloys containing10.7 and 20.0 at. % Molybdenum, J. Phys. Chem. Solids 26 (1965) 811-822.

[36] M. Yamamoto. An Atom-probe FIM study of the short-range order in an Ni4Mo alloy, Scripta Metallurgica 19 (1985) 357-360.

[37] U.D. Kulkarni, G.K. Dey. Ordering and topologically close packed-phase precipitation in a Ni–25at.%Mo–5at.%Al alloy, Acta Materialia 52 (2004) 2711-2720.

[38] P.L. Martin, J.C. Williams. Long range order in $Ni_3Mo$ based ternary alloys-I. Isothermal aging response, Acta Metallurgica 32 (1984) 1681-1693.

[39] M. Kumar, V.K. Vasudevan. Ordering reactions in an Ni-25Mo-8Cr alloy, Acta Materialia 44 (1996) 1591-1600.

[40] K. Binder, D. Stauffer. Theory for the Slowing Down of the Relaxation and Spinodal Decomposition of Binary Mixtures, Physical Review Letters 33 (1974) 1006-1009.

[41] E. Lang. Effect of Thermomechanical Treatments on Short-range Ordering and Secondary-phase Precipitation in Ni-Cr-based Alloys, Materials Science and Engineering All4 (1989) 147-157.

[42] W. Pfeiler. Investigation of short-range order by electrical resistivity measurement, Acta Metallurgica 36 (1988) 2417-2434.

[43] J. Richter, G. Schubert. Physica Status Solidi B 116 (1983) 597-605.

[44] P.L. Rossiter. Electrical resistivity near the critical point in binary alloys, J. Phys. F: Met. Phys. 10 (1980 ) 1787-1793.

[45] J. Soltys, R. Kozubski, A. Michalek. Resistometric study of short-range ordering in Ni-10at.% Mo, Materials Science and Engineering A117 (1989 ) L 17-L 19.

[46] R.J. White, K.M. Miller. The role of quenched-in vacancies in the ageing of Nimonic alloys, Journal of Nuclear Materials 66 (1977) 101-106.

[47] H.G. Baer. Überstruktur und K-Zustand im System Nickel-Chrom, Z. Metallkde. 49 (1958) 614-622.

[48] K. Binder, D. Stauffer. Behavior of the Electrical Resistivity at Phase Transitions in Binary Alloys, Z. Physik B 24 (1976) 407-415.

[49] A. Arya, G.K. Dey, V.K. Vasudevan, S. Banerjee. Effect of chromium addition on the ordering behaviour of Ni–Mo alloy: experimental results vs. electronic structure calculations, Acta Materialia 50 (2002) 3301–3315.

[50] J.W. Gibbs. The Scientific Papers of J. Willard Gibbs, Dover, New York, 1961.

[51] J.W. Christian. The theory of Transformations in Metals and Alloys, Pergamon Press, Oxford, 1975.

[52] D. De Fontaine. Ordering Instabilities and Pretransitional Effects, Metallurgical and Materials Transactions A 12A (1981) 559.

[53] H.E. Cook. Continuous transformations, Materials Science and Engineering 25 (1976) 127 - 134.

[54] M. Hillert. A solid-solution model for inhomogeneous systems, Acta Metallurgica 9 (1961) 525-535.

[55] J.W. Cahn. On spinodal decomposition, Acta Metallurgica 9 (1961) 795-801.

[56] J.W. Cahn. On spinodal decomposition in cubic crystals, Acta Metallurgica 10 (1962) 179-183.

[57] J.W. Cahn. Coherent fluctuations and nucleation in isotropic solids, Acta Metallurgica 10 (1962) 907-913.

[58] H.E. Cook, D. Fontaine de. On the elastic free energy of solid solutions—II. Influence of the effective modulus on precipitation from solution and the order-disorder reaction, Acta Metallurgica 19 (1971) 607-616.

[59] H.E. Cook, D. Fontaine de, J.E. Hilliard. A model for diffusion on cubic lattices and its application to the early stages of ordering, Acta Metallurgica 17 (1969) 765-773.

[60] H.E. Cook, D. Fontaine de. On the elastic free energy of solid solutions—I. Microscopic theory, Acta Metallurgica 17 (1969) 915-924.

[61] H.M. Tawancy, M.O. Aboelfotoh. High strength and high ductility in a nanoscale superlattice of $Ni_2(Cr,Mo)$ deformable by twinning, Scripta Materialia 59 (2008) 846-849.

[62] H.M. Tawancy, M.O. Aboelfotoh. Application of long-range ordering in the synthesis of a nanoscale $Ni_2$ (Cr,Mo) superlattice with high strength and high ductility, Materials Science and Engineering: A 500 (2009) 188-195.

[63] T.B. Massalski. Handbook of Alloy Phase Diagrams, ASM Materials Park, Ohio, 1990.

[64] S. Banerjee, U.D. Kulkarni, K. Urban. Initial stages of ordering in $Ni_3Mo$-thermal and irradiation ordering experiments, Acta Metallurgica 37 (1989) 35–48.

[65] R. Hu, G.M. Cheng, J.Q. Zhang, J.S. Li, T.B. Zhang, H.Z. Fu. First principles investigation on the stability and elastic properties of $Ni_2Cr_{1-x}M_x$ (M=Nb, Mo, Ta, and W) superlattices, Intermetallics 33 (2013) 60-66.

[66] K.S. Chan, Y.M. Pan, Y.D. Lee. First-Principles Computations of Mechanical Properties of $Ni_2Cr$ and $Ni_2Mo$, Metallurgical and Materials Transactions A 37 (2006) 523-537.

[67] L.E. Tanner. The ordering transformation in $Ni_2V$, Acta Metallurgica 20 (1972) 1197-1227.

[68] H.M. Tawancy, R.B. Herchenroeder, A.I. Asphahani. High-Performance Ni-Cr-Mo-W Alloys, J. Metals 35 (1983) 37-43.

[69] U. Czubayko, Y. Zhang, N. Wanderka, V. Naundorf, H. Wollenberger. Analysis of nano-scaled composition fluctuations as observed by 3-dimensional atom probing of alloys, Z. Metallkd. 91 (2001) 897-900.

[70] M. Hirabayashi, M. Koiwa, K. Tanaka, T. Tadki, T. Saburi, S. Nenno, H. Nishiyama. An Experimental Study on the Ordered Alloy Ni2Cr, Tranactions of the Japan Institute of Metals 10 (1969) 365-371.

[71] V. Sears. Neutron scattering lengths and cross section, Neutron News 3 (1992) 29-37.

[72] M.J. Buerger. The Genesis of Twin Crystals, The Ameican Mineralogist 30 (1945) 469 - 482.

[73] M. Sundararaman, P. Mukhopadhyay, S. Banerjee. Some aspects of The Precipitation of Metastable Intermetallic Phases in Inconel 718, Metallurgical and Materials Transactions A 23A (1992) 2015- 2028.

[74] J. Mayer, K. Urban. Spinodal ordering in $Ni_4Mo$, Acta Metallurgica 33 (1985) 539-543.

[75] U.D. Kulkarni, G.K. Dey, S. Banerjee. Ordering in rapidally solified $Ni_2Mo$, Scripta Metallurgica 22 (1988) 437-440.

[76] S. Hata, S. Matsumura, N. Kuwano, K. Oki, D. Shindo. Short Range Order in $Ni_4Mo$ and its High Resolution Electron Microscopic Images, Acta Materialia 46 (1998) 4955-4961.

[77] S. Hata, H. Fujita, C.G. Schlesier, S. Matsumura, N. Kuwano, K. Oki. Monte Carlo study of ordering processes in fcc-based Ni-Mo alloys, Material Transactions - Japan Institute of Metal 39 (1998) 133-138.

[78] S. Hata, D. Shindo, T. Mitate, N. Kuwano, S. Matsumura, K. Oki. HRTEM image contrast of short range order in $Ni_4Mo$, Micron 31 (2000) 533–538.

[79] U.D. Kulkarni. Monte Carlo simulation of ordering transformations in Ni–Mo-based alloys, Acta Materialia 52 (2004) 2721-2732.

[80] D. De Fontaine. K-space symmetry rules for order–disorder reactions, Acta Metallurgica 23 (1975) 553–571.

[81] M.A. Krivoglaz. Theory of X-ray and thermal Neutron Scattering by Real Crystals, Plenum Press, New York, 1969.

[82] A.G. Khachaturyan. Ordering in substitutional and interstitial solid solutions, Progress Material Science 22 (1978) 1-150.

[83] A.G. Khachaturyan. The problem of symmetry in statistical thermodynamics of substitutional and interstitial ordered solid solutions, Physics Statuts Solidi B 60 (1973) 9-37.

[84] R.C. Ruhl. Cooling rates in splat cooling, Material Science and Engineering 1 (1967) 313-320.

[85] X.P. Tan, D. Mangelinck, C. Perrin-Pellegrino, L. Rougier, C.A. Gandin, A. Jacot, D. Ponsen, V. Jaquet. Spinodal Decomposition Mechanism of γ’ Precipitation in a Single Crystal Ni-Based Superalloy, Metallurgical and Materials Transactions A 45 (2014) 4725-4730.

[86] D. Blavette, B. Deconihout, A. Bostel, J.M. Sarrau, M. Bouet, A. Menand. The tomographic atom probe: A quantitative three-dimensional nanoanalytical instrument on an atomic scale Review of Scientific Instruments 64 (1993) 2911-2919.

[87] A. Bostel, D. Blavette, A. Menand, J.M. Sarrau. Toward a Tomographic Atom-Probe, Le Journal de Physique Colloques 50 (1989) C8-501-C508-506.

[88] A. Cerezo, T.J. Godfrey, G.D.W. Smith. Application of a position-sensitive detector to atom probe microanalysis, Review of Scientific Instruments 59 (1988) 862-866.

[89] G.L. Kellogg, T.T. Tsong. Pulsed-laser atom-probe field-ion microscopy, Journal of Applied Physics 51 (1980) 1184-1193.

[90] E.W. Müller. Field Ionization and Field Ion Microscopy, Advances in Electronics and Electron Physics 13 (1960) 83-179.

[91] E.W. Müller. Field Ion Microscopy, Science 149 (1965) 591-601.

[92] M.K. Miller, A. Cerezo, M.G. Hetherington, G.D.W. Smith. Atom Probe Field Ion Microscopy. Oxford: Oxford University Press, 1996.

[93] M.K. Miller, G.D.W. Smith. Atom Probe Microanalysis: Principles and Application to Materials Problems. Pittsburgh, PA: Materials Research Society, 1989.

[94] R. Wagner. Field-Ion-Microscopy in Materials Science. Berlin: Springer-Verlag, 1982.

[95] J. Rüsing, V. Naundorf, N. Wanderka, H. Wollenberger. Analysis of the decomposition of Cu-Ni and Fe-Ni alloys at lower temperatures by atom probe, Ultramicroscopy 73 (1998) 267-272.

[96] Y. Zhang, U. Czubayko, N. Wanderka, V. Naundorf, F. Zhu, H. Wollenberger. Distribution of Boron in Fe-14B before and after Primary Crystallization, Scripta Materialia 44 (2001) 263-267.

[97] U. Czubayko, N. Wanderka, V. Naundorf, V.A. Ivchenko, A.Y. Yermakov, M.A. Uimin, H. Wollenberger. Three-dimensional atom probing of supersaturated mechanically alloyed Cu–20at.% Co, Materials Science and Engineering A 327 (2002) 54-58.

[98] A. Verma, M. Sundararaman, J.B. Singh, S.A. Nalawade. A new method for determining the Curie temperature using a dilatometer, Measurement Science and Technology 21 (2010) 105106-105115.

[99] M. Yamamoto, S. Nenno, T. Saburi, Y. Mizutani. Structural Changes during Isothermal Annealing of the Quenched Ni3Mo Alloy (I), Trans. JIM 11 (1970) 120-126.

[100] S. Hata, T. Mitate, N. Kuwano, S. Matsumura, D. Shindo, K. Oki. Short range order structures in fcc-based Ni–Mo studied by high resolution transmission electron microscopy with image processing, Materials Science and Engineering A 312 (2001) 160–167.

[101] D.M.C. Nicholson, R.H. Brown. Electrical resistivity of $Ni_{0.8}Mo_{0.2}$: Explanation of anomalous behavior in short-range ordered alloys, Physical Review Letters 70 (1993) 3311-3315.

[102] R. Caudron, M. Sarfati, M. Barrachin, A. Finel, F. Solal. In situ diffuse scatterings of neutrons on binary alloys, Physica B 180 & 181 (1992) 822-824.

[103] X. Sauvage, G. Dacosta, R.Z. Valiev. 3rd International Symposium on ultrafine grained materials. In: Zhu YT, Langdon TG, Valiev RZ, Semiatin SL, Shin DH, Lowe TC, (Eds.). TMS Annual Meeting, vol. 31. Charlotte, NC, 2004.

[104] S. Hata, S. Matsumura, N. kuwano, K. Oki. Short range order and its transformation to long range order in $Ni_4Mo$, Acta Materialia 46 (1998) 881-892.

[105] A. Verma, J.B. Singh, M. Sundararaman, N. Wanderka. Resistivity and Transmission Electron Microscopy Investigations of Ordering Transformation in Stoichiometric $Ni_2(Cr_{0.5}Mo_{0.5})$ Alloy, Metallurgical and Materials Transactions A 43 (2012) 3078-3085.

[106] G.W.H. Höhne, W.F. Hemminger, H.J. Flammersheim. Differential Scanning Calorimetry. Second Edition ed., Springer, Germany, 2003.

[107] H.E. Kissinger. Variation of Peak Temperature With Heating Rate in Differential Thermal Analysis, Journal of Research of the National Bureau of Standards 57 (1956) 217-221.

[108] H.E. Kissinger. Anal Chem 29 (1957).

[109] J.A. Augis, J.E. Bennett. Calculation of the Avrami parameters for heterogeneous solid state reactions using a modification of the Kissinger method, Journal of Thermal Analysis 13 (1978) 283-292.

[110] C.A. Schneider, W.S. Rasband, K.W. Eliceiri. NIH Image to ImageJ: 25 years of image analysis, Nature Methods 9 (2012) 671-675.

[111] H.E. Cook. On first-order structural phase transitions—I. General considerations of pre-transition and nucleation phenomena, Acta Metallurgica 23 (1975) 1027-1039.

[112] A. Verma, N. Wanderka, J.B. Singh, M. Sundararaman, J. Banhart. On the evolution of long-range order from short-range order in a $Ni_2(Cr_{0.5}Mo_{0.5})$ alloy, Journal of Alloys and Compounds 586 (2014) 561-566.

[113] A. Verma, N. Wanderka, J.B. Singh, B. Kumar, J. Banhart. Statistical analysis of composition fluctuations and short-range order in stoichiometric Ni–Cr–Mo alloys, Ultramicroscopy 132 (2013) 227-232.

[114] A. Arya, S. Banerjee, G.P. Das, I. Dasgupta, T. Saha-Dasgupta, A. Mookerjee. A first-principles thermodynamic approach to ordering in Ni-Mo alloys, Acta mater. 49 (2001) 3575–3587.

[115] A. Janotti, M. Krcˇmar, C.L. Fu, R.C. Reed. Solute Diffusion in Metals: Larger Atoms Can Move Faster, Physical Review Letters 92 (2004) 085901-085901-085901-085904.

[116] M. Krcmar, C. Fu, A. Janotti, R. Reed. Diffusion rates of 3d transition metal solutes in nickel by first-principles calculations, Acta Materialia 53 (2005) 2369-2376.

[117] K. Hirano, R.P. Agarwala, B.L. Averbach, M. Cohen. Diffusion in Cobalt-Nickel Alloys, Journal of Applied Physics 33 (1962) 3049-3054.

[118] K. Monna, H. Suto, H. Oikawa. J. Jpn. Inst. Metals 28 (1964) 188-192.

[119] C.E. Campbell, W.J. Boettinger, U.R. Kattner. Development of a diffusion mobility database for Ni base superalloys, Acta Materialia 50 (2002) 775-792.

[120] K.S. Chan, Y. Pan, Y. Lee. First-Principles Computation of Transition-Metal Diffusion Mobility, Defect and Diffusion Forum 266 (2007) 73-82.

[121] H. Heidsiek, R. Scheffel, K. LÜCke. The influence of quenched-in and thermal vacancies upon short-range-order formation in a Ni11.4at % Cr alloy, Le Journal de Physique Colloques 38 (1977) 174-177.

[122] W. Kohl, R. Scheffel, H. Heidsiek, K. Lucke. Investigation of the kinetics of short range order formation and quenched-in vacancy annihilation in Au-l5at.%Ag by resistivity measurements, Acta Metallurgica 31 (1983) 1895-1908.

[123] L.D. Landau, E.M. Lifshitz. Statistical Physics, Addison-Wesley, Cambridge, 1958.

[124] A.G. Khachaturyan. Theory of structural transformations in solids, Wiley, New York, 1983.

[125] W.A. Soffa, D.E. Laughlin. Solid → Solid Phase Transformations, T.M.S.-A.I.M.E, Pa, U.S.A, 1982.

[126] J. Rodriguez-Carvajal. Recent advances in magnetic structure determination by neutron powder diffraction, Physica B:COndensed Matter 192 (1993) 55-69.

[127] H.M. Tawancy. Order Strengthening in a Nickel base Superalloy (Hastelloy Alloy S), Metallurgical Transactions A 11A (1980) 1764-1765.

[128] H.M. Tawancy. Deformation behavior of ordered Ni-Mo and Ni-Mo-Cr alloys, Scripta Metallurgica et Materialia 32 (1995) 2055-2060.

[129] H.C. Pai, B.C. Maji, A. Biswas, M. K, M. Sundararaman. Calorimetric Studies of Dissolution Kinetics of $Ni_2$(Cr,Mo) Phase in Ni-Cr-Mo Alloys Using Non-Isothermal Approach, Defect and Diffusion Forum 279 (2008) 111-116.

[130] B.D. Cullity. Elements of X-RAY Diffraction. In: Cohen M, (Ed.). United States of America: ADDISON-WESLEY PUBLISHING COMPANY, INC., 1956.

[131] C. Giacovazzo, H.L. Monaco, G. Atioli, D. Viterbo, G. Ferraris, G. Gilli, G. Zanotti, M. Catti. Fundamentals of Crystallography, IuCr Texts on Crystallography, Oxford University Press, USA, 2002.

[132] International Tables for X-Ray Crystallography, The Kynoch Press, Birmingham, England, 1974.